DOUBLE-ROTOR SWITCHED RELUCTANCE MACHINE FOR INTEGRATED ELECTRO-MECHANICAL TRANSMISSION IN HYBRID ELECTRIC VEHICLES

DOUBLE-ROTOR SWITCHED RELUCTANCE MACHINE FOR INTEGRATED ELECTRO-MECHANICAL TRANSMISSION IN HYBRID ELECTRIC VEHICLES

By

YINYE YANG, B.ENG., M.S.

A Thesis
Submitted to the Department of Electrical and Computer Engineering
and the School of Graduate Studies
of McMaster University
in Partial Fulfillment of the Requirements
for the Degree of
Doctor of Philosophy

Doctor of Philosophy (2013) McMaster University
(Electrical and Computer Engineering) Hamilton, Ontario

TITLE: **Double-Rotor Switched Reluctance Machine for Integrated Electro-Mechanical Transmission in Hybrid Electric Vehicles**

AUTHOR: Yinye Yang, B.Eng. (Tsinghua University), M.S. (University of Illinois at Champaign-Urbana)

SUPERVISORS: Ali Emadi, Ph. D., Fellow IEEE
Canada Excellence Research Chair in Hybrid Powertrain
Director, McMaster Institute for Automotive Research and Technology (MacAUTO), McMaster University

Nigel Schofield, B.Eng. (Hons), Ph.D., C.Eng., MIET
Professor, Department of Electrical and Computer Engineering, McMaster University

NUMBER OF PAGES: XXIV, 285

To my parents Deen and Li, my girlfriend Eileen and my supervisors Ali and Nigel for all your consistent help and support.

ABSTRACT

The world transportation sector has been relying on the oil industry for more than a hundred years, accounting for the largest oil consumption and one third of the greenhouse gas emissions. However, with the boosting demand, escalating national energy security concerns and emerging environmental issues, reducing and displacing petroleum fuel in transportation sector has become an urging global target. As a result, hybrid electric vehicles evolve as one solution to displace petroleum fuel by utilizing vehicle onboard electrical systems, achieving higher fuel economy and less emissions by vehicle electrification and hybridization.

However, since hybrid electric vehicles add additional electrical components and systems to realize better fuel economy, the system complexity increases and thus the cost increases. Hence, it is an objective of this thesis research to focus on the integrations and optimizations, aiming to simplify and optimize the hybrid power-trains in both system level and component level.

This thesis contributes to a novel integrated electro-mechanical hybrid transmission that is potentially more compact and more operational flexible with fewer components compared to the GM Allison Two-Mode hybrid transmission. Comprehensive commercialized power-train transmissions are reviewed and analyzed to serve as background information for comparison. It also contributes to a family of double-rotor switched reluctance machines that are more integrated and suitable for hybrid electric vehicle applications. A prototype double-rotor switched reluctance machine has

been built and tested for concept proving. Detailed machine design process is reported with the emphasis on design novelties. Finite element analysis and optimization techniques are applied and the accuracy is confirmed by the experiments. In addition, methods of machine loss analysis, thermal analysis and drive analysis are established; manufacturing and testing procedures are documented in detail that can be used for future machine designs guidance.

ACKNOWLEDGEMENTS

This research was undertaken, in part, thanks to funding from the Canada Excellence Research Chairs Program.

I am grateful and thankful for all the people who advised me, supported me and helped me. Without your help, the completion of this thesis would have been impossible.

First and foremost, I would like to express my sincere gratitude to my supervisors Dr. Ali Emadi and Dr. Nigel Schofield. This work cannot be done without their expert supervision and guidance, encouragement and patience throughout the course of this work. I am grateful for Dr. Emadi's continuous trust and support. For the past three years, his motivation, enthusiasm and visionary plans have advised me and guided me towards a "clearer" and definitely an "electrified" road. The opportunities he provided and the doors he opened have immensely broadened my horizons. The advices he gave will benefit me for the whole life. I am equally grateful for Dr. Schofield. Without his endless support and valuable consulting, this work cannot be finished. The hours he spent, the designs he drew, the bolts he hammered and the grammars he corrected all contribute remarkably to the completion of this thesis. His profound knowledge and stringent attitude have guided me in both academia and personal life. I will always be thankful for both Dr. Emadi and Dr. Schofield in my life. It has been such a great honor to work with them and be friend with them.

I would like to thank Dr. Saeid Habibi and Dr. James Chen for their precious time and valuable suggestions as been my supervisory committee meeting members. I would

like to thank Dr. Berker Bilgin and Phil Woodley for their helpful discussions and suggestions in the weekly presentation.

I would like to thank Edward Kries of Kries Manufacturing Inc. for his fine work and help in building the prototype machine. I would like to thank Fei Peng for his dedicate design of power electronics and control. Thank him for been working with me for many all-nighters to have the experiments done in time.

I also want to express my thanks to all the colleagues and friends from McMaster Automotive Resource Centre (MARC) for being such a great team and for making our laboratory such a pleasant place to work in.

Finally, I would like to thank my family and my dearest parents in particular. Thank them for their constant love and care for all my life. I would also like to thank my girlfriend Eileen for her understanding, believing, and supporting. Without their support, I would never reach this far.

Contents

List of Figures

List of Tables

List of Abbreviations

AD	Analog to digital converter	250
AHS	GM's Allison Two-Mode Hybrid Transmission	47
APC	Automotive Partnership Canada	32
BAS	Belt alternator starter	18
CO_2	Carbon dioxide	6
CVT	Continuously variable transmission	46
DRSRM	Double-rotor switched reluctance machine	1
DSP	Digital signal processing	250
EPA	Environmental Protection Agency	8
EV	Electric vehicles	9
E-CVT	Electric continuous variable transmission	20
EMI	Electromagnetic interference	249
FEA	Finite Element Analysis	135
FPGA	Field-programmable gate array	250
GM	General Motors	18
HEV	Hybrid electric vehicle	1
HWFET	Highway Fuel Economy Test	97
ICE	Internal combustion engine	3
IMA	Integrated Motor Assist	17
ISG	Integrated starter-generator	20
MHD	Micro Hybrid Drive	16
NSERC	National Sciences and Engineering Research Council	32
NVH	Noise, vibration and harshness	284
PHEV	Plug-in hybrid electric vehicles	12
RPM	Revolution per minute	102

SUV	Sport utility vehicles	3
SRM	Switched reluctance machine	106
THS	Toyota hybrid system	21
U.S.	United States	5
UDDS	U.S. Urban Dynamometer Drive Schedule	97
VPI	Vacuum pressure impregnation	232

Chapter 1

INTRODUCTION

1.1 RESEARCH CONTENTS

The research findings reported in this thesis focuses on improving hybrid electric vehicle (HEV) transmission integration to realize a full hybrid power-train solution that potentially simplifies the system complexity and reduces HEV manufacturing cost, while at the same time satisfying the vehicle performance requirements. The thesis first presents the comprehensive review and comparison analysis of different types of HEVs and their operation modes at a system level. A novel electro-mechanical, integrated HEV transmission that is potentially more compact, lower cost, better performance and high efficiency is proposed. As a subcomponent to this HEV transmission, a novel integrated, double-rotor, switched reluctance machine is proposed. Two patents have been filed and applied on each topic. Then the third stage of this PhD thesis focuses on the detailed electro-mechanical design of the proposed integrated double-rotor switched reluctance machine (DRSRM). The DRSRM machine integrates two switched reluctance machines into one machine housing, whereby two separate rotors share one stator assembly to enable two output shafts from one machine, facilitating a more compact and hence potentially lower manufacturing cost switched reluctance machine.

In order to validate the proposed double-rotor switched reluctance machine, a prototype machine is designed with a common stator, interior and exterior rotors. A comprehensive series of simulations have been conducted to optimize the machine design as well as meet the design goals. It concentrates on electromagnetic simulations while thermal simulations, loss simulations and motor drive simulations have also been carried out. In addition, varies of analysis regarding to the machine efficiency, eccentricity loading, winding configurations, and torque ripple compensations, etc. have been done to fully validate the proposed machine. In the end, a prototype double-rotor switched reluctance machine has been built to validate the concept and to confirm the simulation predictions.

The following Sections will present background detail supporting the motivation of this thesis research.

1.2 FUEL EFFICIENT AND CLEANER ROAD TRANSPORTATION

Modern automotive industry has been evolving for more than a hundred years since Karl Benz built the first Patent-Motorwagen road automobile in 1886[1]. From the less than 1 horsepower low-speed wagon to the hundred-horsepower or even thousand-horsepower supercars of today, the automotive industry is always following the trend to manufacture cars with better performance and higher efficiency. Among the numerous technology advancements, the majority of these improvements were made by enhancing the performance of the internal combustion engine (ICE). Engines with higher combustion ratios, more numbers of cylinders, more accurate valve timing and ignition timing controls etc. have been manufactured and widely applied to the automotive industry. The average vehicle power has steadily increased over this time frame to provide better vehicle performance while at the same time component-level and system-level efficiency has increased as well to maintain and improve fuel efficiency against improving power and heavier weight vehicles such as trucks, vans, and sport utility vehicles (SUV). Figure 1.1 illustrates the trends in engine horsepower and fuel efficiency in U.S. light duty vehicles from 1975 to 2012[2].

However, conventional ICE technology predominantly relies on carbon based products as the combustion fuel. Gasoline and diesel fuel, extracted from the crude oil provides high energy density, and due to their wide accessibility, offer relatively low price such that they have dominated the vehicle fuel for the past a hundred years. Nevertheless, the oil prices have risen significantly over the past few decades mainly due to the rising consumption demands and the supply disruptions[3]. Besides, the concern

about the surpassed peak oil, less discovered oil reserves, district disturbance, national policies etc. all result in instability and unpredictability of the global oil market[3]. According to the International Energy Outlook 2010[3] released by the U.S. Energy Information Administration, the world's annual oil consumption reached 495 quadrillion (495×10^{15}) Btu in 2007, increasing by 36% from the 1980 level. And it is the transportation sector that accounts for the largest oil consumption and shows the largest growth in oil demand during the past few decades. Especially with the current soaring demand from developing countries, the oil consumption rate is increasing faster than ever, which can also be revealed in the substantial increase trend of the crude oil price as in Figure 1.2[4].

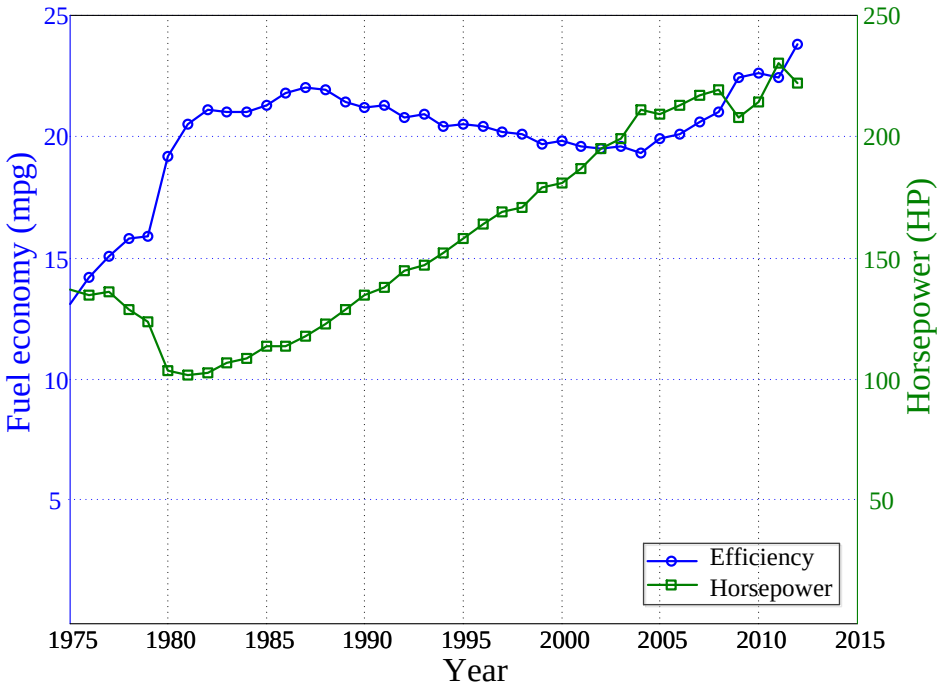

Figure 1.1 Fuel economy and power of U.S. light duty vehicles.

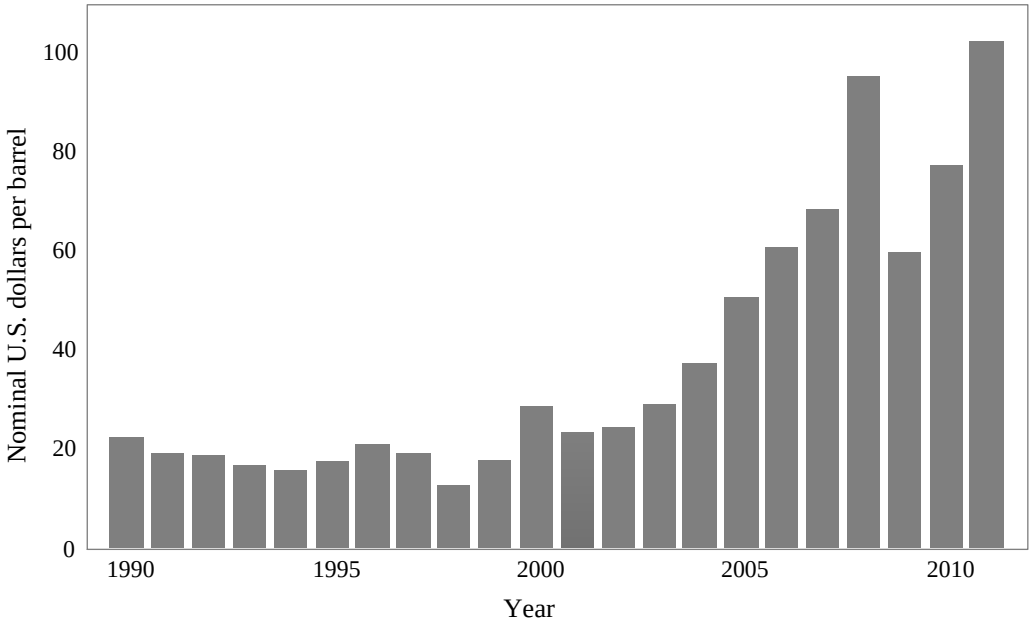

Figure 1.2 U.S. Crude oil refiner acquisition costs 1968-2010[4]

Therefore, automotive companies and consumers are more and more concerned about the feasibility of the conventional fuel and the related conventional vehicle technologies due to their exclusively reliance on the petroleum product.

In addition, energy security is emphasized by many nations as a major priority. Take the United States (U.S.) as an example, U.S. has been relying on foreign oils heavily for the past few decades and it is its government's goal to diversify and reduce its reliance on the imported crude oil and thus to enhance its energy security[5]. Figure 1.3 shows a declining import trend since 2005, which is achieved by producing more domestic crude oil and alternative energy as well as encouraging measures to increase vehicle fuel efficiency[5]. The fuel efficiency standard released by U.S. government in 2012 in collaboration with major auto manufacturers, the United Auto Workers, consumers, and environmental groups required cars and light trucks to achieve an average 54.5 miles per

gallon by 2025[6], saving the average family an estimated $8000 at the pump and helping the United States halfway to its goal to cut imported oil by a third. European countries and Asian countries are also implementing similar fuel efficiency regulations to reduce oil consumption to ensure national energy security[7][8].

Furthermore, there is growing public acceptance that carbon dioxide (CO_2) emissions are one of the primary contributors to global climate change. The burning of conventional petroleum fuels in ICEs generates CO_2, which contributes to a majority portion of the total U.S. greenhouse gas emissions, as illustrated in Figure 1.4[9]. In 2011, the United States generated 6.7 billion (6.7×10^9) metric tons of equivalent CO_2 emissions alone, which is equivalent to the annual greenhouse gas emissions from 1.4 billion (1.4×10^9) passenger vehicles, or carbon sequestered by 171 billion (171×10^9) tree seedlings grown for 10 years[10]. Figure 1.4 illustrates the total U.S. greenhouse emissions by economic sectors in 2011, clearly showing that the transportation sector accounts for nearly one third of the total greenhouse gas emissions, making it the second largest contributor throughout all economic sectors. It has been recorded that the greenhouse gas emissions from the transportation sector have increased by about 18% since 1990 largely due to increased demand for travel and the stagnation of fuel efficiency across the U.S. vehicle fleet[9].

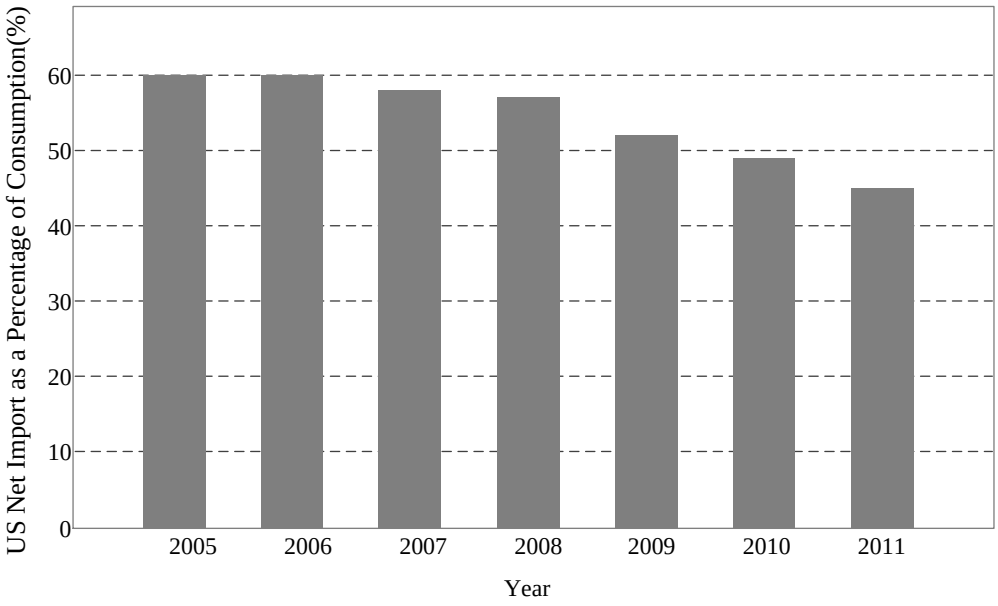

Figure 1.3 U.S. dependence on imported oil declining[5]

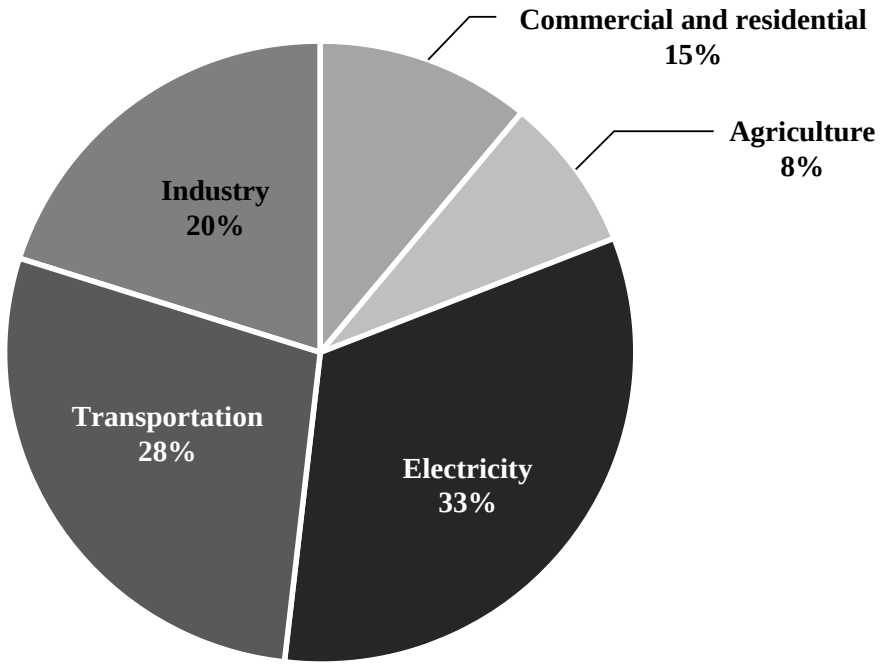

Figure 1.4 Total U.S. Greenhouse gas emissions by economic sector in 2011[9]

In order to reduce the greenhouse gas emissions from transportation sector, regulations have been set in U.S. as well as in many nations for new automotive vehicle models to meet carbon dioxide emission standards. For example in U.S., the Environmental Protection Agency (EPA) released stringent regulations towards CO_2 emissions as shown in Figure 1.5 for passenger cars, light trucks and combined, showing target CO_2 emissions in grams per mile from year 2016 to 2025[11].

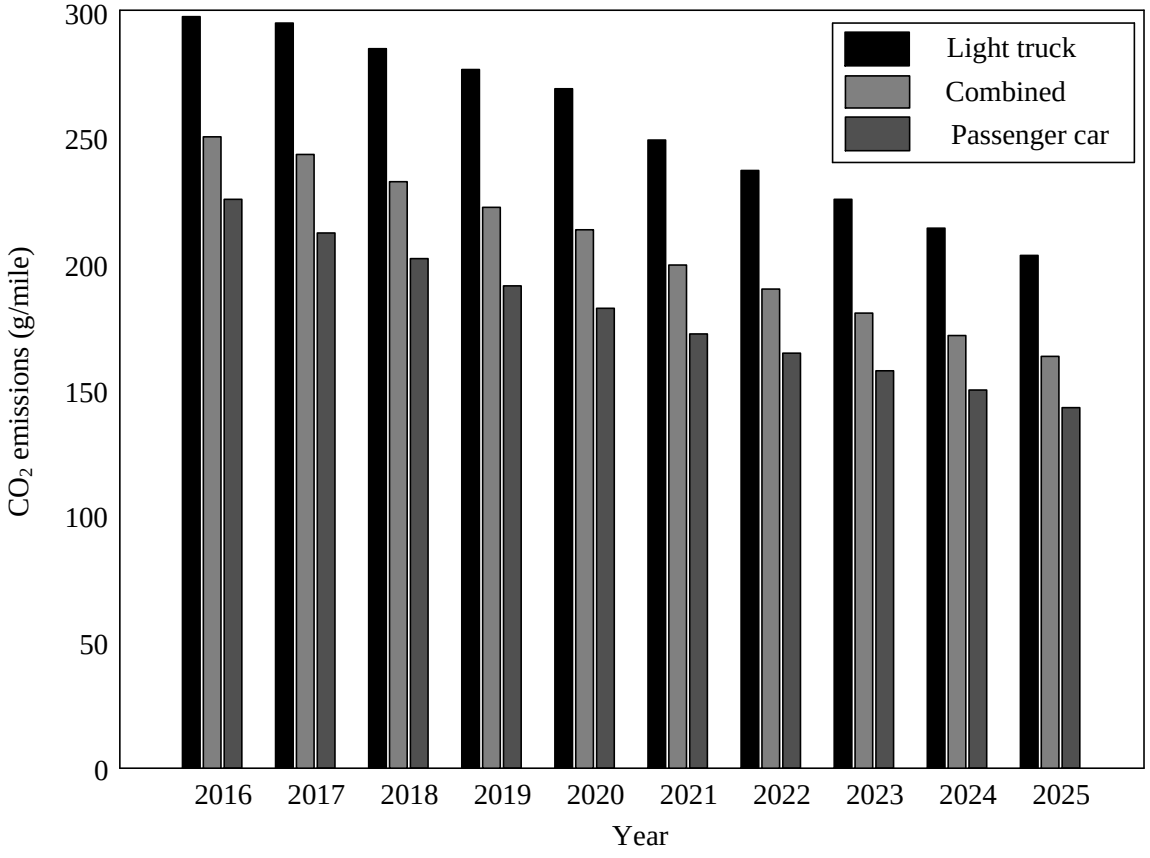

Figure 1.5 Projected CO_2 emissions targets in U.S.[11]

Combining all the factors above, it is evident that the current road transportation sector is almost exclusively dependent on the oil industry. The pressure of oil demand over supply keeps growing and the whole transportation industry is subject to the variation of oil price. On the other hand, the transportation sector significantly impacts the energy security strategies for all nations and the greenhouse gas emissions at the global level. Thus, it is necessary and inevitable for the transportation sector to diversify the fuel sources to avoid the sole dependency on petroleum fuel, improve vehicle efficiency, and reduce greenhouse emissions.

Hence under this background, hybrid electric vehicles (HEV) emerge as one of the transitional vehicles between conventional petroleum-powered vehicles and full all-electric vehicles (EV). As the name suggested, HEV is a type of vehicle that is equipped with at least two sources of on-board energy carriers. One energy carrier usually comes from the conventional products of petroleum, such as gasoline and diesel, which are used to fuel the ICE to generate mechanical power; the other energy carrier is in the form of electricity, which functions to support an additional prime mover on the vehicle.

Figure 1.6 illustrates two simple examples of HEV power-trains highlighting the energy/power flow concepts. The mechanical power and the electric power are integrated either in a series path as shown in the series hybrid configuration or in a parallel path and hence the parallel hybrid. As will be discussed with more details in the following sections, HEVs have great potentials to increase vehicle fuel economy. These potential benefits can be summarized in general for HEVs into three points:

(i) Regenerative braking to retrieving braking energy back into on-board battery.

(ii) Engine shut down to reduce engine energy loss at idling or low speed.

(iii) Engine operation more efficiently with electric machine assistance.

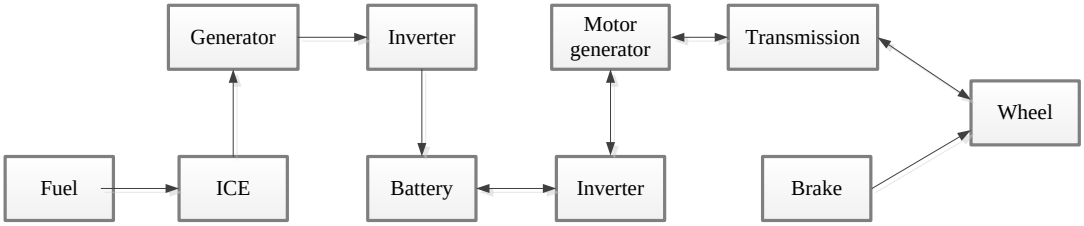

(a) Series hybrid powertrain

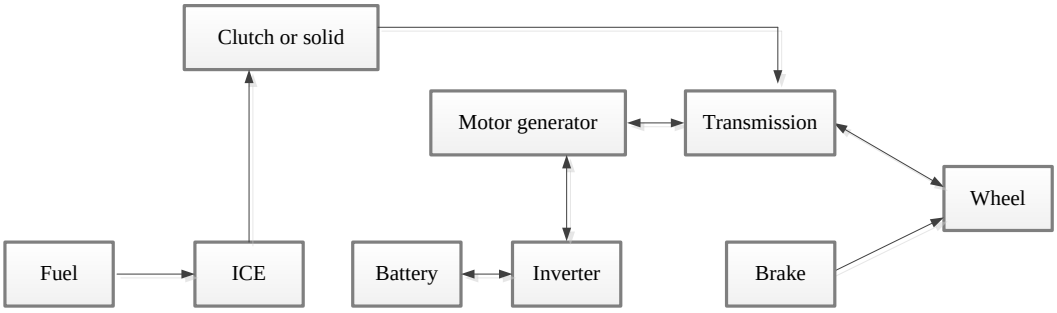

(b) Parallel hybrid powertrain

Figure 1.6 Examples of series and parallel HEV power-trains

1.3 HYBRID ELECTRIC VEHICLES

Unlike conventional vehicles that depend exclusively on petroleum energy, HEVs partially displace petroleum fuels with the use of electricity that can be generated from various forms of energy sources including renewable energy and nuclear energy Furthermore, under proper control and coordination between the internal combustion engine and the electric machines, overall vehicle performance can also be improved while lower emissions and higher fuel economy can be achieved.

In comparison, conventional internal combustion engines are highly inefficient, with an average efficiency of less than 30% due to the maximum heat-work conversion constraint, and they produce a wide range of emissions even with the assistance of after treatment systems[12]. On the other hand, machines that use electricity as their energy source have much higher efficiency, and there are essentially no tailpipe emissions generated because the only by-product of using electric machines is the used battery, which can be recycled or reused for other applications. In general, HEVs produce lower tailpipe emissions than similar conventional vehicles. Even when compared with the well-to-wheel emissions, HEVs significantly reduce the emissions by a third as shown in Figure 1.7[13]. This is because power plants that generate electricity typically have higher efficiency than internal combustion engines; meanwhile, more and more renewable electricity has been generated such as by hydropower and wind power so that the emissions at the generation side are actually decreasing. Thus, by taking advantage of

electricity in electric machines, HEVs can considerably reduce fuel consumed and the air emissions from vehicle tailpipes.

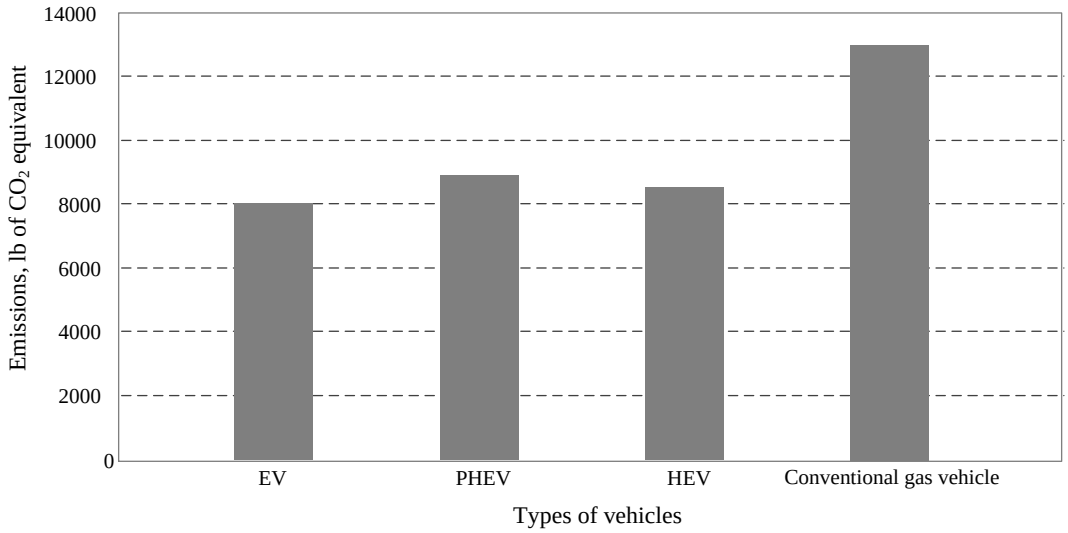

Figure 1.7 U.S. national average annual emissions by vehicle class[13]

The development of HEVs, including plug-in hybrid electric vehicles (PHEV), is considered by many policy makers as one of the most promising and currently practical strategies to displace the oil dependency, improve vehicle fuel efficiency, and reduce environmental pollution from the transportation sector. Regulations have been adopted and incentives have been offered out throughout the world to stimulate research and development. Figure 1.8 plots the HEV sales number as well as the market share[14] up to September 2013 in the United States, which is the largest HEV market in the world. It clearly presents an exponential increasing trend that suggests hybrid electric vehicles are getting more popularity and gradually penetrating into the existing automobile market. Figure 1.9 shows a picture of the 2010 Toyota Prius[15]. Table 1.1 summarizes the current existing commercial HEV models in U.S.

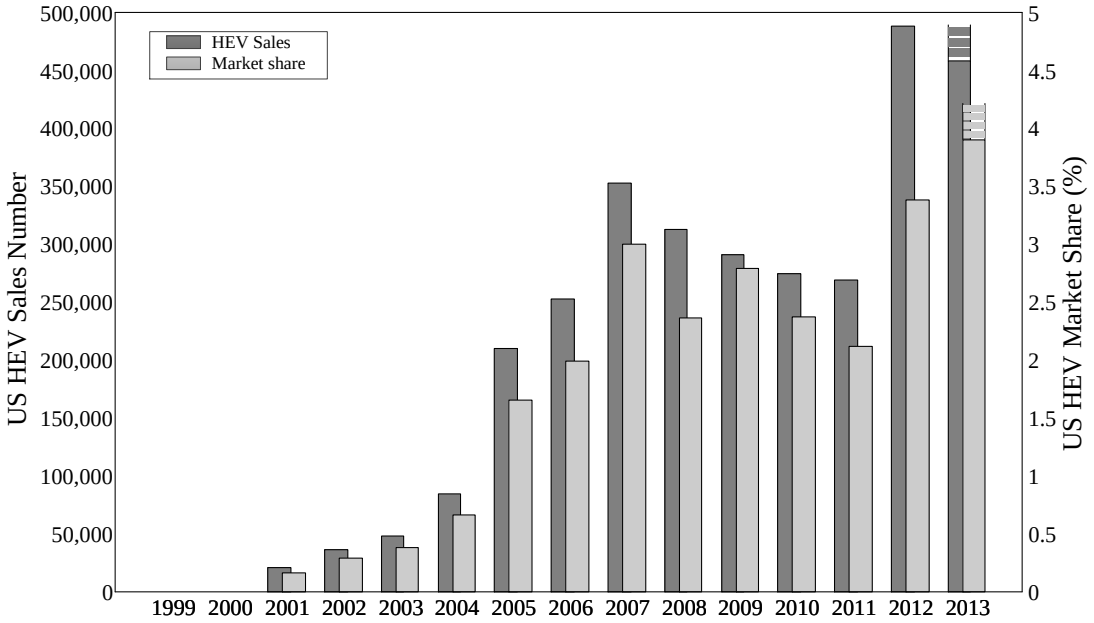

Figure 1.8 U.S. HEV sales[14]

Figure 1.9 Toyota Prius[15]

Table 1.1 HEVs models in U.S. up to September 2013

Acura	ILX Hybrid	BWM	ActiveHybrid 3	Buick	LaCrosse eAssist
Cadillac	Escalade Hybrid		ActiveHybrid 5		
			ActiveHybrid 7		Regal eAssist
Chevrolet	Malibu Eco		ActiveHybrid X6		
	Silverado Hybrid	Ford	Escape Hybrid	GMC	Sierra Hybrid
			Fusion Hybrid		
	Tahoe Hybrid		C-Max Hybrid		Yukon Hybrid
Honda	Civic Hybrid	Hyundai	Sonata Hybrid		
	CR-Z Hybrid	Infiniti	M35h	Mercedes	E400H
	Insight Hybrid	Kia	Optima Hybrid		S400HV
	Accord Hybrid	Lincoln	MKZ Hybrid		ML450 Hybrid
Lexus	CT 200h	Toyota	Avalon Hybrid	Porsche	Cayenne S Hybrid
	GS 450h		Camry Hybrid		
	HS 250h		Prius c		Panamera S Hybrid
	LS 600h		Prius v		
	RX 400h		Prius Liftback	Volkswagen	Jetta Hybrid
	RX 450h		Highlander Hybrid		Touareg Hybrid
	ES 300h				

1.4 HYBRID ELECTRIC VEHICLE TRANSMISSIONS

Hybrid electric vehicles differ from the conventional vehicles in terms of the power-train configurations. In conventional vehicles, the engine is the only power source in the propulsion system, while HEVs typically utilize both mechanical energy from conventional internal combustion engines and electric energy from electric storages to propel the vehicle and power the internal loads, which also defines the two power paths: one mechanical and the other electric. The mechanical path is similar to the conventional petroleum power-train, which includes the fuel tank, engine, clutch or torque converter, transmission, and differential connecting to the wheels, while the electric path, which comprises the battery pack, power electronics for control, and electric machines, is added on par with the mechanical path. The mechanical path and the electric path are intermingled by mechanical couplings such as clutches and gear sets, and they function together to achieve better fuel efficiency and the demanded performance.

With the development of hybrid technology, varieties of HEV transmission configurations have been created. These hybrid transmissions have been widely applied on a range of vehicle types, including passenger cars, sports utility vehicles, trucks, and transit buses. Despite these different configurations and different platforms, all HEV transmissions can be categorized into three groups by looking at the ratio of electric systems power to the overall systems power: micro hybrids, mild hybrids, and full hybrids.

Micro hybrids employ a modest electric portion in the power systems. The typical electric power rating for a micro hybrid sedan is between 3 to 5 kW[16]. Micro hybrids

normally refer to the hybrid vehicles with the start-stop or idle-stop systems, which automatically shut down the engines when vehicles are coasting, braking, or stopped according to certain road conditions, and restart the engines when the speed is back up. The added electric power system can also be used to help supply power to driving accessories such as power steering and air conditioning. Some micro hybrids are also capable of certain levels of regenerative braking. Although micro hybrids are one of the simplest hybrids among the various hybrid configurations, they can provide up to 10% of fuel economy benefits[16], especially in urban driving situations, where frequent stop-and-go is inevitable.

Micro hybrids only incorporate a small portion of the electric system, normally a small motor. This results in a relatively simple structural change and cheaper re-engineering costs while significantly increasing fuel economy and cutting emissions. Therefore, many auto manufacturers applied this technology during the initial transit from conventional petroleum-powered vehicles to HEVs[17]. For example, BMW's micro hybrids incorporated the Efficient Dynamics technologies aimed at reducing fuel consumption and air emissions. Both start-and-stop and regenerative braking functions are available in its micro hybrids. Volkswagen also equipped its micro hybrid fleets with similar features under the name of Blue Motion Technologies. FIAT introduced the PUR-O2 in a range of its micro hybrid models, and Mercedes developed the Micro Hybrid Drive (MHD) onto its Smart hybrid, which is reported to increase fuel economy by nearly 8%[17].

Mild hybrids have a higher level of electric power rating, typically ranging from 7 to 15 kW for a sedan. Consequently, a higher level of fuel-economy gain can be achieved, saving up to 20% in fuel compared with conventional combustion vehicles. Propulsion systems in mild hybrids normally consist of one electrical machine between the engine crankshaft and the transmission input shaft. The added electric machine offers start-stop function, regenerative braking function, and additional electric power to drive the accessories. Some of the mild hybrids can also provide a modest level of power assistance to the engine.

Similar to micro hybrids, mild hybrids are relatively cost effective because they require minimal vehicle platform reconstructions and typically maintain the fundamental manufacturing process. The high diameter-to-length ratio of the electric machine results in a high motor inertia such that the original flywheel of the engine can be replaced by the electric machine. Moreover, the electric machine can also function to start the engine and charge the battery; thus, the added costs of the electric machine and its supporting power electronics are offset by the removal of the starter motor and the alternator from the vehicle.

Mild hybrids have been developed by many auto manufactures. Honda developed the Integrated Motor Assist (IMA) system in 1999 and applied it onto the Honda Insight Hybrid, which was capable of stop-and-start, regenerative braking, and power assisting up to 30% of the engine power. It scored high fuel economy as well as low emissions, and in 2000 was ranked the most efficient gasoline-fueled vehicle certified by the United States

Environmental Protection Agency (EPA). The IMA system was also applied onto Honda Civic hybrid and CR-Z.

The General Motors (GM) Belt Alternator Starter (BAS) system can also be grouped in the mild hybrid category. Similarly, it took advantage of stop-and-start and regenerative braking technologies to improve fuel efficiency and driving performance. The 2007 model Chevrolet Silverado Hybrid pickup truck could achieve an overall fuel savings of 12% compared with its non-hybrid version[17].

Full hybrids have the highest electric portion compared with micro hybrids and mild hybrids. The electric power rating for a full hybrid sedan is typically 30 kW or higher. Full hybrids are defined as those petroleum-electric vehicles that can run on either engine-only mode, battery-only mode, or a combination of the two. In addition to the functions that micro hybrids and mild hybrids are capable of, full hybrids can also operate on an all-electric range where only electric machines are used to propel the vehicle and supply all the internal power loads. However, due to the limited size of the electric machine and the battery pack, full HEVs normally have a relatively short all-electric range with limited electric power output. Typically, full hybrids can achieve more than 40% of fuel economy gains in city drives and have more electric power assistance to increase driving performance.

Table 1.2 summarizes the three categories of HEVs, including their electric rating, average fuel saving amount, cost increasing extent, typical features and several examples under each category.

Table 1.2 Three categories of HEVs and their features

	Electric rating	Fuel saving	Cost Increase	Added Features	Examples
Micro Hybrids	3-5 kW	~10%	Low	Start-and-stop Moderate Regenerative braking Accessories Powering	Mercedes Smart BMW Efficient Dynamics Volkswagen Blue Motion
Mild Hybrids	7-15 kW	~20%	Moderate	Start-and-stop Regenerative braking Accessories Powering Moderate Electric Assistance	Honda Insight Chevrolet Silverado Hybrid Mercedes S-Class Hybrid BMW 7-series Hybrid
Full Hybrids	>30 kW	~40%	High	Start-and-stop Regenerative braking Accessories Powering Electric Assistance Electric-only Drive	Toyota Prius Ford Escape Hybrid Chevrolet Tahoe Hybrid BMW X6 Active Hybrid

Compared with micro and mild hybrids, full hybrids employ the largest electric power portions in HEV power-train systems, and thus a larger battery pack is required to achieve the desired electric drive level. Meanwhile, since the motor is directly coupled with the output drive shaft in the electric-only mode, a robust motor with sufficient speed and torque is demanded. Full hybrids also have relatively more complicated configurations. Most full hybrids integrate the electric power path with the mechanical power path by means of power split devices such as planetary gear sets. Power split devices serve to divide the power from the onboard power plants, i.e., the engine and batteries, and redistribute the power flow between the electric path and the mechanical path to achieve optimal fuel efficiency and driving performance. These added mechanical

components all add to the complexity of full hybrid systems. Therefore, though the full hybrids achieve significantly higher fuel economy and better performance, the manufacturing costs also increase as larger battery packs, more powerful electric machines, and more complicated configurations are implemented.

Full hybrids have attained the highest acceptance compared with the other two as full hybrids fulfill the demanded purpose of reducing fuel consumption and emissions. Up to the end of 2013, Toyota had achieved phenomenal success with its full hybrid model, Toyota Prius, which had sold more than 3 million units throughout the world[18]. GM, Daimler Chrysler and BMW also released several models based on their two-mode hybrid transmission system[19], which is a complex full hybrid system capable of both high efficiency and high performance. In addition, governments around the world released targets and regulations to guide and force automobile industry into more hybridized and more electrified forms, and large incentives were provided to compensate for the initial high costs of the full hybrid technologies.

A substantial portion of research and development also concentrates on the hybridization of the vehicles' propulsion systems in which power-train transmission integration is of significant importance. Chau and Chan[20] presented some emerging energy-efficient technologies for hybrid electric vehicles including two types of hybrid power-trains. One is a power-train with an integrated starter-generator (ISG), which can be applied to either a micro hybrid driven by a belt or a mild hybrid in which the ISG is placed in between the engine and the transmission. The other power-train is the so-called electric continuous variable transmission (E-CVT), which is a full hybrid transmission

power-train utilizing the power-split device to achieve the performance and fuel economy gains. Toyota hybrid system (THS) was taken as one of the E-CVT transmission examples and the fundamental operating principles of the E-CVT were explained in this article. As will be more detailed presented in Chapter 2, Toyota THS system provides high efficiency and compact configuration, which offers features like engine optimal operating, engine idle shut down, regenerative braking, etc. However, the drawback of the THS system is a relatively large power requirement on the traction motor and the lack of efficiency when vehicle runs under high speed.

THS system was also detailed written by Miller[21] , in which the author mainly focused on the full hybrid architectures. In this article, the THS system was named as the input-split hybrid transmission, or input-split e-CVT. In addition, the author also discussed and analyzed the compound-split hybrid transmission, or two-mode hybrid transmission. The two-mode hybrid transmission contains the input-split mode as its first mode, thus achieving similar fuel saving and performance as the input-split hybrid transmission at low speeds. It has an additional power-split mode at high speed to adjust the engine power and the electric power ratio so that to reduce the speed and torque requirement of the traction motor, downsizing the motor as well as reducing the losses on the electric path, thus achieving high efficiency and high performance at high speeds. The drawbacks of the two-mode hybrid transmissions are their high complexity, large volume and weight, and high manufacturing costs, as will also be discussed in Chapter 2.

Different E-CVT hybrid transmission variations were presented in literatures based on the implementation of the planetary gear sets to split the mechanical power and

electric power. U.S. patent 20080242498A1[22] described the E-CVT configuration that Ford Motors invented that utilized the input-split architecture. Schmidt's patents US5558589[23], US5577973[24], US5931757[25], and US6953409[26] presented different variations of two-mode compound-split electromechanical hybrid transmissions. US7427252B2[27] and US7491144B2[28] recorded the two other E-CVT technologies filed by General Motors based on the compound-split hybrid transmission concept. Patent US20100048338A1[29] presented the dual mode input-split compound-split hybrid transmission filed by Caterpillar Inc. Besides, the Timken Company invented the output-split compound-split infinitely variable transmission as detailed in U.S. patent US6964627B2[30] and US6994646B2[31]. Renault had similar inventions based on the infinitely variable transmission concept as described in U.S. patent US7582033B2[32][33]. Figure 1.10 presents some of the integrated power-trains.

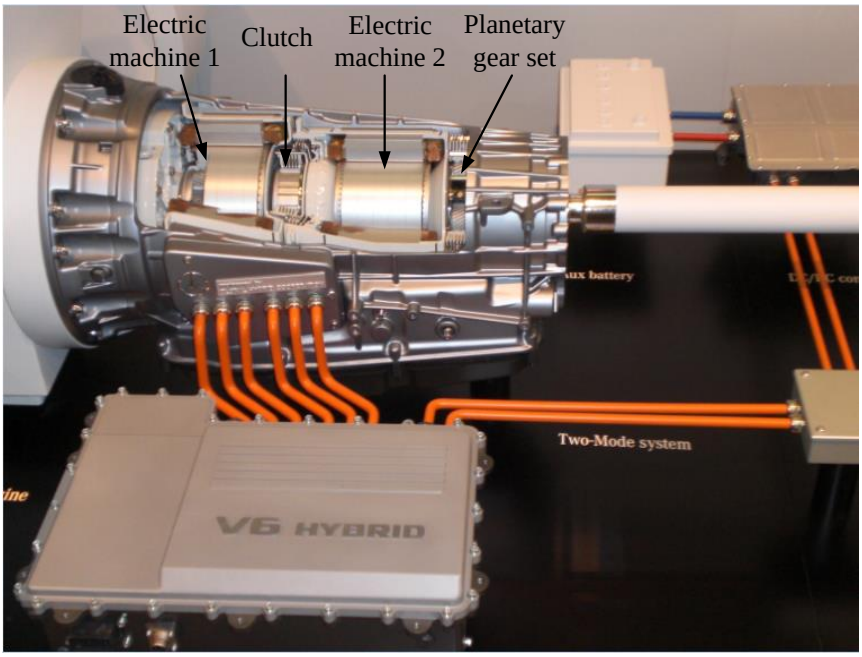

Figure 1.10 Two-Mode hybrid transmission[34]

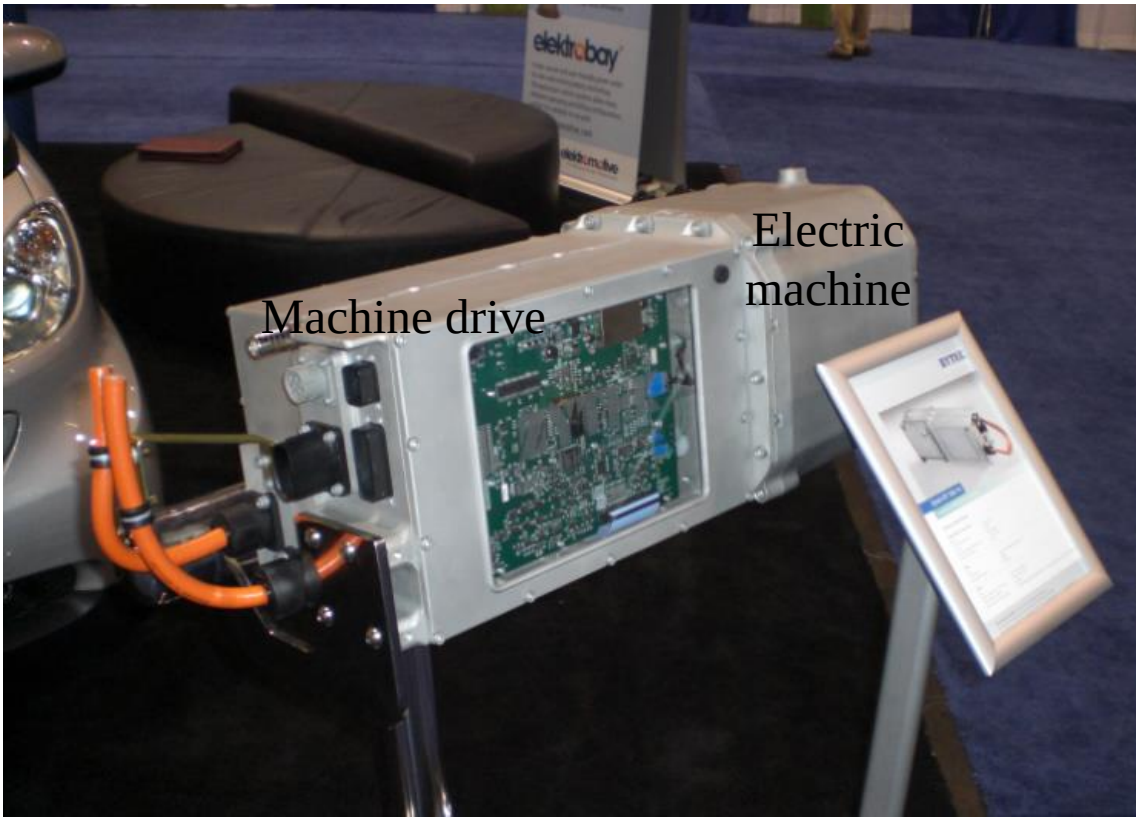

Figure 1.11 Zytek integrated transmission[34]

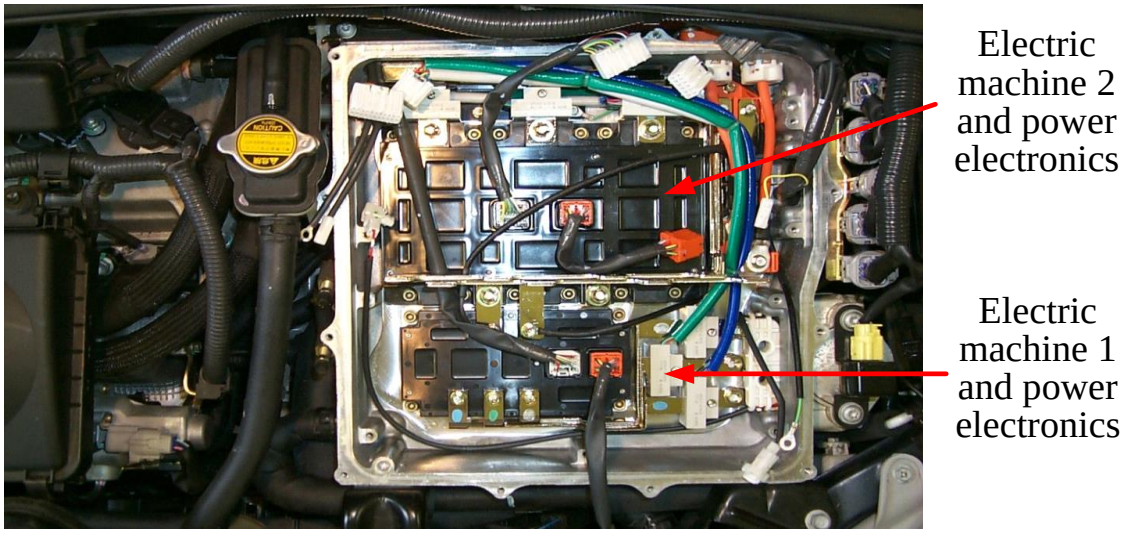

Figure 1.12 First generation Toyota Prius integrated power-train[34]

In both the input-split hybrid transmission and the two-mode hybrid transmission, the mechanical planetary gear sets are used as the power-split devices to split the mechanical power and the electric power. Alternatively, instead of using mechanical devices as the power-split devices, electric power-split devices can also be implemented in the hybrid transmission, potentially further simplifying the overall hybrid transmission configurations.

Nordlund and Sadarangani[35] introduced a power-split hybrid transmission called electric variable transmission using double-rotor electric machine. The double-rotor electric machine serves as the transmission that is placed in between the engine and the output shaft. One of the rotors is connected with the engine output while the other connected with the output driveshaft. The two rotors together form a rotating electric machine by using one of them as a floating "stator".

Other literatures[36][37][38][39][40] also elaborated the double-rotor electric variable transmission concept with induction machines. The fundamental operating principles were explained in details in all these articles. Xu studied the flux paths in the double-rotor electric machine configuration by using electromagnetic simulation[37]. Cui et al. built a prototype double-rotor machine based on induction machines to validate the concept[38] and focused on the optimization design of the double-rotor electric machines to improve the machine power density[39]. Cheng et al. studied the operating modes of the double-rotor electric variable transmission as well as their control strategies[40].

In addition, Yang (not to be confused with the author of this thesis) et al. presented a double-rotor electric machine composed of switched reluctance machines.

Design considerations and operation modes were briefly explained and simple simulation was given[41]. However, the authors did not manufacture any prototypes or do experiments to verify the concept due to manufacturing difficulty and control complexity.

The double-rotor electric variable transmission provides compact and light weight architecture as a full hybrid solution. It achieves the power split function by controlling the two rotors so that the mechanical power and the electric power are divided accordingly to the road demand. However, the double-rotor electric variable transmission may encounter issues such as reliability problems in slip rings and carbon brushes and the heat dissipation problem in the inner rotor with windings on.

Sum the above discussions in hybrid electric transmissions, full hybrid transmissions offer the highest degrees of petroleum fuel displacement and emissions reductions compared to micro and mild hybrids. With the substantial fuel economy benefits, full hybrid transmissions have been successfully commercialized in the current automotive models such as Toyota Prius and GM Tahoe hybrid. However, disadvantages and obstacles such as complicated system architectures and high electric system cost typically exist, and the trade-off between fuel efficiency and vehicle performance brings in further challenges. Thus it is necessary to realize full hybrid transmissions in more integrated and optimized forms so that reduced system complexity and component costs can be achieved, hence the manufacturing cost.

1.5 THESIS CONTRIBUTIONS

The author has contributed to a number of original developments and several design novelties during the course of this Ph.D. research, which will be presented in this thesis and briefly summarized here.

In this thesis, a novel integrated electro-mechanical hybrid transmission configuration is proposed that is capable of two continuous variable transmission modes and five fixed gear ratios. The novel transmission compactly integrates a double-rotor electric machine with two planetary gear sets and two torque transfer devices, typically mechanical clutches and brakes, so that it achieves potentially high fuel efficiency throughout a wide range of vehicular speed and flexible operational modes to satisfy varying output demands. The moderate system complexity and compact volume reduces the assembly difficulties and manufacturing costs, enabling this transmission to be applied more broadly into various sectors of hybrid automobiles.

The integrated electro-mechanical hybrid transmission optimizes the General Motors (GM) Allison Two-mode hybrid transmission system by reducing mechanical components including 1 planetary gear set, 1 clutch and 1 brake. Furthermore, the original two electric machines used in the Allison Two-mode hybrid transmission are replaced by one integrated double-rotor electric machine, thus achieving more compact, lighter and smaller configuration, and hence lower manufacturing cost.

The integrated electro-mechanical hybrid transmission also provides matching or equivalent functions and operation modes as those in the Allison Two-mode hybrid transmission. The optimized transmission structure does not sacrifice the power-train

operation, but instead, it improves the power-train performance by enabling one more fixed gear ratio mode, the engine only mode, in which the electric machines are switched off to avoid energy losses on the electric path.

It is another novelty of this Ph.D. work to establish a family of electric machines that use double-rotor switched reluctance machines that consists of two rotors and one stator integrated in one machine set. The integration of stators and rotors presents a more compact, multi-port output, and lower manufacturing cost switched reluctance machine. Meanwhile, the proposed double-rotor switched reluctance machine has the full capability to operate as two individual switched reluctance machines by utilizing the double rotors separately. It is also possible to operate the two rotors simultaneously as one device by synchronizing the two rotors electrically or mechanically to enhance the power output or reduce torque ripple. Furthermore, the double-rotor switched reluctance machine can be operated as a torque coupler device such as mechanical clutches in hybrid power-train system when either of the rotors is held static or synchronized.

The double-rotor switched reluctance machine serves as an ideal candidate in automotive power-train transmissions. One of the rotors is capable of high torque output to supplement the engine torque while the other rotor is capable of high speed operation that can be coupled with the engine to regulate the engine speed. Thus, the engine can be decoupled from the output drive shaft and operate in its optimal fuel efficiency regions.

The proposed double-rotor switched reluctance machine can be applied to most of the full hybrid vehicles to replace the original two electric machines so that to achieve more integrated and thus more compact and lower cost transmission configurations. The

double-rotor switched reluctance machine can be controlled such that the two rotors operate independently and fully function as two conventional electric machines.

In addition, several novelties have been introduced in the double-rotor switched reluctance machine design phase.

A compact integrated stator geometry design is proposed so that the original two stators of two electric machines are combined into one. The integrated stator reduces the machine volume and weight while maintaining the mechanical rigidity. By utilizing specific designed air gaps to separate the flux in the stator, the two integrated double rotor switched reluctance machines can be separately controlled and work independently.

A Matlab Simulink based motor drive simulation model was created using current source control block to model the actually real time current and inductance in machine windings. A good modeling precision with faster computational time was achieved compared with FEA coupled analysis. Another Matlab Simulink voltage based feedback model that use voltage source control block to model the actually phase inductor was also created with good accuracy. The results of the two drive simulation models match each other and have both been verified by the FEA coupled analysis.

Inter-polar stands were created between the neighboring poles on the stator for both the interior switched reluctance machine and the exterior switched reluctance machine. These inter-polar stands are used to separate the slots for different pole windings and provide better guidance for the windings to be fit in. They also serve to locate the insulation wedges so that windings are kept firmly in the slots. It has been

proved during the machine winding process that the inter-polar stands significantly reduced the manufacturing difficulty and secure the machine with better insulation.

The double-rotor switched reluctance machine provides another novelty in terms of reducing torque ripples by dislocating the double rotors so that the turn on angles of the interior switched reluctance machine offset those of the exterior switched reluctance machine. This happens when both rotors are electrically synchronized with one common output torque frequency. The turn on angles are shifted with a phase difference from the exterior stator winding to the interior stator winding so that the torque peaks are offset from each other and thus compensating each other. Hence, the double-rotor switched reluctance machine can achieve reduced torque ripples as well as less vibration and noise, which are typically the disadvantages that switched reluctance machines are criticized.

1.6 OUTLINE OF THE THESIS

This thesis mainly focuses on the invention of the integrated electro-mechanical hybrid transmission with double-rotor switched reluctance machine.

Chapter 1 introduces the concept of hybrid electric vehicles and hybrid electric transmissions. The background information, literature reviews and motivations of the research in integrated full hybrid transmissions are presented. Research contents of this thesis are briefly stated, while contributions and novelties of the proposed integrated electro-mechanical hybrid transmission with double-rotor switched reluctance machine are claimed.

Chapter 2 comprehensively reviews and analyzes two types of the currently commercialized full hybrids: the input-split hybrid transmission and the two-mode hybrid transmission. Detailed transmission operation principles are analyzed and control strategy modes are discussed. Torque speed analysis and power analysis for each mode are fully explained, and the advantages and disadvantages of each transmission are discussed. Chapter 2 then proposes an integrated electro-mechanical hybrid transmission with double-rotor switched reluctance machine. Comparisons are made between the proposed integrated electro-mechanical hybrid transmission and the original full hybrid transmissions, and the benefits and advantages of the proposed hybrid transmission are stated. Based on the power-train drive cycle simulations, preliminary specifications for the double-rotor switched reluctance machine are derived in the end of Chapter 2.

Chapter 3 then focuses on the design of the double-rotor switched reluctance machine, which is the core component of the proposed integrated electro-mechanical

hybrid transmission. Comprehensive design procedures have been recorded in this chapter. Initial machine geometry is established by analytical calculations and experience equations. Then wide ranges of simulations including electro-mechanical simulation, thermal simulation, frequency simulation, etc. are applied to refine the design and achieve the optimal performance in all aspects. A final design is selected based on the finite element simulation results that satisfy the demanded torque and power output while giving the least torque ripples, volume and weight, and the highest machine operating efficiency.

Chapter 4 presents the details of the prototype double-rotor switched reluctance machine. Mechanical design of the double-rotor switched reluctance machine is illustrated and the manufacturing process of the prototype machine is recorded in details.

Chapter 5 presents the testing results of the prototype double-rotor switched reluctance machine. Comparison between the testing results and the finite element simulations are given and the overall machine performance is evaluated.

Chapter 6 concludes the whole thesis with summary of the Ph.D. work and the possible future plans for the following work.

Chapter 2

INTEGRATED ELECTRO-MECHANICAL HYBRID TRANSMISSION

2.1 INTRODUCTION

Hybrid electric vehicles (HEVs) have continued to draw increasing public attention since the first modern hybrid car, the Toyota Prius, went into production in 1997. Especially recently, with soaring gasoline prices and the further stringent governmental emissions control standards internationally, automotive researchers and manufacturers have been urged to study and develop greater energy efficient power-train solutions. For example, the Automotive Partnership Canada (APC), an affiliate of the National Sciences and Engineering Research Council (NSERC) of Canada has recently announced an $18.1 million (Canadian) funded project investigating in the next generation of hybrid electrified power-train concepts[42]. HEVs are one of the most promising vehicle technologies that can address the energy and environmental problems in the transportation sector since they are building on the established automotive manufacturing base.

A substantial portion of hybrid electric vehicle (HEV) research and development is primarily concentrated on the hybridization of the vehicle propulsion systems in which transmission integration is of significant importance. Thus, hybrid transmissions serve as

key components in hybrid electric vehicle power-trains. Electro-mechanically integrated transmissions refer to transmissions that combine electrical energy to the conventional mechanical energy via integrated mechanisms, i.e. gears, clutches, that enable the variable control of power from the two energy sources. Typically, the electro-mechanical integrated transmission will take the form of power split configurations where part of the mechanical energy is directly transferred via gear stages to provide part of wheel load, while the remaining energy is merged with the electric energy to provide the remaining load. The combined power from internal combustion engines and electric machines are outputted with a certain mechanical-to-electric power split ratio depending on the demanded road load and achievable transmission efficiency.

Different types of advanced hybrid power-trains have already been developed. Toyota for example, their Hybrid Synergy Drive System (THS), an integrated electro-mechanical hybrid transmission system has been commercially mass-produced since 1997. The THS is currently the most popular hybrid transmission system on the market[43]. The two-mode hybrid is another type of full hybrid that was jointly developed by General Motors (GM), DaimlerChrysler, and BMW under the name of Global Hybrid Cooperation. Both the THS and the two-mode hybrid utilize full hybrid transmission architectures to achieve high efficiency and performance. This Chapter will discuss the operating principles, advantages and disadvantages of these two types of full hybrid transmissions and propose an integrated electro-mechanical hybrid transmission that will be used as the design foundation to define the integrated double-rotor electric machine.

2.2 INPUT-SPLIT HYBRID TRANSMISSION

2.2.1 Toyota Hybrid Synergy Drive System

An input-split hybrid transmission utilizes power split devices at the input side of the transmission that connects to the engines and the electric machines such that power can be directly split into the mechanical path and/or the electric path. It is one of the most common full hybrid transmission configurations and it is the simplest and most compact. Toyota Hybrid Synergy (THS) Drive System[44][45] uses this type of architecture. As shown in Figure 2.1, the THS system combines a gasoline engine with two electric machines through a planetary gear set. The planetary gear set splits the engine power into a mechanical path and an electric path. By adjusting the portions of power transferred through these two paths, the THS achieves the variable output speed and torque. A planetary gear set is comprised of an outer ring gear, an inner sun gear, and a set of planet gears that are mounted on a movable carrier and mesh with both the ring gear and the sun gear. The carrier, the ring gear and the sun gear rotate concentrically, as illustrated in Figure 2.2, showing the mechanical arrangement schematically (a), the mechanical symbolic representation (b) and block diagram representation (c), where R represents the ring gear, C the planetary gear carrier and S the sun gear.

As can be observed in Figure 2.2 (c), each planetary gear set has three mechanical ports. Thus, input from any two of the ports will define the output for the third one. The fundamental equation governing the planetary gear sets can be derived based on the relative motions of the three gears[46]:

$$\omega_s + k\omega_r = (1+k)\omega_c \tag{2.1}$$

where ω_s is the angular speed of the sun gear, ω_r is the angular speed of the ring gear, ω_c is the angular speed of the planet carrier and k is the gear ratio between the ring gear and the sun gear (the ratio of the ring gear radius to the sun gear radius). Here, we neglect losses in the system in order to derive the dynamic relationship between the input and the output.

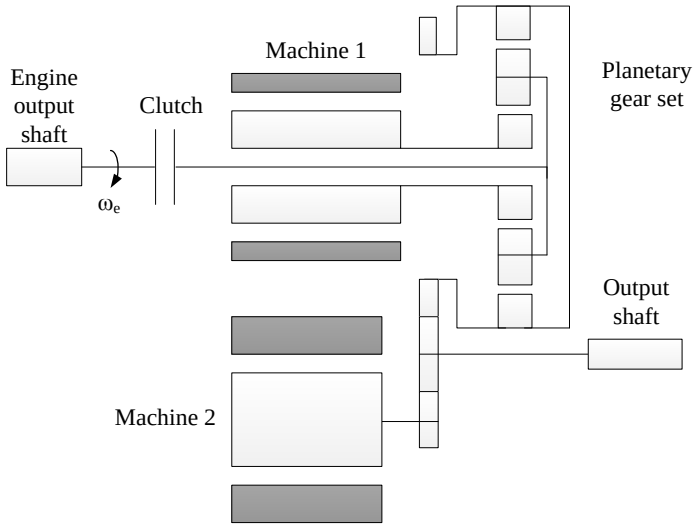

Figure 2.1 Toyota Hybrid Synergy Drive System

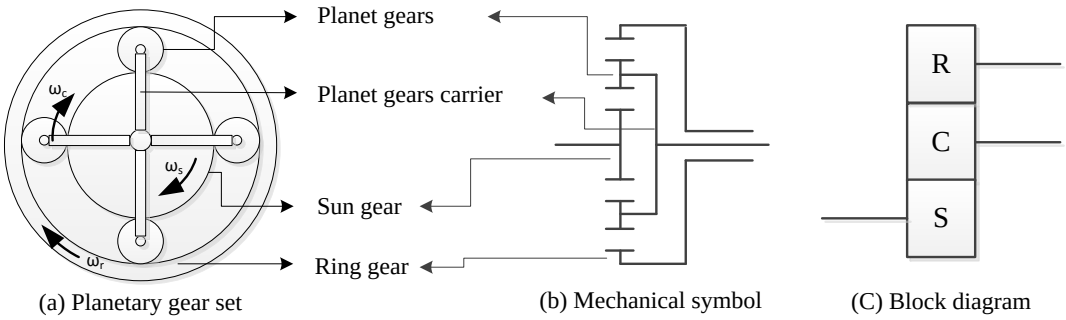

Figure 2.2 Architecture of planetary gears

For the THS configuration shown in Figure 2.1, the engine output shaft is connected to the planet carrier of the planetary gear set through a clutch which acts to connect or can detach the engine from the power-train when necessary. Therefore, the engine speed, ω_e in Figure 2.1, equals to the planet carrier speed, ω_c, when the clutch is closed. Machine 1 is directly connected to the sun gear of the planetary gear set, providing the speed coupling. The ring gear and Machine 2 are coupled through a pair of engaged gears and, together, supply the output torque and hence power to the vehicle wheels. Machine 2 functions to supplement the engine torque, thus allowing the engine to operate at more efficient or less polluting areas of its performance envelope. Machine 1 acting as a generator and Machine 2 acting as a motor together electrically perform the function of a mechanical speed variator by transferring power via a battery pack (not shown here). When engine power is transferred to the transmission input shaft, the planetary gear set functions to split this power into a mechanical path and an electric path. Most of the power would directly transfer through the mechanical path to the final drive, while the remaining power transfers to the Machine 1 acting in generator mode, i.e., the electric variator path. Based on the drive system load requirements and the battery state-of-charge, the generator (Machine 1) either transfers the power to the battery to store additional energy from the engine, to absorb the regenerative braking energy, or to power Machine 2, which acts in the motoring mode. Machine 2 thus converts electric power into mechanical power to drive the vehicle. The THS system can be simply represented as shown in Figure 2.3.

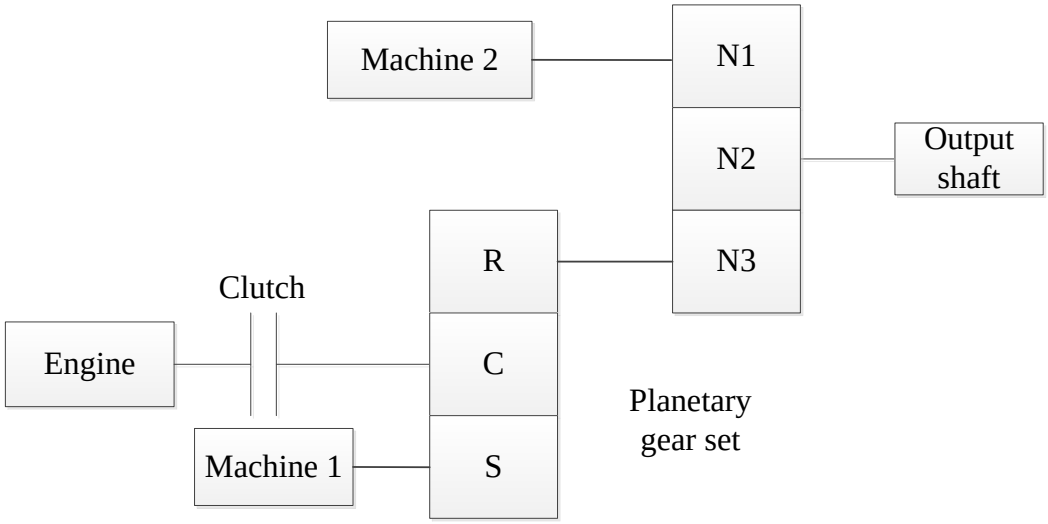

Figure 2.3 Simplified block diagram representation of the THS system

Referring to Figure 2.3, the symbols N1, N2, and N3 represent the number of gear teeth in the spur gear system that connects Machine 2 with the planetary gear set as well as the output driveshaft. Based on equation (2.1), the output speed of the engine and that of Machine 1 together determine the output speed of the ring gear, which thus determines the output speed of the drive shaft. The output shaft speed can be derived:

$$\omega_o = \frac{N_3}{N_2}\left(\frac{1+k}{k}\omega_e - \frac{1}{k}\omega_1\right) \tag{2.2}$$

where ω_e is the engine angular speed, ω_1 is the angular speed of Machine 1 and ω_o is the drive shaft output speed. Since Machine 2 is directly connected to the output drive shaft through spur gears, the output shaft speed can also be expressed as:

$$\omega_o = \frac{N_1}{N_2}\omega_2 \tag{2.3}$$

where ω_2 is the angular speed of Machine 2.

Equation (2.2) indicates that the drive shaft output speed can be decomposed into two parts, one from the engine and the other Machine 1. Thus, the engine speed is detached from the vehicle road speed, and Machine 1 functions to adjust the engine speed. The static torque relationships between the planetary gear set can be derived based on Kane's method[47][48]:

$$T_s = -\frac{1}{1+k}T_c \tag{2.4}$$

$$T_r = -\frac{k}{1+k}T_c \tag{2.5}$$

where T_s, T_c, and T_r are the overall external torques applied on the sun gear, planet carrier and ring gear respectively. The negative sign in (2.5) indicates that the external torques applied have opposite rotations. In order to simplify the calculation and the expression, only steady state conditions are considered. The instantaneous dynamic equations can be simply derived from the steady state equations by adding the inertial and acceleration terms. Equations (2.4) and (2.5) indicate the torque relationship between the three planetary gear components, from which it is apparent that torque values of any two components in the planetary gear system depend on each other. Once one of the input torque values is known, the other two components will have fixed values. Hence, as in the steady-state, the torque relationships between the power sources and the output shaft are shown as below:

$$T_o = \left(\frac{N_3}{N_2}\right)\left(\frac{1}{1+k}\right)T_e + \left(\frac{N_3}{N_1}\right)T_2 \tag{2.6}$$

where T_e and T_2 are the torque output from the engine and Machine 2 respectively, and T_o is the drive shaft output torque.

From equations (2.2) and (2.6), it is apparent that either the engine speed or the engine torque is decoupled from the final drive output shaft, thus by appropriate control, the engine can be operated optimally for improved fuel economy and reduced emissions. The integrated feature of the transmission also improves vehicle performance by facilitating various operating modes that coordinate motoring and generating functions according to the road conditions:

(i) ***Electric only mode***

The engine is turned off and mechanically detached by opening the clutch. Machine 2 provides the traction power to drive the vehicle either forward or backward within a limited distance range, typically restricted by the size of the battery, or in essence, the available battery state-of-charge. The maximum torque that can be applied is therefore constrained by the rating of Machine 2.

(ii) ***Maximum power mode***

When the vehicle accelerates, both Machine 2 and Machine 1 are in motoring mode to assist the engine to realize the demanded peak power.

(iii) ***Battery charging mode***

The engine provides power in excess of that demanded by the road load or when the vehicle is at rest, i.e. at traffic lights. Rather than turning the engine off for short periods, this additional power goes to the battery via Machine 1 in generation mode. Machine 2 can still work in motoring mode to regulate the engine torque.

(iv) ***Regenerative mode***

When the vehicle decelerates, both Machine 1 and Machine 2 work in the generating mode to absorb the kinetic energy and charge the battery.

Since both of the electric machines can operate in either motoring or generating modes, greater system flexibility is achieved. With appropriate machine controls, the THS system can achieve high fuel efficiency while maintaining acceptable performance.

A drawback of the THS system is that Machine 2, the main traction machine always engages with the output shaft, as shown in equation (2.3). Thus, a machine capable of high speed operation is required to meet the designed maximum vehicle speed. The maximum vehicle speed is also limited by the maximum speed of Machine 1, which is smaller and acts as the speed coupler to regulate the engine speed. The fuel economy benefits would decrease as the vehicle speed increases due to the high speed operation of both the machines, which is not operating in their optimum efficiency regions[49].

Further, the THS system has a relatively lower efficiency on the electric path. Since the THS system utilizes the planetary gear set to divide the engine power into the mechanical path and the electric path, the portion of the power that goes into the electric path will suffer the losses incurred in Machine 1 and Machine 2 windings, core losses, losses of the AC/DC, DC/AC converters, and the energy conversion losses through the battery. The energy is converted from mechanical to electric power and then again back to mechanical power, which impacts on efficiency. In comparison, the mechanical path has a much higher efficiency since the gear-to-gear transmission efficiency is typically 98% or better[50]. It is typically estimated that the efficiency in the electric path is close to 70% while the efficiency in the mechanical path is greater than 90%[49].

2.2.2 Mode Analysis and operating principles

By equating the input power of Machine 1 to the output power of Machine 2, it can be assumed that all the power at the output drive shaft comes from the engine input power. Thus, the power can be expressed by the product of speed and torque:

$$\omega_1 T_1 + \omega_2 T_2 = 0 \tag{2.7}$$

where ω_1 and T_1 are the input speed and torque of Machine 1, ω_2 and T_2 are the input speed and torque of Machine 2. From the torque equation (2.4) and speed equation (2.2), the torque and speed relationships between Machine 1 and the engine can be derived as:

$$T_1 = -\left(\frac{1}{1+k}\right)T_e \tag{2.8}$$

$$\omega_1 = (1+k)\omega_e - k\left(\frac{N_2}{N_3}\right)\omega_o \tag{2.9}$$

According to the speed and torque relationship in the THS transmission, the portion of the electric path power to the total engine input power can be expressed as:

$$\frac{P_1}{P_e} = \frac{T_1\omega_1}{T_e\omega_e} = \frac{-\left(\frac{1}{1+k}\right)T_e\left[(1+k)\omega_e - k\frac{N_2}{N_3}\omega_o\right]}{T_e\omega_e}$$

$$\frac{P_1}{P_e} = \left(\frac{k}{1+k}\right)\left(\frac{N_2}{N_3}\right)\frac{\omega_o}{\omega_e} - 1 \tag{2.10}$$

where P_1 is the power that goes through Machine 1 and P_e is the total engine input power.

The second term of the first equation in (2.10) can be used to determine the power-train operation mode for a given ratio of the output shaft angular speed to the engine angular speed:

(a) When $0 < \frac{k}{1+k}\frac{N_2}{N_3}\frac{\omega_o}{\omega_e} < 1$, then $-1 < \frac{P_1}{P_e} < 0$

Part of the engine power flows into the electric path and Machine 1 functions as a generator.

(b) When $\frac{k}{1+k}\frac{N_2}{N_3}\frac{\omega_o}{\omega_e} > 1$, then $\frac{P_1}{P_e} > 0$

Machine 1 is motoring to provide power to the final drive.

(c) When $\frac{k}{1+k}\frac{N_2}{N_3}\frac{\omega_o}{\omega_e} = 0$, then $\frac{P_1}{P_e} = -1$

The transmission output speed is zero and all the engine power goes via Machine 1 to charge the battery.

(d) When $\frac{k}{1+k}\frac{N_2}{N_3}\frac{\omega_o}{\omega_e} = 1$, then $\frac{P_1}{P_e} = 0$

All the engine power goes into the final drive via the mechanical path.

Depending on the ratio of the output speed to the engine input speed, the portion of the engine power that goes into the electric path can be determined from equation (2.10). The more engine power that goes into the electric path, the more power is lost due to the inefficiencies in the electric path during the power conversions than the mechanical path.

For scenario (d), when $P_1 / P_e = 0$, there is no engine power transmitted through the electric path. This particular drive shaft output speed to input engine speed ratio ω_o / ω_e associated with the zero electric power is called the "mechanical point", where there is no electric path loss in the transmission system, as indicated on Figure 2.4.

When ω_o / ω_e is around the mechanical point, the portion of the engine power that goes into the electric path is low, as shown by the arrows on Figure 2.4, which is the implementation of equation (2.10) for representative values of *k*, N_2 and N_3. More engine power will be split into the electric path as ω_o / ω_e moves away from the mechanical point. Since there is only a single mechanical point, the input-split hybrid transmission

can also be categorized as a single mode hybrid transmission. It will be seen later in Section 2.3 that the two-mode hybrid transmission has more than one mechanical point. It is noted in this analysis the values for k, N_2 and N_3 are arbitrary chosen as an example to illustrate the concept of the power portion and the single mechanical point, i.e. when $P_1 / P_e = 0$. In this case, k =1.5 and $N_2 / N_3 = 1.5$.

Typically in the input-split hybrid transmission, the engine speed is expected to be within a certain limited range where high engine operating efficiency can be achieved. Thus, the mechanical point in the THS system is typically designed at the point where high fuel economy for the most frequently used operating points under specific drive cycles can be achieved. This inevitably sacrifices some vehicle performance at other operating points since there is only one mechanical point in the input-split hybrid transmission. The THS system efficiency typically reduces at high vehicle speed[51].

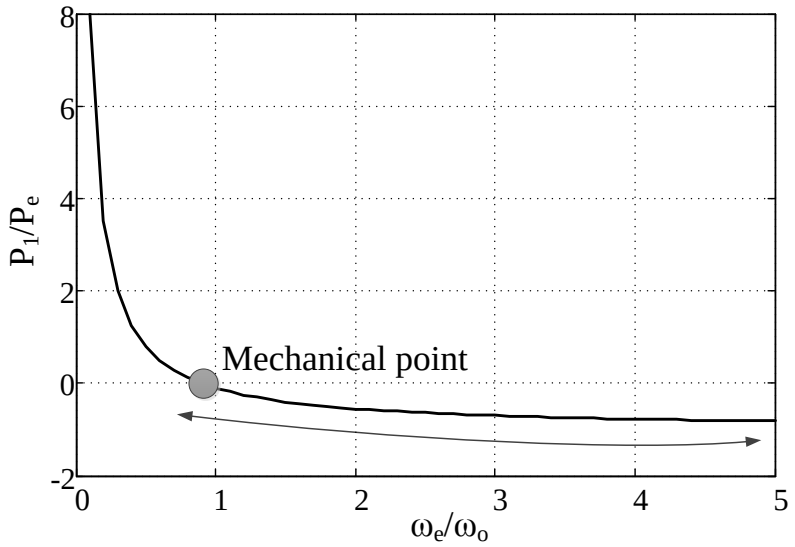

Figure 2.4 Power split ratio in input-split mode

However, in spite of the shortcomings described in this section, the Toyota power split compound hybrids achieve good fuel-economy improvements and emissions reductions compared to conventional ICE vehicles[52]. Meanwhile, the relatively simple structure of the power split configuration offsets the cost increments of the additional electric components such as the battery, power conversion electronics and electric machines, thus maintaining a reasonable sale price compared with conventional vehicles as evidenced by increasing sales volumes. The unchanged driving performance also contributes to the sales success of the Toyota power split hybrids.

2.3 COMPOUND TWO-MODE HYBRID TRANSMISSION

2.3.1 Introduction

Hybrid transmissions that contain both input-split operational mode and compound-split operational mode are referred as compound two-mode hybrid transmission. The input-split mode is the same as discussed in the THS system, while the compound-split hybrid refers to a hybrid transmission that utilizes power split devices at both the input end and the output end of the transmission such that the engine power and the electric machine power can be split and combined in a compound way. As discussed in Section 2.2.2, the input-split operational mode has one mechanical point, while the compound-split operational mode provides another two mechanical points, thus reducing the power transmitted through the electric path at higher speeds, hence improving the overall transmission efficiency, as will be detailed discussed in Section 2.3. GM commercializes the two-mode hybrid and utilizes the compound-split hybrid transmission configuration.

The two-mode hybrid is a type of compound hybrid transmission that was jointly developed by GM, DaimlerChrysler, and BMW under the name of Global Hybrid Cooperation. The transmission incorporates the engine, electric motor and generator, and mechanical gear sets in a compound two-mode hybrid transmission system[53][54]. Similar to the Toyota's THS transmission system, the two-mode hybrid transmission takes advantage of planetary gear sets to integrate the mechanical power path with the electric power path. However, unlike the THS system, the two-mode hybrid transmission can operate in two different continuously variable transmission (CVT) modes by using

multiple planetary gear sets together with clutches and brakes. Depending on the vehicle speed and load requirements, the transmission system selects one of the CVT operation modes, either the input-split mode or the compound-split mode, to achieve the optimal fuel economy without sacrificing vehicle performance[55][56].

Recapping on the discussion in Section 2.2, the input-split transmission refers to the configuration in which engine power is transmitted to an input member of the transmission, and then splits through a power differential device into two paths, i.e. the mechanical path and the electric path, to finally supply the output power to the road load. The ratio of the electric power path to the mechanical power path in the input-split configuration can be adjusted by controlling the power differential device. The compound-split transmission mode differs from the input-split configuration by adding another power differential device at the output of the transmission. This device implements one more power splitting ratio. The electric-to-mechanical power ratio can be adjusted by controlling both of the power differential devices. Typically, the input-split mode is used for low vehicle speeds, while the compound-split mode works better for high-speed or high-load conditions[57]. In addition to these two continuous operating modes, the two-mode hybrid transmission also includes four fixed gear ratios[58].

Figure 2.5 depicts the block diagram of the two-mode hybrid transmission architecture based on GM's Allison Two-Mode Hybrid Transmission (AHS)[58]. The GM's AHS is comprised of three planetary gear sets, four clutches/brakes, two electric machines, and a battery pack.

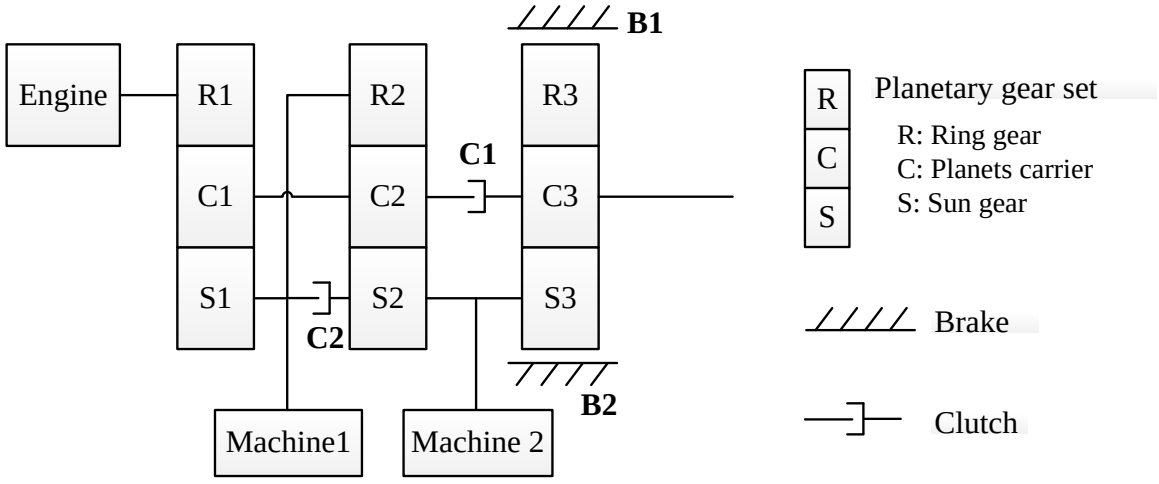

Figure 2.5 Block diagram of the GM (AHS) two-mode hybrid transmission

By controlling the two machines as well as switching the clutches and brakes, the GM (AHS) two-mode hybrid transmission provides more operating modes when compared to the Toyota THS system. Modes switching can be done smoothly without any discrete changes in the transmission. By selecting the operating modes according to the road conditions, the two-mode hybrid transmission can achieve improved fuel savings while providing uncompromised performance regardless of low or high operating speed. Table 2.1 lists the different operation modes and the corresponding clutches and brakes engagements.

Table 2.1 Two-mode hybrid transmission operation modes and the corresponding clutches and brakes engagements

		Brake B1	Clutch C1	Brake B2	Clutch C2
Continuously variable transmission modes	Input-split Mode	○			
	Compound-split Mode		○		
Fixed gear ratio modes	1st Fixed Gear Ratio	○			○
	2nd Fixed Gear Ratio	○	○		
	3rd Fixed Gear Ratio		○		○
	4th Fixed Gear Ratio		○	○	

2.3.2 Input-Split Mode

Referring to Figure 2.6, the input-split mode is achieved by engaging Brake B1 while disengaging other clutches or brakes. Here, the engine transmits power to the first planetary gear set, which splits the power into two paths (i) one is the mechanical path through the three sets of planetary gears and then to the final drive; (ii) the other is the electric path composed of the two machines and the battery pack. In the input-split configuration, only the first planetary gear set actually functions as a power differential device to distribute power between the electric and mechanical power paths. The other two planetary gear sets function as regular spur gear sets to directly combine the two power paths together.

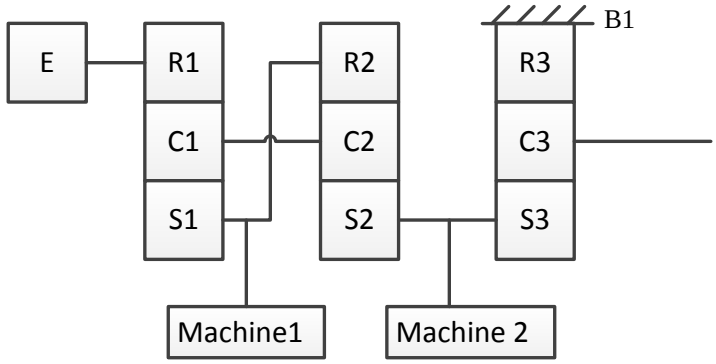

Figure 2.6 Input-Split mode

Based on the equations (2.2), (2.4), and (2.5) of the planetary gear sets, the transmission output-input relationships can be derived as:

$$\omega_o = \left(\frac{k_1}{1+k_1}\frac{1+k_2}{1+k_3}\right)\omega_E + \left(\frac{1-k_1k_2}{1+k_1}\frac{1}{1+k_3}\right)\omega_1 \tag{2.11}$$

$$T_o = \left(1+k_3\right)\left(T_2 + \frac{1}{1+k_2}\frac{1+k_1}{k_1}T_E\right) \tag{2.12}$$

where k_1, k_2, and k_3 are the gear ratios of the three planetary gear sets respectively, ω_E is the engine revolution speed, ω_1 is the revolution speed of Machine 1, ω_o is the transmission output speed, T_o is the transmission output torque, T_2 is the torque from Machine 2 and T_E is the torque from the engine.

In the input-split mode, the electric machine is still directly coupled with the output drive shaft. Therefore, the whole transmission system functions like the THS system. The output speed can be expressed as a function of the Machine 2 speed:

$$\omega_o = \frac{1}{1+k_3}\omega_2 \tag{2.13}$$

where ω_2 is the revolution speed of Machine 2. From equation (2.11) and equation (2.12), it is observed that Machine 1 serves as the speed coupler (ω_1) while Machine 2 serves as the torque coupler (T_2) to regulate the engine speed (ω_E) and torque (T_E). Similar to the THS system, the input-split mode has higher efficiency at low speeds because the electric power portion is less at lower speeds, and thus the power losses are reduced as illustrated by the results of Section 2.2.2. Therefore, the input-split mode is more often used for relatively lower-speed driving.

To get a better understanding of the operating modes, speed and torque arrow indicators are used in Figure 2.7 to analyze the block diagrams of Figure 2.6. Here, the angular speed and torque are assigned positive when they have the same rotational direction as the engine. It is also assumed that when the vehicle is moving forward, both the engine and the transmission output shaft are rotating clockwise, which is designated by the arrows on the block diagrams in Figure 2.7. The same convention is applied to torque, where the down arrow refers to the clockwise external torque. The gray arrows in the blocks refer to the speeds, and the black arrows next to the blocks refer to the torques. By using equation (2.4) and (2.5), we can derive the Machine 1 torque:

$$T_1 = \left(\frac{1}{1+k_2}\right)\left(\frac{1-k_1k_2}{k_1}\right)T_E \tag{2.14}$$

where T_1 is the torque generated by Machine 1.

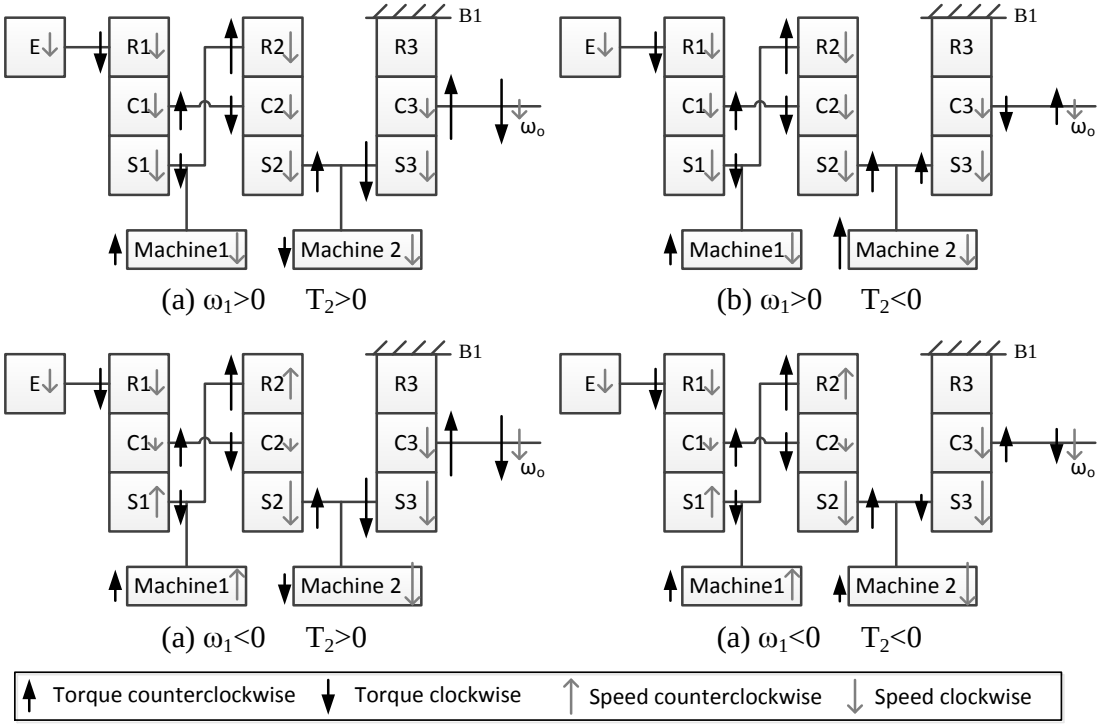

Figure 2.7 Schematics for torque and speed analysis of the input-split mode

Since k_1 and k_2 are defined as the gear ratio between the ring gears and the sun gears, we have $k_1 > 1$and $k_2 > 1$. Therefore, $T_1 < 0$ based on equation (2.14), i.e. Machine 1 only has counterclockwise output torque in the input-split mode, as shown in Figure 2.7. In addition, Machine 2 has the same speed direction with the output drive shaft. When the vehicle speed is positive, i.e. the output drive shaft rotates clockwise, Machine 2 only has clockwise output speed. Hence, there are four operating scenarios depending on the rotational speed of Machine 1 and the torque direction of Machine 2.

(a) $\omega_1 > 0,\ T_2 > 0$

All the gear components are rotating clockwise. Machine 1 serves as a generator to regulate the engine speed and Machine 2 serves as a motor to regulate the

engine torque. The transmission is in the low speed driving range where the engine drives the vehicle and supplies power to Machine 1.

(b) $\omega_1 > 0,\ T_2 < 0$

Both Machine 1 and Machine 2 serve as generators. When $\left(T_2 + \frac{1}{1+k_2}\frac{1+k_1}{k_1} T_E \right) < 0$, $T_o < 0$, the transmission is in its regenerative braking mode. When $\left(T_2 + \frac{1}{1+k_2}\frac{1+k_1}{k_1} T_E \right) > 0$, T_o still remains positive, thus the engine supplies all the demanded power to the final drive while Machine 1 and Machine 2 charge the battery.

(c) $\omega_1 < 0,\ T_2 > 0$

Both Machine 1 and Machine 2 work as motors. The transmission provides the maximum power to the final drive when vehicles are accelerating under low speed with relatively large power demand.

(d) $\omega_1 < 0,\ T_2 < 0$

Machine 1 works as a motor and Machine2 works as a generator. When $\left(T_2 + \frac{1}{1+k_2}\frac{1+k_1}{k_1} T_E \right) > 0$, T_o remains positive, and a small amount of power is supplied to the final drive.

When $\left(T_2 + \frac{1}{1+k_2}\frac{1+k_1}{k_1} T_E \right) < 0$, $T_o < 0$, the transmission is in regenerative braking mode.

Cases (b) and (d) have the same expression of output torque and both can work in the battery charging mode and regenerative braking mode, depending on the term $T_2 + \left(\frac{1}{1+k_2} \right)\left(\frac{1+k_1}{k_1} \right) T_E$. The difference between these two cases is the transmission output speed. Observed from equation (2.11), the transmission output speed depends on the speed of Machine 1. If Machine 1 changes its direction of rotation, the transmission output speed will be changed accordingly. Therefore, case (b) and case (d) work at different speeds for the input-split mode. This helps the transmission to achieve battery charging or regenerative braking without major changes of the power-train elements in city driving conditions.

In addition, electric-only mode can be achieved by operating Machine 2 as a motor to propel the vehicle when the engine is turned off. It can also realize reverse driving by rotating Machine 2 backwards.

It is reported by GM that (i) the multiple operation modes in input-split range helps the transmission achieve smooth and continuous driving performance. (ii) the motor assistance function and the regenerative braking function contribute to higher fuel efficiency[55]. However, similar to the THS system, an increasing portion of power passes through the electric path when the vehicle speed increases. This has lower efficiency

compared to the mechanical path, and thus the overall transmission efficiency drops in the input-split mode[56]. It is this reason that GM created a second continuous operation mode to improve fuel efficiency and performance of the two-mode hybrid.

2.3.3 Compound-Split Mode

Compound-split mode is achieved by engaging Clutch C1 and disengaging the other clutches, as shown in Figure 2.8. In the compound-split configuration, both the first planetary gear set and the third planetary gear set function as power differential devices to adjust the power ratio between the electric power path and the mechanical power path. The engine power is split by the first planetary gear set into the mechanical path and the electric path and they are rejoined together by the third planetary gear set.

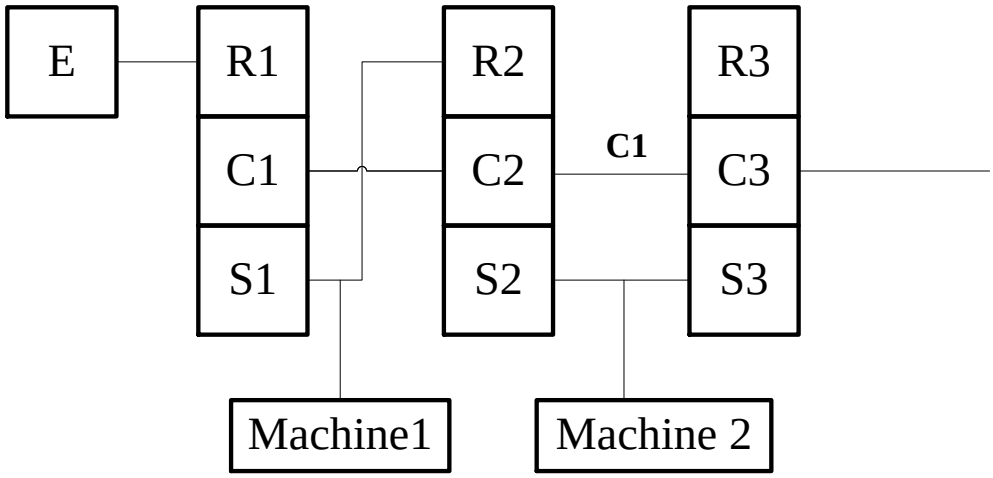

Figure 2.8 Compound-Split of GM's two-mode hybrid transmission

Based on equations (2.2), (2.4), and (2.5), we can derive the output speed and output torque in terms of the engine and electric machines input speeds and torques:

$$\omega_o = \left(\frac{1}{1+k_1}\right)\omega_1 + \left(\frac{k_1}{1+k_1}\right)\omega_E \tag{2.15}$$

$$T_o = (1+k_2)T_2 + \left(\frac{1+k_1}{k_1}\right)T_E \tag{2.16}$$

The speed and torque relationship between the engine and the two electric machines can be written as:

$$\omega_2 = \left(\frac{1-k_1k_2}{1+k_1}\right)\omega_1 + k_1\left(\frac{1+k_2}{1+k_1}\right)\omega_E \tag{2.17}$$

$$T_1 = k_2T_2 + \frac{1}{k_1}T_E \tag{2.18}$$

As previously, speed and torque arrow indicators are included on the transmission schematic diagrams to illustrate operating modes and analyze the speed and torque under each mode, as shown in Figure 2.9 to 2.11. Depending on the different combinations of torque and speed, multiple transmission output and operating modes can be achieved.

2.3.4 Compound-Split Mode Speed and Torque Analysis

Figure 2.9 shows three cases when Machine 1 rotates counterclockwise, while Machine 2 rotates clockwise, i.e. $\omega_1 < 0,\ \omega_2 > 0$. It is observed from the speed equation (2.15), that the output speed is the summation of the engine and Machine 1 speed each modified by their respective gear ratios. When $\omega_1 < 0$, the first term of the output speed

in equation (2.15) is negative. Therefore, the output drive shaft speed equation is composed of one negative term and one positive term. Thus, the vehicle is operating in the medium speed range. Figure 2.10 and 2.11 indicate the high operating speed ranges since Machine1 rotates clockwise, i.e. $\omega_1 > 0$, and thus both terms of the transmission output drive shaft speed components are positive.

For cases (a) to (c) of Figure 2.10, $\omega_2 > 0$, while cases (a) to (c) of Figure 2.11 have $\omega_2 < 0$. It can be observed from equation (2.17) that the first term is negative since $k_1 > 1,\ k_2 > 1$, and $\omega_1 > 0$ for the cases shown in Figure 2.10 and 2.11. Therefore, with a constant engine speed, Machine 2 speed can decrease only when Machine 1 speed increases. This indicates that the transmission operations modes in Figure 2.11 have the highest speed.

Based on the torque equation (2.16), case (a) of Figure 2.9, 2.10 and 2.11 indicate large torque output since the torque of Machine 2 is positive. The remaining cases have relatively smaller torque output since $T_2 < 0$.

The operating differences between the cases of (b) and (c) of Figure 2.9, 2.10 and 2.11 are the torque difference between the engine and Machine 2. In all of these cases, $T_2 < 0$, the summation of the engine torque and the Machine 2 torque determine the Machine 1 torque and the operation mode for Machine 1 based on equation (2.18). Case (b) of Figure 2.9, 2.10 and 2.11 represent the scenarios when $T_1 > 0$, and case (c) of Figure 2.9, 2.10 and 2.11 represent the scenarios when $T_1 < 0$. In addition, for all of these cases, if the output torque is negative, the transmission is absorbing the regenerative power. This

can be achieved by having both the machines working as generators like case (b) of Figure 2.9 in the medium speed range and case (c) of Figure 2.10 in the high speed range, or only one of the machines serves as generator to absorb the energy, for example case (c) of Figure 2.9 and 2.11 and case (b) of Figure 2.10.

For case (a) of Figure 2.10 and case (b) of Figure 2.11, both of the Machines serve as motors to assist the engine to propel the final drive. Since the case (b) of Figure 2.11 has a higher output speed, then if the power applied is the same, case (a) of Figure 2.10 would have a higher torque output due to the conservation of power.

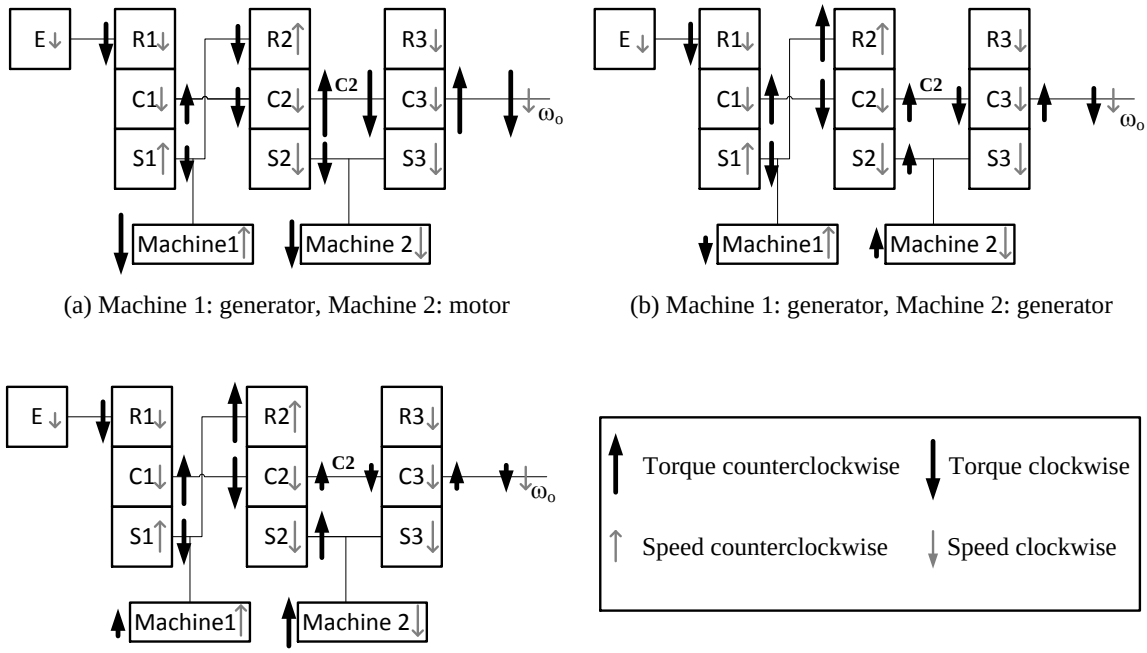

(a) Machine 1: generator, Machine 2: motor

(b) Machine 1: generator, Machine 2: generator

(c) Machine 1: motor, Machine 2: generator

Figure 2.9 Torque and speed modes of the compound-split transmission

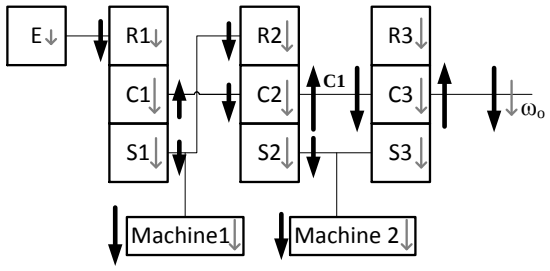

(a) Machine 1: motor, Machine 2: motor

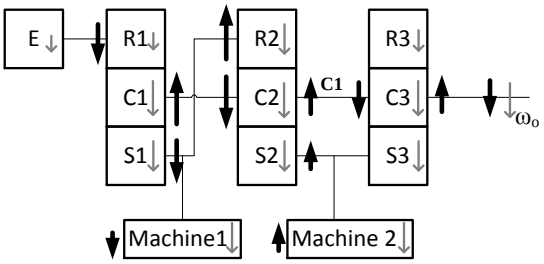

(b) Machine 1: motor, Machine 2: generator

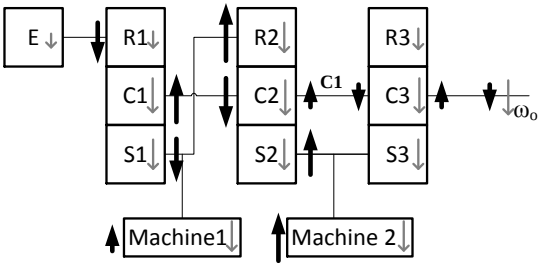

(c) Machine 1: generator, Machine 2: generator

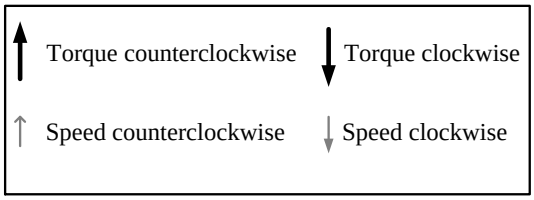

Figure 2.10 Torque and speed modes of the compound-split transmission

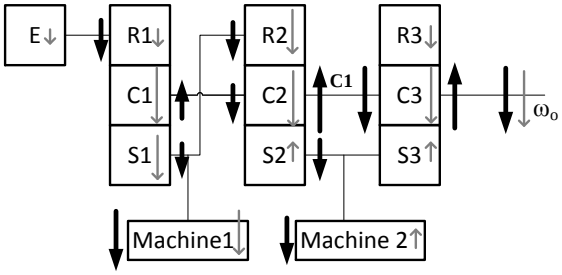

(a) Machine 1: motor, Machine 2: generator

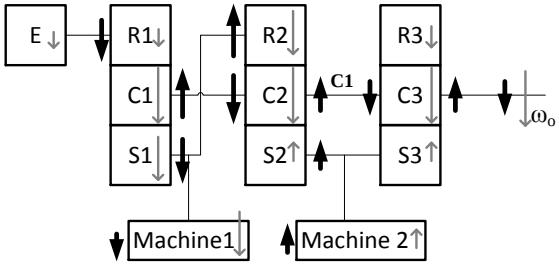

(b) Machine 1: motor, Machine 2: motor

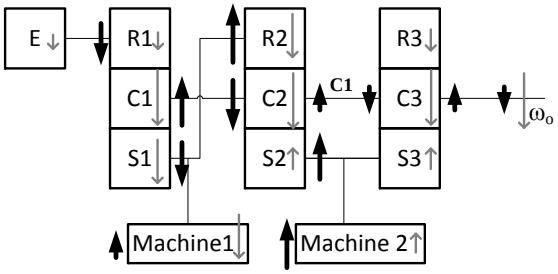

(c) Machine 1: generator, Machine 2: motor

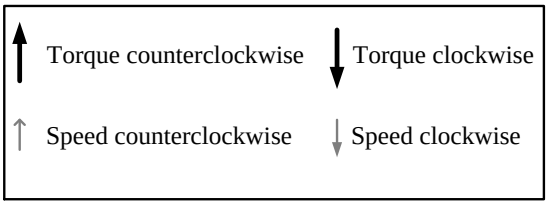

Figure 2.11 Torque and speed modes of the compound-split transmission

The preceding discussion has illustrated that the compound-split mode can provide the hybrid transmission with multiple operational modes that enables great system flexibility. Due to the different power combinations of the planetary gear sets, functions such as electric machine power assistance and regenerative braking can be performed. A wide range of output torques over a large span of speeds can be realized since the electric machines have full ability to merge between generating and motoring modes of operation. The transmission can also change its operation modes without any sudden operation changes of the power-train elements. Further, the engine can still operate in the fuel optimum regions by controlling the speeds and torques of the two electric machines.

Similar to what can be done in the input-split mode, the engine can be regulated in its fuel optimal regions in the compound-split mode by the incorporation of the two electric machines, improving the engine efficiency and thus the fuel economy. However, differing from the input-split mode in which Machine 1 serves as the speed regulator while Machine 2 serves as the torque regulator, in the compound-split mode both electric machines operate together to regulate engine output speed and output torque.

Combining equations (2.15) and (2.17), the transmission speed output can be rewritten as a function of Machine 2 speed and engine speed, and combining equation (2.16) and (2.18) yields the alternative output torque result:

$$\omega_o = \left(\frac{1}{1-k_1k_2}\right)\omega_2 - \left(\frac{k_1k_2}{1-k_1k_2}\right)\omega_E \tag{2.19}$$

$$T_o = \left(\frac{1+k_2}{k_2}\right)T_1 + \left(\frac{k_1k_2-1}{k_1k_2}\right)T_E \quad (2.20)$$

These equations show both the engine speed and torque can be decoupled from the transmission output drive shaft while both Machine 1 and Machine 2 can be utilized to regulate the engine operating regions and satisfy the transmission output demand. This decouples Machine 2 from directly connecting to the transmission output shaft thus lowering speed requirement for the machine.

2.3.5 Two-Mode Hybrid Transmission Power Analysis

Compared to the input-split mode, the compound-split mode offers two additional mechanical points. Proper selection of the parameters of the three planetary gear sets enables a relatively low power portion through the electric path at high-speed driving, thus improving fuel efficiency at high speeds[57]. The combined engine and electric machine function also helps improve output torque performance when towing or hill climbing. Thus, both fuel efficiency and driving performance are improved. Figure 2.12 illustrates the power-train configuration compared to an input-split architecture.

Similar to the calculation process of the THS transmission, the electrical power ratio can be calculated as a function of the engine input speed to the drive shaft output speed.

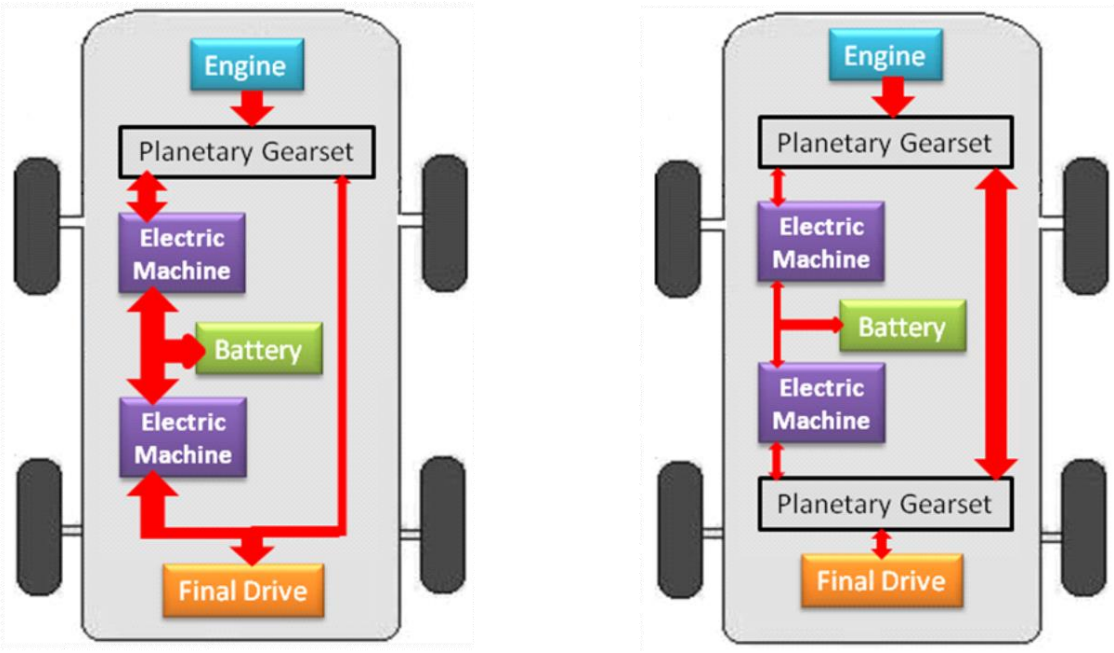

(a) Input-split architecture (b) Compound-split architecture

Figure 2.12 Power flow in the input-split mode and the compound-split mode

Based on equation (2.11), the speed of Machine 1 in the input-split mode can be expressed as:

$$\omega_1 = \left(\frac{1+k_1}{1-k_1k_2}\right)\left(\frac{1+k_3}{k_1}\right)\omega_o - \left(k_1\frac{1+k_2}{1-k_1k_2}\right)\omega_E \tag{2.21}$$

Combined with equation (2.14), the power going into Machine 1 can be expressed as:

$$P_1 = \left[-\left(\frac{1+k_1}{1-k_1k_2}\frac{1+k_3}{k_1}\right)\omega_o + \left(k_1\frac{1+k_2}{1-k_1k_2}\right)\omega_E\right]\left(\frac{1}{k_1}\right)\left(\frac{1-k_1k_2}{1+k_2}\right)T_E \tag{2.22}$$

Thus, the electric power ratio can be expressed as the power into the electric system divided by the engine power and written as a function of the engine speed divided by the transmission output shaft speed:

$$\frac{P_1}{P_E} = 1 - \left(\frac{1+k_1}{k_1} \frac{1+k_3}{1+k_2} \right) \left(\frac{1}{\omega_E / \omega_o} \right) \tag{2.23}$$

One mechanical point exists in the input-split mode by equating equation (2.23) to zero:

$$\left. \frac{\omega_E}{\omega_o} \right|_1 = \left(\frac{1+k_1}{1+k_2} \right) \left(\frac{1+k_3}{k_1} \right) \tag{2.24}$$

Figure 2.13 presents the electric power ratio curve as a function of the speed ratio in the input-split mode. It is noted in this analysis that the values for k_1, k_2 and k_3 are arbitrarily chosen as an example to illustrate the power portion in the input-split mode. In this case, k_1=1.5, k_2=2 and k_3=2.5.

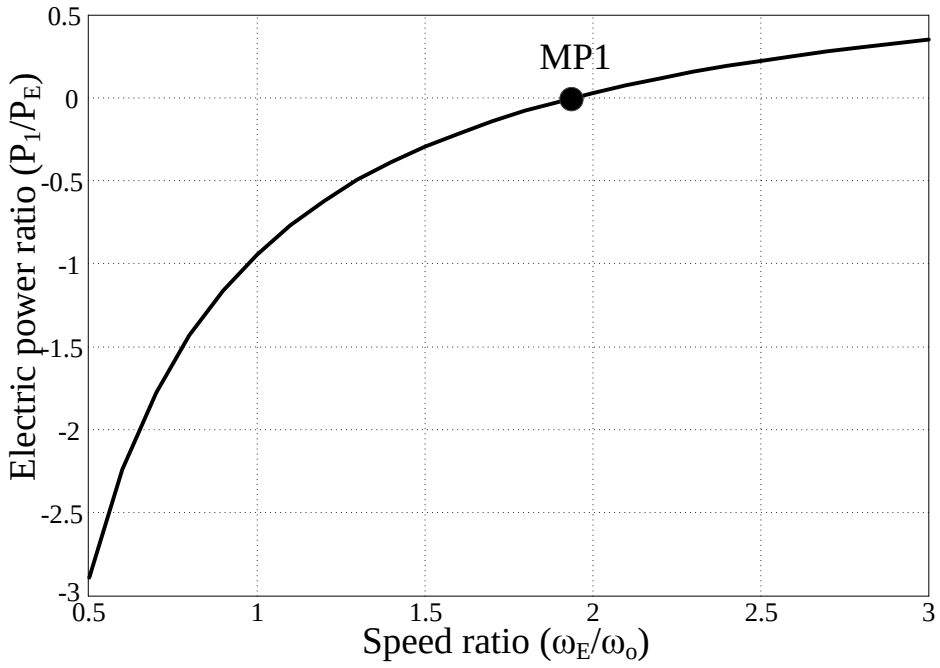

Figure 2.13 Input-split mode electric path power ratio

In the compound-split mode, the torque of Machine 1 has been derived in equation (2.18) while the speed of Machine 1 is given by rearranging equation (2.15), i.e.:

$$\omega_1 = (1+k_1)\omega_o - k_1\omega_E \tag{2.25}$$

By equating the input power of Machine 1 to the output power of Machine 2, it can be assumed that all the power at the output drive shaft comes from the engine input power. Thus, the power can be expanded by the product of speed and torque as already shown in equation (2.7). Combining equations (2.7) and (2.18), the ratio between the torque of Machine 1 and engine can be derived as:

$$\frac{T_1}{T_E} = \frac{\left(\frac{1}{k_1 k_2}\right)\omega_2}{\omega_1 + \left(\frac{1}{k_2}\right)\omega_2} \tag{2.26}$$

and by substituting equations (2.17) and (2.25) into (2.26), the ratio can be further derived as:

$$\frac{T_1}{T_E} = \frac{1 - k_1 k_2 + k_1 k_2 \frac{\omega_E}{\omega_o}}{k_1(1+k_2)} \tag{2.27}$$

Hence, the electric power ratio in the compound-split mode can be derived as:

$$\frac{P_1}{P_E} = -\frac{\omega_1 T_1}{\omega_2 T_E} = -\left[\left(\frac{1+k_1}{\frac{\omega_E}{\omega_o}}\right) - k_1\right]\left[\frac{1 - k_1 k_2 + k_1 k_2\left(\frac{\omega_E}{\omega_o}\right)}{k_1(1+k_2)}\right] \tag{2.28}$$

By equating equation (2.28) to zero, it can be shown that two mechanical points (points 2 and 3) exit in the compound-split mode:

$$\left.\frac{\omega_E}{\omega_o}\right|_2 = \frac{1+k_1}{k_1} \quad \text{and} \quad \left.\frac{\omega_E}{\omega_o}\right|_3 = \frac{k_1 k_2 - 1}{k_1 k_2} \tag{2.29}$$

Figure 2.14 presents the electric power ratio curve as a function of the speed ratio in the compound-split mode. It is also noted in this analysis that the values for k_1, k_2 and k_3 are arbitrarily chosen to simply illustrate the power portion in the compound-split mode. In this case, k_1=1.5, k_2=2 and k_3=2.5.

The electric path power ratio of the input-split mode and the compound-split mode are combined into one chart in Figure 2.15 where it can be seen that there are three mechanical points in total in the two-mode hybrid transmission, one due to the input-split mode and the other two due to the compound-split mode. The combinations cover a wide speed range. The input-split mode is preferred in the low speed region in which the first mechanical point, MP1, locates and the electric power ratio is relatively low. The compound-split mode is preferred in the high speed region in which the second and third mechanical points, MP2 and MP3, are located. The engine power that splits into the electric path is small between the three mechanical points from MP1 to MP3, as well as around MP1 and MP3, as indicated by the arrows in Figure 2.15. Thus, lower losses in the electric path and higher transmission efficiency can be achieved for a wide range of operating points from low speed to high speed.

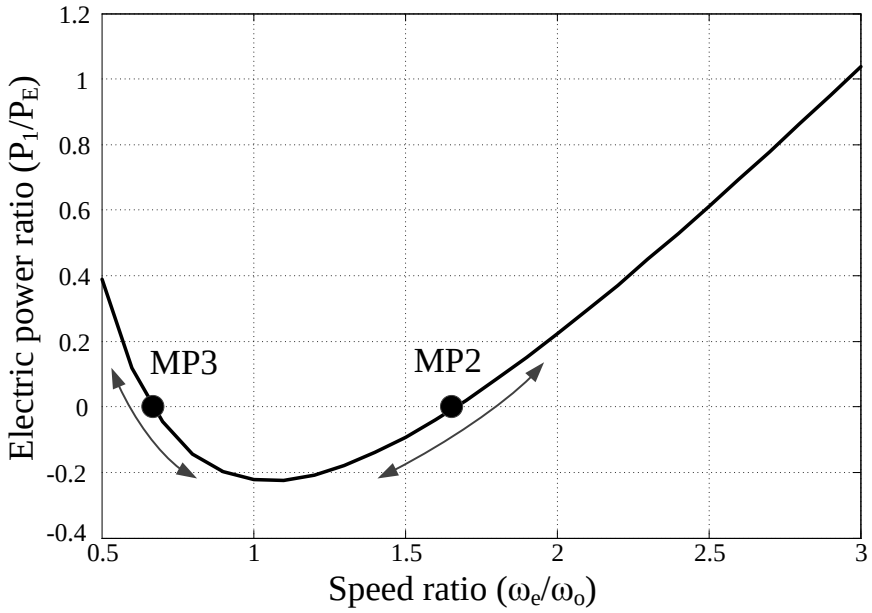

Figure 2.14 Compound-split mode electric path power ratio

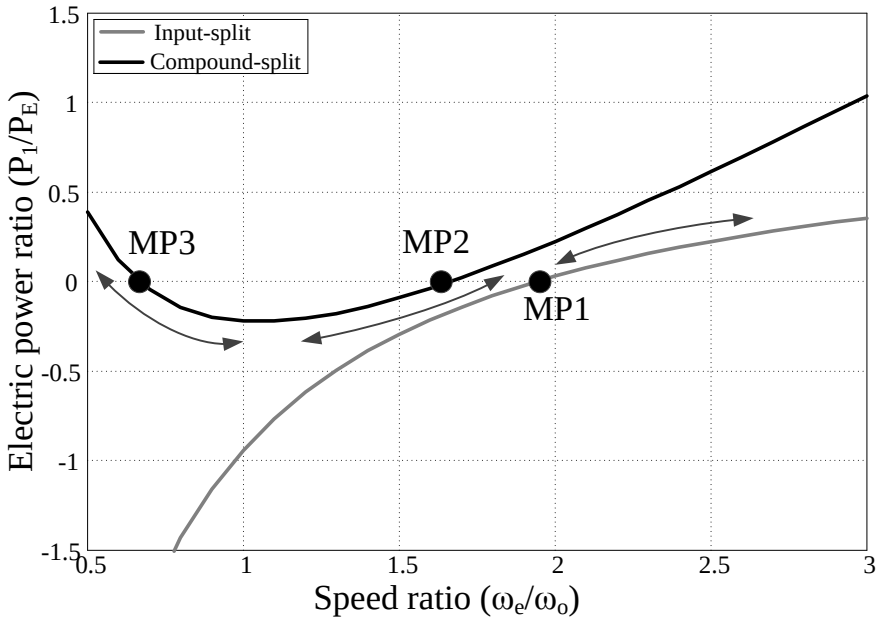

Figure 2.15 Two-mode hybrid transmission electric path power ratios

2.3.6 Fixed Gear Ratio Mode

GM's Allison two-mode hybrid transmission is equipped with four fixed gear ratios apart from the two continuous variable modes. By applying two clutches at the same time, it can switch from the continuous variable modes to fixed gear ratio modes. Figure 2.16 shows the four fixed gear ratio configurations of the GM Allison two-mode hybrid transmission.

The first fixed gear ratio takes place when Brake B1 and Clutch C2 are engaged. Clutch C2 locks the sun gear of the second planetary gear set to its ring gear so that all the gears in the first gear set and the second gear set have the same angular speed and, thus, the engine, Machine 1 and Machine 2 have the same rotational speed which is proportional to the transmission output speed:

$$\omega_o = \frac{1}{1+k_3}\omega_E = \frac{1}{1+k_3}\omega_1 = \frac{1}{1+k_3}\omega_2 \tag{2.30}$$

By energy conservation, we can derive the torque output:

$$T_o = (1+k_3)(T_1 + T_2 + T_E) \tag{2.31}$$

The first fixed gear is used to increase the output torque when high torque is required during vehicle acceleration, especially during low speed range, where it could be switched from the input-split mode by simply engaging Clutch C2. Both of the electric machines can work as motors to boost the vehicle acceleration.

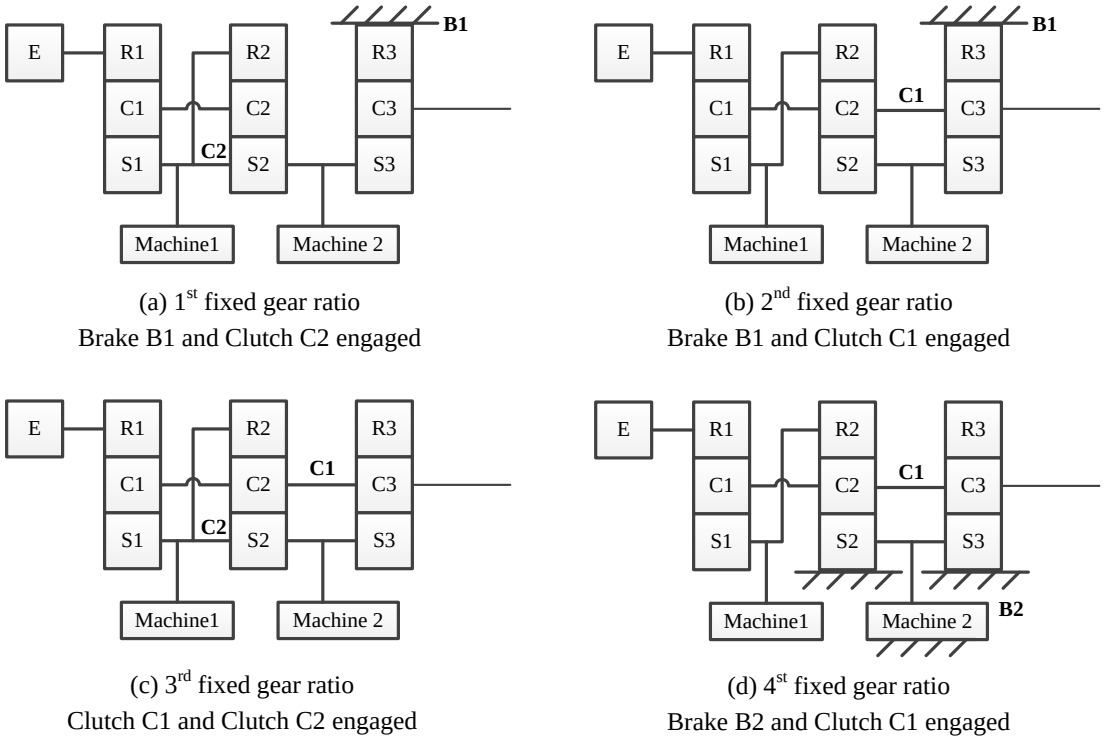

(a) 1st fixed gear ratio
Brake B1 and Clutch C2 engaged

(b) 2nd fixed gear ratio
Brake B1 and Clutch C1 engaged

(c) 3rd fixed gear ratio
Clutch C1 and Clutch C2 engaged

(d) 4st fixed gear ratio
Brake B2 and Clutch C1 engaged

Figure 2.16 Fixed gear ratio configurations

The second fixed gear ratio is engaged when Brake B1 and Clutch C1 are engaged. It can also be directly switched from the input-split mode by engaging Clutch C1. The second fixed gear ratio is typically used during the transition from input-split mode to compound-split mode. Clutch C1 is engaged at the beginning of the second fixed gear ratio and Brake B1 is released at the end of this mode. Thus, a smooth transmission is achieved between the two continuous variable modes. Equations (2.32) and (2.33) give the speed and torque output relationships:

$$\omega_o = \left(\frac{1}{1+k_3}\right)\omega_2 = \left(\frac{k_1 k_2}{k_1 k_2 + k_3}\right)\omega_E \tag{2.32}$$

$$T_o = \left(\frac{k_1 k_2 + k_3}{k_1 k_2}\right) T_E + (1 + k_3) T_2 + \left(\frac{k_2 - k_3}{k_2}\right) T_1 \tag{2.33}$$

The third fixed gear ratio is realized by engaging both Clutch C1 and Clutch C2. This achieves a 1:1 input-output gear ratio since all the gears in the three planetary gear sets are all locked together. The output torque is the combination of the three input sources torques:

$$T_o = T_E + T_2 + T_1 \tag{2.34}$$

The fourth Fixed Gear Ratio provides an overdrive gear ratio. Brake B2 locks Machine 2 while Clutch 1 engages to output the speed and torque. It can also be used in the high speed range so that only the engine drives the vehicle in its efficient regions with Machine 1 powering the accessories or generating if battery recharging is demanded.

$$\omega_o = \left(\frac{k_1 k_2}{k_1 k_2 - 1}\right) \omega_E \tag{2.35}$$

$$T_o = \left(\frac{k_1 k_2 - 1}{k_1 k_2}\right) T_E + \left(\frac{k_2 + 1}{k_2}\right) T_1 \tag{2.36}$$

2.3.7 Example of the Two-Mode Hybrid Operations

Combining the two continuous variable modes and the four fixed gear ratio modes above, two-mode hybrid transmission offers numerous operating modes by controlling the electric machines as well as switching the clutches and brakes. By properly choosing

the operating modes according to the road conditions, the two-mode hybrid transmission can achieve significant fuel savings while providing uncompromised performance[57]. Figure 2.17 shows an example two-mode hybrid transmission operating from zero speed to high speed with a constant acceleration. The transmission output revolution speed is assumed to be 50 times of the vehicle speed, i.e. $\omega_o = 50V$, in which V is the vehicle speed with the unit of miles per hour. The planetary gear set ratios were chosen as k_1=1.5, k_2=2 and k_3=2.5.

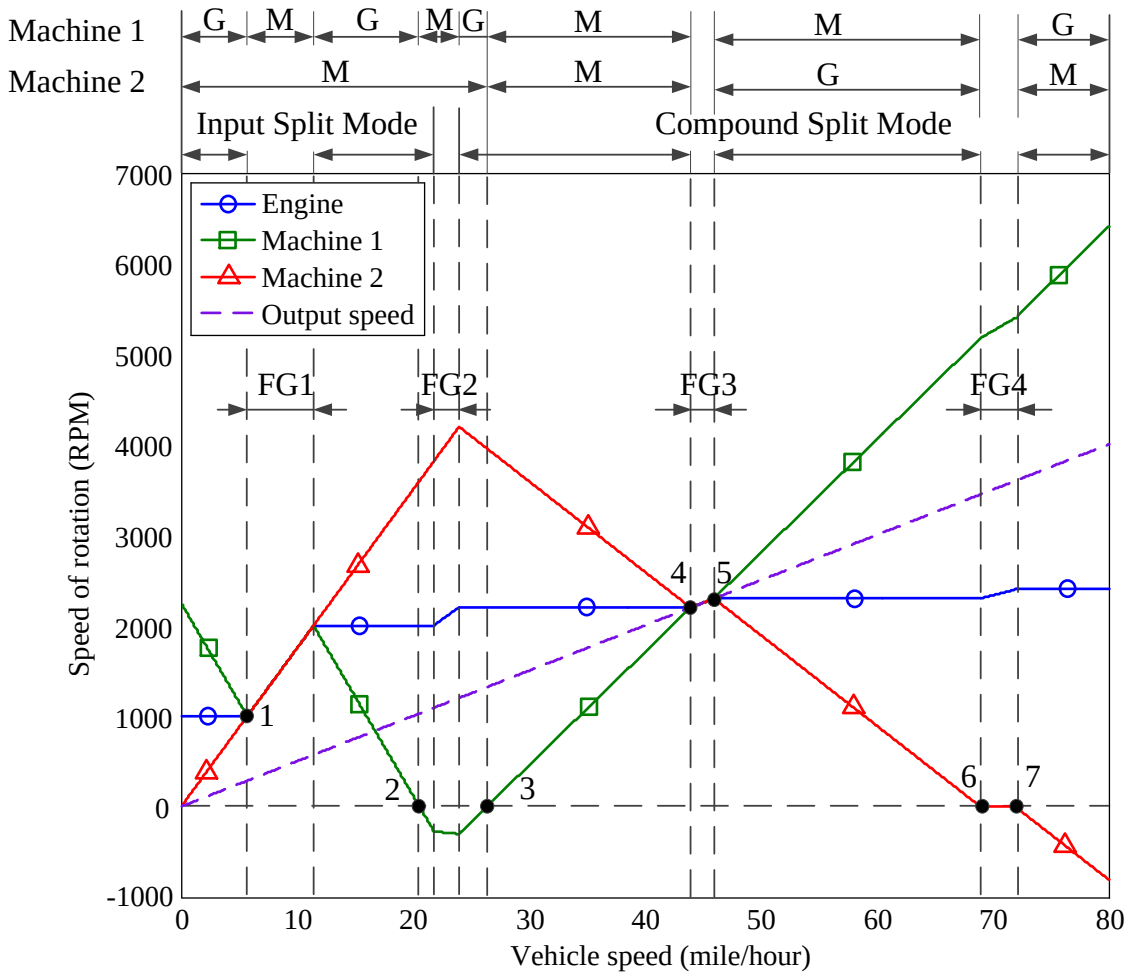

Figure 2.17 GM Allison two-mode hybrid operation example

Starting from zero speed, the transmission is operating in the input-split mode with Machine 1 serving as a generator and Machine 2 serving as a motor. The engine speed is constant at 1000RPM as an example. Based on the speed relationship in the input-split mode, i.e. equations (2.11) and (2.13), the speed of Machine 1 and Machine 2 can be calculated as:

$$\omega_1 = -\frac{875}{4}V + 2250 \tag{2.37}$$

$$\omega_2 = 175V \tag{2.38}$$

The first input-split mode ends when the speeds of the engine, Machine 1 and Machine 2 are synchronized as shown at point 1, the vehicle speed at this point can be calculated by using either equation (2.37) or equation (2.38), in which $\omega_1 = \omega_2 = 1000$. Thus, V_1= 5.71 mph. This phase corresponds to the transmission configuration shown in Figure 2.7(a) where both Machine 1 and Machine 2 have positive speed while Machine 2 output positive torque to achieve higher acceleration.

At point 1, Clutch C2 engages to switch the transmission into the first fixed gear ratio, FG1, supplying the maximum power to the final drive by having both of the electric machines working as motors. The speeds of the engine, Machine 1, and Machine 2 are all the same in proportional to the transmission output speed:

$$\omega_E = \omega_1 = \omega_2 = 175V \tag{2.39}$$

Clutch C2 disengages when the maximum acceleration is no longer required or engine speed increases to certain level, i.e. $\omega_E = 2000$ RPM and V=11.43 mph in this case. Machine 1 now reverts back to a generator and the transmission switches back to the

input-split mode as shown in Figure 2.7(a). The first mechanical point is reached when the speed of Machine 1 reduces to zero, as shown at point 2, transmitting all the engine power through the mechanical path. When Machine 1 speed drops below zero, it reverts to motoring mode, and the transmission corresponds to the configuration shown in Figure 2.7(c). The engine speed now keeps constant at 2000 RPM while the speed of Machine 1 and Machine 2 can still be calculated based on the input-split mode speed equations (2.11) and (2.13):

$$\omega_1 = -\frac{875}{4}V + 4500 \tag{2.40}$$

$$\omega_2 = 175V \tag{2.41}$$

During the transition from input-split mode to compound-split mode, Clutch C1 engages to realize the second fixed gear ratio, FG2. The speed of each component can be calculated based on equation (2.32):

$$\omega_E = \frac{275}{3}V \tag{2.42}$$

$$\omega_1 = -\frac{25}{2}V \tag{2.43}$$

$$\omega_2 = 175V \tag{2.44}$$

Both of the electric machines can work in motoring mode to assist the engine to provide maximum output torque. At the end of the transition, Brake B1 is released to switch into the compound-split mode. In this case, Brake B1 is released when the engine speed reaches 2200 RPM, i.e. at a vehicle speed of 24 mph.

At the beginning of the compound-split mode, Machine 1 still rotates in the reverse direction as a generator. The engine speed keeps constant at 2200 RPM while the speed of Machine 1 and Machine 2 can be calculated based on the speed relationship in the compound-split mode, i.e. equations (2.15), (2.17) and (2.19). Equations (2.45) and (2.46) present the speed results:

$$\omega_1 = 125V - 3300 \tag{2.45}$$

$$\omega_2 = -100V + 6600 \tag{2.46}$$

Machine 2 still works in the motoring mode to provide output torque. Thus, the beginning phase of the compound-split mode in this example corresponds to the transmission configuration shown in Figure 2.9(a). When Machine 1 speed goes to zero again, the transmission reaches its second mechanical point, as shown at point 3. Thereafter, both Machine 1 and Machine 2 turn to motoring mode to provide the maximal torque, corresponding to the transmission configuration in Figure 2.10(a).

The third fixed gear ratio, FG3, can be realized when the speeds of the engine, Machine 1 and Machine2 all synchronize to the transmission output shaft speed, i.e. 1:1 input to output ratio, as shown at point 4. Clutch C2 engages to switch into FG3 at this point from the compound-split mode in which Clutch C1 is already engaged. Equation (2.47) presents the speed relationship in FG3:

$$\omega_1 = \omega_2 = \omega_E = \omega_o = 50V \tag{2.47}$$

The transmission switches back into the compound-split mode after the engine speed reaches 2300 RPM, where the vehicle speed is 46 mph, as shown at point 5. Machine 1 still operates in the motoring mode while Machine 2 generates to charge the battery in order to sustain the battery state-of-the-charge. This phase corresponds to the transmission configuration shown in 2.10(b).

The third mechanical point is reached at high speed when the rotation speed of Machine 2 drops to zero, as shown at point 6. From point 6 to point 7, the fourth fixed gear ratio mode, FG4, is enabled by engaging Brake B2 and Clutch C1 to achieve the overdrive ratio in which the transmission output speed is greater than the engine speed. The speed of Machine 2 remains zero while the speeds of the engine and Machine 1 can be calculated based on equation (2.35):

$$\omega_E = \frac{100}{3}V \tag{2.48}$$

$$\omega_1 = 75V \tag{2.49}$$

Depending on the battery state-of-the-charge or the engine operating speed, for instance in this case $\omega_E = 2400$ RPM, the transmission can switch back from FG4 to the compound-split mode in which Machine 2 now serving as a motor with negative rotation speed and Machine 1 generates to sustain the torque and speed required at the high speed. The engine speed in this phase keeps constant at 2400 RPM, while the speeds of Machine 1 and Machine 2 can be calculated based on equations (2.15) and (2.19):

$$\omega_1 = 125V - 3600 \tag{2.50}$$

$$\omega_2 = -100V + 7200 \tag{2.51}$$

It should be noted that the modes of the two machines in this example only serves to illustrate the operating principles of the transmission. Depending on the torque and speed requirement from the transmission output shaft, it is also possible for the machines to switch their operating modes and realize either one of the transmission configurations as drawn in Figure 2.9, 2.10 and 2.11.

As observed from Figure 2.17, the engine speed is bounded around 2000 RPM where the engine is operating at its optimum fuel combustion regions and thus increasing the engine efficiency. Meanwhile, by combining the input-split mode and the compound-split mode, three mechanical points, 2, 3, and 6, are allocated throughout the transmission operation range, achieving a relatively low portion of engine power flowing through the electric path. Besides, the mode switches can be smoothly realized by engaging or disengaging the clutches and brakes. Motor assistance and regenerative braking can also be readily achieved by coordinating the electric machines. Therefore, the compound two-mode hybrid transmission achieves both high fuel efficiency and satisfactory performance throughout its operation range without sacrificing either.

However, the drawback of the compound two-mode hybrid transmission lies in its complicated configuration. For example, the GM Allison two-mode hybrid transmission is composed of three sets of planetary gear sets, four clutches, and two electric machines, which results in higher weight, larger volume and consequently higher cost than say, for example, the Toyota THS system. Currently two-mode hybrid transmissions are only applied on large vehicles such as SUVs, mini vans, and buses. The cost of the hybrid

system also presents a significant purchase barrier for the majority of the vehicle consumers.

Considering the previous discussions, this thesis presents the concept of a novel integrated electro-mechanical hybrid transmission that utilizes a double-rotor electric machine to simplify the compound two-mode hybrid transmission architecture while maintaining or improving the fuel economy and performance.

2.4 INTEGRATED ELECTRO-MECHANICAL HYBRID TRANSMISSION WITH DOUBLE-ROTOR ELECTRIC MACHINE

In the above two sessions, two of the currently commercialized full hybrid transmissions have been discusses, the Toyota Hybrid Synergy transmission and the GM compound two-mode hybrid transmission. The THS transmission successfully combines the mechanical and electric power together to power the vehicle and thus achieves a significantly better fuel efficiency within a certain speed range. However, this efficiency gain decreases or even suffers at high vehicle speed, and a large rated electric machine is required to satisfy the output demands under all driving conditions. The compound two-mode hybrid transmission overcomes these drawbacks by providing two power split modes at different speed ranges. For example, one mode for low speed and the other for high speed, thus achieving relatively high efficiency throughout the whole speed range and reduced power rating for the electric machines. The two-mode hybrid transmission also provides four fixed gear ratios to improve the vehicle performance. However, all these improvements are at the expense of increased system components, thus resulting in a more complicated system, higher system volume and weight, and higher manufacturing costs.

In order to simplify the two-mode hybrid transmission and to compare the system complexity of different hybrid transmissions, a double-rotor transmission topology has been previously investigated by a number of authors[59][60][61]. Figure 2.18 shows a typical diagram of one scheme (although they are all similar).

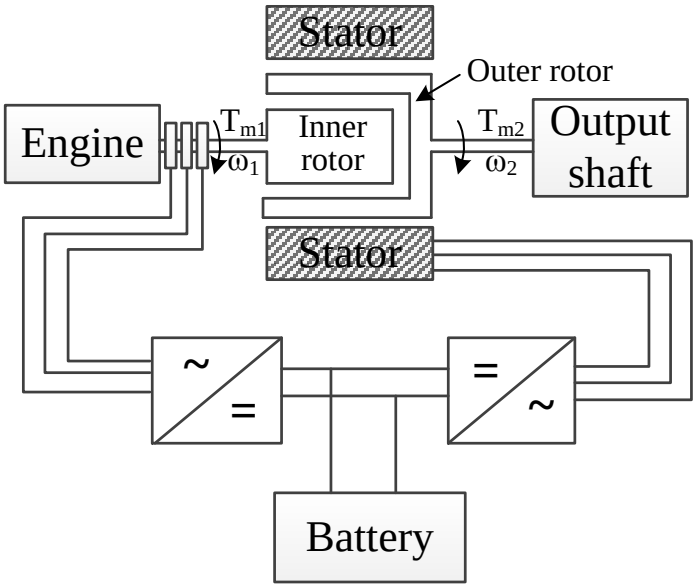

Figure 2.18 Double-rotor transmission topology

The double-rotor transmission is composed of one stator and two rotors which are labeled as the inner rotor and the outer rotor on Figure 2.18. The inner rotor is directly connected to the engine output crankshaft and the outer rotor is sandwiched in between the inner rotor and the stator and connects to the output shaft. The inner rotor and the outer rotor comprise the first electric machine, defined as Machine 1, while the stator and the outer rotor comprise the second electric machine, defined as Machine 2. Rather than having a fixed stator, Machine 1 generates power by the relative rotational speeds of the two rotors. Typically, the three-phase windings are wound on the stator and the inner rotor, the latter connecting via slip rings and carbon brushes and AC/DC converter to the battery DC link.

The input-output relationship can be easily derived by assuming steady state situations and ignoring all losses. The engine input power is:

$$P_1 = T_{m1}\omega_1 \tag{2.52}$$

in which ω_1 is the engine crankshaft output speed and T_{m1} is the input torque into the transmission. The engine power is split into two parts: P_{m1}, the mechanical path that transmits through Machine 1 to the output shaft and P_{e1}, the electric path that goes through the AC/DC converter onto the DC link:

$$P_{m1} = T_{m1}\omega_2 \tag{2.53}$$

$$P_{e1} = P_1 - P_m = T_{m1}(\omega_1 - \omega_2) \tag{2.54}$$

The electric power P_{e1} could either supply the power to Machine 2, or charge the battery. The total output power to the final drive is:

$$P_2 = P_{e2} + P_{m1} = T_{m1}\omega_1 + P_B \tag{2.55}$$

in which P_B is the power provided by the battery. Output torque is:

$$T_{m2} = \frac{P_2}{\omega_2} = T_{m1}\frac{\omega_1}{\omega_2} + \frac{P_B}{\omega_2} \tag{2.56}$$

A relatively simple control strategy can be applied on the double-rotor, one-stator transmission. For example, Machine 1 regulates the transmission output speed and Machine 2 regulates the output torque. Figure 2.19 shows the speed and torque control. Here, Point 1 stands for the demanded engine speed and torque from the final drive shaft. It is desired that the engine runs at its optimum point thus, the transmission needs to

regulate the engine from point 1 to point 2, which is its constant power equivalent point on the engine optimal operating line. Thus, the inner rotor of Machine 1 is operated at the speed of point 2 while its outer rotor is running at the speed of point 1 as a result of the road traction. Meanwhile, Machine 2 supplies the torque difference between the demanded torque and the engine optimum operation torque. Therefore, the engine can be regulated to run in its optimum operating regions[60].

The double-rotor, one stator transmission offers a relative simple transmission topology, in which engine directly connects to the output shaft via the electric machine. The double-rotor, one stator electric machine splits the engine power between the output shaft and the battery and functions to combine mechanical power with electric power to provide transmission output power. However, since the electric path always engages in the power split of the transmission, a significant amount of power is lost through the power conversions. The windings on the inner rotor generate heat presenting challenges for cooling. The slip rings and brushes on the outer rotor also bring down the system efficiency and reliability due to friction loss and wear.

Considering the positive and negative aspects of the double-rotor, one stator transmission and the two-mode hybrid transmission systems, a novel integrated electro-mechanical hybrid transmission with double-rotor machine is proposed as illustrated in Figure 2.20 that combines the merits of both the systems.

Figure 2.21 presents the proposed advantages of the novel integrated electro-mechanical hybrid transmission that combines the benefits of the two-mode hybrid transmission and the double-rotor transmission.

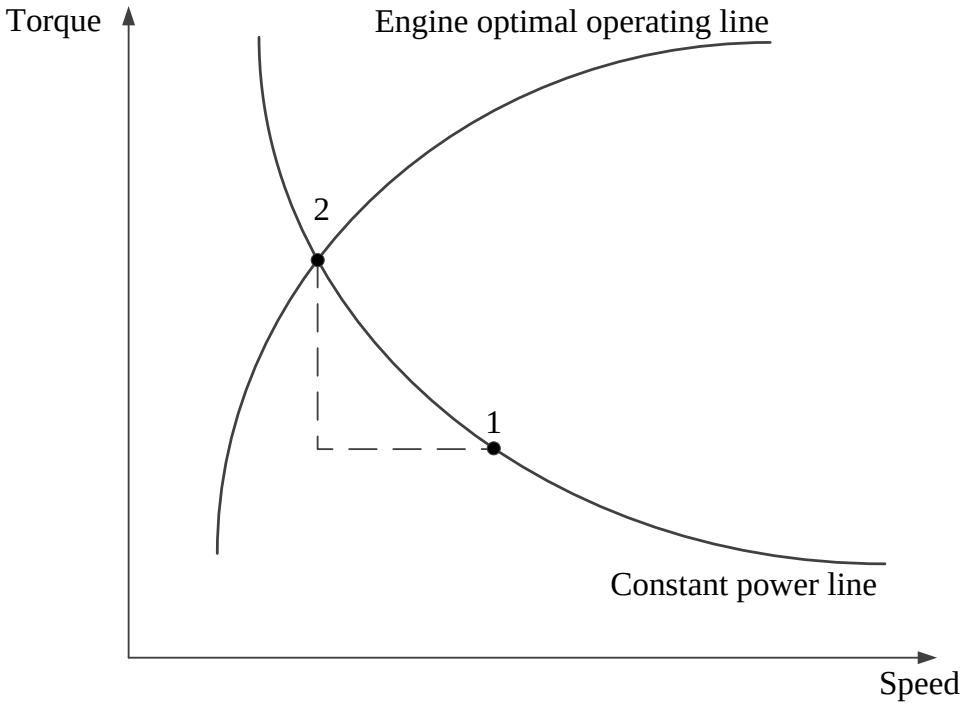

Figure 2.19 Double-rotor one-stator transmission control

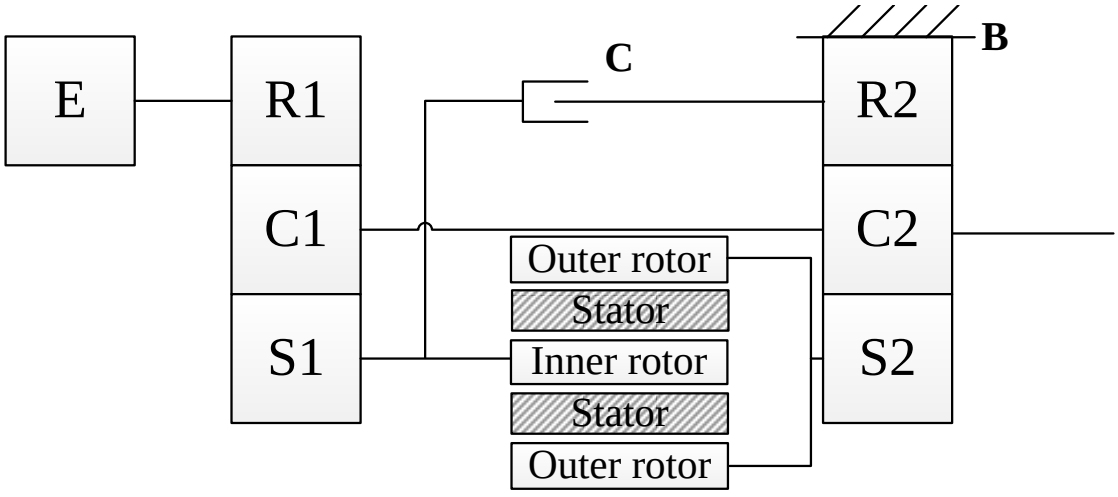

Figure 2.20 Integrated electro-mechanical hybrid transmission with double-rotor electric machine

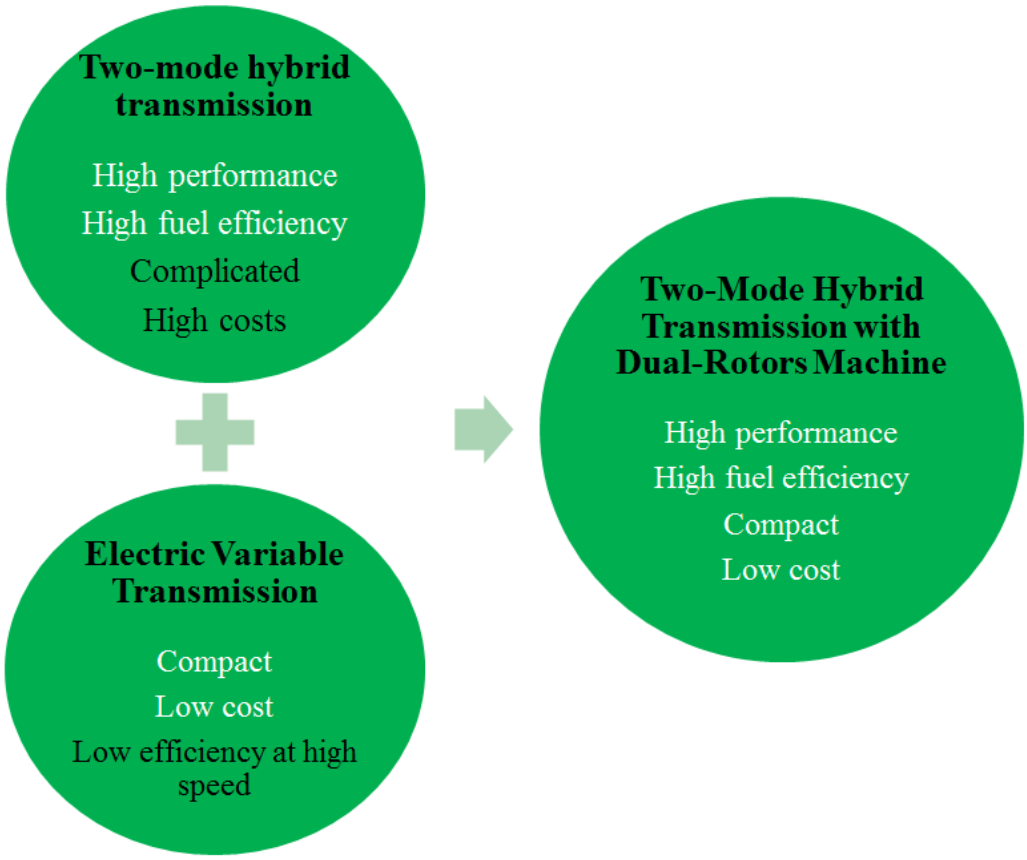

Figure 2.21 Combined benefits of the two hybrid transmissions

Comparing the proposed integrated electro-mechanical hybrid transmission in Figure 2.20 to the original two-mode hybrid transmission in Figure 2.5, it can be seen that the system complexity is simplified by reducing one planetary gear set, one clutch, and one brake. The two individual machines are replaced by one double-rotor machine such that the system is more compact and the motor drive wiring harness can also be reduced. On the other hand, the proposed integrated electro-mechanical hybrid transmission maintains the full functions of the original two-mode hybrid transmission. Figure 2.22 compares the proposed electro-mechanical hybrid transmission to the GM two-mode

hybrid transmission in terms of its first continuous variable transmission mode, the input-split mode.

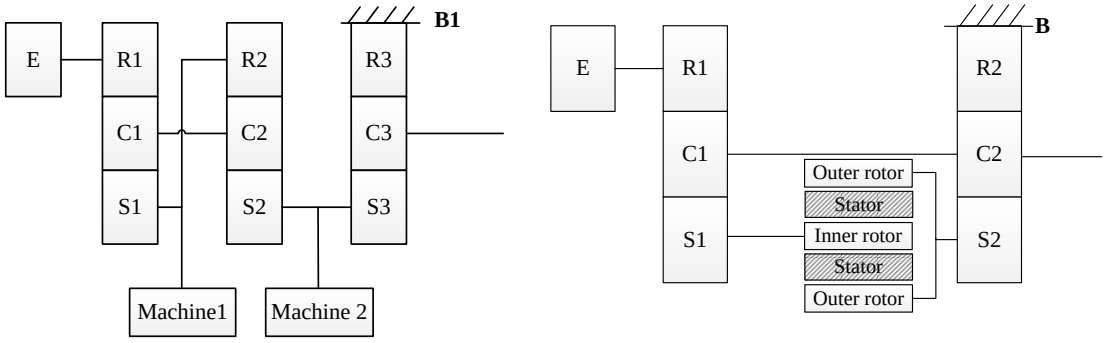

(a) GM Allison two-mode hybrid transmission (b) Integrated electro-mechanical hybrid transmission

Figure 2.22 The Input-split mode comparisons

In the GM Allison two-mode hybrid transmission, Brake B1 engages to operate the transmissions into input-split mode while Brake B engages to achieve the same mode in the proposed integrated electro-mechanical hybrid transmission. Based on the governing equations of planetary gear sets (2.1), (2.4) and (2.5), the output speed and the output torque equations for the GM Allison two-mode hybrid transmission have been previously derived as (2.11), (2.12) and (2.13). These equations are restated for ease of comparisons with the output speed and the output torque of the proposed integrated electro-mechanical hybrid transmission as:

$$\omega_o = \left(\frac{k_1}{1+k_1}\right)\left(\frac{1+k_2}{1+k_3}\right)\omega_E + \left(\frac{1-k_1k_2}{1+k_1}\right)\left(\frac{1}{1+k_3}\right)\omega_1 \tag{2.11}$$

$$T_o = (1+k_3)T_2 + \left(\frac{1+k_3}{1+k_2}\right)\left(\frac{1+k_1}{k_1}\right)T_E \tag{2.12}$$

$$\omega_o = \left(\frac{1}{1+k_3}\right)\omega_2 \tag{2.13}$$

and the relating equations of the proposed integrated electro-mechanical hybrid transmission are:

$$\omega_o = \left(\frac{k_1}{1+k_1}\right)\omega_E + \left(\frac{1}{1+k_1}\right)\omega_1 \tag{2.57}$$

$$T_o = \left(1+k_2\right)T_2 + \left(\frac{1+k_1}{k_1}\right)T_E \tag{2.58}$$

$$\omega_o = \left(\frac{1}{1+k_2}\right)\omega_2 \tag{2.59}$$

Comparing the two sets of three equations, it is observed that both the output speeds and the output torques are of similar forms except for the coefficients. This is obvious by the case since the proposed integrated electro-mechanical hybrid transmission only utilizes two sets of the planetary gear sets, and thus there is no k_3 in equations (2.57), (2.58) and (2.59).

Therefore, the proposed integrated electro-mechanical hybrid transmission can realize the continuous variable transmission operation in input-split mode in the same way as in the GM Allison two-mode hybrid transmission.

The mechanical point in the input-split mode of the proposed integrated electro-mechanical hybrid transmission can also be calculated by equating the ratio of the engine power into the electric path to the engine input power to zero:

$$\frac{P_1}{P_E} = \frac{\omega_1 T_1}{\omega_E T_E} = -\left(\frac{1+k_1}{1}\right)\frac{1}{\omega_E / \omega_o} + 1 \tag{2.60}$$

$$\left.\frac{\omega_E}{\omega_o}\right|_1 = \frac{1+k_1}{k_1} \tag{2.61}$$

Comparing with equation (2.24) where the mechanical point in the input-split mode of the two-mode hybrid transmission was derived, the similar form can be observed in the proposed transmission. Figure 2.23 compares the proposed electro-mechanical hybrid transmission to the two-mode hybrid transmission in terms of its second continuous variable transmission mode, the compound-split mode.

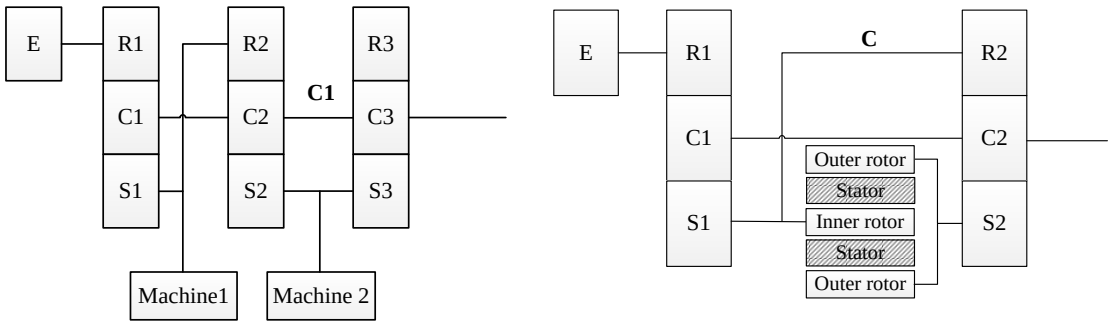

(a) GM Allison two-mode hybrid transmission (b) Integrated electro-mechanical hybrid transmission

Figure 2.23 The Compound-split mode comparisons

Clutch C1 engages to achieve the compound-split operation mode in the GM Allison two-mode hybrid transmission while Clutch C engages to achieve the same mode in the proposed integrated electro-mechanical hybrid transmission.

In the GM Allison two-mode hybrid transmission, the output speed and output torque have been derived as:

$$\omega_o = \left(\frac{1}{1+k_1}\right)\omega_1 + \left(\frac{k_1}{1+k_1}\right)\omega_E \tag{2.15}$$

$$T_o = (1+k_2)T_2 + \left(\frac{1+k_1}{k_1}\right)T_E \tag{2.16}$$

$$\omega_2 = \left(\frac{1-k_1k_2}{1+k_1}\right)\omega_1 + \frac{k_1(1+k_2)}{1+k_1}\omega_E \tag{2.17}$$

$$T_1 = k_2T_2 + \frac{1}{k_1}T_E \tag{2.18}$$

The output speed and the output torque of the proposed integrated electro-mechanical hybrid transmission can be similarly derived based on the governing equations of the planetary gear sets:

$$\omega_o = \left(\frac{1}{1+k_1}\right)\omega_1 + \left(\frac{k_1}{1+k_1}\right)\omega_E \tag{2.62}$$

$$T_o = (1+k_2)T_2 + \left(\frac{1+k_1}{k_1}\right)T_E \tag{2. 63}$$

$$\omega_2 = \left(\frac{1-k_1k_2}{1+k_1}\right)\omega_1 + \frac{k_1(1+k_2)}{1+k_1}\omega_E \tag{2.64}$$

$$T_1 = k_2T_2 + \frac{1}{k_1}T_E \tag{2.65}$$

It is clear that equations (2.62) to (2.65) match exactly with those for the GM Allison two-mode hybrid transmission, i.e. (2.15) to (2.18). Thus, the proposed integrated electro-mechanical hybrid transmission provides the same output speed and output torque

in the compound-split operational mode as the GM Allison two-mode hybrid transmission.

Since the speed and torque outputs match with those of the compound two-mode hybrid transmission, and so do the motions for all the gear members and electric machines, the proposed integrated electric-mechanical hybrid transmission will have the same mechanical points as the two-mode hybrid transmission. The electric power portion of the proposed integrated electric-mechanical hybrid transmission in the compound-split mode can be expressed as:

$$\frac{P_1}{P_E} = \frac{\omega_1 T_1}{\omega_E T_E} \tag{2.66}$$

$$\frac{P_1}{P_E} = \left[(1+k_1)\frac{\omega_o}{\omega_E} - k_1\right]\left[\frac{1-k_1k_2}{k_1(1-k_2)} + \left(\frac{k_2}{1-k_2}\right)\frac{\omega_E}{\omega_o}\right] \tag{2.67}$$

Thus, the two mechanical points are:

$$\frac{\omega_E}{\omega_o} = \frac{1+k_1}{k_1} \tag{2.68}$$

$$\frac{\omega_E}{\omega_o} = \frac{k_1k_2 - 1}{k_1k_2} \tag{2.69}$$

which are the same as those for the two-mode hybrid transmission, i.e. in equation (2.29). In addition to matching the two continuous variable transmission modes, the proposed integrated electro-mechanical hybrid transmission also provides operational modes to match the four fixed gear ratio modes as in the GM Allison hybrid transmission. Figure 2.24 compares the proposed electro-mechanical hybrid transmission to the two-mode hybrid transmission in terms of its first fixed gear ratio mode.

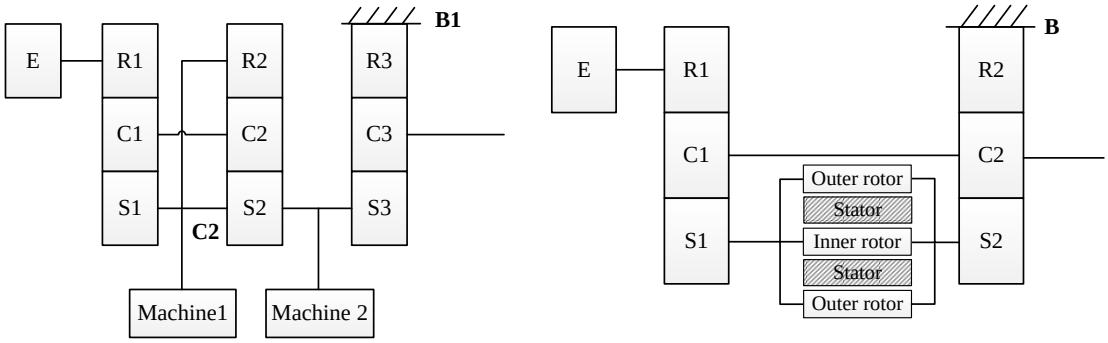

(a) GM Allison two-mode hybrid transmission (b) Integrated electro-mechanical hybrid transmission

Figure 2.24 The first gear ratio mode comparisons

The GM Allison two-mode hybrid transmission utilizes two clutches to realize the fixed gear ratio modes. The first fixed gear ratio mode is realized by engaging Brake B1 and Clutch C2 at the same time so that all the gear members of the first two planetary gear sets share the same speed, which is also the engine speed and the electric machines' speed. The transmission output speed is proportional to the engine speed by a gear ratio that is the ratio between the sun gear and the carrier of the third planetary gear set. The transmission output torque is the combination of the engine torque and two of the electric machines' torque divided by the same ratio:

$$\omega_o = \left(\frac{1}{1+k_3}\right)\omega_E = \left(\frac{1}{1+k_3}\right)\omega_1 = \left(\frac{1}{1+k_3}\right)\omega_2 \tag{2.19}$$

$$T_o = (1+k_3)(T_1+T_2+T_E) \tag{2.20}$$

In comparison, the proposed integrated electro-mechanical hybrid transmission achieves the first fixed gear ratio mode by engaging just one brake, Brake B, while locking the two electric machines, Machine 1 and Machine 2, together, i.e., the interior

rotor and the exterior rotor rotate at the same speed. This can be achieved by either using mechanical lock devices to lock the exterior rotor with the interior rotor or by utilizing the magnetic field and speed feedback control to synchronize the double rotors.

The output speed and the output torque of the proposed integrated electro-mechanical hybrid transmission in the first fixed gear ratio can then be derived as below:

$$\omega_o = \left(\frac{k_1}{k_1 - k_2}\right)\omega_E = \left(\frac{1}{1+k_2}\right)\omega_1 = \left(\frac{1}{1+k_2}\right)\omega_2 \tag{2.70}$$

$$T_o = (1+k_2)\left[T_1 + T_2 + \left(\frac{1}{1+k_2}\right)\left(\frac{k_1 - k_2}{k_1}\right)T_E\right] \tag{2.71}$$

The two electric machines are rotating with the same speed, while the engine now is operating with a lower speed since $\frac{k_1}{k_1 - k_2} > 1$ and $\frac{1}{1+k_2} < 1$. This facilitates the transmission to achieve the maximum torque output with a smaller engine rotational speed. Figure 2.25 compares the proposed electro-mechanical hybrid transmission to the two-mode hybrid transmission in terms of its second fixed gear ratio mode:

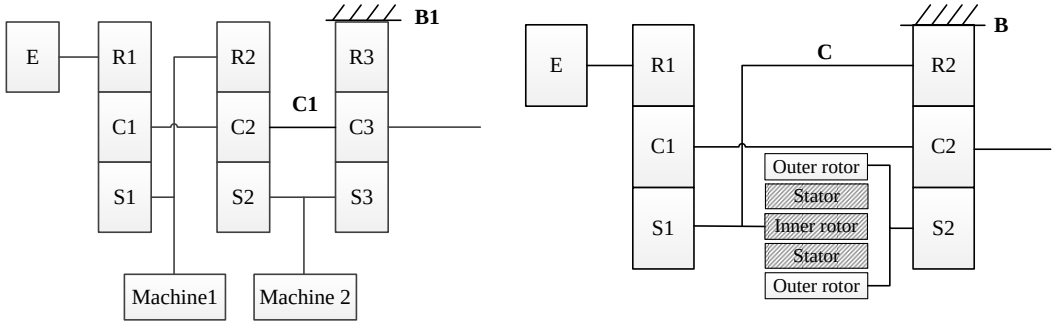

(a) GM Allison two-mode hybrid transmission (b) Integrated electro-mechanical hybrid transmission

Figure 2.25 The second gear ratio mode comparisons

The second fixed gear ratio mode in the GM Allison two-mode hybrid transmission is realized by engaging Brake B1 and Clutch C1 at the same time. The transmission output speed and torque have been previously derived as:

$$\omega_o = \left(\frac{1}{1+k_3}\right)\omega_2 = \left(\frac{k_1 k_2}{k_1 k_2 + k_3}\right)\omega_E \tag{2.21}$$

$$T_o = \left(\frac{k_1 k_2 + k_3}{k_1 k_2}\right)T_E + (1+k_3)T_2 + \left(\frac{k_2 - k_3}{k_2}\right)T_1 \tag{2.22}$$

The proposed integrated electro-mechanical hybrid transmission achieves the second fixed gear ratio mode also by engaging Brake B and Clutch C. Once Clutch C is engaged, the exterior rotor is grounded as well, thus only one machine, Machine 2, is working in the second fixed gear ratio mode. The output speed and the output torque of the proposed integrated electro-mechanical hybrid transmission in the second fixed gear ratio can then be derived as below:

$$\omega_o = \left(\frac{1}{1+k_2}\right)\omega_2 = \left(\frac{k_1}{1+k_1}\right)\omega_E \tag{2.72}$$

$$T_o = \left(\frac{1+k_1}{k_1}\right)T_E + (1+k_2)T_2 \tag{2.73}$$

Again, the above equations express the similar form of output speed and torque compared with the two-mode hybrid transmission. It can be observed that by equating the planetary gear set coefficients $k_2 = k_3$, the equations (2.70) and (2.71) are exactly the same as equations (2.21) and (2.22). Figure 2.26 compares the proposed electro-mechanical

hybrid transmission to the two-mode hybrid transmission in terms of its third fixed gear ratio mode.

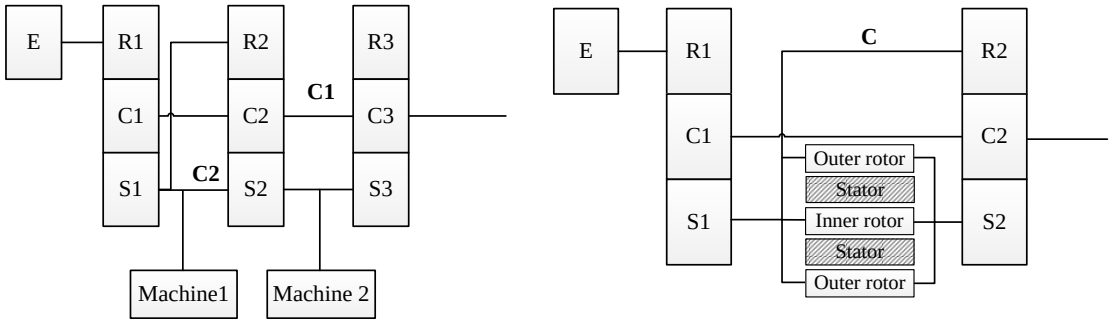

(a) GM Allison two-mode hybrid transmission (b) Integrated electro-mechanical hybrid transmission

Figure 2.26 The third gear ratio mode comparisons

The third fixed gear ratio of the two-mode hybrid transmission is achieved by engaging Clutch C1 and Clutch C2 at the same time, which forces all of the gear components, the engine, and the two electric machines to rotate at the same speed as the output speed, thus enabling a 1:1 input-output speed ratio.

The proposed electro-mechanical hybrid transmission achieves the third fixed planetary gear ratio by engaging only one clutch, Clutch C, while locking the two electric machines, Machine 1 and Machine 2, together, i.e. the interior rotor and the exterior rotor rotate at the same speed. The output speed and output torque are exactly the same as that in the two-mode hybrid transmission:

$$\omega_o = \omega_E = \omega_2 = \omega_1 \tag{2.74}$$

$$T_o = T_E + T_2 + T_1 \tag{2.75}$$

Figure 2.27 compares the proposed electro-mechanical hybrid transmission to the two-mode hybrid transmission in terms of its fourth fixed gear ratio mode.

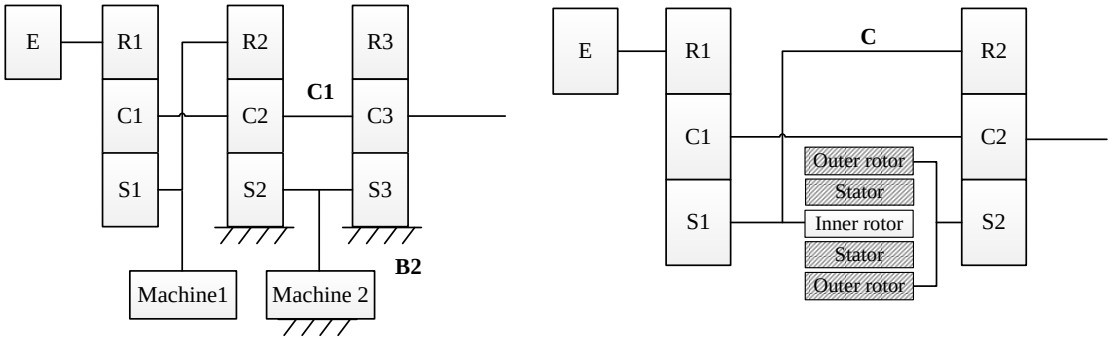

(a) GM Allison two-mode hybrid transmission (b) Integrated electro-mechanical hybrid transmission

Figure 2.27 The fourth gear ratio mode comparisons

The fourth fixed gear ratio of the two-mode hybrid transmission is achieved by engaging Clutch C1 and Brake B2 at the same time, which locks Machine 2. The resulted output speed is typically applied in overdrive range where the output speed of the transmission is greater than the input speed:

$$\omega_o = \left(\frac{k_1 k_2}{k_1 k_2 - 1}\right)\omega_E \tag{2.24}$$

$$T_o = \left(\frac{k_1 k_2 - 1}{k_1 k_2}\right)T_E + \left(\frac{k_2 + 1}{k_2}\right)T_1 \tag{2.25}$$

In comparison, the proposed electro-mechanical hybrid transmission achieves the fourth fixed planetary gear ratio by engaging only one clutch, Clutch C, while locking the exterior rotor, i.e., $\omega_2 = 0$. The output speed and output torque are exactly the same as that in the two-mode hybrid transmission:

$$\omega_o = \left(\frac{k_1 k_2}{k_1 k_2 - 1}\right)\omega_E \tag{2.76}$$

$$T_o = \left(\frac{k_1 k_2 - 1}{k_1 k_2}\right) T_E + \left(\frac{k_2 + 1}{k_2}\right) T_1 \tag{2.77}$$

Thus, based on the previous analysis, the proposed electro-mechanical hybrid transmission can achieve all the two continuous variable transmission modes and the four fixed gear ratio modes of the two-mode hybrid transmission.

Furthermore, the proposed electro-mechanical hybrid transmission can achieve one more fixed gear ratio mode, the engine only mode, which is not available in the original two-mode hybrid transmission, as shown in Figure 2.28.

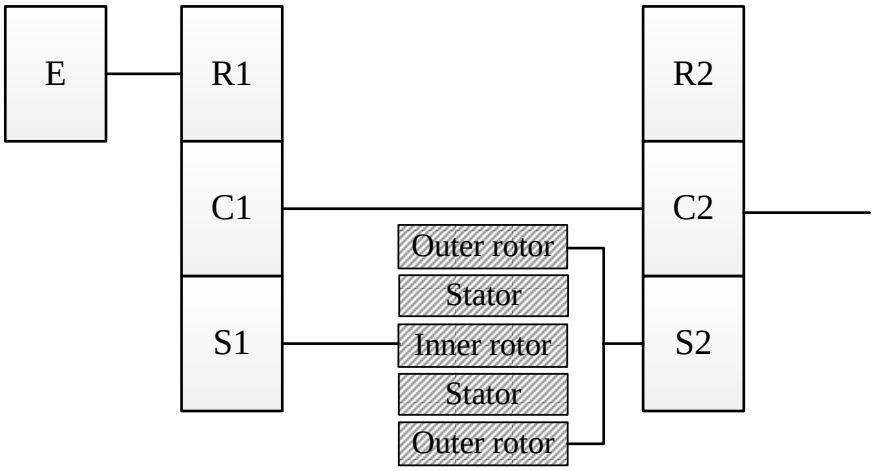

Figure 2.28 The fifth fixed gear ratio mode for the proposed integrated transmission

By locking the two rotors in the proposed electro-mechanical hybrid transmission, the engine power can be directly transmitted to the output shaft via the mechanical path while the electric machines can be switched off:

$$\omega_o = \left(\frac{k_1}{1 + k_1}\right) \omega_E \tag{2.78}$$

$$T_o = \left(\frac{1+k_1}{k_1}\right) T_E \tag{2.79}$$

However, if the two electric machines are off in the GM two-mode hybrid transmission, $\omega_1 = \omega_2 = 0$, which also applies to the second planetary gear set, $\omega_{r2} = \omega_{s2} = 0$, the output speed of the planetary carrier is also zero and the engine power cannot be transmitted to the output shaft.

The engine only mode in the proposed integrated electro-mechanical hybrid transmission can be applied to medium or high speed where the engine is operating in its most fuel efficient regions, thus, the power in the transmission is regulated in the mechanical path only and no loss occurs in the less efficient electric path.

In summary, the electro-mechanical, double-rotor, compound hybrid transmission combines the benefits of the two-mode hybrid transmission and the double-rotor transmission while offering more operational flexibility. The proposed hybrid transmission employs two continuous variable transmission modes to achieve high efficiency at both low vehicle speed and high vehicle speed, respectively. Meanwhile, it is capable of the multiple fixed gear ratio operational modes as in the GM Allison two-mode hybrid transmission while it offers one more fixed gear ratio to realize engine only mode to further increase system efficiency. Moreover, the present hybrid transmission reduces system complexity by using only one integrated, double-rotor, electric machine instead of the two electric machines as in the two-mode hybrid transmission. The double rotors function as clutches or brakes by synchronizing or locking the rotors either electromagnetically or through some mechanical devices inside the electric machine such

that several mechanical clutches or brakes in the, for example GM transmission power-train, are removed. Furthermore, only two planetary gear sets instead of three are needed in the proposed integrated electro-mechanical hybrid transmission due to the coordination between the double-rotor electric machine and the mechanical clutches. Therefore, the present integrated electro-mechanical hybrid transmission has a more compact and thus potentially smaller and lighter configuration with fewer mechanical components than the two-mode hybrid transmission, factors that ultimately lead to reduced manufacturing and operating costs in high volume.

Various mechanical configurations can be realized based on the proposed integrated electro-mechanical hybrid transmission. Figure 2.29 illustrates the first four embodiments. The double-rotor electric machine has an outer stator and two internal rotors placed in between the two planetary gear sets as shown in Figure 2.29 (a). The second embodiment uses a split type double-rotor electric machine where the exterior rotor is split into two connected parts and aligned along the axial direction shown in Figure 2.29 (b). One piece of the exterior rotor is paired with the stator to form one machine while the other piece is paired with the interior rotor to form the second machine. This embodiment realizes a hybrid transmission with a smaller outer diameter by sacrificing axial length. The third and fourth embodiments are two different mechanical implementations placing the double-rotor on the left side and the right side of the planetary gear sets, respectively, Figure 2.29 (c) and (d). Figure 2.30 illustrates another four embodiments using the double-rotor electric machine.

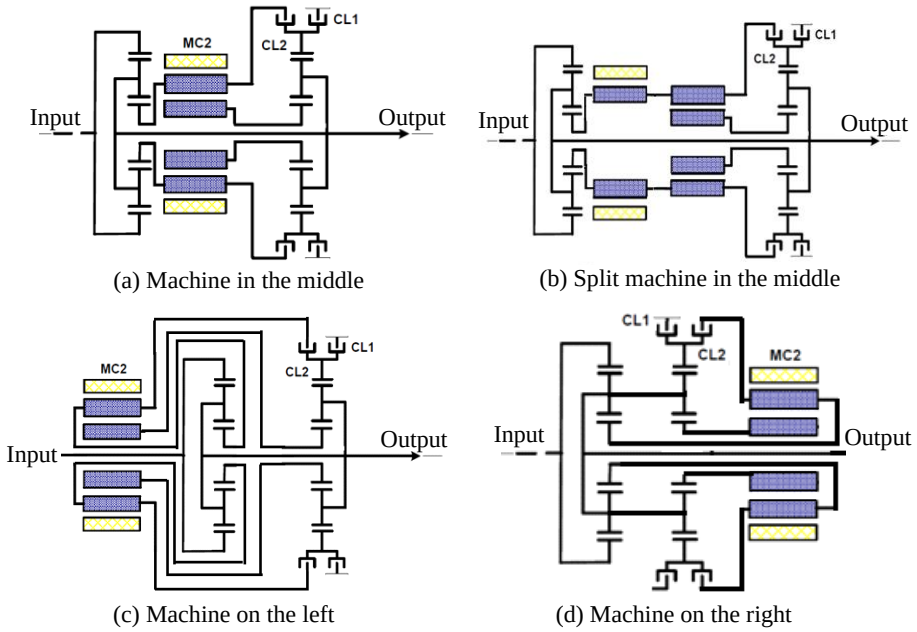

(a) Machine in the middle (b) Split machine in the middle

(c) Machine on the left (d) Machine on the right

Figure 2.29 Mechanical embodiments of the integrated electro-mechanical hybrid transmission with external stator

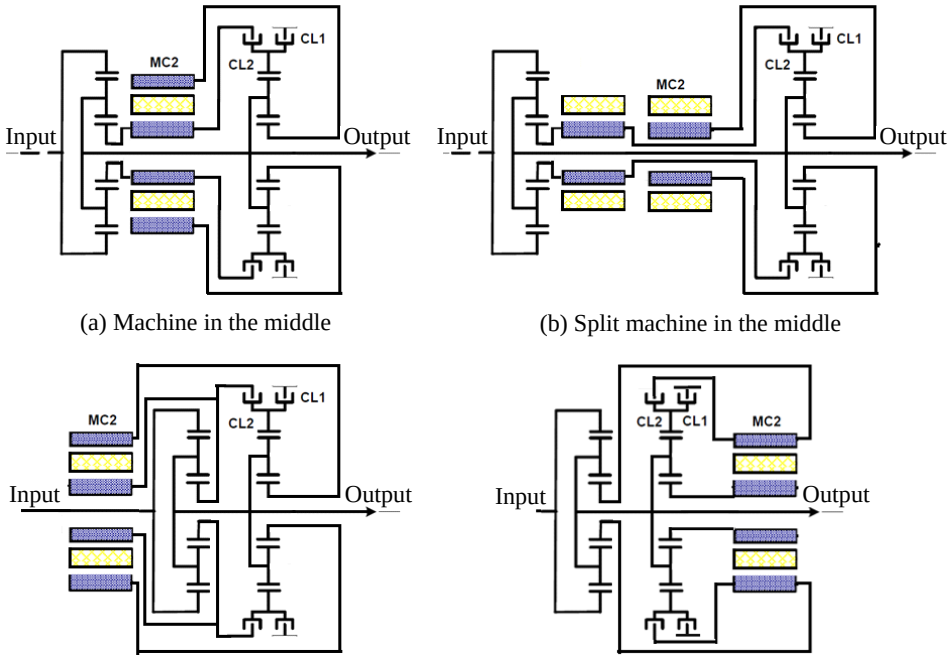

(a) Machine in the middle (b) Split machine in the middle

(c) Machine on the left (d) Machine on the right

Figure 2.30 Mechanical embodiments of the integrated electro-mechanical hybrid transmission with internal stator

2.5 DOUBLE-ROTOR ELECTRIC MACHINE

In the proposed concept of the integrated electro-mechanical hybrid transmission, the core component is the double-rotor electric machine, which enables the integration and simplification of the power-train architecture.

In a typical fully hybrid electric vehicle power-train as discussed in Sections 2.1 to 2.3, two electric machines are utilized with one serving more frequently as a motor while the other serves more frequently as a generator coupled to the engine. The machine serving as the motor is typically rated with a high torque capability to provide the traction torque required at the output shaft while the machine serving as the generator is typically rated with a high speed capability since it is predominantly coupled with the high speed engine. It is thus desirable to have one of the machines designed for high torque and the other capable of high speed operation. Figures 2.31 and 2.32 show the speed and torque characteristics of the two electric machines in the Toyota Prius Model Year 2004[62] for a standard U.S. Urban Dynamometer (UDDS) and Highway Fuel Economy Test (HWFET) driving schedules[63], respectively. The characteristics were obtained from the simulation software, "Autonomie", an Argonne National Laboratory benchmarking tool that has a complete Prius drivetrain model.

From Figures 2.31 and 2.32, it can be observed that Machine 2 speed is coupled with the vehicle speed while Machine 1 functions to regulate engine operation into more fuel efficient regions. Machine 1 is required to provide high speeds and relatively low torques while Machine 2 is required to provide high torques and relatively low speeds to meet the power-train demands for torque and speed. Here positive power equates to

motoring operation, i.e. a net power output mechanically, while negative power is indicative of electrical generation back to the system DC link and/or battery. Figure 2.31 shows that Machine 1 acts predominantly as a generator while Machine 2 as a motor for urban driving. At high speeds, Machine 2 predominantly operates as a generator while Machine 1 provides the majority motoring power, as shown in Figure 2.32. Thus, the operation of Machines 1 and 2 can, or will, change according to the energy management philosophy implemented in the vehicle controller. However, there will be a requirement for two distinct machines having very different torque-speed characteristics.

A double-rotor electric machine would therefore have to satisfy the torque and speed requirements of the two individual electric machines if applied in hybrid electric power-trains. Since the torque capability of an electric machine is related to the square of the machine air gap diameter[64], the exterior machine can be designed for high torque at lower speeds while the interior machine can be designed with lower torque and higher speed due to its smaller rotor size.

Figure 2.33 plots the operating points for both machines under the quoted torque-speed envelopes while Table 2.2 summarizes the torque-speed performance of the two machines.

From Table 2.2, the two electric machines have approximately 1:4 and 1:5 torque ratios for the UDDS and HWFET drive duty cycles, respectively. In addition, the maximum torques of both machines are rated higher to meet higher torque demands such as when steep hill climb grades and higher wind friction are encountered. Thus, the maximum torque ratio between the two machines is closed to 1:3.

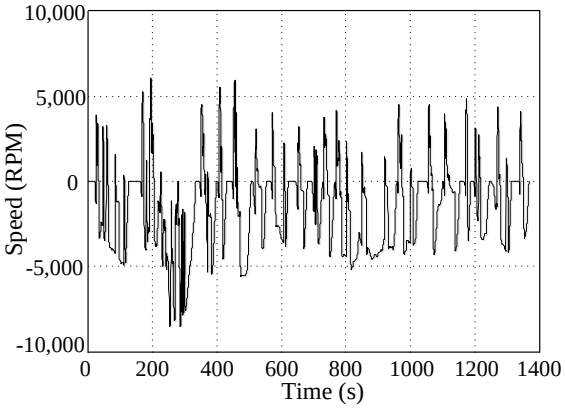

(a) Speed of Machine 1

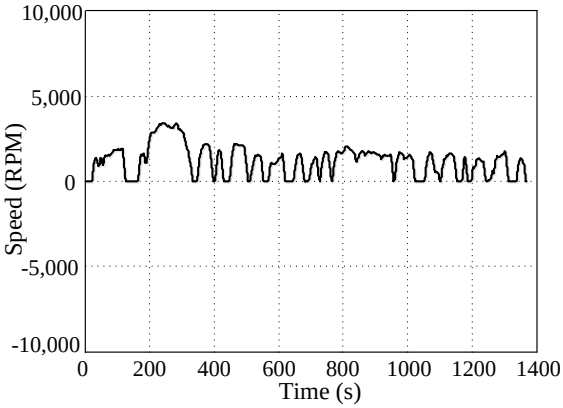

(b) Speed of Machine 2

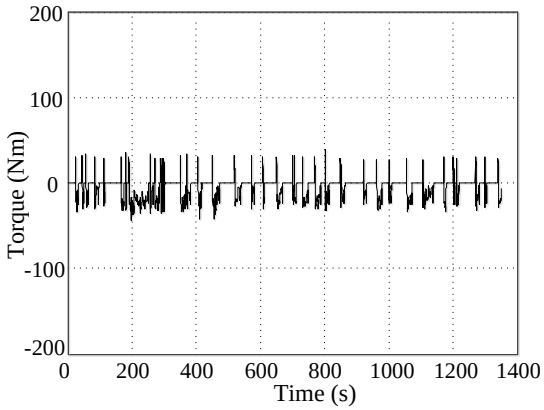

(c) Torque of Machine 1

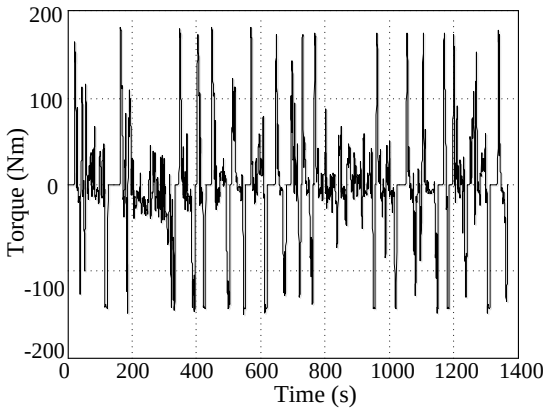

(d) Torque of Machine 2

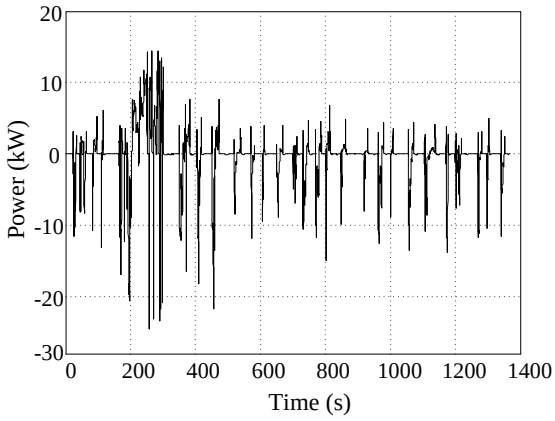

(e) Power of Machine 1

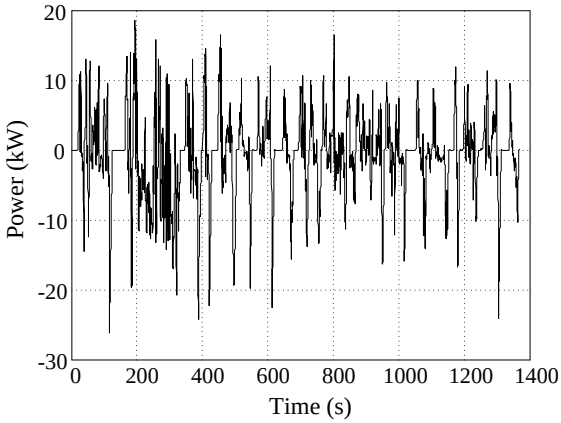

(f) Power of Machine 2

Figure 2.31 Speed and torque characteristics of the two electric machines for UDDS

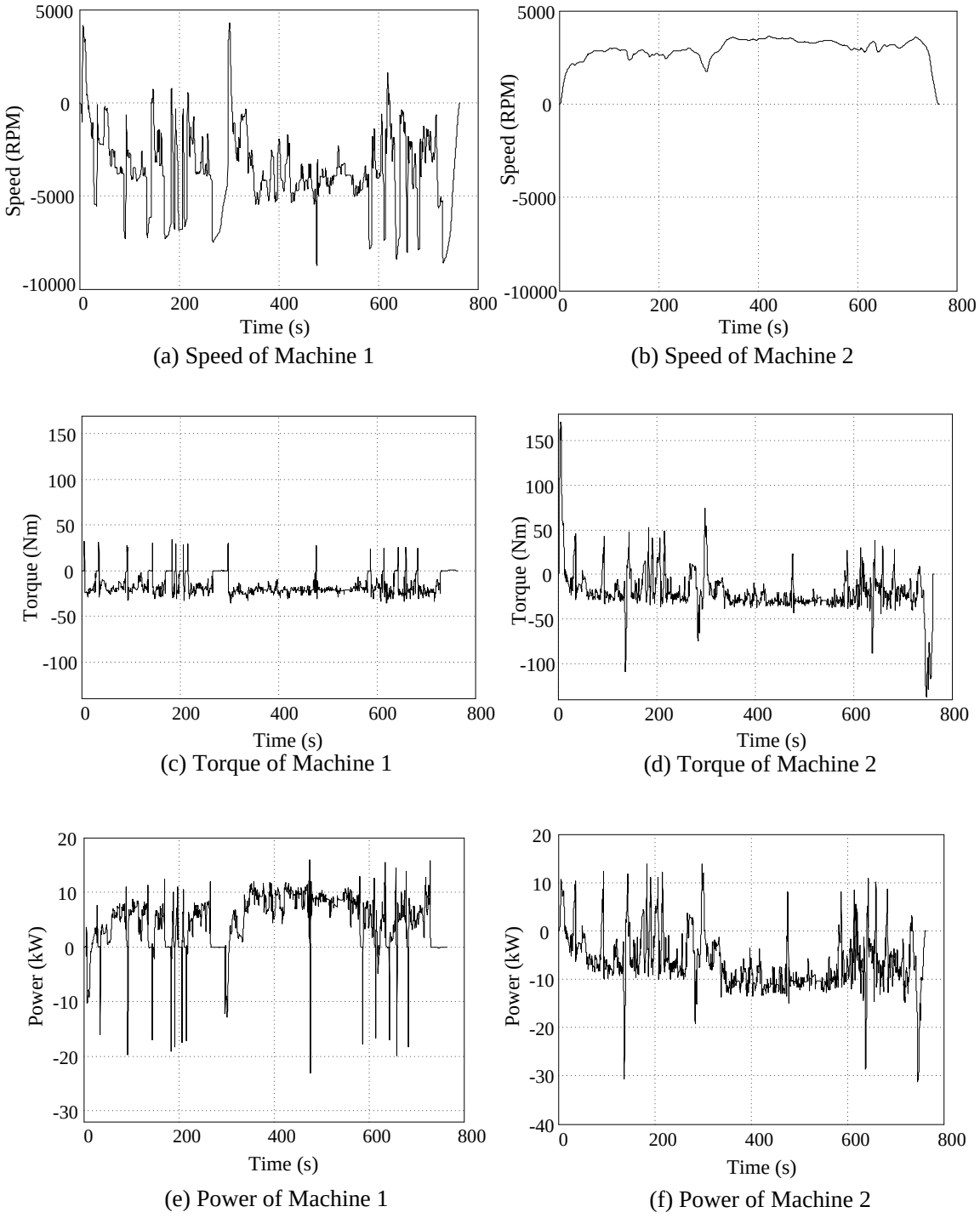

(a) Speed of Machine 1 (b) Speed of Machine 2

(c) Torque of Machine 1 (d) Torque of Machine 2

(e) Power of Machine 1 (f) Power of Machine 2

Figure 2.32 Speed and torque characteristics of the two electric machines for HWFET

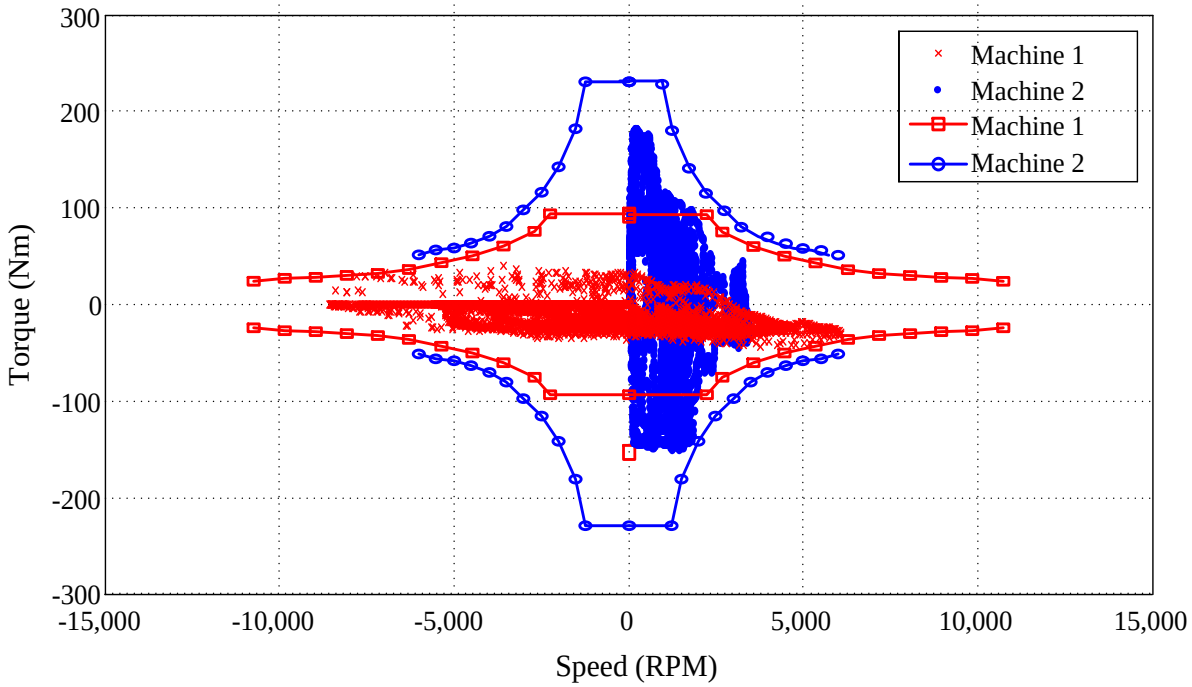

(a) UDDS City drive operation points

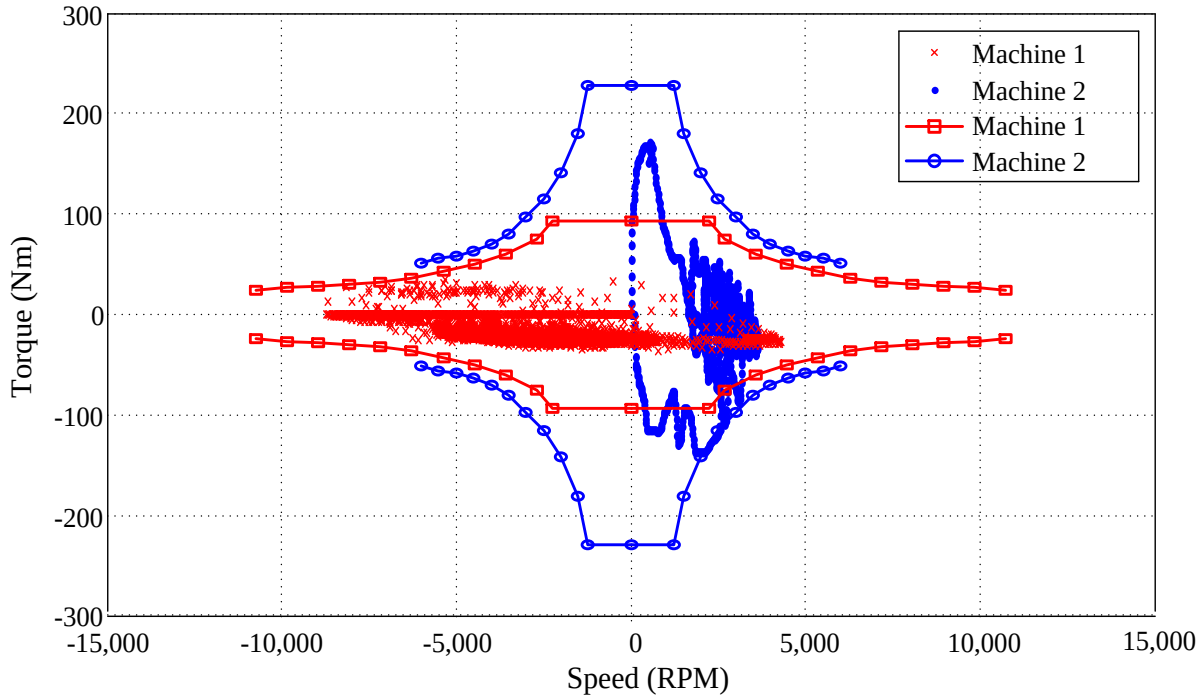

(b) HWFET Highway drive operation points

Figure 2.33 Torque and speed operating points for the two electric machines

Table 2.2 Torque and speed specifications for Machine 1 and Machine 2

Drive cycle	UDDS		HWFET	
Machine	Machine 1	Machine 2	Machine 1	Machine 2
Maximum torque (Nm)	42	183	34	170
Maximum speed (RPM)	8566	3436	8670	3629
Ratio of the duty torques	1 : 4.3		1 : 5	
Ratio of the duty speeds	2.5 : 1		2.4 : 1	

2.6 Summary

This Chapter has reviewed and discussed different types of existing full hybrid transmissions, in which the configurations, fundamentals of operating principles and various operating modes were comprehensively explained and analyzed. Both the input-split hybrid transmission and the two-mode hybrid transmission were presented, the advantages and disadvantages of the two hybrid transmissions were compared, and then a novel integrated electro-mechanical hybrid transmission with double-rotor electric machine has been proposed which could potentially simplify the compound two-mode hybrid transmission architecture while maintaining or improving the power-train fuel economy and performance. The functions and importance of double-rotor electric machines in hybrid electric power-trains were discussed and emphasized. Typical torque-speed requirements for the hybrid power-train transmissions were illustrated. Considering the UDDS and HWFET duty cycles, an average torque ratio of 1:4 between the two

machines is thus taken forward as the benchmark specification for a prototype double-rotor electric machine to be studied in the remaining Chapters of this thesis. The power rating of the prototype double-rotor electric machine will be downscaled from that of an actual vehicle power-train to a level suitable for laboratory test validation. The two machines of the double-rotor concept will be designed to have the same power ratings for the prototype and, given laboratory power supply and test constraints, a target total power of 1 kW was chosen for the prototype, along with the torque ratio of 1:4 and speed ratio of 4:1, for the interior and exterior designs respectively.

One outcome of the analysis presented in this Chapter is a pending patent regarding the proposed integrated electro-mechanical hybrid transmission using double-rotor electric machines. This records all of the power-train novelties discussed and was filed on July 30th, 2013 as the U.S. Patent Application 13/954,015. However, due to the timeline limit of the PhD, the work reported in the remaining Chapters on the integrated electro-mechanical hybrid transmission will focus exclusively on the development of the double-rotor electric machines.

Chapter 3

DOUBLE-ROTOR SWITHCED RELUCTANCE MACHINE DESIGN

Chapter 2 developed the concept of the integrated electro-mechanical hybrid transmission that has potentials to be more compact, fuel efficient at both low speed and high speed, and maintains the performance advantages and operational flexibility compared to the original two-mode hybrid transmission.

In the integrated electro-mechanical hybrid transmission, one of the core components is the double-rotor electric machine. The double-rotor electric machine functions to provide speed and torque to the hybrid transmission by connecting to both the engine and the output drive shaft via the planetary gear sets. By utilizing either the stator or one of the two rotors as a common member of the two individual electric machines, the double-rotor electric machine integrates the two machines into one machine set and only uses three machine members instead of four as opposed to the conventional design, thus potentially reducing the system volume, saving manufacturing materials as well as costs. Meanwhile, by controlling the operation modes of the two electric machines, various output modes can be achieved by the hybrid transmission. In addition, the double-rotor electric machines can either be electrically synchronized together or mechanically locked to change the hybrid transmission configuration, effectively

functioning as clutches to replace the mechanical ones and thus reducing system complexity.

Compared with other types of electric machines, switched reluctance machines offer simple construction configurations since they do not require windings or magnets on the rotor, and thus there is less or no need for rotor cooling. Switched reluctance machines are more robust and have potentials for fault tolerance compared to other AC machines that require synchronous fields, or DC machines with slip rings and brushes. In addition, no magnet is needed in switched reluctance machine since the torque is generated by reluctance torque, which is the torque between relative rotor and stator poles that tend to align the two components in order to achieve the maximum inductance. Thus, combining all of these advantages, the switched reluctance machine is considered as a promising candidate with low manufacturing costs, all ideal attributes for automotive traction applications.

In this Chapter, a double-rotor switched reluctance machine (DRSRM) is chosen and designed, while subsequent chapters discuss manufacture and test to demonstrate the concept of the double-rotor electric machine.

3.1 SWITCHED RELUCTANCE MACHINE FUNDAMENTALS

The switched reluctance machine (SRM) is a type of electric machine in which torque is generated exclusively by reluctance torque, the tendency between the stator and rotor components to move the rotor to a position where the inductance of the excited winding is maximized[65]. Stator windings are excited or discretely switched via a power converter according to the rotor position so that continuous rotation is maintained. Both the stator and the rotor have poles that are salient, with the number of the stator poles and rotor poles defining the machine topology. For instance, a switched reluctance machine with 6 stator poles and 4 rotor poles is named a 6/4 SRM, as illustrated in Figure 3.1. By way of example, supplying current to Phase A will cause the SRM rotor to rotate clockwise from the unaligned position (a) to the aligned position (b) of Figure 3.1.

The SRM has changing inductance due to salient pole configurations. It has the smallest inductance when the excited stator pole tooth is in between of two neighboring rotor pole teeth, or the largest reluctance at the unaligned position, Figure 3.1 (a); and it has the largest inductance when the rotor pole tooth aligns with the excited stator pole tooth, or the smallest reluctance at the aligned position, Figure 3.1 (b).

By supplying current to the relevant stator phase winding, a reluctance torque will be generated on the corresponding rotor teeth to pull the rotor towards a higher inductance position, i.e., the aligned position. From the unaligned position to the aligned position, the inductance under the excited winding increases and it then decreases from the aligned position to unaligned position. From basic electromagnetic principles, the switched reluctance machine operates in motoring mode if the phase current is injected

when the inductance rises, while it operates in generating mode if the phase current is injected when the inductance is reducing. Figure 3.2 shows the inductance waveform for an SRM phase winding as a function of rotor position and phase current.

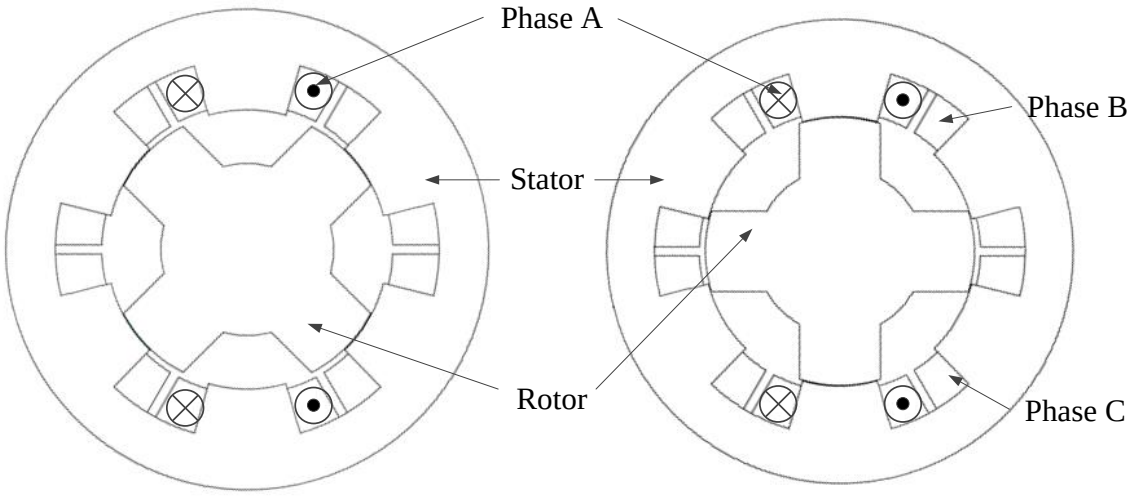

(a) Unaligned position (b) Aligned position

Figure 3.1 Aligned position and unaligned position of SRM

The waveforms shown in Figure 3.2 are the inductance waveforms under one stator phase current excitation, or single pole excitation. In a 6/4 SRM configuration, three phase windings are distributed sequentially around the machine bore periphery. Each phase has two sets of coils wound on diametrically opposite poles and connected in a way such that the flux directions in the two coils are the same. The inductance increases when the excited current in the winding increases at the same rotor position. However, the inductance is independent of the current direction, i.e. either positive current or negative current in the excited winding produces the same inductance. Thus, switching the direction of the exciting current will not change the direction of torque.

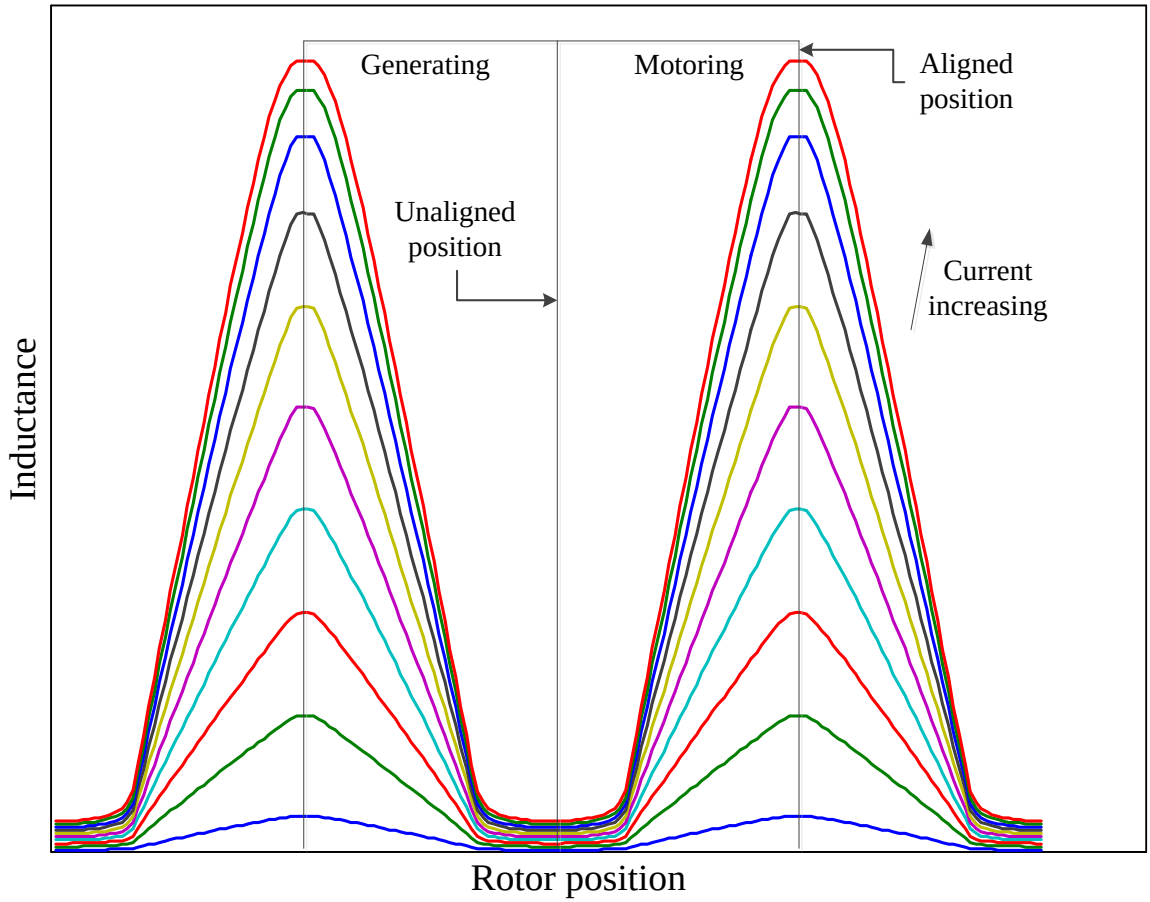

Figure 3.2 SRM phase inductance waveform as a function of rotor position and current

The inductance waveforms shown in Figure 3.2 can also represent the flux-linkage as a function of the rotor position due to the constant current in each curve. The flux-linkage curves can also be represented as a function of the excited current while the rotor position serving as variable parameter, as shown in Figure 3.3.

The torque production can also be derived from Figure 3.3. The input electrical energy can be expressed as the integral of the current and voltage:

$$W_e = \int eidt = \int -\frac{d\lambda}{dt} idt = -\int_{\lambda_A}^{\lambda_B} id\lambda \tag{3.1}$$

in which W_e is the input electrical energy, e is the input voltage, i is the input current, t is time and λ is the flux-linkage. The minus sign indicates that the energy is consumed.

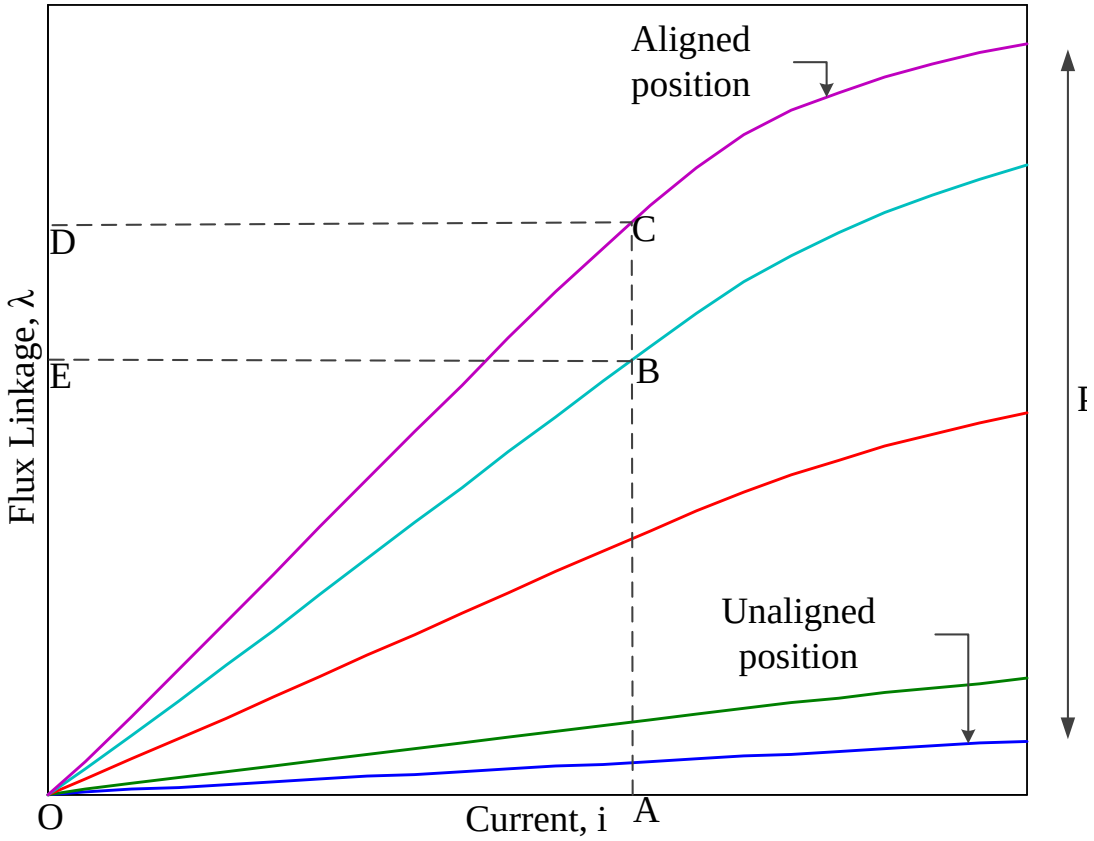

Figure 3.3 Flux-linkage characteristics

Part of the input electrical energy is converted into mechanical work W_m, while the rest is stored in the magnetic field W_f:

$$W_e = W_m + W_f \tag{3.2}$$

The stored field energy can be expressed as the integral of the excited current over the flux-linkage:

$$W_f = \int id\lambda \tag{3.3}$$

which can also be viewed as the area on the left side of the flux-linkage curve. For example, the area OBEO stands for the stored field energy at point B and the area OCDO stands for the stored field energy at point C.

The complement area under the flux-linkage curve is termed as coenergy, which can be expressed as the integral of the flux-linkage over excited current:

$$W_c = \int \lambda di \tag{3.4}$$

For a finite incremental change of the flux-linkage along the constant current line, for instance from point B to point C, the total input electrical energy change is the area of BCDE. The change of the stored field energy is from the area of OBEO to the area of BCDO. Thus, the change of mechanical energy can be expressed as:

$$\delta W_m = \delta W_e - \delta W_f = BCDE - (OCDO - OBEO) = OBCO \tag{3.5}$$

in which δW_m is the finite change of the mechanical energy, which can also be viewed as the change of the coenergy δW_c, δW_e is the finite change of the electrical energy, δW_f is the finite change of the stored field energy. Thus, the instantaneous torque can be expressed as:

$$T = \frac{\delta W_m}{\delta \theta} = \frac{\delta W_c}{\delta \theta} \tag{3.6}$$

If there is no saturation in the machine, the flux-linkage characteristics in Figure 3.3 are all linear[66]. Thus, the area of the stored field energy equals to the coenergy, which equals to half of the total input electrical energy:

$$W_c = \frac{1}{2}\lambda i = \frac{1}{2}Li^2 \tag{3.7}$$

in which L is the phase inductance. Hence, the torque under magnetic linear conditions is:

$$T = \frac{1}{2}i^2 \frac{dL}{d\theta} \tag{3.8}$$

Under linear conditions, the phase voltage equation can be expressed as:

$$v = Ri + \frac{d\lambda}{dt} = Ri + \frac{dLi}{dt} \tag{3.9}$$

in which v is the input phase voltage and R is the phase resistance. Since both inductance and current are functions of time, the derivative in the second term can be expanded to yield the decomposed terms of the input phase voltage:

$$v = Ri + L\frac{di}{dt} + i\omega\frac{dL}{d\theta} \tag{3.10}$$

in which $\omega = \frac{d\theta}{dt}$ is the rotor rotational velocity. It can be observed from equation (3.10) that the supply voltage equates to the voltage drop due to three constituent parts: the circuit resistance, the circuit inductance, and due to a rotational EMF, commonly termed the back EMF.

Multiplying (3.10) by the instantaneous current, *i*, yields:

$$vi = Ri^2 + Li\frac{di}{dt} + i^2\omega\frac{dL}{d\theta} \tag{3.11}$$

where the terms equate to winding copper loss, energy stored in the magnetic field and mechanical output power. Thus, thee instantaneous torque can be calculated from the mechanical output power:

$$\tau = i^2\frac{dL}{d\theta} \tag{3.12}$$

where τ is the instantaneous torque.

The above text briefly discusses the fundamental theory and operating principles of SRMs, which is well developed in the reference books[65][66][67]. These principles are equally valid and applicable to the design of the double-rotor switched reluctance machine in the following sections.

3.2 DOUBLE-ROTOR SWITCHED RELUCTANCE MACHINE

During considerations of the structure of double-rotor switched reluctance machines, a family of possible candidates was evolved. A pending patent application, U.S. Patent Application, 61/717,808 was filed on October 24th, 2013 as one outcome of this thesis research. In total, 13 different topology implementations of these designs were presented in the pending patent, in which 8 configurations apply the double-rotor-one-stator topology while others have double-rotor, two-or-more-stator topologies, which increase the system complexity and manufacturing difficulty and are thus not considered in this thesis. The 8 DRSRM configurations of interest are:

(i) wound central stator assembly

(ii) external stator and rotating windings on the inner rotor

(iii) internal stator windings and rotor windings on the external rotor

(iv) mechanically synchronized inner and outer rotors with central stator assembly

(v) mechanically synchronized inner and outer rotors with central segmented stator assembly

(vi) to (viii) configurations with axially displaced components

3.2.1 DRSRM with Wound Central Stator Assembly

Here, the stator is radially sandwiched in between the interior and exterior rotors so that each of the rotors forms a conventional switched reluctance machine with one side of the stator, as illustrated in Figure 3.4.

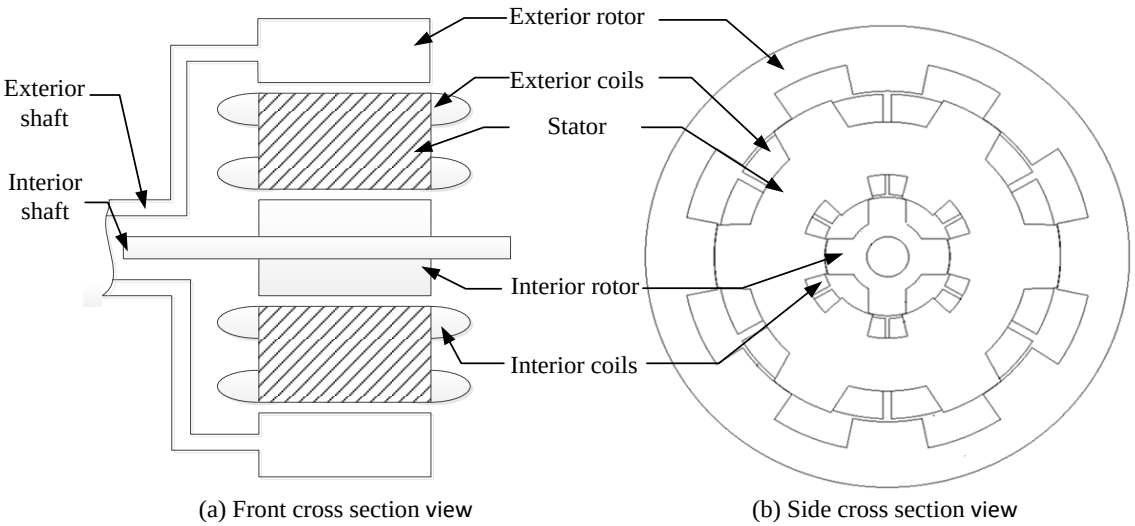

Figure 3.4 DRSRM with wound central stator assembly

3.2.2 DRSRM with External Stator and Rotating Windings on the Inner Rotor

It is possible to place an inner wound rotor in the middle of the DRSRM assembly so that this inner rotor and an external rotor form a switched reluctance machine, while the external rotor and the outer wound stator form the second switched reluctance machine, as illustrated in Figure 3.5.

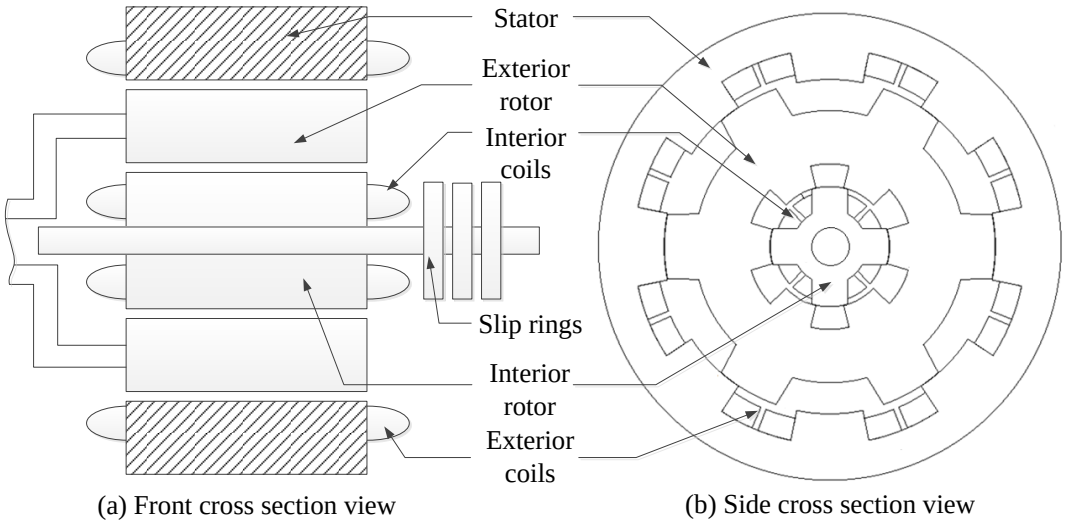

Figure 3.5 DRSRM with external stator and rotating windings on the inner rotor

3.2.3 DRSRM with Internal Wound Stator and Rotating Windings on the External Rotor

Similar in structure to the preceding configuration (3.2.2), here the inner assembly is a wound stator, the intermediate assembly a salient rotor and the external assembly a wound rotor with rotating windings, as illustrated in Figure 3.6.

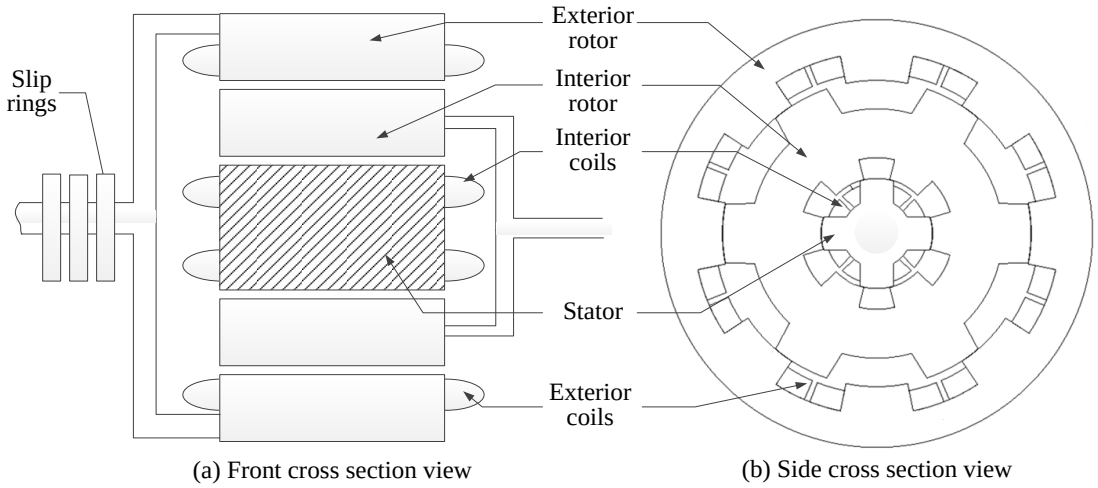

Figure 3.6 DRSRM with internal stator and rotating windings on the external rotor

The DRSRM configurations with rotating windings (3.2.2 and 3.2.3) add complexity to the drive system and decrease the system robustness due to the added brushes and slip-rings. However, they provide better operational flexibility since the two rotors can be easily synchronized or locked together either mechanically or electrically. They also reduce the switching frequency of the rotating windings, depending on the relative speeds between the two rotors instead of the absolute speed.

The above DRSRM configurations realize two switched reluctance machine integrated into as one machine, providing two output paths: One from the exterior rotor, and the other from the interior rotor. The exterior rotor connects directly with the exterior shaft and the interior rotor connects directly with the interior shaft. The shafts can be placed either toward one direction or toward opposite directions to adjust to the specific transmission architecture.

3.2.4 DRSRM with Mechanically Synchronized Inner and Outer Rotors and Central Stator Assembly

The rotors of the DRSRM may be mechanically synchronized to realize a single output shaft configuration, as shown in Figure 3.7.

The flux of the exterior rotor and the flux of the interior rotor are linked together to form a loop. The number of the exterior rotor and interior rotor poles are the same. Each one of the exterior poles is radially aligned with one corresponding interior pole. Flux always conducts through pairs of rotor poles at the same time since the exterior rotor and the interior rotor are mechanically locked together and thus always have the same

rotating speed. The number of the stator poles is different from the number of the rotor poles to enable self-starting capability.

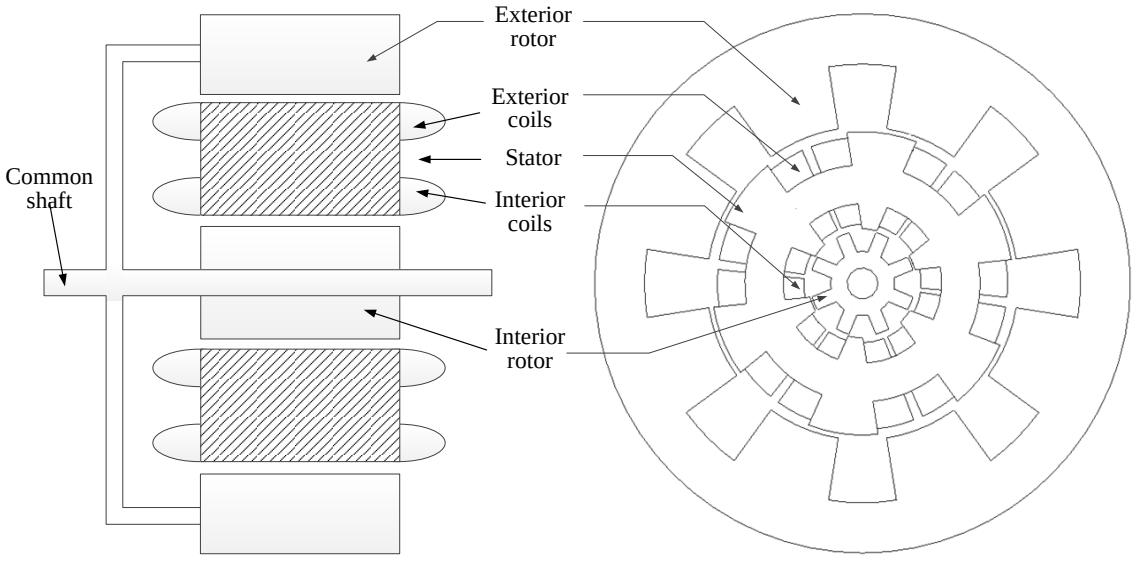

(a) Front cross section view (b) Side cross section view

Figure 3.7 DRSRM with mechanically synchronized inner and outer rotors

3.2.5 DRSRM with Mechanically Synchronized Inner and Outer Rotors and Central Segmented Stator Assembly

An alternative configuration of the previous DRSRM, Section 3.2.4, is shown in Figure 3.8. This topology employs the double rotors to function as one mechanical output, but differing from the previous topology, the stator is composed of segmented components. All the stator segments are mechanically connected to the housing (not shown). Each stator segment is wound by stator coils on both sides. This potentially reduces the weight of the stator by removing the connections between stator segments and increasing the winding areas for stator coils.

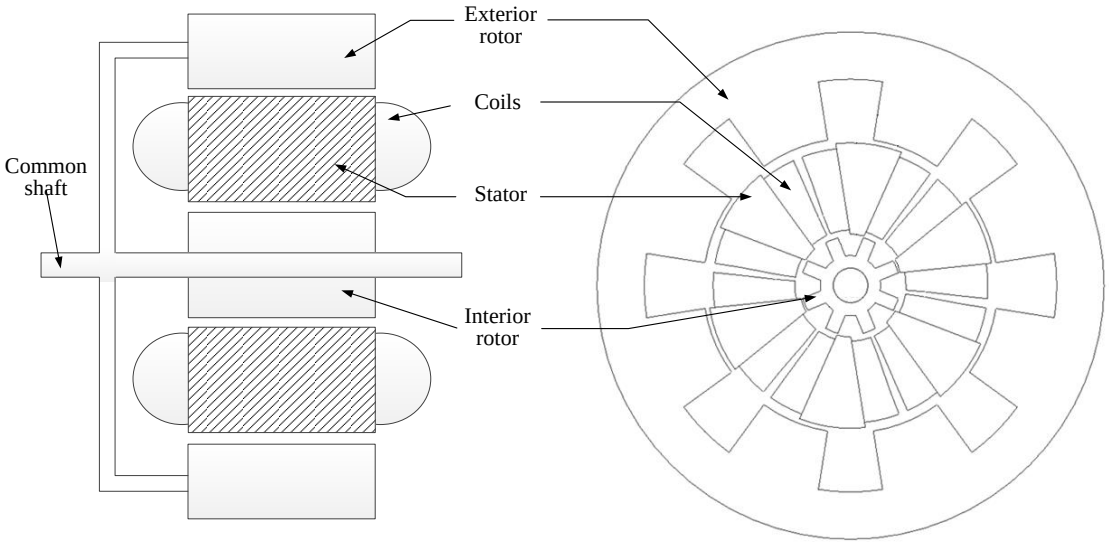

(a) Front cross section view (b) Side cross section view

Figure 3.8 DRSRM with mechanically synchronized inner and outer rotors and central segmented stator assembly

3.2.6 DRSRM with Axially Displaced Components

Three configurations of the DRSRM can be realized by axially displacing the individual machine components to achieve better flexibility in the transmission housing, as illustrated in Figure 3.9. The topology in Figure 3.9 (a) is an alternative representation of that in Section 3.2.1. This topology differs by displacing the double rotors at different positions along the axial direction, which results in more simplicity in terms of machine construction and more flexibility in power-train assembly, especially for those situations where assembly space is limited and predetermined by other components in the power-train. The axially displaced double-rotor configuration also allows for a thinner stator back-iron since the flux paths in the two machines are axially separated. In addition, more room will be available to support the stator from the machine housing to reduce the

cantilever drawback of the stator construction so that more rigidity and reliability of the double-rotor switched reluctance machine can be achieved.

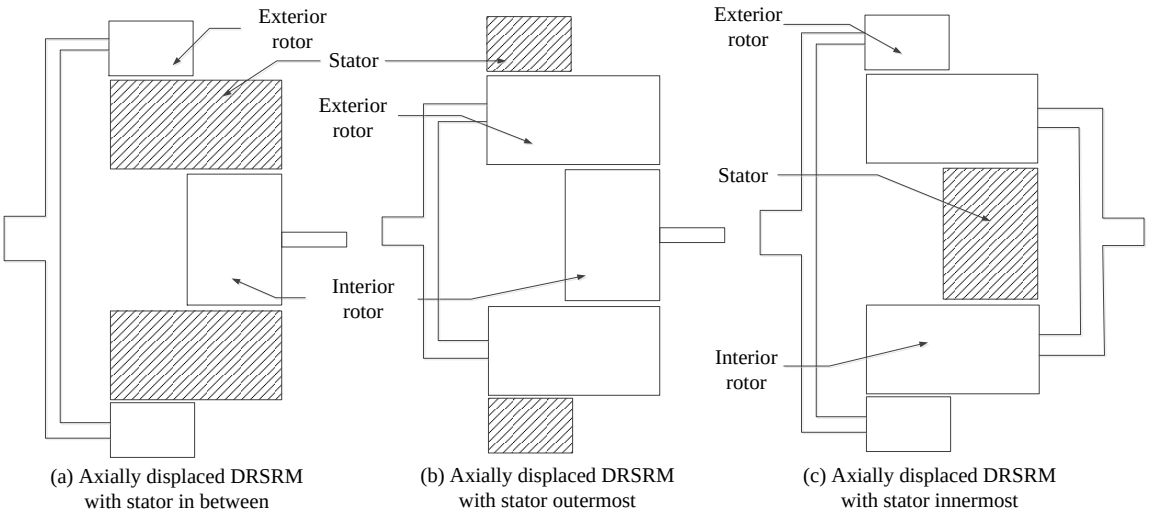

Figure 3.9 Configurations of DRSRM with axially displaced components

Similarly, the topology in Figure 3.9 (b) is an alternative representation of that of Section 3.2.2 in which a stator is placed outermost while the topology in Figure 3.9 (c) is an alternative representation of the third embodiment which a stator is placed innermost. All these variations of the DRSRM allows for more flexibility of the machines in order to fit in the transmission environment.

In summary, there are numerous variations of the DRSRM, and a family of such configurations has been proposed here. Instead of using just one rotor, the DRSRM employs double rotors rotating concentrically with the same stator, either outside the stator or inside, to realize two mechanical shafts output and achieve higher flexibility by running as two separate machines: two motors, two generators, or a motor and a generator at the same time. The double rotors can also be synchronized to have just one output

shaft. The integration reduces the need for another set of stator, machine housing, cooling system, etc., and thus potentially reduces the overall assembly weight and volume for a given power level. The DRSRM can be implemented into full hybrid and plug-in hybrid electric vehicle transmission power-trains to replace the conventional motor and generator. It can also be implemented into a hybrid airplane, a hybrid ship, or some other electro-mechanical integrated transmissions to serve as the electric prime mover and receiver.

Considering all the possible presented configurations, the DRSRM with wound central stator assembly provides the most compact configuration with no axially displaced components or slip-rings. It also provides two output shafts which can be controlled independently and thus suitable for a hybrid transmission application. Therefore, the DRSRM with wound central stator assembly configuration is selected for benchmarking.

3.3 DESIGN OF THE DOUBLE-ROTOR SWITCHED RELUCTANCE MACHINE

In order to validate the concept of the double-rotor switched reluctance machine, a machine is designed as a first generation prototype, i.e. chosen to be within 1 kW laboratory test capabilities. It should be noted here that the prototype DRSRM is therefore a scaled representation of the integrated electro-mechanical hybrid transmission discussed in Chapter 2 in terms of torques, speeds and hence powers.

The DRSRM design starts by an initial sizing exercise where published mathematical equations[67] that estimate the SRM major geometries based on the rated parameters are used as initial starting points for power and torque:

$$P_d = k_e k_d \left(\frac{\pi^2}{120}\right)\left(1-\frac{1}{\sigma\lambda_u}\right) BA_{sp} D^2 LN \tag{3.13}$$

$$T = k_e k_d k_3 k_2 BA_{sp} D^2 L \tag{3.14}$$

where P_d is the machine rated output power, T is the rated torque, k_e is the machine efficiency, k_d is the duty cycle, which is unity if each phase of the switched reluctance machine is conducting consecutively and there is no overlap between any two phases, σ is the inductance ratio at the aligned position between the actual saturated value and the ideal unsaturated value: $\sigma = \frac{L_a^s}{L_a^u}$, L_a^s is the actual saturated inductance value at the aligned position, L_a^u is the ideal unsaturated inductance value at the aligned position, λ_u is

the inductance ratio between the ideal unsaturated value at the aligned position and the unaligned inductance: $\lambda_u = \frac{L_a^u}{L_u}$, the term in the bracket can be written as $k_2 = 1 - \frac{1}{\sigma\lambda_u}$, B is the magnetic flux density at the aligned position, A_{sp} is the specific electric loading, D is the bore diameter in the air gap, L is the lamination stack length, and N is the rotational speed in rpm. It is suggested that some of these coefficients have a certain range based on previous design experience[68][69]:

$$0.65 < k_2 < 0.75 \tag{3.15}$$

$$25000 < A_{sp} < 90000 \tag{3.16}$$

Typically, the machine rated speed, power, torque and required efficiency is pre-determined as the major power-train requirements. Thus, based on equations (3.13) and (3.14), the term indicating the machine volume, D^2L, can be estimated. Then from the application of the motor as well as the space limitation, a specific diameter over length ratio D/L can be chosen as a starting point to define the general contour of the switched reluctance machine.

For the DRSRM prototype application, the interior SRM is defined to work at 0.5 kW, 2000 RPM; while the exterior SRM is defined to work at 0.5 kW, 500 RPM, giving the 4:1 ratios in torques and speeds previously discussed. Given the small rating and physical size of the prototype, the machine efficiency k_e is targeted to be above 80%, while k_2 and A_{sp} are chosen at the middle point of the suggested range as a starting point.

The aligned flux density, B, is chosen to be 1.8T, which is the saturating "knee" point of the most commonly used silicon steels[71]. The machine stack length is initially chosen to be 75mm, and therefore, the bore diameters of both the machines can be calculated from equations (3.13) and (3.14): D_i = 80mm, D_e = 260mm.

Once the major geometries are selected, more detailed machine geometries can be defined thereafter. The machine air gap dimension is chosen to be 0.3mm to minimize the air gap reluctance and thus maximize the reluctance torque while being close to a typical air gap distance of an industrial machine. Pole number configurations of the double-rotor SRM are chosen to be 6/4 for the interior machine due to its simplicity, which offers larger space for windings under the same volume, and 6/8 for the exterior machine. The higher number of rotor poles than stator poles for the exterior SRM reduces the torque ripple and increases the average torque[68]. The same number of the stator poles for the interior and exterior machines also makes it easy for the structure symmetric design as well as simplifies the motor drives design so that two identical motor drives can be applied without changing the drive components.

In order for the designed machine to be structurally feasible, both the stator pole angle and the rotor pole angle should be smaller than the corresponding minimum pole pitch[70]. Figure 3.10 defines the pole angles and the pole pitches for both the interior and exterior switched reluctance machines.

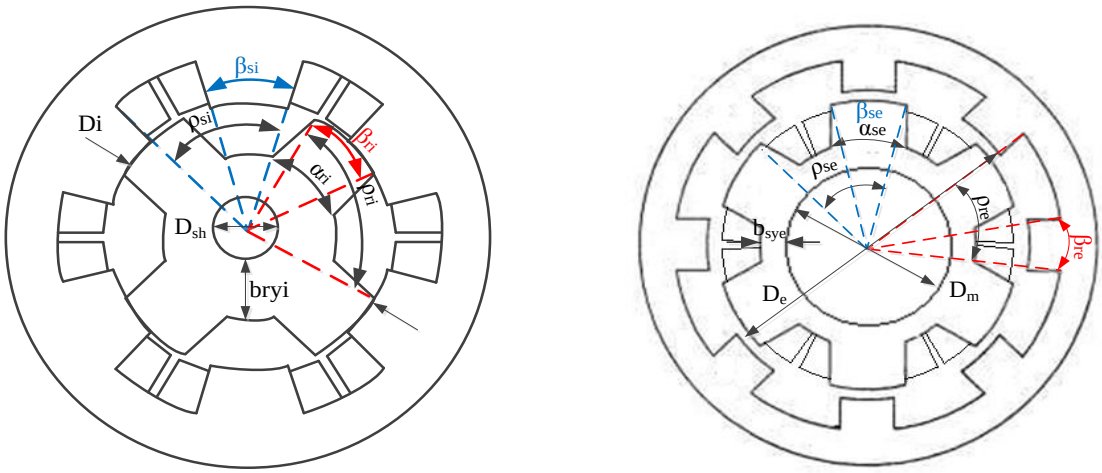

(a) Interior SRM (b) Exterior SRM

Figure 3.10 Mechanical structural feasibility

Referring to Figure 3.10, the following are defined: β_{si} is the stator pole angle of the interior SRM, β_{ri} is the rotor pole angle of the interior SRM, α_{ri} is the rotor pole angle at the pole base of the interior SRM, ρ_{si} is the stator pole pitch angle of the interior SRM, ρ_{ri} is the rotor pole pitch angle of the interior SRM, β_{se} is the stator pole angle of the exterior SRM, α_{se} is the stator pole angle at the pole base of the exterior SRM, β_{re} is the rotor pole angle of the exterior SRM, ρ_{se} is the stator pole pitch angle of the exterior SRM, ρ_{re} is the rotor pole pitch angle of the exterior SRM.

Based on the geometry arrangement shown in Figure 3.10, the following relationships apply:

$$\beta_{si} \leq \rho_{si} = \frac{2\pi}{N_{si}} \tag{3.17}$$

$$\alpha_{ri} = 2\sin^{-1}\left[\frac{\frac{D_i}{2}\sin\left(\frac{\beta_{ri}}{2}\right)}{\frac{D_{sh}}{2}+b_{ryi}}\right] \le \rho_{ri} = \frac{2\pi}{N_{ri}} \tag{3.18}$$

where N_{si} is the number of the interior stator pole, N_{ri} is the number of the interior rotor pole, D_i is the bore diameter of the interior machine, D_{sh} is the shaft diameter of the interior machine, b_{ryi} is the interior rotor back-iron thickness.

Equations (3.17) yields $\beta_{si} \le 60^\circ$ for a 6 poles interior SRM. Based on the interior SRM geometry arrangement, the maximum bore diameter of the interior rotor at the base of the rotor pole should be smaller than the bore diameter of the interior machine, i.e. $\frac{\frac{D_i}{2}}{\frac{D_{sh}}{2}+b_{ryi}} \ge 1$, thus equation (3.18) yields $\beta_{ri} \le 90^\circ$ for a 4 pole interior switched reluctance machine rotor.

Similarly, equations (3.19) and (3.20) present the structural feasibility requirement for the exterior stator and rotor:

$$\alpha_{se} = 2\sin^{-1}\left[\frac{\frac{D_e}{2}\sin\left(\frac{\beta_{se}}{2}\right)}{\frac{D_m}{2}+b_{sye}}\right] \le \rho_{se} = \frac{2\pi}{N_{se}} \tag{3.19}$$

$$\beta_{re} \le \rho_{re} = \frac{2\pi}{N_{re}} \tag{3.20}$$

where N_{se} is the number of the exterior stator pole, N_{re} is the number of the exterior rotor pole, D_e is the bore diameter of the exterior machine, D_m is the bore diameter at the interface between the two machines, or the inner diameter of the exterior machine, b_{sye} is the exterior stator back-iron thickness, as illustrated on Figure 3.10.

Based on the geometry arrangement of the exterior SRM, the maximum bore diameter at the base of the stator pole should be smaller than the bore diameter of the exterior machine, i.e., $\frac{\frac{D_e}{2}}{\frac{D_m}{2}+b_{sye}} \geq 1$, thus equation (3.19) yields $\beta_{se} \leq 60^\circ$ for a 6 pole exterior switched reluctance machine stator while equation (3.20) yields $\beta_{re} \leq 45^\circ$.

Secondly, it is necessary for switched reluctance machine to have fully unaligned position so that the minimum inductance can be reached and thus the maximum torque can be extracted. This requires the stator pole arc length to be smaller than the arc length between two neighboring rotor poles. Figure 3.11 illustrates the second geometry criteria for switched reluctance machines.

Based on the machine geometry, equations (3.21) and (3.22) are summarized for the interior SRM and the exterior SRM respectively as:

$$\beta_{si} \leq \rho_{ri} - \beta_{ri} \tag{3.21}$$

$$\beta_{se} \leq \rho_{re} - \beta_{re} \tag{3.22}$$

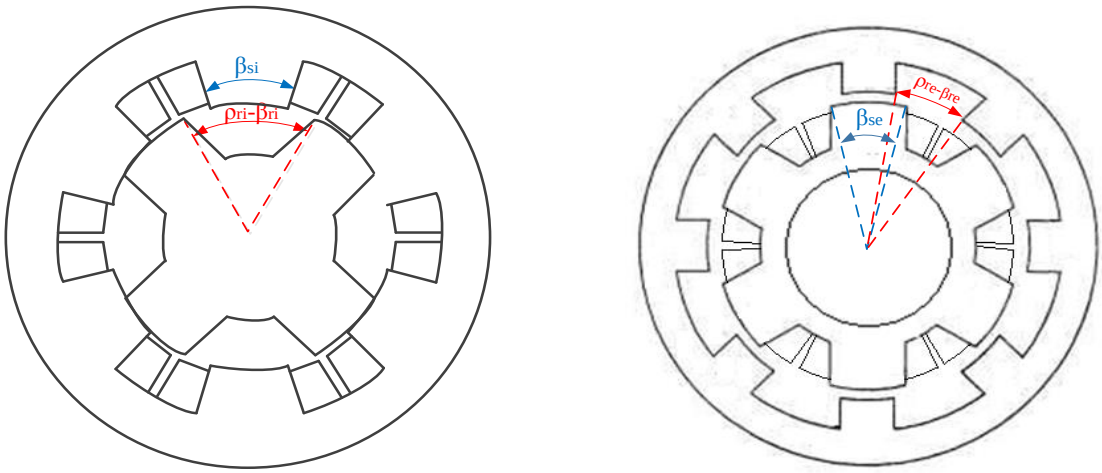

(a) Interior SRM fully unaligned criteria (b) Exterior SRM fully unaligned criteria

Figure 3.11 Fully unaligned geometry requirements for the DRSRM

The pole pitch angles can be expressed as functions of the pole numbers as well as the bore diameter and the gap distance, and thus the above two inequalities can be expanded and rewritten as:

$$\left(\frac{2\pi}{N_{ri}}-\beta_{ri}\right)\left(\frac{D_i}{2}-g\right)-\frac{D_i}{2}\beta_{si} \geq 0 \tag{3.23}$$

$$\left(\frac{2\pi}{N_{re}}-\beta_{re}\right)\left(\frac{D_e}{2}+g\right)-\frac{D_e}{2}\beta_{se} \geq 0 \tag{3.24}$$

where g is the air gap distance, which is designed to be the same for both machines.

Since the air gap distance is typically much smaller than the machine bore diameter, in this case the air gap distance is 0.3mm, the air gap distance in the above inequalities can be neglected and thus the two equations can be simplified as:

$$\beta_{ri} + \beta_{si} \leq \frac{2\pi}{N_{ri}} \tag{3.25}$$

$$\beta_{se} + \beta_{re} \leq \frac{2\pi}{N_{re}} \tag{3.26}$$

Since the interior rotor has 4 poles while the exterior rotor has 8 poles, equations (3.25) and (3.26) yield:

$$\beta_{ri} + \beta_{si} \leq 90^{\circ} \tag{3.27}$$

$$\beta_{se} + \beta_{re} \leq 45^{\circ} \tag{3.28}$$

Finally, in order for the switched reluctance machine to have self-starting capability, when one of the rotor poles is fully aligned with one of the stator poles, the next rotor pole in sequence should start to align with the corresponding stator pole, i.e. there should be some overlap between the next rotor pole and the corresponding stator pole so that at standstill, there should always be at least one pole that can provide positive torque. The angles and geometries to satisfy the self-starting criteria are illustrated in Figure 3.12 which shows the case for both the interior SRM and the exterior SRM rotating counterclockwise, and both rotors are at the fully aligned positions. Here, the center line of the aligned stator pole teeth is coincident with the center line of the aligned rotor pole teeth. The self-starting criteria require that the next phase rotor pole starts to overlap with the next phase stator pole when the currently excited rotor pole fully enters the overlap position, i.e. when $\gamma_{i1L} = 0$ for the interior rotor and $\gamma_{e1L} = 0$ for the exterior rotor.

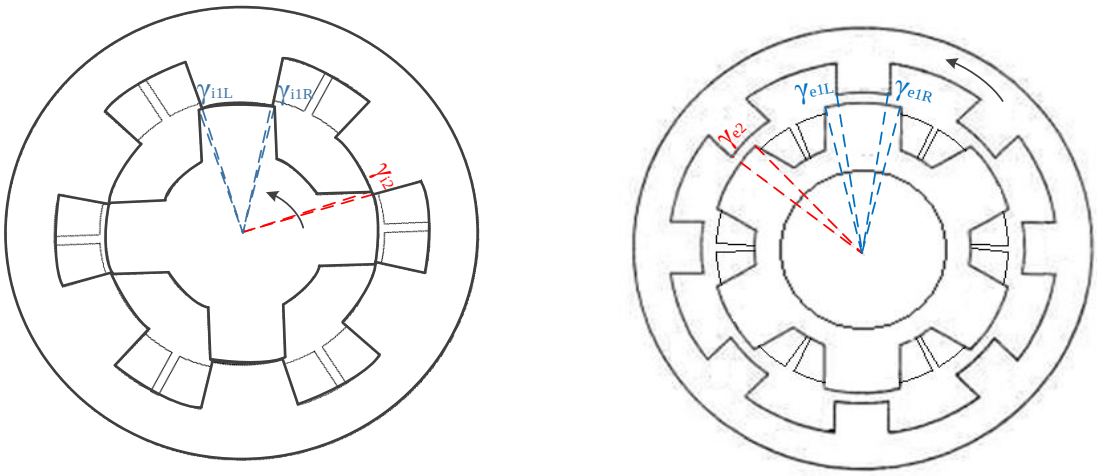

(a) Interior SRM self-starting requirements

(b) Exterior SRM self-starting requirements

Figure 3.12 Self-starting geometry requirements for the DRSRM

The overlapped angles under the next phase excitation period should be greater than zero degrees, i.e.:

$$\gamma_{i2} - \gamma_{i1L} \geq 0^{\circ} \tag{3.29}$$

$$\gamma_{e2} - \gamma_{e1R} \geq 0^{\circ} \tag{3.30}$$

It can be observed from the geometry of the interior SRM, Figure 3.12(a), that the difference angle in equation (3.29) is equivalent to the stator pole angle plus stator pole pitch angle, minus the rotor pitch angle. Similarly, the difference angle in equation (3.30) is equivalent to the rotor pole angle plus rotor pitch angle, minus the stator pitch angle, where these angles are defined in Figures 3.10 and 3.11. Thus, equations (3.29) and (3.30) can be rewritten using the machine pole angles and pitch angles:

$$\rho_{si} + \beta_{si} - \rho_{ri} \geq 0 \tag{3.31}$$

$$\rho_{re} + \beta_{re} - \rho_{se} \geq 0 \tag{3.32}$$

By replacing the pitch angles with the pole numbers, the pole angles of both of the SRM machines based on the self-starting criteria can be written as:

$$\beta_{si} \geq \frac{2\pi}{N_{ri}} - \frac{2\pi}{N_{si}} = 30^{\circ} \tag{3.33}$$

$$\beta_{re} \geq \frac{2\pi}{N_{se}} - \frac{2\pi}{N_{re}} = 15^{\circ} \tag{3.34}$$

It should be noted here that the air gap distance g is also neglected in the calculation since it is insignificant when compared to the machine bore diameters. Therefore, combining all of the criteria, i.e. the mechanical construction feasibility, the fully unaligned position requirements, and the self-starting requirements, the constrained pole angles for the interior SRM design are expressed as:

$$30^{\circ} \leq \beta_{si} \leq 60^{\circ} \tag{3.35}$$

$$\beta_{ri} \leq 90^{\circ} \tag{3.36}$$

$$\beta_{si} + \beta_{ri} \leq 90^{\circ} \tag{3.37}$$

and the constrained pole angles for the exterior SRM design are expressed as:

$$\beta_{se} \leq 60^{\circ} \tag{3.38}$$

$$15^{\circ} \leq \beta_{re} \leq 45^{\circ} \tag{3.39}$$

$$\beta_{se} + \beta_{re} \leq 45^{\circ} \tag{3.40}$$

The above criteria set the constraints for the initial machine pole angles design. In addition, a good stator pole-arc over pole-pitch ratio can be chosen between 0.35 and 0.5 in order to output high torque based on previous sensitivity studies[72]. Thus, the initial stator pole-arc angles and the rotor pole-arc angles are chosen to be 30° and 32° respectively for the interior SRM and 21° and 22° respectively for the exterior SRM, which yield the pole-arc over pole-pitch ratio 0.35 and 0.49, respectively.

Stator pole widths can be directly found once the stator pole angles and the bore diameters are known. Stator pole heights can be found by multiplying a coefficient to the unaligned pole lengths:

$$h_{si} = \frac{1}{2} k_{hs} \frac{D_i}{2} \left(\frac{2\pi}{N_{ri}} - \beta_{ri} - \beta_{si} \right) \tag{3.41}$$

$$h_{se} = \frac{1}{2} k_{hs} \frac{D_e}{2} \left(\frac{2\pi}{N_{se}} - \beta_{re} - \beta_{se} \right) \tag{3.42}$$

where h_{si} is the stator pole height in the interior SRM, h_{se} is the stator pole height in the exterior SRM and k_{hs} is the stator pole height coefficient. By using the pole angles for the interior SRM and the exterior SRM respectively and a coefficient of 1.05[67] in the above equation, the stator pole heights of each machine can be calculated as 10.26mm for interior SRM and 20.25mm for the exterior SRM.

Then the stator back-iron thickness can be found via equations (3.43) and (3.44) for the interior stator and the exterior stator, respectively:

$$y_{si} = \frac{D_m - D_i}{2} - h_{si} \tag{3.43}$$

$$y_{se} = \frac{D_e - D_m}{2} - h_{se} \tag{3.44}$$

where D_m is the bore diameter at the interface of the two SRM machines, which is assigned to be 150mm. Thus, the stator back-iron thicknesses are 24.74mm for the interior SRM and 34.75mm for the exterior SRM.

The rotor pole height and back-iron thickness for the interior SRM and the exterior SRM can be both defined by multiplying the stator pole height and stator back-iron thickness, respectively by suitable coefficients as discussed in references[67][68]:

$$h_{ri} = k_{hri} h_{si} \tag{3.45}$$

$$y_{ri} = k_{yri} y_{si} \tag{3.46}$$

$$h_{re} = k_{hre} h_{se} \tag{3.47}$$

$$y_{re} = k_{yre} y_{se} \tag{3.48}$$

where h_{ri} is the interior rotor pole height, y_{ri} is the interior rotor back-iron thickness, h_{re} is the exterior rotor pole height, y_{re} is the exterior rotor back-iron thickness, k_{hri}, k_{yri}, k_{hre} and k_{yre} are the corresponding coefficients between the stator parameters and the rotor parameters. Substituting the coefficients k_{hri} = 0.9, k_{yri} = 0.8, k_{hre} = 1.2 and k_{yre} =

1.05, the rotor pole heights for the interior SRM and the exterior SRM are: 9.23mm and 24.3mm; the rotor back-iron thickness for the interior SRM and the exterior SRM are: 19.79mm and 36.48mm, respectively.

Hence, from the above calculations, all the major parameters for the interior SRM and the exterior SRM have been defined. Figure 3.13 presents the initial designed machine geometries for both the interior SRM and the exterior SRM, while Table 3.1 summarizes the major design parameters as in the initial designs for both the interior SRM and the exterior SRM.

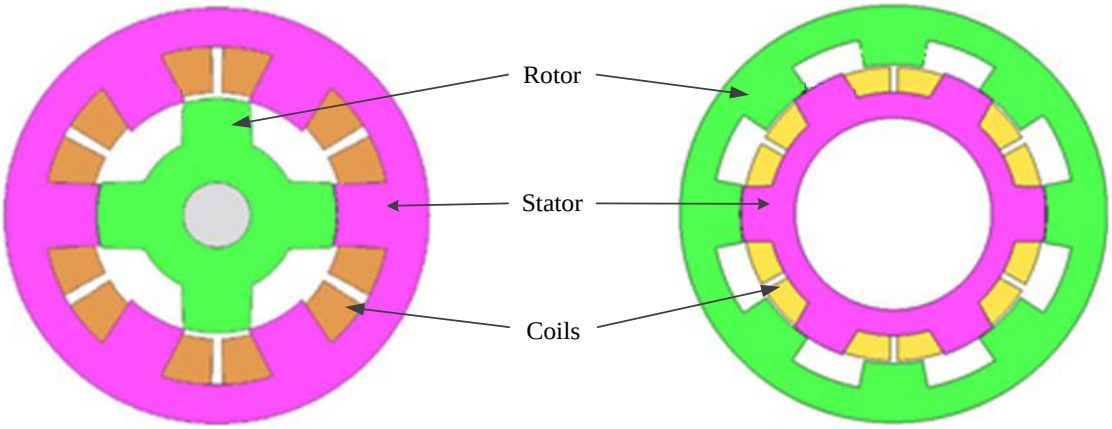

(a) Interior SRM geometry (b) Exterior SRM geometry

Figure 3.13 Initial designed geometries

Table 3.1 Initial design parameters of the DRSRM

	Interior SRM	Exterior SRM
Number of poles	4	8
Number of slots	6	6
Bore diameter (mm)	80	260
Stator pole angle (degree)	30	21
Stator pole height (mm)	10.26	20.25
Stator back-iron thickness (mm)	24.74	34.75
Rotor pole angle (degree)	32	22
Rotor pole height (mm)	9.23	24.3
Rotor back-iron thickness (mm)	19.79	36.48
Shaft diameter (mm)	25	160
Stack length (mm)	75	75
Air gap distance (mm)	0.3	0.3

3.4 SIMULATIONS OF THE DOUBLE-ROTOR SWITCHED RELUCTANCE MACHINE

Having arrived at a preliminary design for the double-rotor machine, the magnetic design can be studied in greater details via Finite Element Analysis (FEA). For such complicated geometries as presented by the DRSRM and where a major aspect of the machine performance is experienced in the saturated or magnetically non-linear region of the machine soft magnetics, FEA is critical tool required to assess electric machine design, optimization and validation. FEA serves as a crucial intermediate step between analytical calculations and experimental prototype validation. Generally, it provides more accurate and thorough information compared to analytical calculations that are typically based on equations and subjected to certain assumptions or simplifications. Further, by utilizing numerical iteration techniques, the prototype developing time is considerably reduced and unnecessary product generation costs are avoided. Thus, the FEA tool has been widely adopted in the electric machine design process, especially to validate the design concept and optimize the machine parameters before manufacturing of costly prototypes.

As discussed, the SRM operates in highly magnetically nonlinear regions where tooth and back-irons regions experience high saturation in order to extract the maximum energy conversion, hence torque and power. In addition, the saliency of both the stator and the rotor presents further complexity since the flux-linkage from the aligned to unaligned positions varies with positions and current levels. A number of valuable reference publications discussed the mathematical modeling and analytical solutions of

switched reluctance machines[73][74][75][76][77][78][79], from which it can be concluded that the nonlinear modeling and analytical solution of switched reluctance machines is complicated and the results gained are not always accurate due to the simplifying assumptions or model fidelity. It is also much more time-consuming to develop a switched reluctance machine analytical model than running the FEA simulation due to the complicated and changing flux paths. Thus, FEA simulations are applied in the DRSRM design process to validate the initial design as well as further optimize the machine performance.

Typically, several types of multi-physical studies can be carried out in electric machine FEA analysis, i.e., electromagnetic analysis, frequency harmonics analysis, thermal analysis, and mechanical analysis to give comprehensive studies regarding the different but linked design perspectives. These studies can be implemented by choosing either 2-dimensional (2D) simulation or 3-dimensional (3D) simulation based on specific analysis objectives. A 2D simulation is generally much less demanding than a 3D simulation in terms of computation time and is generally acceptable for electric machines that have large length-to-diameter ratio, so that the impact of axial contributions may be assumed negligible and only the cross section area is used to get the radial and circumferential results. On the other hand, 3D simulation builds up meshes in three dimensional spaces and fully takes account of axial direction effects and interactions of different components along different axes. Even though 3D simulation significantly increases the mesh complexity, and thus, the computation time, it is possible to provide more precise calculation and can capture some of the specific problems that 2D FEA

simulations approximates, such as the effect of end windings and temperature distribution. However, with increased mesh complexity solution convergence has to be checked thus the trade-off between results and computation time have to be judged. For this study, 2D FEA is used throughout but the final design is checked with 3D FEA.

3.4.1 Electromagnetic Simulation

Electromagnetic simulation is applied first to study the machine performance and the influence of design parameters. In order to precisely study the preliminary designed double-rotor switched reluctance machines, extensive 2D simulations have been carried out, so that a comprehensive performance study is provided. Both the interior SRM and the exterior SRM are studied individually then the combined DRSRM is studied to analyze the overall performance. All simulations are carried out via the commercial FEA electromagnetic software JMAG[84], which is also capable of thermal, frequency, and structural simulation. Most of the subsequent post-processing of results can be carried out by JMAG while Matlab and Excel are used in some data-processing cases.

Each machine model contains several components: the rotor, the stator and coils. Shafts are ignored in the models since they do not affect the flux patterns in the electromagnetic field, and thus do not contribute to output performance. The losses on the shaft are also negligible.

Model Geometries

2D cross section models of each machine have already been shown in Figure 3.13, showing the stators, the rotors and three phase windings that are evenly distributed in the slots around the machine periphery.

In addition, both the stators and rotors of the two machines are assumed to be laminated so as to reduce eddy current losses in the cores. A stacking factor of 98% is applied on both rotor and stator components.

Material Settings

Different materials have been assigned to the different parts of the models. Both the stator core and the rotor core for both machines are manufactured with soft magnetic steel material AK Steel M15 Gauge 29, which is an industrial grade steel having an thickness for each lamination of 0.35mm and 3.2 W/kg at 1.5T peak, 60Hz. However, since JMAG is a Japanese software, it does not have the loss information for M15. The most equivalent material then is 35JN300 from JFE Steel, with 0.35mm thickness on each lamination and the same loss characteristics. Figure 3.14 shows the B-H curves of both the materials (which are essentially identical) and Figure 3.15 compares the loss information of the lamination steels[71]. Since the materials are equivalent, 35JN300 will be used in the subsequent simulations. Manufacture iron loss data based on frequency and the magnetic flux density[71] is used to assess iron losses. Typically, only a set of loss curves are given. However, by transforming the loss data into logarithmic axes, the estimation of other frequencies by applying linear interpolation and logarithmic

approximation is enabled. Section 3.4.2 will further discuss and illustrate this procedure. Furthermore, each coil is assigned as copper with the default parameters in JMAG.

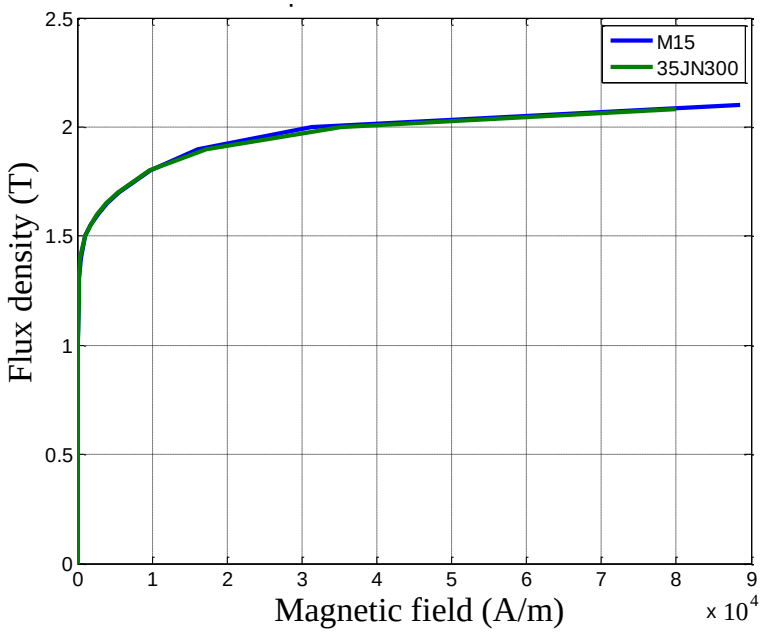

Figure 3.14 Magnetic characteristics of M15 and 35JN300

Grade	Thickness mm (in.)	Assumed Density kg/dm³	Resistivity μΩ-cm	Core Loss								Magnetic Flux Density T			
				Watts per kilogram				Watts per pound							
				50Hz		60Hz		50Hz		60Hz					
				1.0T	1.5T	1.0T	1.5T	1.0T	1.5T	1.0T	1.5T	B10	B25	B50	B100
35JN210	0.35 (0.0138)	7.60	59	0.85	2.05	1.05	2.55	0.39	0.93	0.48	1.16	1.47	1.57	1.65	1.77
35JN230		7.60	55	0.89	2.10	1.10	2.60	0.40	0.95	0.50	1.18	1.47	1.57	1.66	1.78
35JN250		7.60	54	0.93	2.25	1.20	2.75	0.42	1.02	0.54	1.25	1.48	1.57	1.66	1.78
35JN270		7.65	54	1.00	2.40	1.25	2.95	0.45	1.09	0.57	1.34	1.48	1.58	1.67	1.79
35JN300		7.65	51	1.10	2.60	1.40	3.20	0.50	1.18	0.64	1.45	1.50	1.59	1.68	1.80
35JN360		7.65	47	1.25	2.95	1.60	3.60	0.57	1.34	0.73	1.63	1.51	1.61	1.69	1.81
35JN440		7.70	38	1.45	3.40	1.77	4.23	0.66	1.54	0.80	1.92	1.53	1.62	1.71	1.82

Grade	Thickness in. (mm)	Max. Core Loss at 1.5T			
		Watts per kilogram		Watts per pound	
		50Hz	60Hz	50Hz	60Hz
M-15	0.014 (0.36)	2.53	3.20	1.15	1.45
M-19		2.75	3.48	1.25	1.58
M-22		2.93	3.70	1.33	1.68
M-27		3.13	3.97	1.42	1.80
M-36		3.31	4.19	1.50	1.90

Figure 3.15 Core loss characteristics of lamination steels

Mesh Settings

A typical finite element mesh assembled for DRSRM simulation is shown in Figure 3.16. Higher mesh density is applied along the stator-rotor air gap interfaces that locate on both sides of the stator.

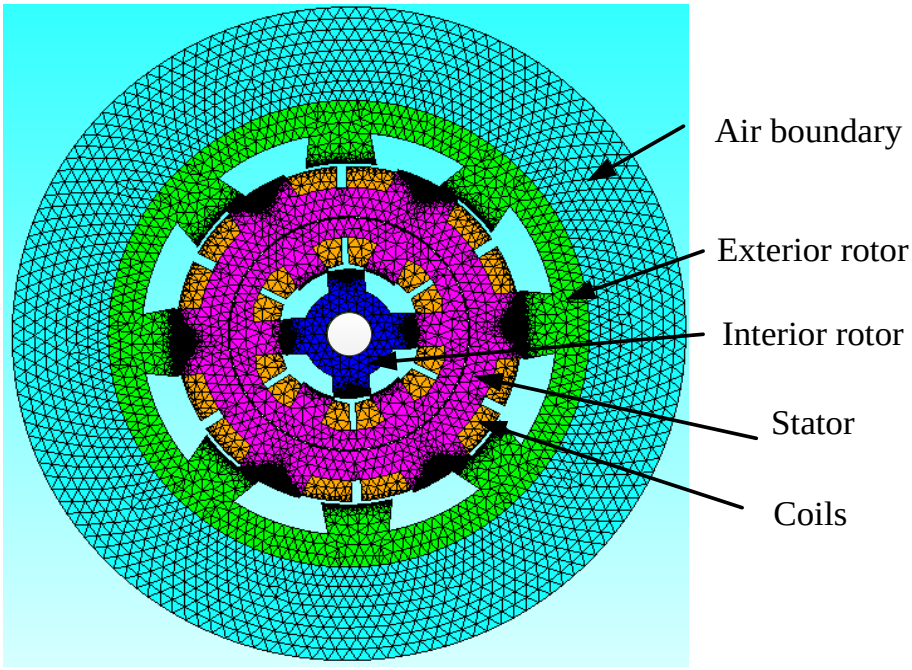

Figure 3.16 Mesh of the DRSRM

A sliding mesh algorithm is applied by the JMAG solver at the air gap interfaces, thus the rotor rotates from the stator at every step increment so that meshes in the air gap automatically match with successive solution. Finally, air regions are created to complete the simulation model. The air regions in the rotor gaps rotate with the rotor in order to keep the model solution. An external region of air is modeled, the outer diameter of which is set with zero magnetic vector potential.

Circuit and Excitation

Each phase of the switched reluctance machine is connected to an electronic circuit simulation model that implements a current supply. Each phase is switched on and switched off at angles defined by reference to rotor positions. Different switch-on and switch-off angles have been investigated to optimize the machine torque output, which will be further explained in the following sections. Once all of the initial settings are assigned, the simulation can be carried out by defining the time step as well as the sampling frequency.

Winding and Excitation

The machine winding design is subject to the stator slot geometry and the machine drive capability including the maximum DC link voltage and the maximum current that the machine drive can supply. The wire gauge used in the winding is influenced by the drive current capability and thermal design of the coil. The number of turns is limited by the available stator slot space subject to the size of the wire gauge. For the prototype DRSRM drive system, the DC link voltage is 300V and the power electronic drive is limited to 10A maximum current so as not to compromise future testing. Assuming ideal rectangular current pulse excitation, for a 3-phase SRM, the peak phase current has a 1:3 duty, i.e. on for one period and off for 2 periods. The RMS phase current is equal to $\frac{1}{\sqrt{3}}$ of the peak current value, i.e. 0.577 I_{pk} or 5.77A RMS. Thus, the winding coil is selected to be 4 strands of AWG 24 wires. Each strand of the wire is rated for 1.93A, giving a

thermal current capability of 7.72A continuous for a naturally ventilated machine scenario. This figure allows 38% margin on design at this point in the design process. The AWG 24 wire has an outer diameter of 0.51mm copper, or 0.57mm including the heavy built enamel insulation coating. The small wire gauge and parallel combination used for the machine winding increases the winding flexibility and thus making it easier for hand winding as discussed in Chapter 4.

Once the size of the wire is selected, the maximum number of turns per phase can be determined by the available stator slot areas. Figure 3.17 illustrates the winding areas and the available winding space for both the interior SRM and the exterior SRM. The total winding copper area divided by the total slot available area per phase is defined as the slot fill factor, or simply fill factor. It is a typical practice in manually wound switched reluctance machines to limit the designed fill factor to be less than 40%. The other part of the space will be taken by the wire insulations, slot wedges, slot liners and the space between wires, which is inevitable and could be substantial for hand wound machines. In this case, the interior SRM winding is designed with 93 turns that yields a fill factor of 35.5%, and the exterior SRM winding is designed with 160 turns that yields a fill factor of 38.9%. The DC phase resistance can thus be estimated by calculating the overall winding length, copper conducting area and the resistivity of copper. A factor of 1.05 is used to determine the AC resistance[86]. Thus, the SRM machine copper loss can be calculated based on the fundamental equation of $3I^2R$, where I is the RMS phase current and R is the total phase AC resistance.

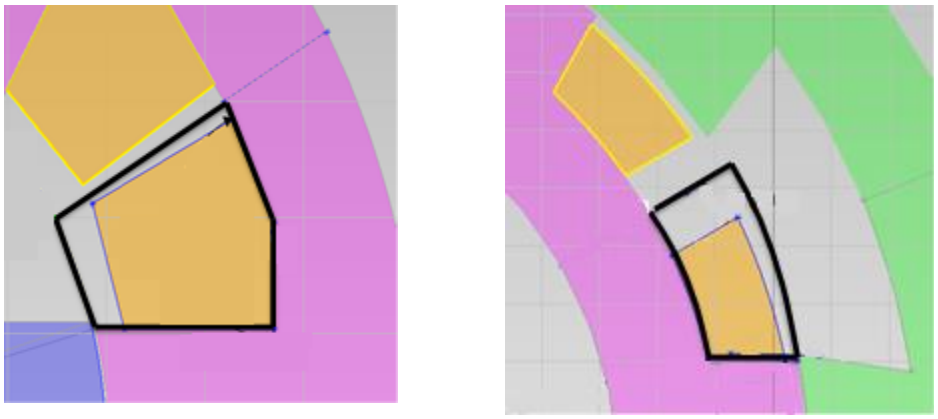

(a) Fill factor of the interior SRM (b) Fill factor of the exterior SRM

Figure 3.17 Winding space and fill factor

3.4.2 Iron Loss Analysis

The JMAG FEA solves for the magnetic field of the DRSRM and generates results of the flux distribution and variation during rotation. By using the field solutions from the electromagnetic simulation, the amplitude and frequency of the flux density at each part of the machine can be gained, and thus the iron loss of each component can be analyzed[80].

The loss information of the lamination steel can be found from the manufactures specifications[71]. Various curves represent the iron loss per volume at different frequencies as functions of the flux density. Figure 3.18 (a) shows the iron loss curves for 35JN300. The iron loss curves can be re-plotted using logarithm scales to linearize the trends as shown in Figure 3.18 (b), in which each curve is approximated by a linear function:

$$\log(P) = a\log(B) + b \tag{3.49}$$

where P is the iron loss per unit volume, B is the flux density, a is the slope of the linear trend line and b is the interception of the trend line on the y axis to the logarithmic scale. Table 3.2 summarizes the a values and b values at different excitation frequencies using the linear approximation.

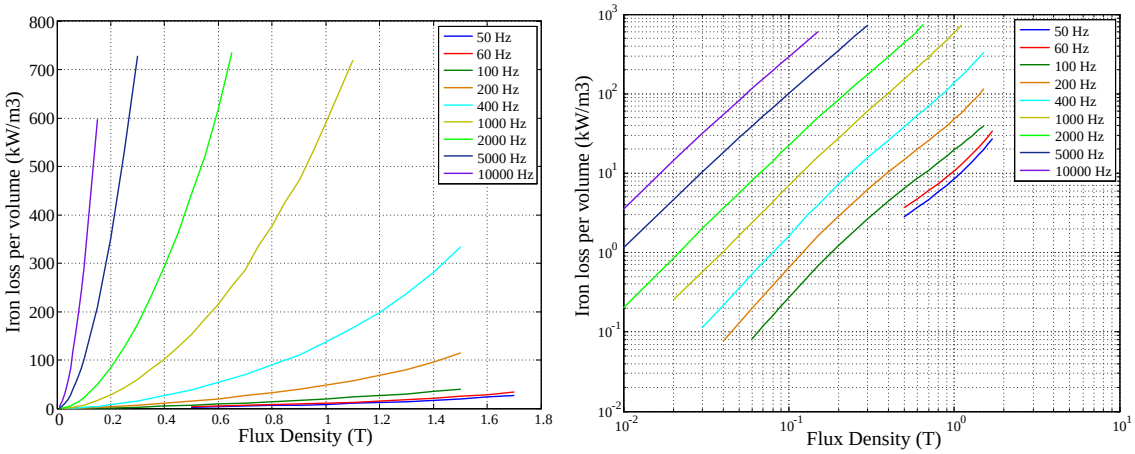

(a) Iron loss curves in linear scale (b) Iron loss curves in logarithm scale

Figure 3.18 Iron loss curves for 35JN300

Table 3.2 Values for a and b for 35JN300 lamination steel

Frequency	50Hz	60Hz	100Hz	200Hz	400Hz
a	1.85	1.80	1.88	1.93	1.99
b	3.96	4.06	4.31	4.72	5.17
Frequency	1000Hz	2000Hz	5000Hz	10000Hz	
a	1.96	1.93	1.88	1.89	
b	5.78	6.24	6.88	7.36	

It can be observed from Figure 3.18 (b) that all the trends lines are closely parallel and thus an average value of a can be taken from Table 3.2, i.e. a=1.90. The average value of b can be derived by plotting b as a function of frequency and using a logarithmic trend line to approximate the b curve, shown in Figure 3.19. Therefore, the loss per unit mass values, based on varying frequency, can be interpolated by applying logarithmic approximation as:

$$P = \log^{-1}\left[1.9\log(B) + 0.64\ln(f) + 1.37\right] \tag{3.50}$$

After an (or number of) integer electrical cycles, the magnetic field variation with time for each element in the FEA solution can be decomposed into different harmonic orders and the flux density amplitude and the frequency of each order analyzed by Fourier techniques. Equation (3.50) can then applied to each harmonic component to estimate the iron loss at each harmonic frequency order, *n*:

$$P_n(B_n, f_n) = \log^{-1}\left[1.9\log(B_n) + 0.64\ln(f_n) + 1.37\right] \tag{3.51}$$

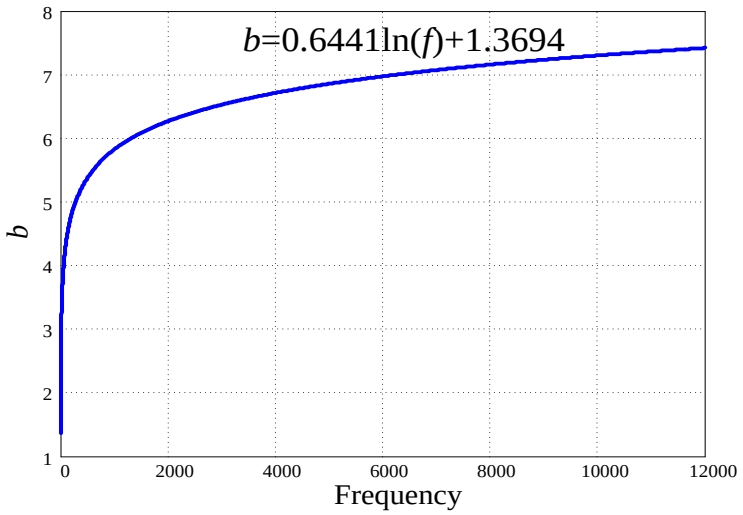

Figure 3.19 Value of *b* as a function of frequencies

Summing all frequency contributions, equation (3.52) yields the total iron loss per unit volume for all harmonic orders:

$$P_{Total} = \sum_{n=1}^{\infty} P_n(B_n, f_n) \tag{3.52}$$

Interrogation of the full FEA solution at an element level would be somewhat cumbersome and time consuming. Hence, a number of profiles were defined on the machine lamination and then a simplifying assumption made, i.e. that the flux waveform at the profile was consistent through the part. Figures 3.20 and Figure 3.21 present the flux waveforms of the interior rotor and the interior stator, respectively, at the chosen profile on each part.

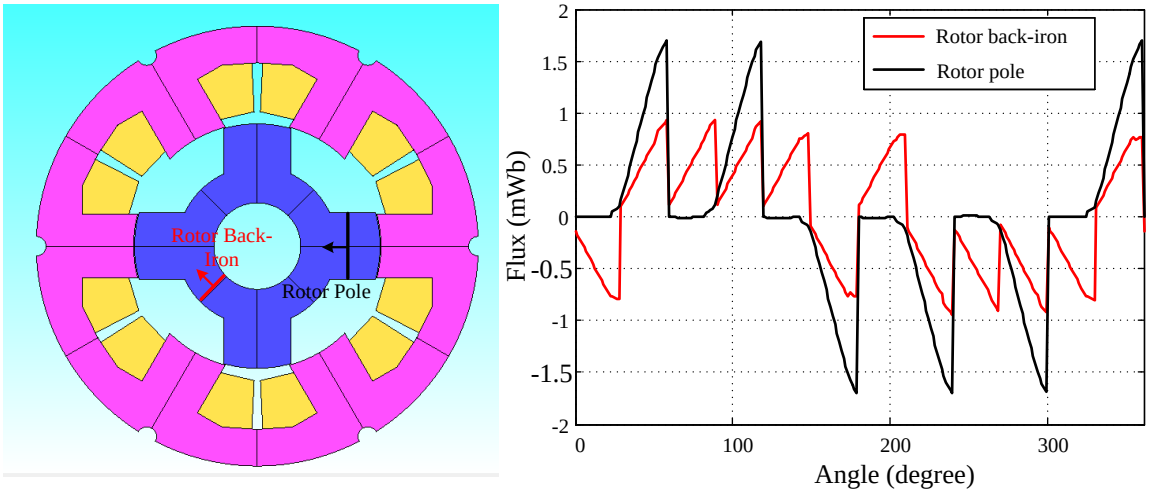

Figure 3.20 Sample flux waveforms for the interior rotor

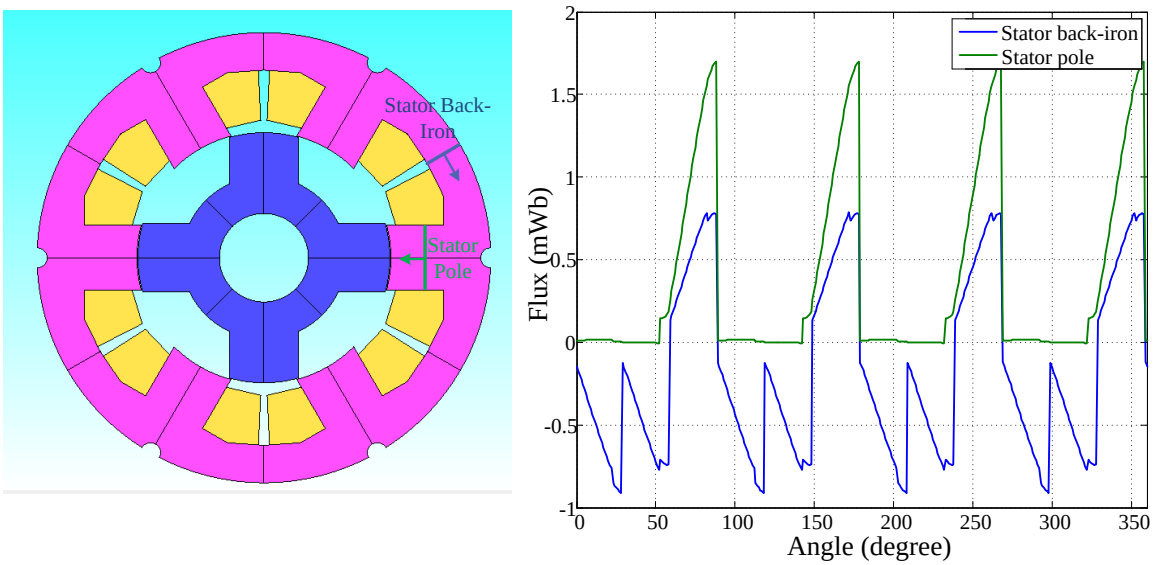

Figure 3.21 Sample flux waveforms for the interior stator

It can be observed that different parts of the machine are subject to different flux variations. Thus, it is necessary to divide the machines into a number of constituent parts and then take the harmonic content of the flux densities on each part to calculate the part iron loss and summating to get the total loss [81]. The machine can be effectively divided into 4 main parts to calculate the iron loss: (i) the rotor back-iron, (ii) the rotor pole, (iii) the stator back-iron and (iv) the stator pole. For the interior machine operating at 2000RPM and the exterior machine operating at 500RPM, the fundamental frequencies for the rotor and the stator as well as their individual volume are summarized in Table 3.3. Based on the fundamental frequencies of each part, Fourier analysis can be carried out to calculate the flux density of different harmonic orders. Figure 3.22 presents the rotor back-iron and the rotor pole flux density harmonics and Figure 3.23 presents the stator back-iron and the stator pole flux density harmonics.

Based on equation (3.52) and the above procedure, the iron loss at its associated harmonic frequency per unit volume is derived. The iron loss on each part is thus calculated by summating the loss on all the harmonics over the entire volume. Table 3.4 shows the total iron loss as well as the iron loss at individual harmonics for the interior rotor back-iron, the interior rotor pole, the interior stator back-iron, and the interior stator pole, respectively. It can be observed that the stator back-iron generates the largest proportion of the iron loss, accounting for three quarters of the total iron loss. The loss analysis for the exterior SRM machine is similar to the process discussed above and is therefore not repeated here for the sake of brevity.

Table 3.3 Fundamental frequencies and volumes of different parts

		Rotor back-iron	Rotor pole	Stator back-iron	Stator pole
Interior SRM	Fundamental frequency (Hz)	33.33	33.33	133.33	133.33
	Volume (cm^3)	133	14	279	95
Exterior SRM	Fundamental frequency (Hz)	6.25	6.25	50	50
	Volume (cm^3)	836	297	453	189

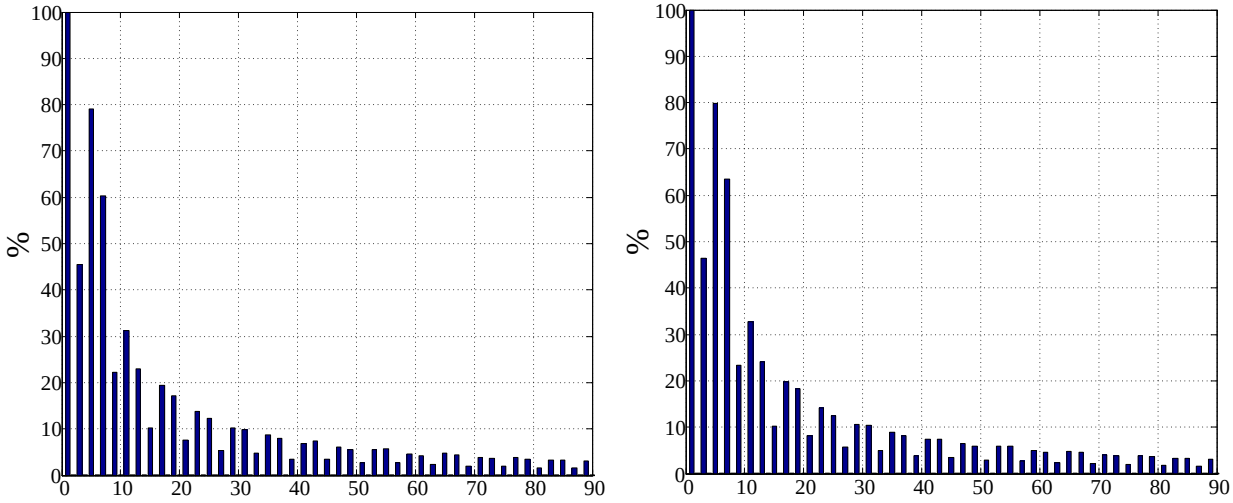

(a) Interior rotor back iron (b) Interior rotor pole

Figure 3.22 Flux density harmonics in the interior rotor

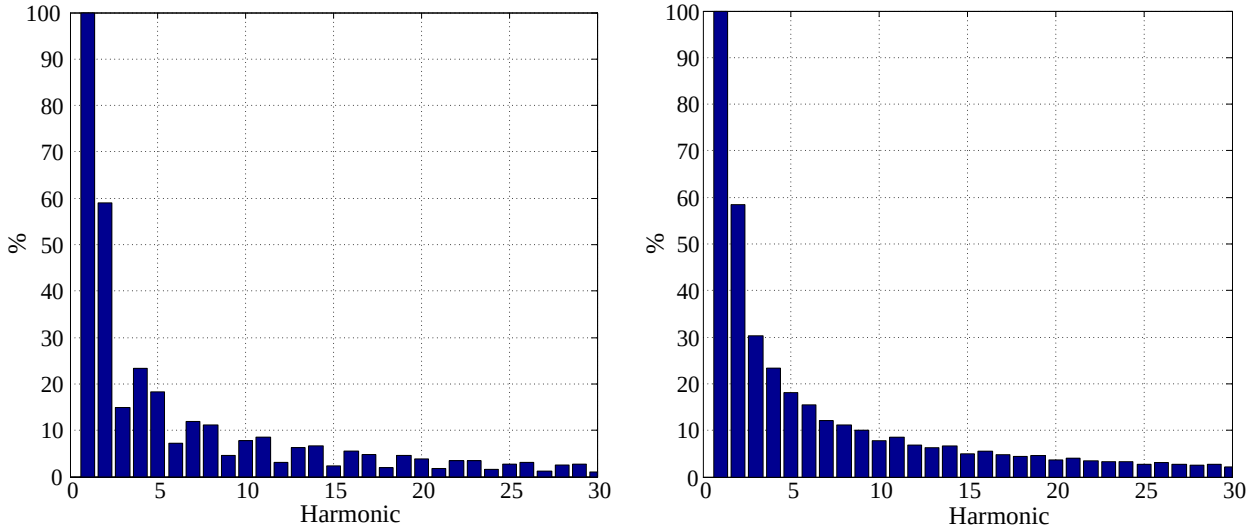

(a) Interior stator back iron (b) Interior stator pole

Figure 3.23 Flux density harmonics in the interior stator

Table 3.4 Iron loss of the interior SRM machine

Iron loss (W)	Rotor back-iron	Rotor pole	Stator back-iron	Stator pole
Total	**27.26**	**2.37**	**174.36**	**25.62**
Fundamental	0.82	0.07	27.39	3.24
2	0.00	0.00	28.07	3.27
3	0.93	0.08	3.73	1.71
4	0.00	0.00	13.43	1.59
5	5.66	0.47	11.69	1.36
6	0.00	0.00	2.66	1.33
7	5.57	0.50	8.69	1.03
8	0.00	0.00	9.21	1.08
9	1.20	0.11	2.11	1.06
10	0.00	0.00	6.52	0.76
11	3.10	0.28	9.02	1.07
12	0.00	0.00	1.52	0.77
13	2.23	0.20	6.45	0.77
14	0.00	0.00	7.72	0.93
15	0.58	0.05	1.24	0.60

3.4.3 Thermal Simulation

The thermal analysis of machines is a key factor that must be taken into account during machine design process. The thermal behavior of electric machines is subject to different levels of machine power as well as various machine geometries. When machines operate, different parts of the machine serve as different heat sources, i.e. heat from the rotor, stator, coils, etc. On the other hand, the interfaces between each part of the on load machine, as well as the interfaces between the machine and air transfer and dissipate the generated heat. Thus, the machine temperature will keep rising until balanced heat equilibrium is established. The maximum temperature of the machine should be controlled within certain limit. For a machine with Class H insulation, the maximum

temperature the machine insulation can withstand is 180℃, above which the insulation of the machine may be damaged or fail completely.

Thus, in order to study the thermal impacts on the designed DRSRM and optimize the rated input current and hence power developed, a thermal network model is built and detailed thermal analysis and simulation are carried out.

The thermal analysis is carried out based on the (copper and iron) loss analysis results. The iron loss of the stator laminations, the rotor laminations and the stator copper losses can be calculated respectively in the electromagnetic simulation. The lamination loss can be treated as a distributed heat source throughout all the finite elements, i.e. each finite element of the stator and rotor lamination generates heat due to the iron loss. Since the thermal constant is far greater than the electric field constant, the copper loss from the stator windings can be taken as the average loss value of the windings during an electric period. Figure 3.24 illustrates the heat sources in the DRSRM thermal simulation model.

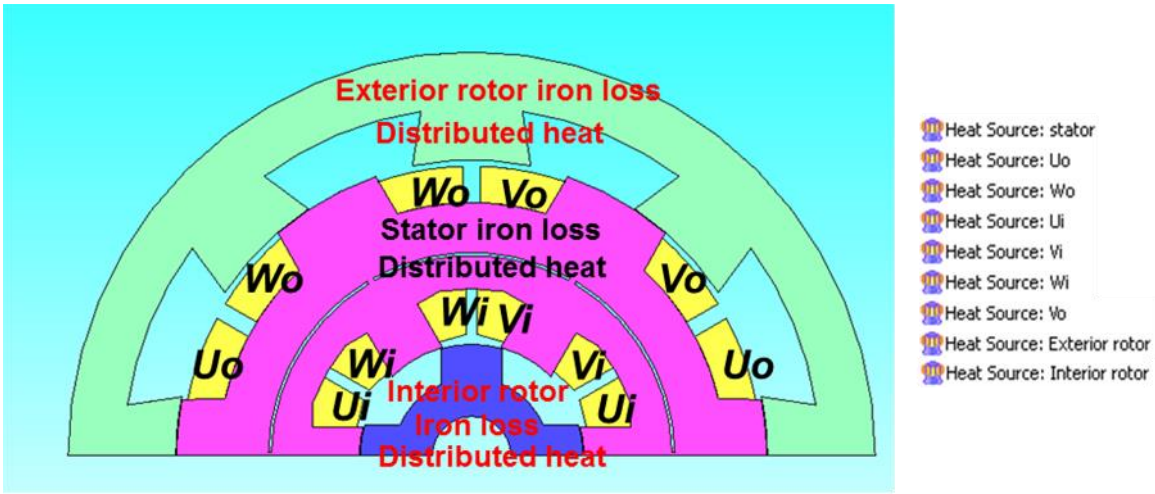

Figure 3.24 Heat sources in the DRSRM thermal analysis model

Thermal contact resistances are defined between any two of the contacting parts. In the case of the DRSRM, the interior stator teeth are contacted to the interior winding coils while the exterior stator teeth are contacting with the exterior winding coils. The thermal contact resistances of these contacting surfaces can be captured by the thermal conductivity coefficient. Typically, insulation paper such as Nomex paper is placed in between the stator winding and the stator. For a 0.3mm thick Nomex insulation paper, the thermal conductivity is 0.14 W/m/℃, which is measured at 150 ℃ and can be assumed constant in the simulation[82]. Figure 3.25 highlights the thermal contacting surfaces between the stator and the windings. In addition to the heat that transfers by direct surface contacts, heat can also be transferred between boundaries via air. Figure 3.26 shows the boundary surfaces between the stator teeth and the rotor teeth via the air gaps.

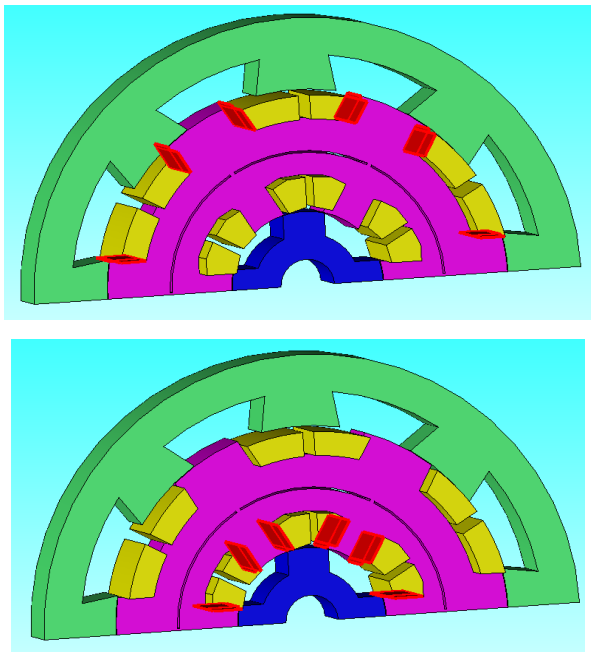

Figure 3.25 Thermal contacting surfaces between the stator and the windings

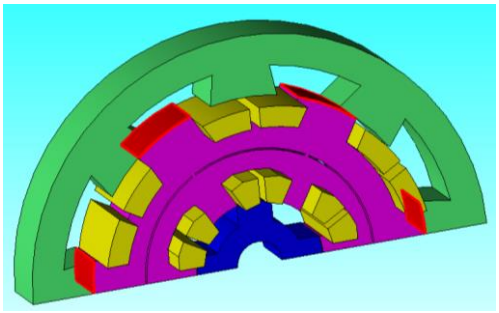

(a) Stator to exterior gap

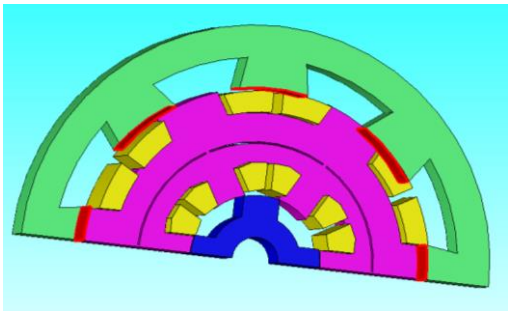

(b) Exterior rotor to exterior gap

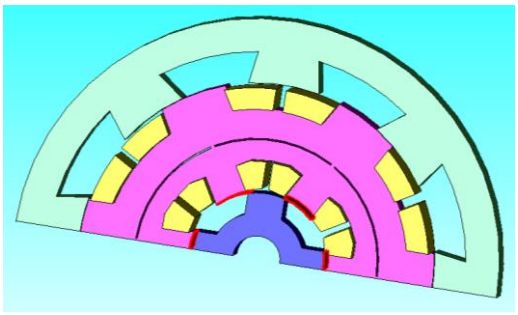

(c) Stator to interior gap

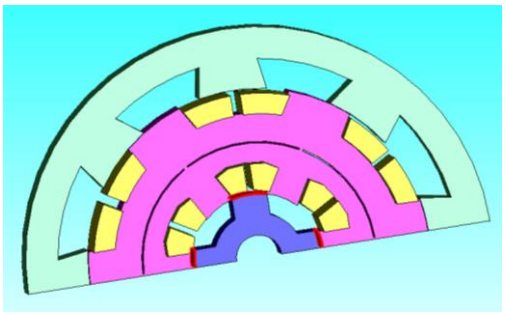

(d) Interior rotor to interior gap

Figure 3.26 Boundary surfaces between stator teeth and rotor teeth

The heat transfer coefficients between rotational parts and air gaps can be calculated by[83]:

$$h = \frac{6.6}{10^5}\frac{\omega\pi D^{0.67}}{\mathrm{g}^{0.33}}10^4 \tag{3.53}$$

where h is the heat transfer coefficient W/(m^2℃), ω is the rotational speed in revolutions per second, D is the rotor bore diameter in cm, $\omega\pi D$ is then the outer circumference rotor bore in cm and g is the gap length in cm. The heat transferred in between the rotor and stator air gap is then calculated from:

$$Q = hA\Delta T \tag{3.54}$$

where Q is the heat flow rate in W or J/s, A is the heat transfer surface area in m^2, ΔT is the difference in temperature between the two heat transfer surfaces. Thus, once the rotational speed and the dimension of the machine are known, the heat transferred between the stator and the rotor can be calculated.

In addition, the boundary conditions between the machine and the surrounding structures, and between the machine and air can also be set up by specifying the heat transfer coefficients. Figure 3.27 and Figure 3.28 show these boundary surfaces highlighted as in red for clarity. The black arrows on the assembly drawings illustrate the direction of heat dissipation for each part.

Thermal networks can be established in JMAG[84] based on the thermal boundaries illustrated in Figure 3.29, where the thermal boundaries shown in Figure 3.26 between the interior rotor and stator are connected via the interior gap, and the exterior rotor boundary and the stator boundary are connected via the exterior gap. The boundary surfaces between the machine and the housing shown in Figure 3.27 are connected to a module called "cover" in the thermal circuit which is modeled by a heat capacitance and a heat flow source. The capacity is determined by the volume of the housing as well as the thermal properties of the material:

$$C = VC_p\rho \tag{3.55}$$

where C is the heat capacity of the heat capacitor (J/℃), V is the volume of the housing (m^3), C_p is the specific heat for the housing material (J/kg/℃) and ρ is the material density of the housing (kg/m^3).

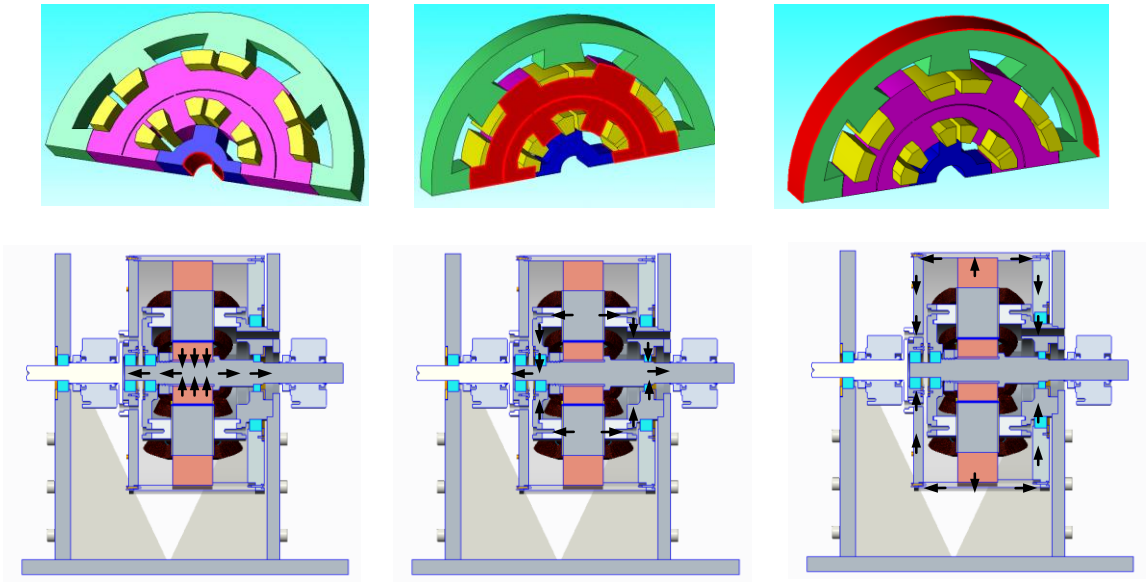

(a) Interior rotor to shaft (b) Stator to clamps (c) Exterior rotor to case

Figure 3.27 Boundary surfaces between machine and mounting structures

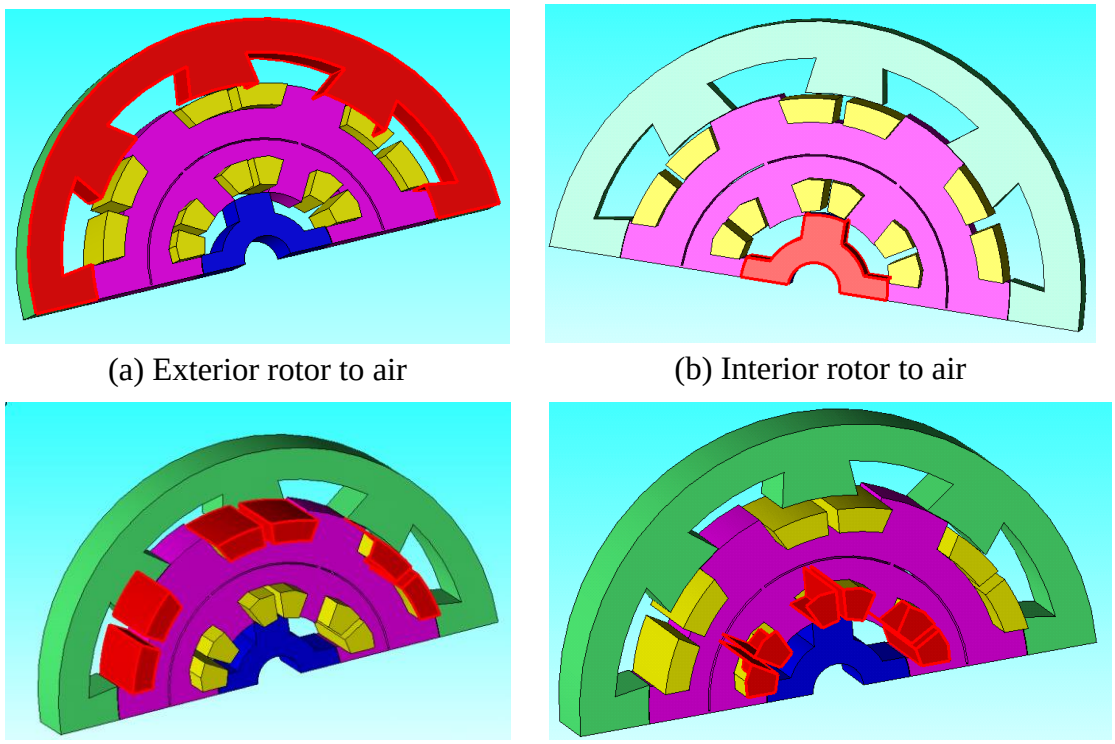

(a) Exterior rotor to air (b) Interior rotor to air

(c) Exterior coils to air (d) Interior coils to air

Figure 3.28 Boundary surfaces between machine and air

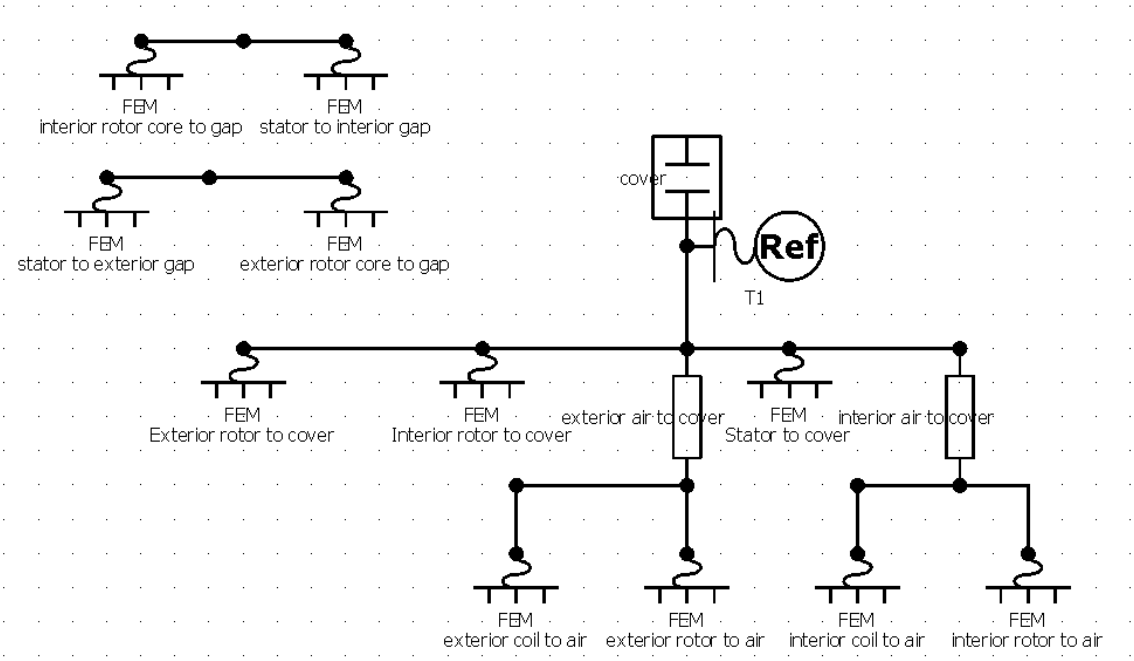

Figure 3.29 Thermal circuit in JMAG based on thermal boundaries

The heat flow source models the heat transferred from the housing to the air with a typical coefficient between 10 and 25 W/℃. And the reference temperature is set to be 20℃ as the ambient temperature. In addition, as shown in Figure 3.28 and Figure 3.29, the boundary surfaces between the machine and the air inside the machine housing transfer heat to the air, and then transfer heat to the machine housing via thermal resistances, which can be calculated as:

$$R_T = \frac{1}{Ah} \tag{3.56}$$

where R_T is the thermal resistance (℃ /W), A is the area inside the housing (m^2), h is the heat transfer coefficient between the air inside the housing and the housing W/(m^2 ℃), which can also be set between 10 and 25 W/℃. Table 3.5 lists all the applied parameters.

Once all of the heat transfer boundary surfaces are specified and the thermal circuit is constructed, the thermal simulation in JMAG will calculate the heat dissipation in each of the machine component as well as the heat transfer between the boundaries for a given load condition. Therefore, the temperature rise on each part of the machine can be calculated as presented in Figure 3.30, from where it can be seen that the maximum temperature of the machine is below 180℃ at thermal steady state for full load operation, which meets the Class H standard. Figure 3.31 presents the temperature distribution in the machine at steady state (300 minutes):

Table 3.5 Thermal analysis parameters

Parameter	Location	Unit	Value
Heat transfer coefficient	Interior rotor to air	W/(m^2℃)	10
	Interior rotor to interior gap	W/(m^2℃)	119.92
	Stator to interior gap	W/(m^2℃)	119.92
	Interior coils to air	W/(m^2℃)	10
	Exterior rotor to exterior gap	W/(m^2℃)	144.8
	Exterior coils to air	W/(m^2℃)	10
	Stator to exterior gap	W/(m^2℃)	144.8
	Interior rotor to cover	W/(m^2℃)	20
	Stator to cover	W/(m^2℃)	30
	Exterior rotor to cover	W/(m^2℃)	30
Contact resistance	Stator to windings	W/(m^2℃)	0.14
Ambient temperature	Room	℃	293
Heat capacity	Housing	J/℃	24846
Heat flow	Housing to air	W/℃	20

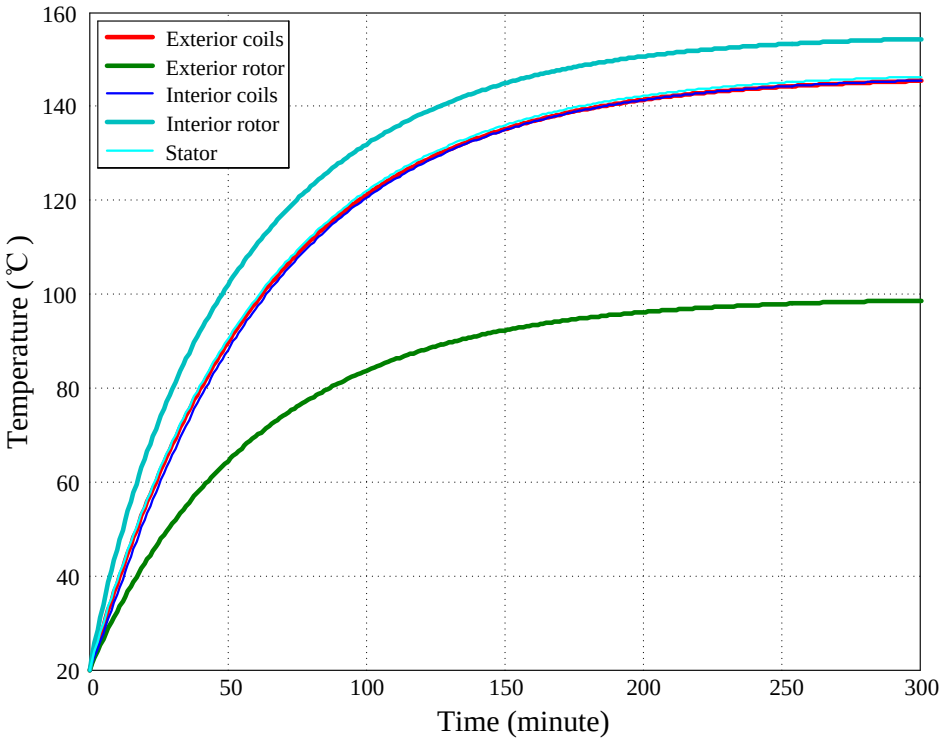

Figure 3.30 Temperature rise for the various machine components

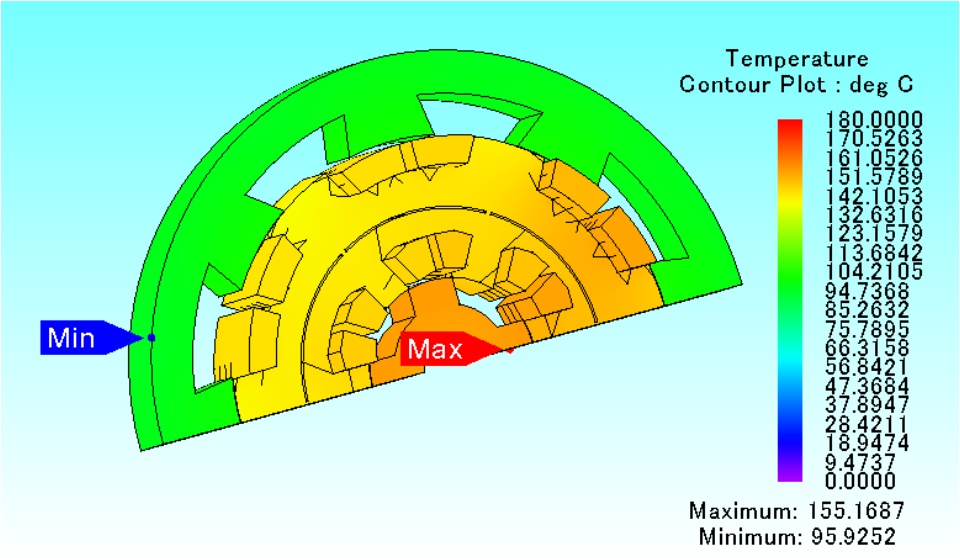

Figure 3.31 Temperature distribution of the machine at the steady state

3.4.4 SRM Drive simulation

FEA based electromagnetic simulation presented in the previous section was based on the current source type of control, where current sources are directly connected to phase windings. However, in reality current in the windings can never change instantaneously due to phase inductance and, thus, there is always a delay for current to reach the desired level after the phase switch is turned on or turned off. In addition, a constant current source assumes an infinite DC voltage supply to drive the necessary current through the machine circuit impedance. In practical drive systems, phase current is typically "chopped" at the desired level, such that the corresponding phase switches are controlled to turn-on and turn-off frequently to maintain the current level within a narrow range near the designed value. These distortions of current impact the performance of the machine such as the torque ripple and average output torque. Therefore, it is necessary to study the electric machines together with their respective drive circuits to analyze the real time machine performance. Hence in real time, a drive simulator was built in Matlab Simulink in order to verify the DRSRM performance, as shown in Figure 3.32. The Simulink model comprises of four parts: (i) The SRM machine module, (ii) the switching components module, (iii) the controller module and (iv) the mechanical load module. Figure 3.33 shows the SRM machine module.

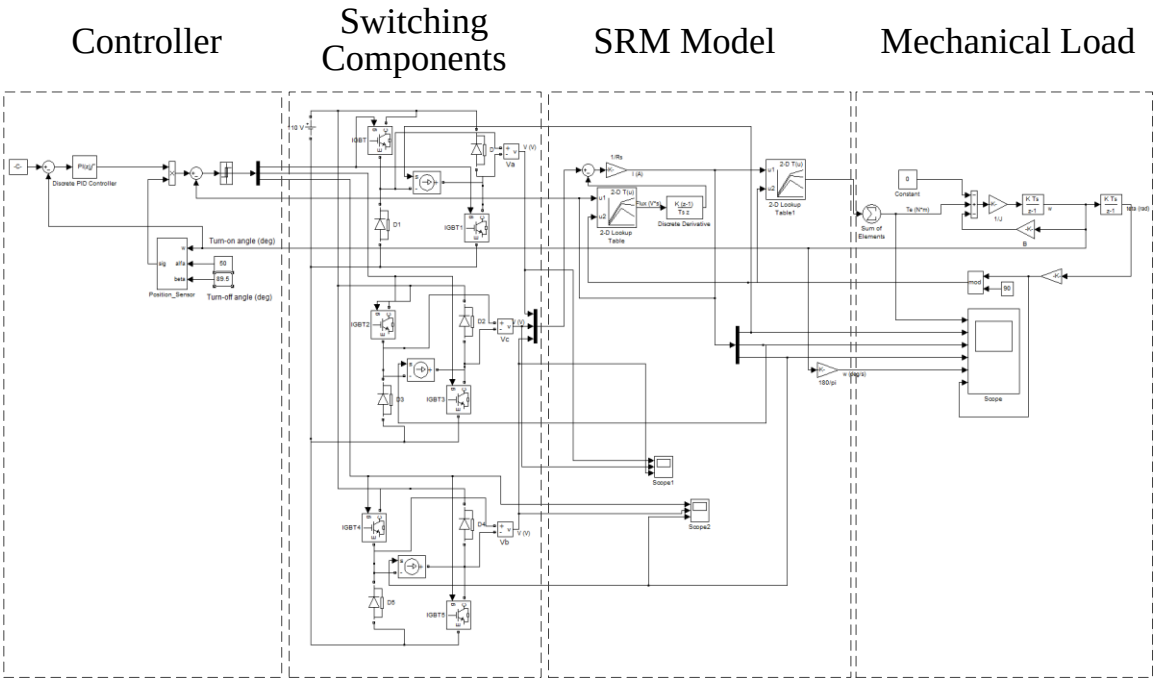

Figure 3.32 Real time drive circuit for DRSRM

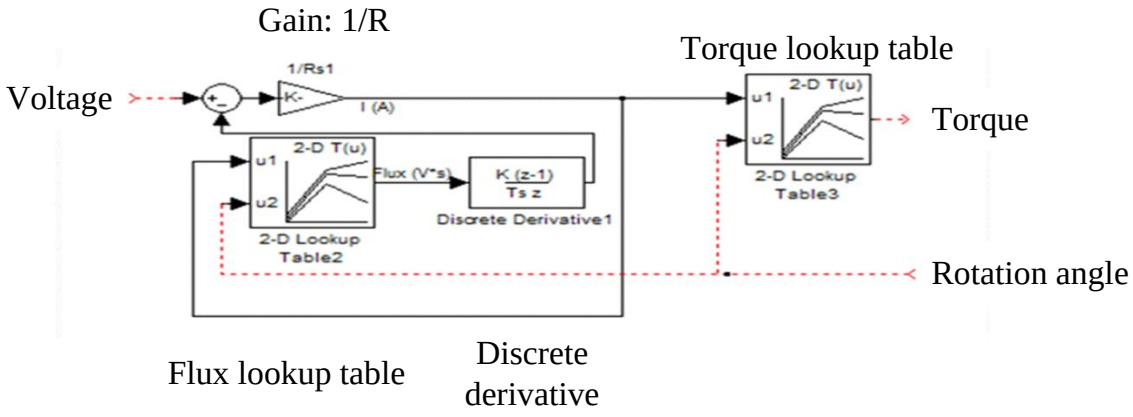

Figure 3.33 The SRM machine module

The basic machine parameters such as the phase flux-linkage and the torque under each current and rotational angle are gained by running the electromagnetic simulation in which just one stator pole is excited. The flux-linkages and torques at every step under different current excitations are then converted into two lookup tables in Simulink, as shown in Figure 3.33, to represent the machine properties. Figure 3.34 presents the flux-linkage lookup table and the torque lookup table for the interior SRM. The machine properties of the exterior SRM can be similarly gained and have the similar shapes as those of the interior SRM. The governing equation for each phase is:

$$V = Ri + \frac{d\lambda}{dt} \tag{3.57}$$

where V is the phase voltage, R is the phase resistance, i is the phase current and $\frac{d\lambda}{dt}$ is the rate of change of flux-linkage of each phase over time.

Based on the module in Figure 3.33, the phase terminal voltage and the rotor position serve as the input parameters into the module. The flux-linkage at the specific rotor position is then a function of the phase current, which can be calculated from equation (3.57) with the known phase voltage and resistance values. Therefore, once the rotor position and the phase current are determined, the output torque can be calculated from the torque lookup table.

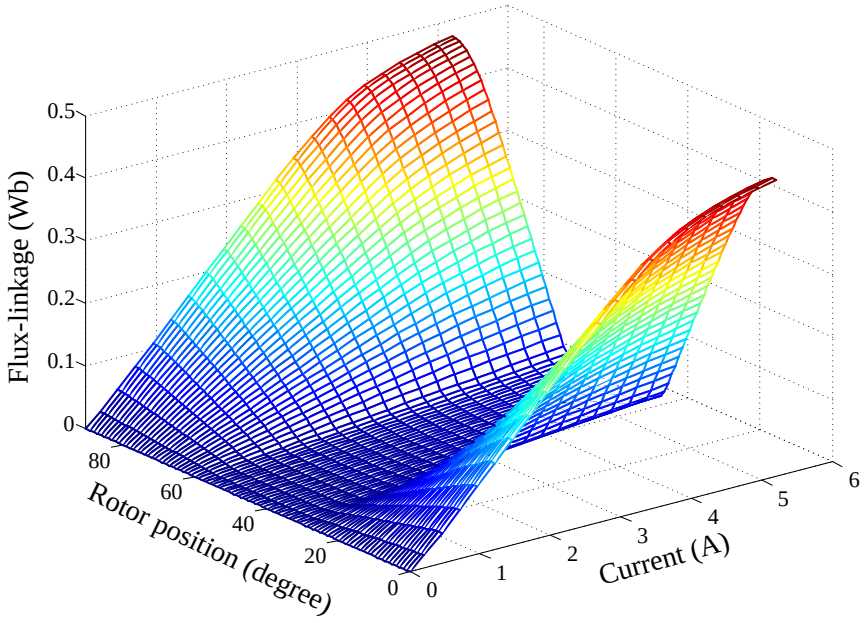

(a) Flux linkage lookup table

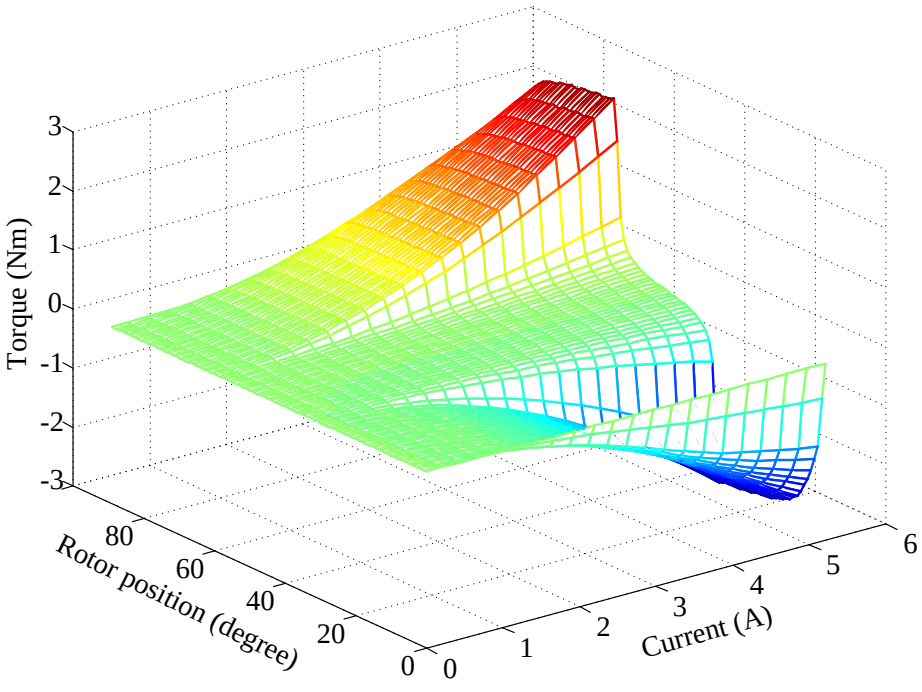

(b) Torque lookup table

Figure 3.34 Lookup tables for flux-linkage and torque

Figure 3.35 shows the simulation module of the switching components in one phase, where the standard asymmetric bridge is used to drive and control the SRM. Two IGBTs and two diodes forming an "H" bridge are implemented for one phase to control the phase current. The input gate drive signal g is controlled by the output of the controller module, which determines the switch on and off timing sequence of the IGBTs. When both IGBTs are on, the phase winding terminals are directly connected with the DC link voltage, which applies a positive voltage onto the phase winding and drives the phase current up (provided the back-EMF is smaller than the DC link voltage as a typical case). When the IGBTs are switched off, the phase current in the winding continues to flow in the same direction, forcing the diodes to conduct and thus a negative DC link voltage is applied on the phase winding terminals to drive the current down.

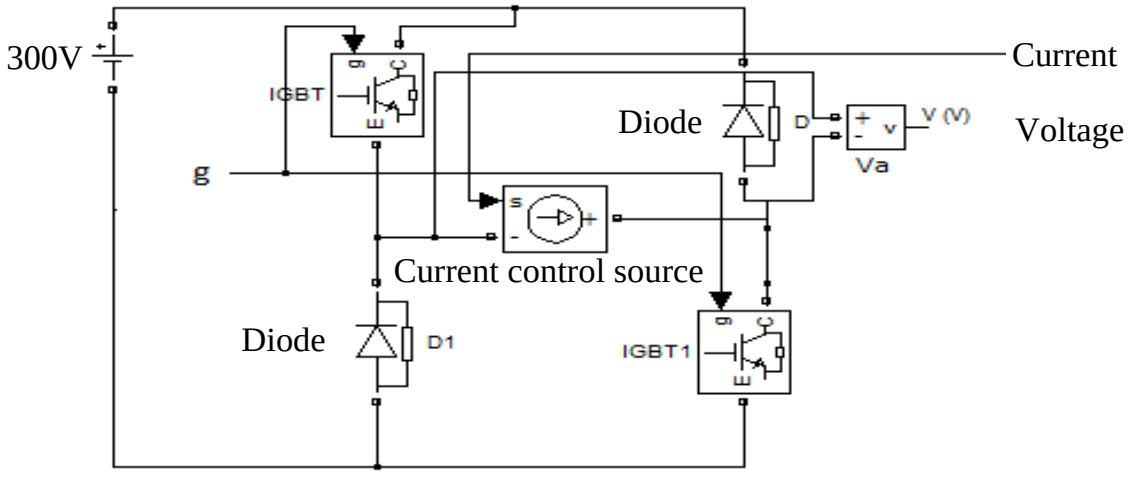

Figure 3.35 Simulation module of the switching components in one phase

In the switching components module, a current controlled source is applied in between the IGBTs to model the actual current value in the phase winding. The input phase current value is gained from the SRM machine module calculated by equation (3.52). Then the phase terminal voltage is measured across the current controlled source to output the voltage value to the SRM machine module.

Figure 3.35 only shows the switching components module for one phase. In total, six of the same switching components modules are used to model all six phases as in the case of the DRSRM, i.e. three for the interior SRM and three for the exterior SRM. Each phase is driven by its own gate drive signal so that each phase is individually controlled. The controller module is illustrated in Figure 3.36.

The controller is composed of three parts: (i) the current control loop, (ii) the speed control loop and (iii) the switch angle controller. The core part of the current control loop is the hysteresis relay which compares the actually phase current with the reference current. The output value of the relay is binary and remains unchanged until the difference of current value exceeds the thresholds, i.e.:

$$\begin{cases} g = 1, \text{ when } \ i^* - i \ > 0.1 \\ g = 0, \text{ when } \ i^* - i < -0.1 \end{cases} \tag{3.58}$$

where g is the gate drive signal that control the switches in the switching components module, i is the phase current, i* is the reference phase current. In this sense, the current is chopped within a narrow range around the reference current i*.

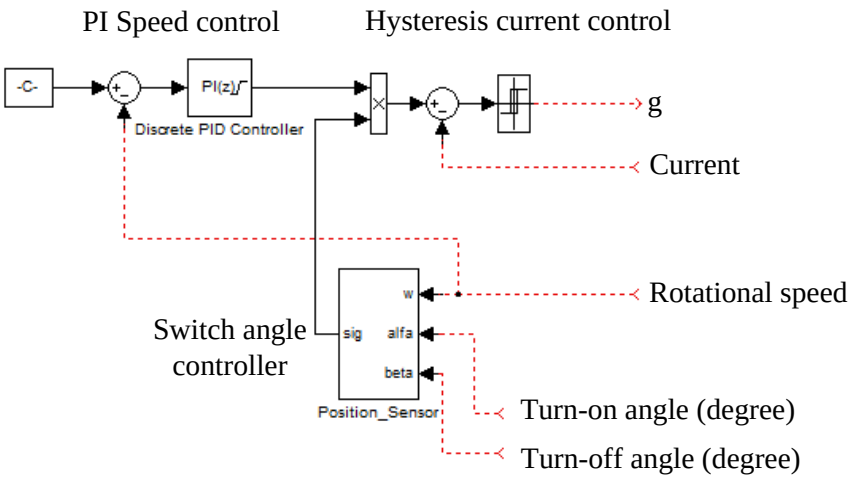

Figure 3.36 The controller module

The speed loop is a PI controller that compares the rotor speed ω with the reference speed ω^*. The difference between the two speeds is then multiplied by proportional and integral gain values to generate the reference current i^*. The PI controller is also integrated with a saturation function so that the maximum current level is kept within the rated current.

The switch angle controller is a logic block that compares the rotor position with the selected switch on and off angles to determine the switch firing sequences. Figure 3.37 presents the logic of the block for the interior SRM. The rotational speed of the rotor is converted from radians to degrees and integrated to get the rotor position. It is then divided by 90 degrees (as in a four pole machine) and the modulus is compared to the turn-on angle and the turn-off angle which controls the gate drive signal.

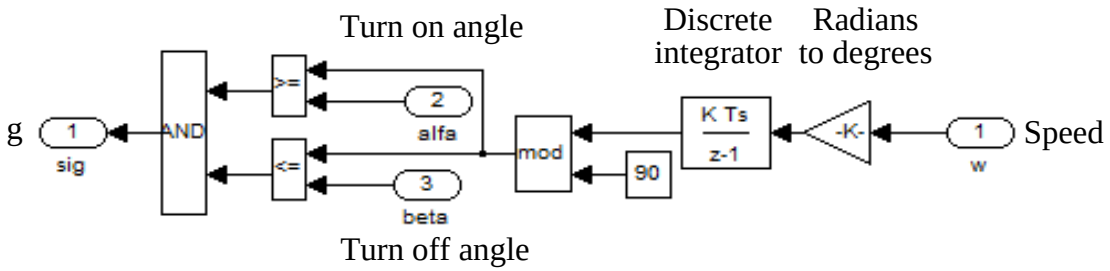

Figure 3.37 The switch angle controller logics

The last part of the SRM drive model is the mechanical load module, which is shown in Figure 3.38. The output electromagnetic torque from the SRM machine module serves as the input of the mechanical load module. It overcomes the friction torque term as well as the damping torque term to accelerate the rotor. The acceleration is then integrated twice to get the position of the rotor. The governing mechanical system equation is:

$$T_e - T_f - B\omega = J\ddot{\theta} \tag{3.59}$$

where T_e is the electromagnetic torque, T_f is the friction torque term, B is the damping ratio, ω is the rotational speed of the rotor, and θ is the rotor angular position.

The rotor angular position is then feedback to the input of the SRM machine module and the controller module to complete the drive model. Figure 3.39 shows a simulation result where the input speed command changes from 1000rpm to 3000rpm and then back down to 2000rpm. The first row presents the torque waveform, the second to fourth rows present the three phase currents and the last row presents the rotor rotational speed.

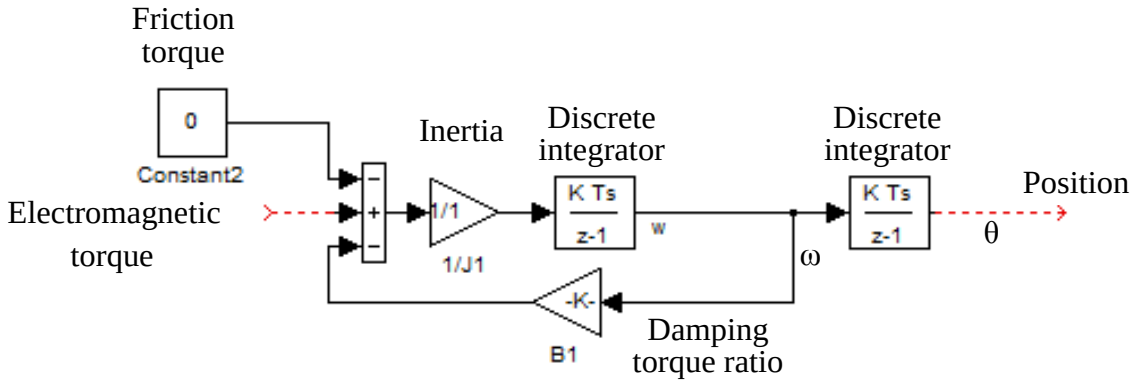

Figure 3.38 The mechanical load module

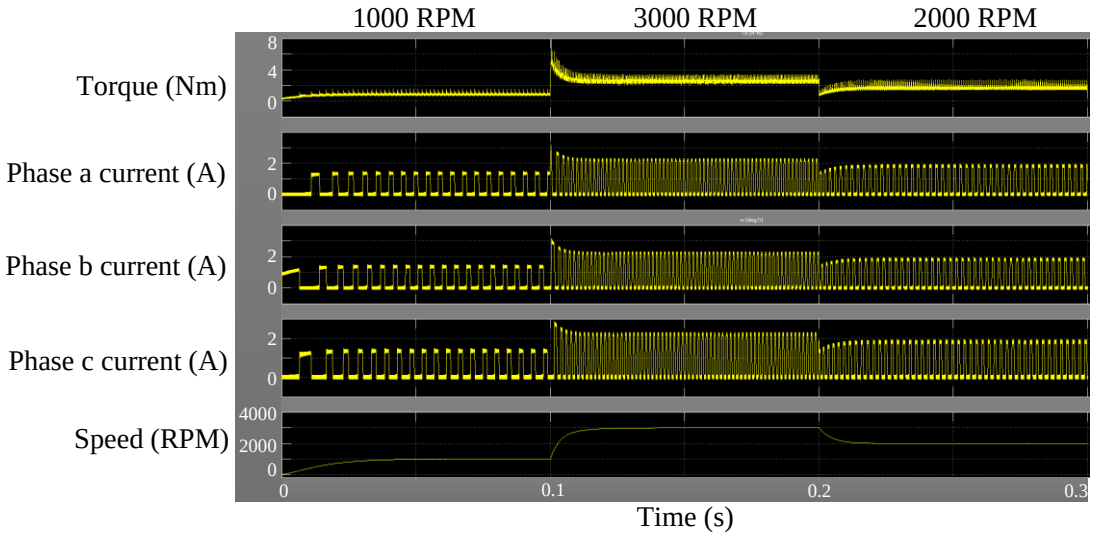

Figure 3.39 SRM drive simulation results

As shown in Figure 3.39, the rotor rotational speed responds well to the controller speed demand. The steady output torque increases as speed increases to overcome the higher speed-related damping torque. Figure 3.40 presents a magnified view of the waveforms in steady-state. It can be observed that the current is chopped at a constant level due to the hysteresis controller. It rises from 0 to the demand level faster than its fall time due to the smaller phase inductance at the unaligned position when the phase is

(typically) turned-on and the larger phase inductance at the aligned position when the phase is (typically) turned-off. Two other Simulink circuits were built to verify the drive simulation results, as shown in Figures 3.41 and 3.42. Figure 3.41 uses an existing JMAG SRM motor drive Simulink model[85] where a motor model is created by the electromagnetic simulation and imported into JMAG real-time simulation, "JMAG-RT". The mechanical load module is also embedded into the motor model. The switch module and the controller module are quite similar to the drive modules as explained above.

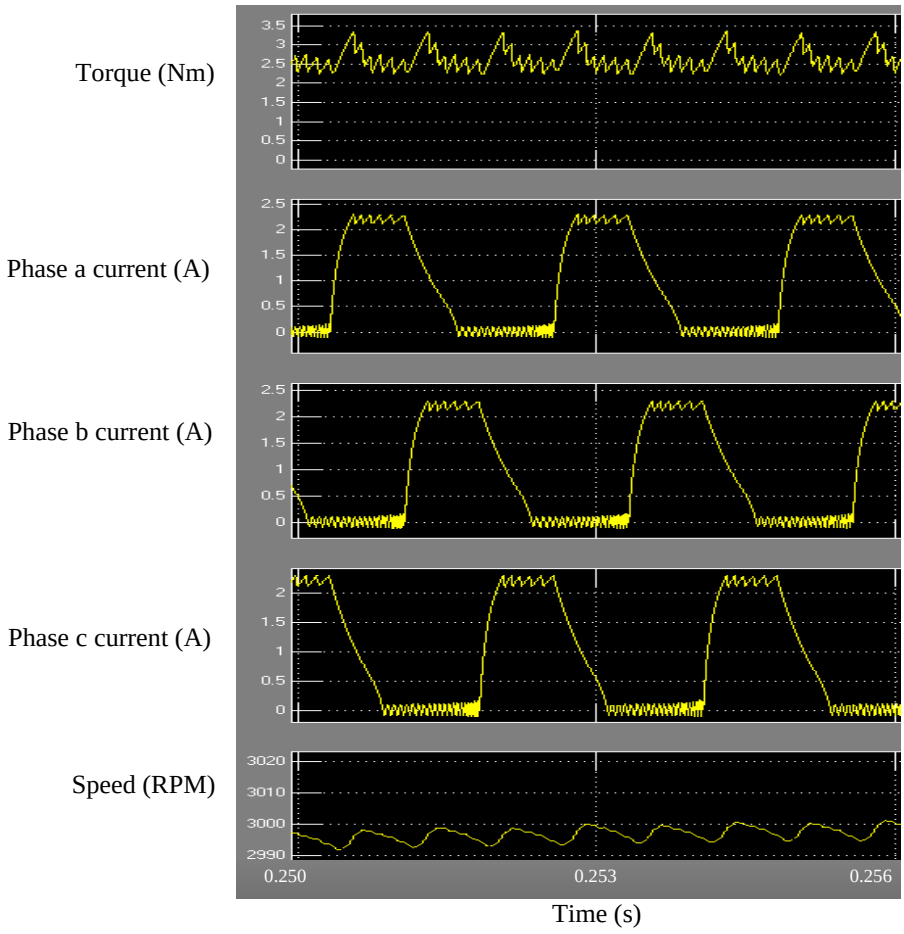

Figure 3.40 SRM drive simulation waveforms

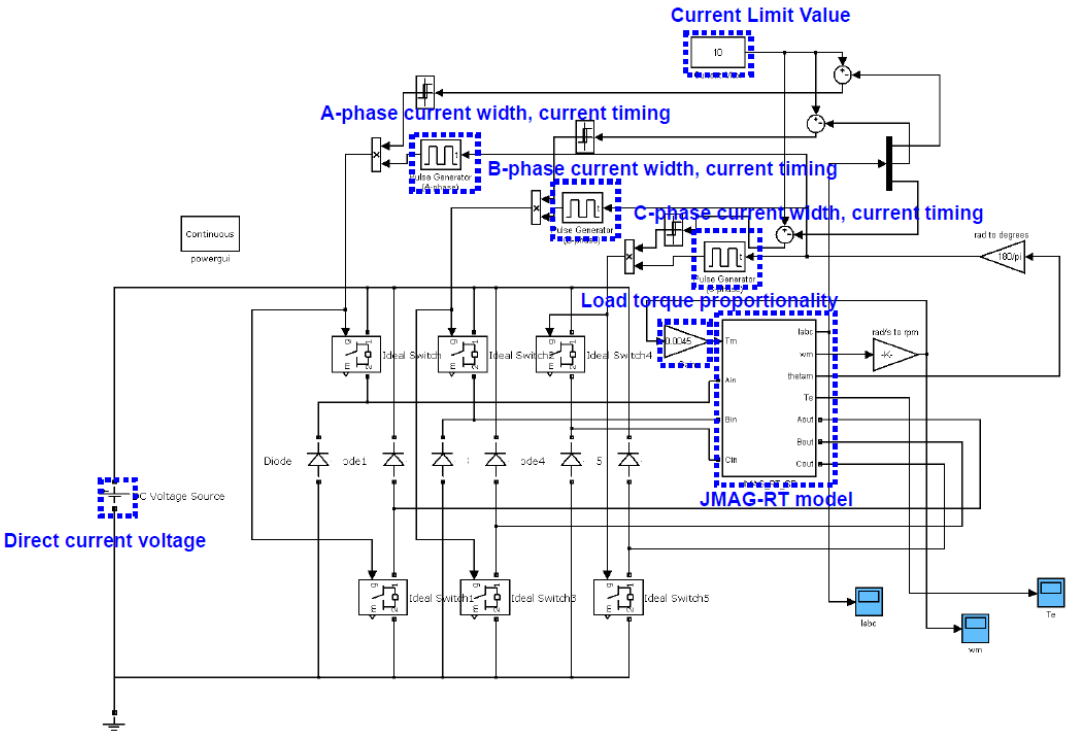

Figure 3.41 JMAG RT model

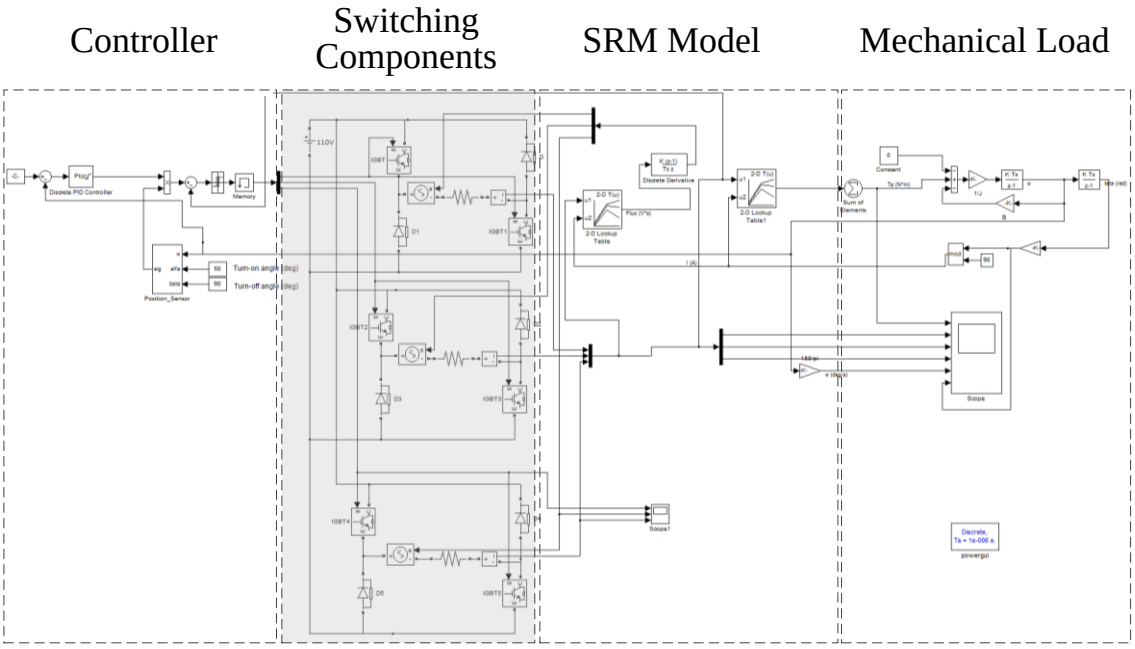

Figure 3.42 Voltage feedback model

Figure 3.42 replaces the current controlled source with a voltage controlled source and a resistor to model the voltage term V in equation (3.57), The overall voltage drop across the phase terminal is gained by interpolating the flux-linkage lookup tables and taking the derivative of the flux-linkage:

$$V - Ri = \frac{d\lambda}{dt} \tag{3.60}$$

Thus, the derivative of the flux-linkage over time is feedback to the voltage controlled source between the IGBTs. The resistor models the phase resistance of the winding. Figure 3.43 compares the Matlab/Simulink current feedback model results to the JMAG-RT model results. Figure 3.44 presents a magnified view to aid the comparison.

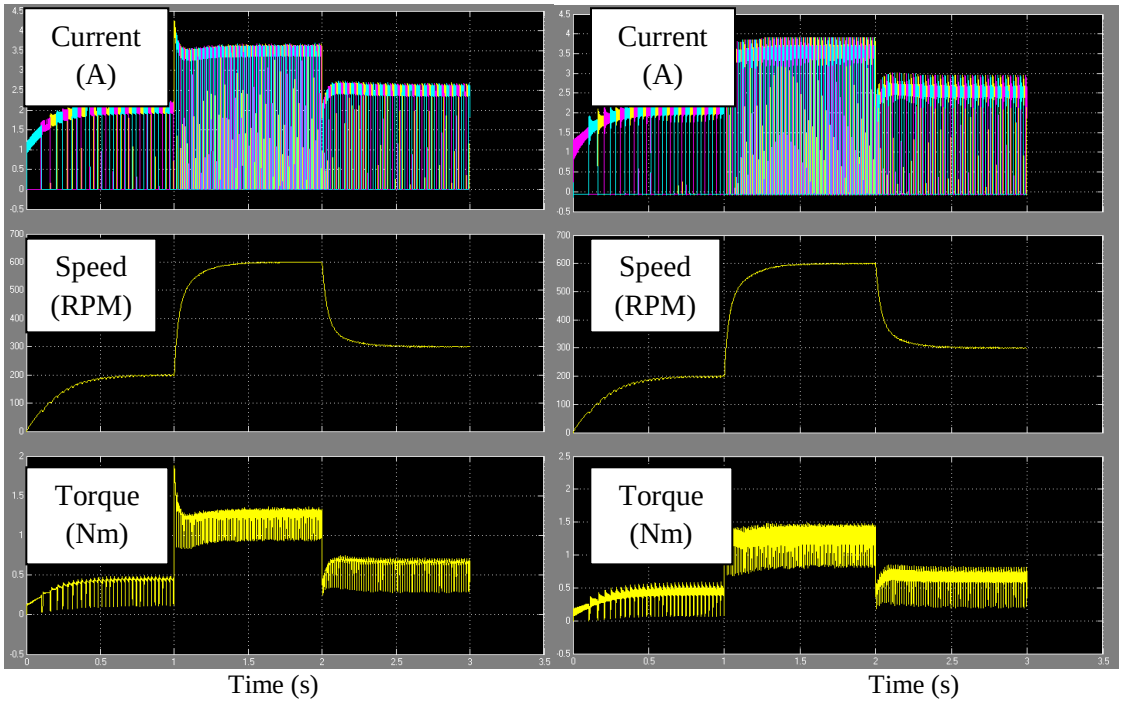

(a) Matlab/Simulink current feedback model (b) JMAG-RT model

Figure3.43 Comparison of the Matlab/Simulink current feedback model and the JAMG-RT model

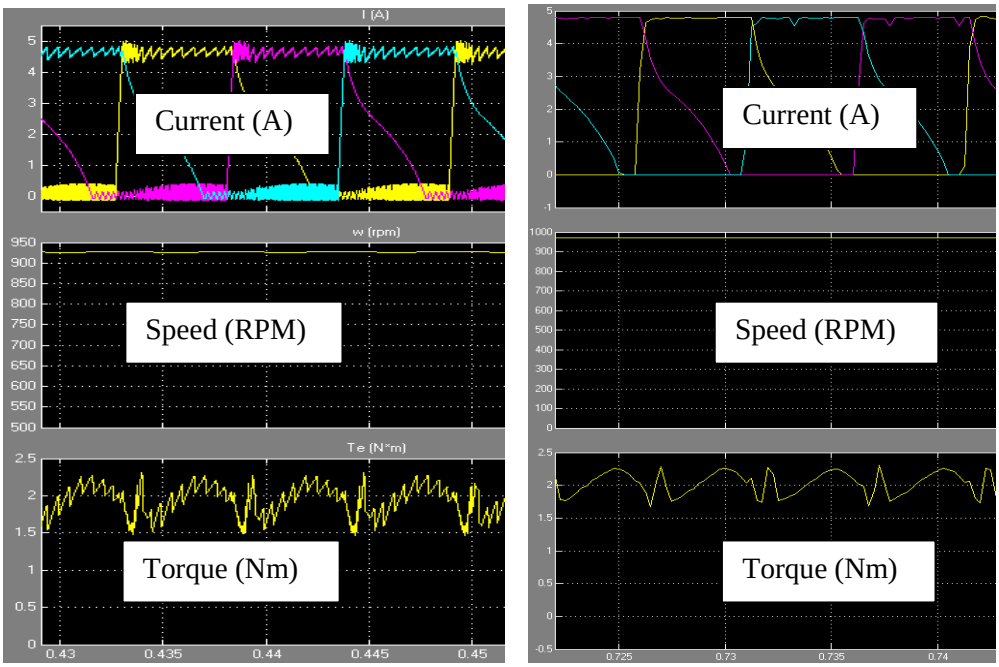

(a) Matlab/Simulink current feedback model (b) JMAG RT model

Figure3.44 Comparison of the Matlab/Simulink current feedback model and the JAMG RT model

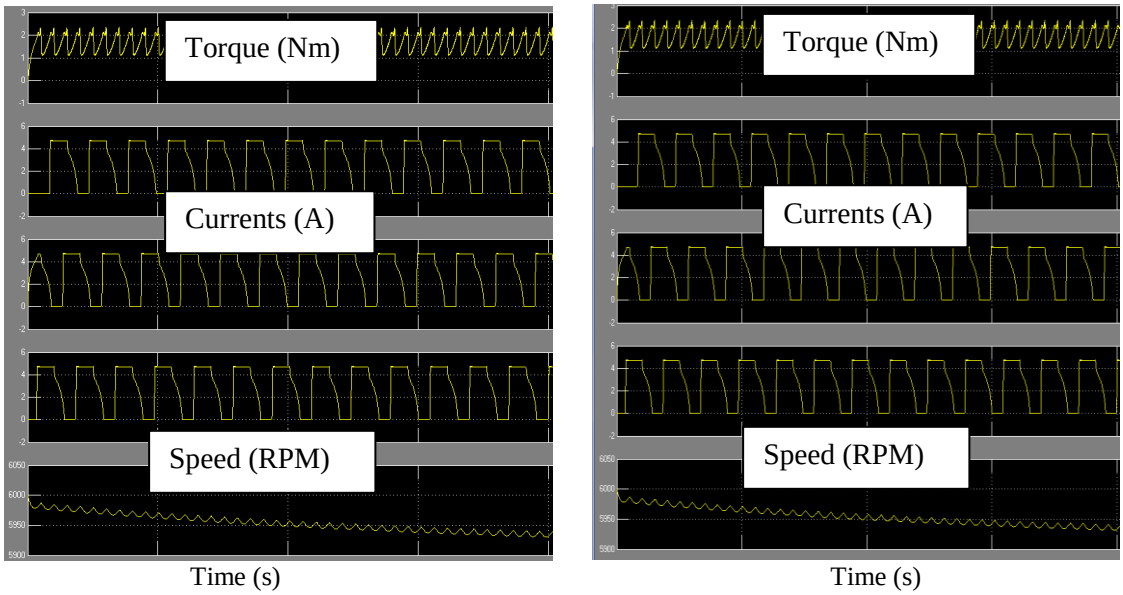

(b)Matlab/Simulink current feedback model (b) Voltage feedback model

Figure 3.45 Comparison of the Matlab/Simulink current feedback and the voltage feedback models

Figure 3.45 compares the voltage feedback model with the Matlab/Simulink current feedback model with the same hysteresis relay bandwidth.

It can be easily observed from Figures 3.43 to 3.45 that all three models generate matched results in terms of speed, currents and output torque. Thus, it is proven that all three simulation circuits have the same output results, and the results from the current feedback model are verified. It should be noted here that in Figure 3.44, the JMAG-RT model yield more smoother curves than the current feedback model. This is because the JMAG-RT model is using a higher current modulation bandwidth, which constrains the current in a narrower range around the designed level.

It is also noted that there are two sections of curvatures in the current waveforms during the turn-off period in Figures 3.44 and 3.45. These are a result of the changing coil inductances from the inductance rising period to the inductance falling period. Observing from equation (3.10):

$$v = Ri + L\frac{di}{dt} + i\omega\frac{dL}{d\theta} \tag{3.10}$$

During the inductance rising period, the derivative $\frac{dL}{d\theta}$ is positive and can be assumed to be constant in the linear region, and thus equation (3.10) turns to be a first order linear system in terms of the phase current i. The solution can be approximated as the solution to the first order linear system:

$$i = C_0(t) + C_1(t)e^{-\frac{t}{\tau(t)}} \tag{3.61}$$

where C_0 and C_1 are time varying constants and $\tau(t)$ is a time constant that is positive and time-varying. The second term exponentially decays with time since the sign of the exponential term is negative.

During the inductance falling period, the derivative $\frac{dL}{d\theta}$ is negative, and thus the waveform of current i can be approximated as a solution of a first order linear system with a negative time constant:

$$i = C_{0'}(t) + C_{1'}(t)e^{\frac{t}{\tau(t)}} \tag{3.62}$$

where $C_{0'}$ and $C_{1'}$ are time varying constants and $\tau(t)$ is a time constant that is positive and time-varying. It can be observed that the magnitude of the second term increases exponentially with time instead of decaying as in the first case. Therefore, the change of curvatures in the current waveforms actually means the machine operates from the motoring mode to the generating mode, when the inductance goes from the rising period to the falling period.

3.5 OPTIMIZATIONS OF THE DOUBLE-ROTOR SWITCHED RELUCTANCE MACHINE

The previous sections set up the initial parameters for the DRSRM design based on analytical calculations and experience related design coefficients. Detailed simulation was also discussed and results were presented. Using the parameters and selected settings, the performance of the initial designed DRSRM can be checked and validated by using the FEA simulations.

However, the initial design serves as a starting point to approach the desired machine objectives. In order to get a higher performance and higher efficiency electric machine, many iterations of simulations and optimizations have to be carried out to further refine the machine so that the design objectives of minimum weight and volume, minimum cost and maximum performance can be achieved.

The tasks of optimizations involve fine tuning of the machine geometries including the stator and rotor pole angle, pole height, back-iron thickness, outer diameter, inner diameter, etc. Thousands of simulations have been done here to find out the best geometry that yields the highest torque with smallest torque ripple. The selection of the turn-on and turn-off angles have been parametrically optimized and verified in SRM real-time drive simulation. Loading and excitation have also been investigated to select the best operating point, i.e., the rated point. Further, the optimized stack length is studied and chosen to obtain the highest efficiency. The following sections will describe the optimization process in detail.

3.5.1 Geometry Optimizations

Various combinations of the machine components geometries have been studied as in the parameterized analysis.

Pole-arc to pole-pitch ratios

Since the pole pitch values have already been fixed when the numbers of poles were selected, it is the stator pole angles and the rotor pole angles that need to be optimized for both the interior SRM and exterior SRM. Table 3.6 summarizes the optimization result for the interior SRM by comparing the output performance under different pole angles conducting different current degrees. Table 3.7 summarizes the optimization result for the exterior SRM under similar procedures.

Table 3.6 Interior SRM pole angles and current conducting angles optimization

Stator pole angle (degree)	Rotor pole angle (degree)	Turn on angle (degree)	Turn off angle (degree)	Conducting angle (degree)	Average torque (Nm)	Torque ripple (%)
30	32	50	89	39	3.00	23
30	34	50	89	39	3.02	25
30	36	50	88	38	3.02	25
32	34	56	88	32	2.91	21
32	36	55	85	30	2.91	18
32	35	56	86	30	2.92	22
32	33	57	87	30	2.90	26
33	**35**	**55**	**85**	**30**	**2.92**	**17**
33	36	55	85	30	2.93	18
34	36	55	85	30	2.90	18

Table 3.7 Exterior SRM pole angles and current conducting angles optimization

Stator pole angle (degree)	Rotor pole angle (degree)	Turn on angle (degree)	Turn off angle (degree)	Conducting angle (degree)	Average torque (Nm)	Torque ripple (%)
22	**23**	**23**	**38**	**15**	**5.60**	**13**
23	22	23	38	15	5.59	13
22	21	24	39	15	5.64	17
23	20	24	40	15	5.63	15
19	20	26	41	15	5.56	19
20	21	25	40	15	5.68	18
18	21	26	41	15	5.63	22
18	19	27	42	15	5.61	22
18	20	26	41	15	5.66	23
18	22	25	40	15	5.68	21
16	19	28	43	15	5.56	30
16	21	26	42	15	5.57	29

In Table 3.6 and Table 3.7, the turn-on and turn-off angles showed in each row represent the optimal switch angles that give the smallest torque ripple while maintaining a relatively large average torque output under one specific pole angle combination, i.e., a specific geometry. Varying geometries with different pole-arc versus pole-pitch angles were also studied and compared. The indicated lines in the above tables outline the optimal pole angle combination that yields the minimum torque ripple, which is chosen to be the pole angle combination for the designed DRSRM.

Integrated Stator with Flux Barrier

Figure 3.46 illustrates typical field solutions showing lines of equal magnetic vector potential or "flux" lines for the DRSRM with both of the stator windings excited. The difference between the two machines is the flux barrier, or air gap, dividing the two stators. The machine shown in Figure 3.46 (a) has an air gap between both stators that functions to separate the flux from the interior and exterior SRMs, as illustrated by comparison of the flux contours of magnetic flux density distribution. It can be observed that for the machine without an intermediate air gap, flux merges between interior and exterior machine magnetic circuits, adding unnecessary coupling between the two systems, Figure 3.46 (b). Note, for ease of comparison, machines in Figure 3.46 (a) and (b) have the same geometry, both with an intermediate region between the two stators, which can be set as air for the case of Figure 3.46 (a) and lamination steel for the case of Figure 3.46 (b). Figure 3.47 compares example torque outputs for both machines with and without an intermediate stator air gap, while Table 3.8 summarizes the results. It can be observed that for this case there exists a maximum 5% torque variation for both machines between the geometries, highlighting the magnetic field interference problem between the exterior and interior SRMs. The level of magnetic coupling between the two machines varies with load, speeds and rotor directions and is thus difficult to present and quantify for all operating scenarios. Needless to say, the results presented at the full torque base speed operating points give rise to a level of coupling that is unwanted from an output control perspective. Thus, the intermediate air gap solution therefore has clear benefits and will be continued through to final design.

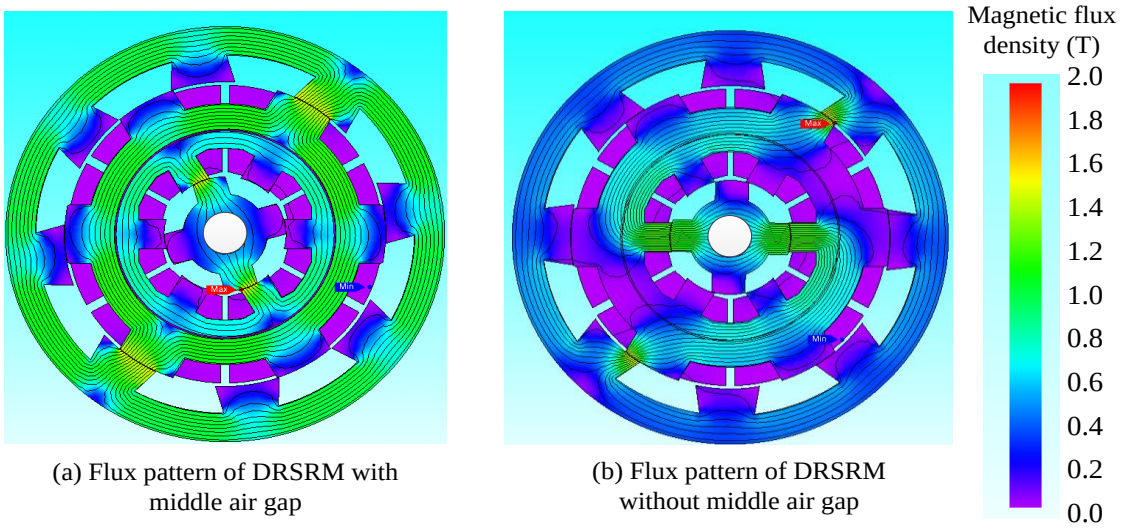

(a) Flux pattern of DRSRM with middle air gap

(b) Flux pattern of DRSRM without middle air gap

Figure 3.46 DRSRM flux pattern with and without air gap

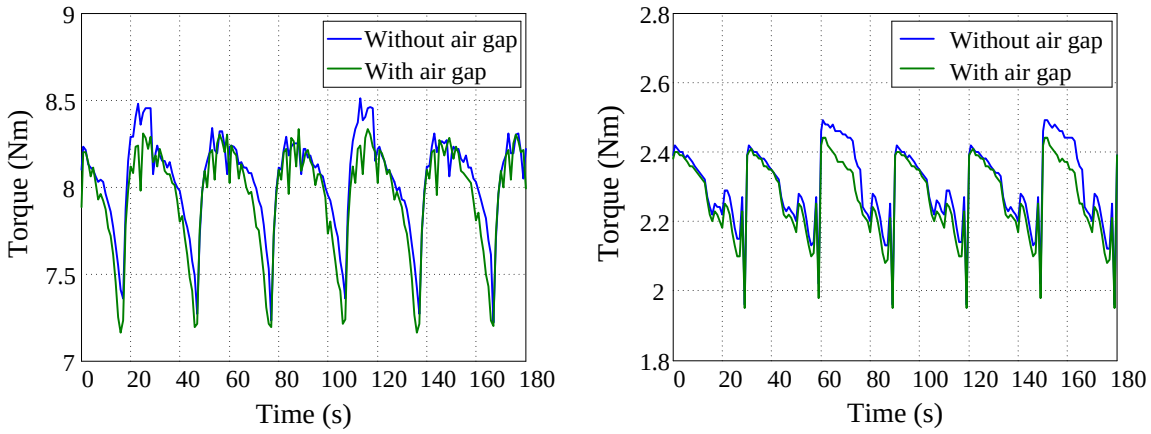

(a) Exterior SRM

(b) Interior SRM

Figure 3.47 Torque waveform comparisons with and without air gap

As observed from Figure 3.47, the magnetic field interference in the DRSRM geometry without intermediate air gap causes torque variations and localized flux density perturbations that result in difficulties for machine control. An integrated stator structure is proposed that separates the flux paths in the stator while maintaining the mechanical rigidity of the stator lamination, as shown in Figure 3.48. The stator intermediate air flux

barriers that separate the flux paths are 1mm wide, while 2 mm wide radial bridges are used to connect the inner and outer stator lamination such that the stator lamination remains a rigid single piece component. These narrow bridges are designed to saturate during machine operation so that the majority of the flux paths of the two machines are well separated. Further, clearance holes are placed under each stator pole so that the stator laminations can be bolted together for assembly. Figure 3.49 presents comparison field solutions for the DRSRM for a machine with a middle air gap (a) and one with a middle air gap and clearance holes (b). The results highlight the negligible impact of the clearance holes on field solution, a conclusion that is reflected in the machine performance comparison.

Table 3.8 Torque differences with and without air gap

	Exterior SRM		**Interior SRM**	
	Without air gap	With air gap	Without air gap	With air gap
Average torque (Nm)	8.05	7.95	2.30	2.27
Maximum torque (Nm)	8.51	8.33	2.49	2.44
Minimum torque (Nm)	7.22	7.16	1.96	1.95
Maximum torque difference (Nm)	0.39		0.11	
Maximum torque variation (%)	5%		5%	

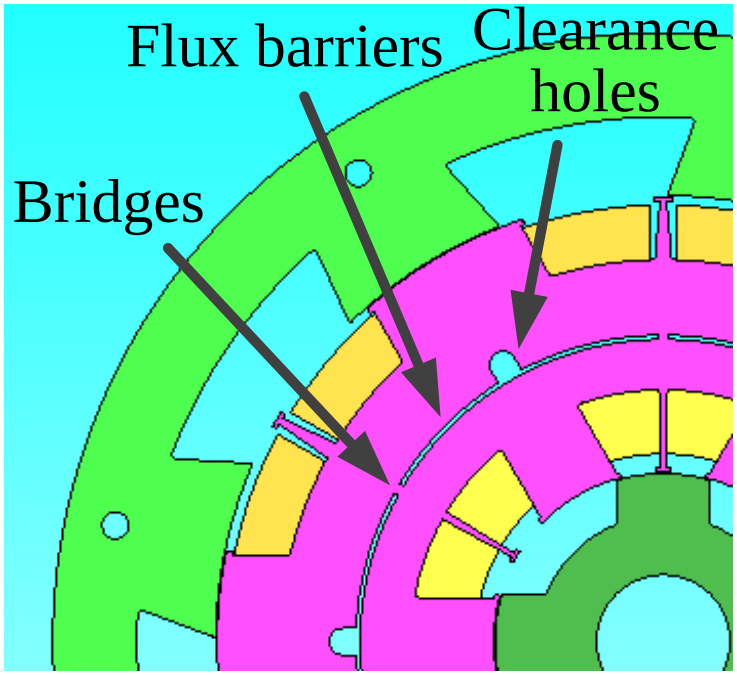

Figure 3.48 Integrated stator with flux separating air gap

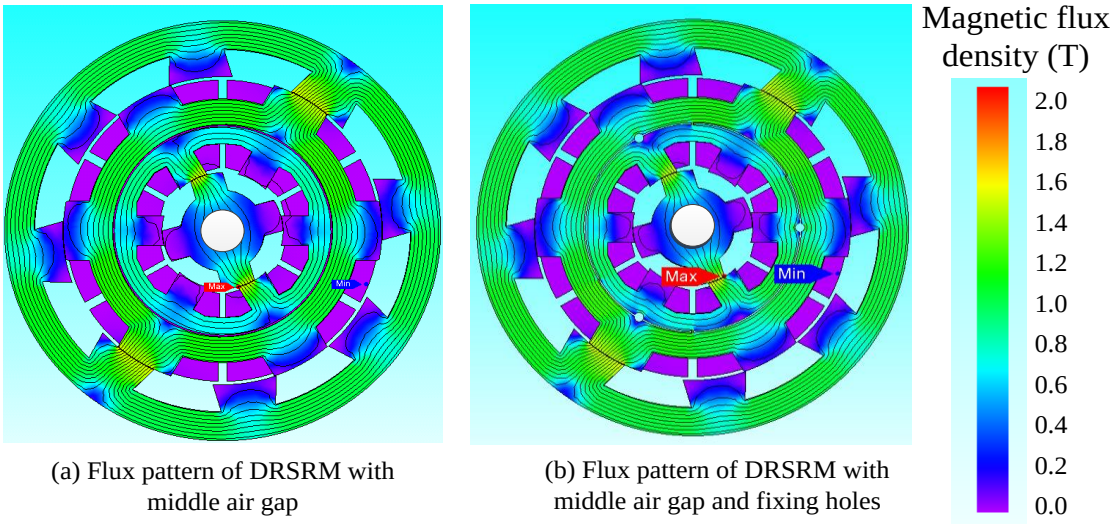

(a) Flux pattern of DRSRM with middle air gap

(b) Flux pattern of DRSRM with middle air gap and fixing holes

Figure 3.49 Flux paths of DRSRM designs

Geometry optimizations

Other geometry optimizations have also been studied to meet the performance, efficiency, and volume criteria. Various bore diameters for both the machines have been investigated, different stator pole height and stator pole height have been parameterized and studied, and multiple pole shapes have been analyzed to give the optimized output performance.

Figure 3.50 presents some of the optimization results, showing a smaller inner machine (a) and a machine with tapered rotor pole (b). Both design serve to reduce the overall machine weight and volume.

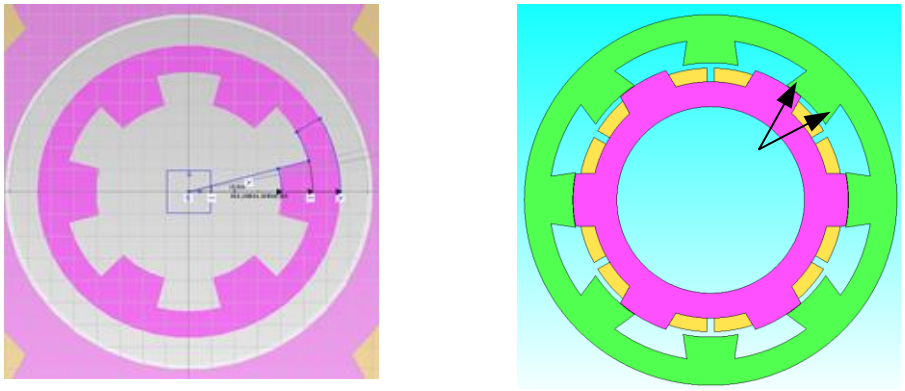

(a) Smaller interior stator bore diameter (b) Tapered exterior rotor poles

Figure 3.50 Machine optimizations to reduce the rotor volume

Machine back-iron thicknesses are subject to the lamination steel saturation limit as well as the corresponding iron loss. Typically, the higher degrees of saturation on the machine back-irons result in greater iron losses as well as larger torque ripples, which can be observed as illustrated in Figures 3.60 and 3.64, shown in Section 3.5.2. Figure 3.51 compares the saturation level for the exterior SRM with different back-iron thickness.

The smaller back-iron thickness on both the stator and the rotor, for design Figure 3.51 (b), results in higher saturation compared to (a), which is highlighted by the flux density contours.

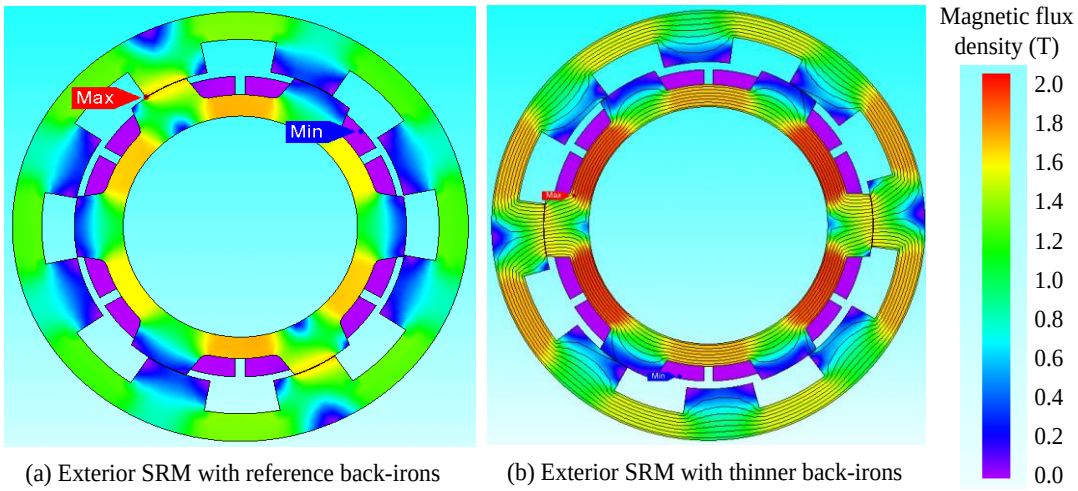

(a) Exterior SRM with reference back-irons (b) Exterior SRM with thinner back-irons

Figure 3.51 Saturation level versus back-iron thickness

The iron loss for different back-iron thickness is illustrated in Figure 3.52, clearly showing the trend that smaller back-iron thickness results in higher iron loss due to the higher saturation levels, which is intuitively obvious. However, the iron loss only reduces slightly when further increasing the back-iron thickness while the machine volume increases. Therefore, a good selection of the machine back-iron thicknesses are made around the knee points from the loss chart of Figure 3.52.

Hence, in the case of the exterior SRM, the stator back-iron thickness is selected to be 20mm while the stator back-iron thickness of the interior SRM is selected to be 13mm.

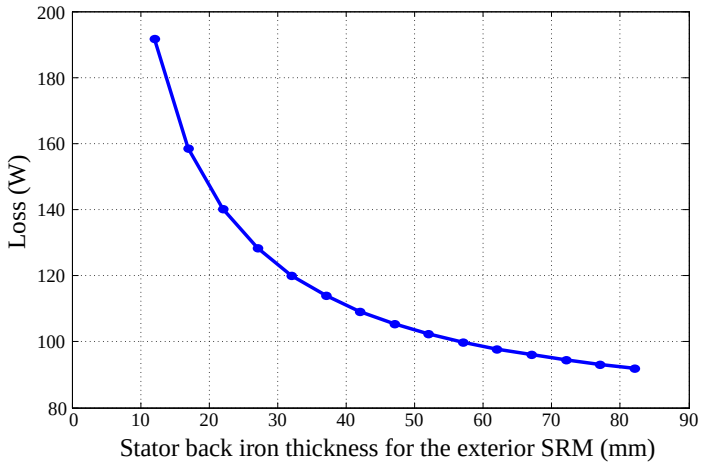

Figure 3.52 Iron losses versus back-iron thickness

In addition, the shape of stator back-iron in the interior SRM has been modified from the annulus, or ring shape, by using round arcs, to straight edges as shown in Figure 3.53. This provides extra slot space for windings and wedges, which increases the fill factor of the interior SRM and facilitates an easier winding process since the interior SRM is subjected to its small bore diameter and relatively high number of turns. Simulation results show similar electromagnetic performance when comparing the straight edges stator with the initial ring shape stator design under the same excitation conditions. The saturation level is adjusted and kept within the limit so that both the corner points and the thinnest section of the back-irons have no concentrated saturations.

Other geometric optimizations were implemented to further improve the machine reliability and performance. Figure 3.54 shows same results from a study into the fillet effects on the torque ripple. It shows that even a 0.5mm fillet on the stator pole corner would result in higher torque ripple due to high flux concentration on the pole corner areas. Adding pole “shoes” to the stator pole tips significantly reduces the torque ripple.

Further, the extruded pole shoes can be used as one mechanical stand to place a coil wedge, which is used to secure the coil in the stator slot.

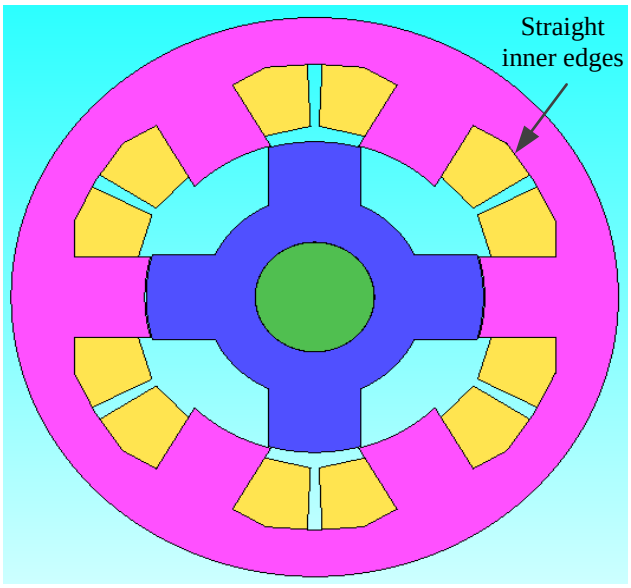

Figure 3.53 Interior SRM stator design with straight inner edges

Figure 3.55 shows the added mid-pole stands that are also designed to help locate the stator coil wedges. Further electromagnetic study proves that the added mid-pole stands do not interfere with the existing magnetic field. The effects of clearance holes and key ways have also been studied to ensure that they do not influence the machine performance as shown in Figures 3.56 and 3.57.

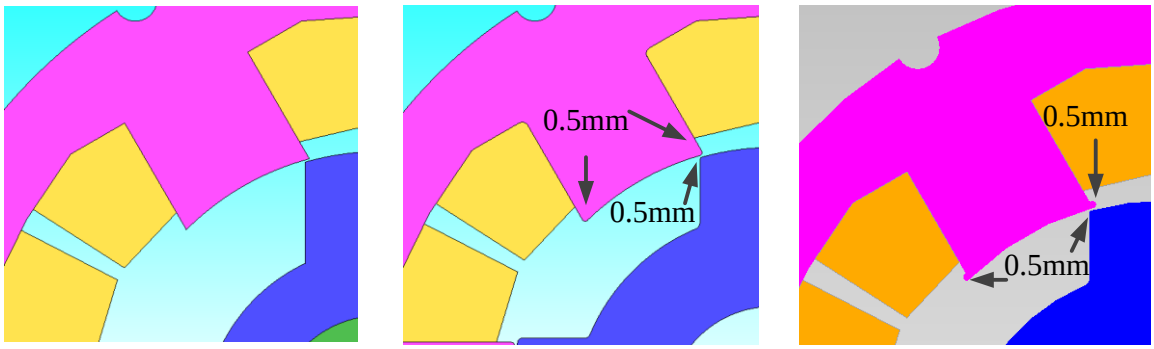

Average torque: 2.07Nm
Torque ripple: 12%

(a) Without fillets

Average torque: 2.03Nm
Torque ripple: 46%

(b) With fillets

Average torque: 2.06Nm
Torque ripple: 13%

(c) With pole tips

Figure 3.54 Pole detail effects on the total average torque and torque ripple

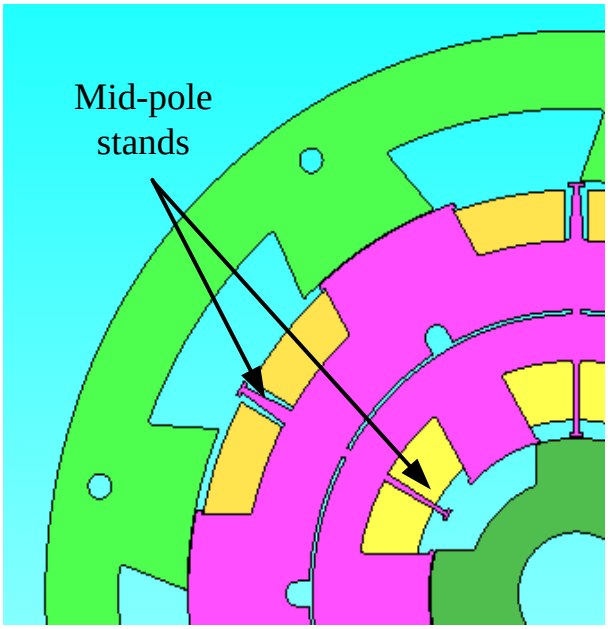

Figure 3.55 Mid-pole stands designed to place the wedges

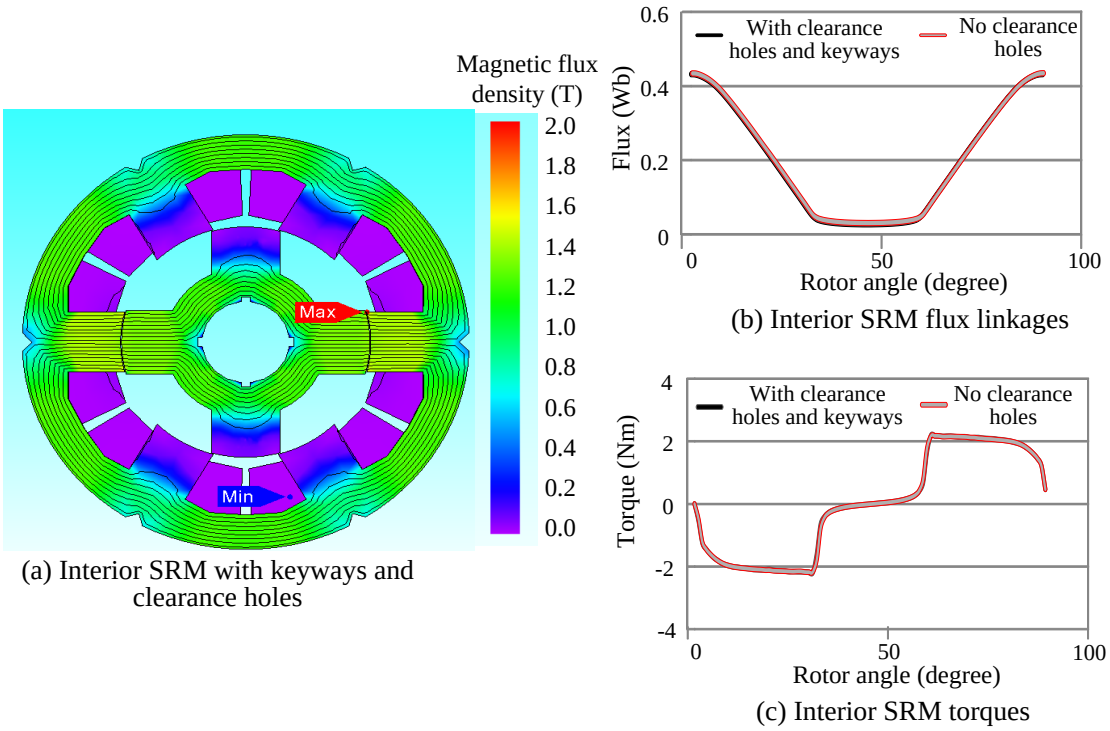

(a) Interior SRM with keyways and clearance holes

(b) Interior SRM flux linkages

(c) Interior SRM torques

Figure 3.56 Effects of the interior stator clearance holes and the shaft keyways

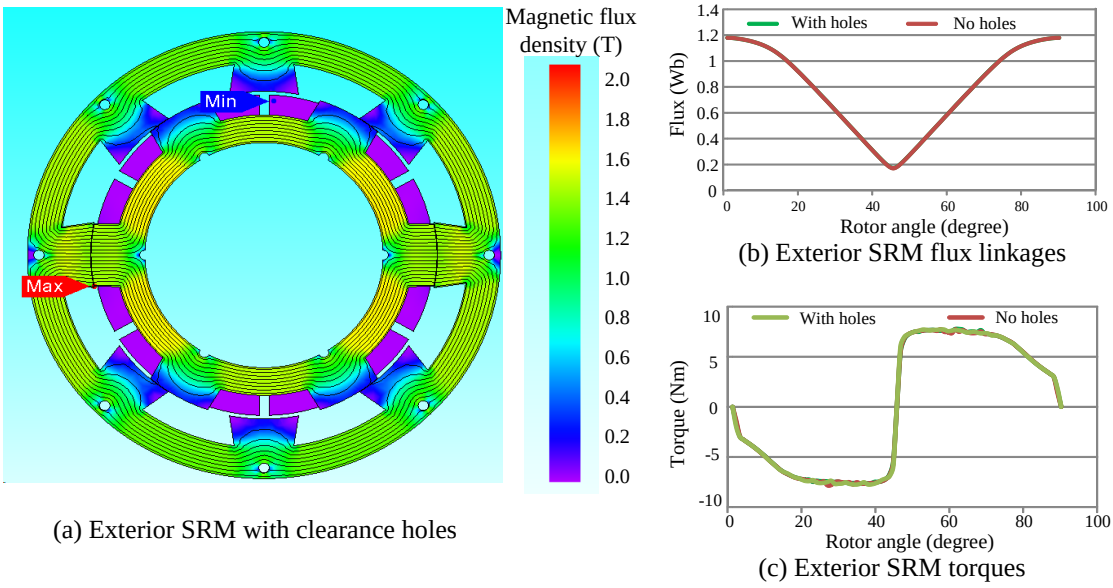

(a) Exterior SRM with clearance holes

(b) Exterior SRM flux linkages

(c) Exterior SRM torques

Figure 3.57 Effects of the exterior bolt holes

3.5.2 Turn-on and Turn-off angles Optimizations

The optimization of turn-on and turn-off angles can be first studied based on the single pole excitation analysis in which constant current is applied to one phase. Single pole excitation analysis gives typical torque waveforms as shown in Figures 3.56 (c) and 3.57 (c). The overall torque waveform can then be derived by shifting and truncating the single pole excitation torque waveform and then summating the contributions from each phase. Figure 3.58 shows the torque waveforms for the interior SRM under single pole excitation.

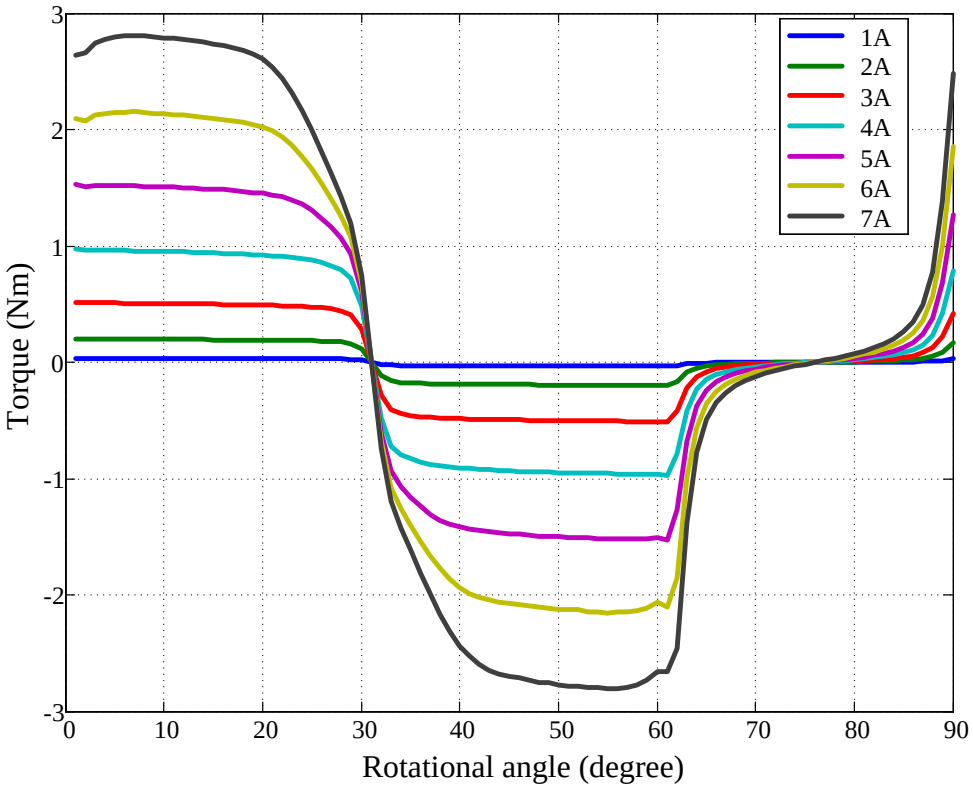

Figure 3.58 Interior SRM torque waveforms under single pole excitation

Since the interior SRM has three phases and four rotor poles, the electric period is 30 degrees as calculated from:

$$\gamma = \frac{360}{mN_r} \tag{3.63}$$

where γ is the electric period in degrees, m is the number of phases, and N_r is the number of rotor poles.

Thus, by shifting positive 30 degrees and negative 30 degrees, the torque waveforms of the other two phases can be derived from the torque waveform under the single pole excitation as shown in Figure 3.59.

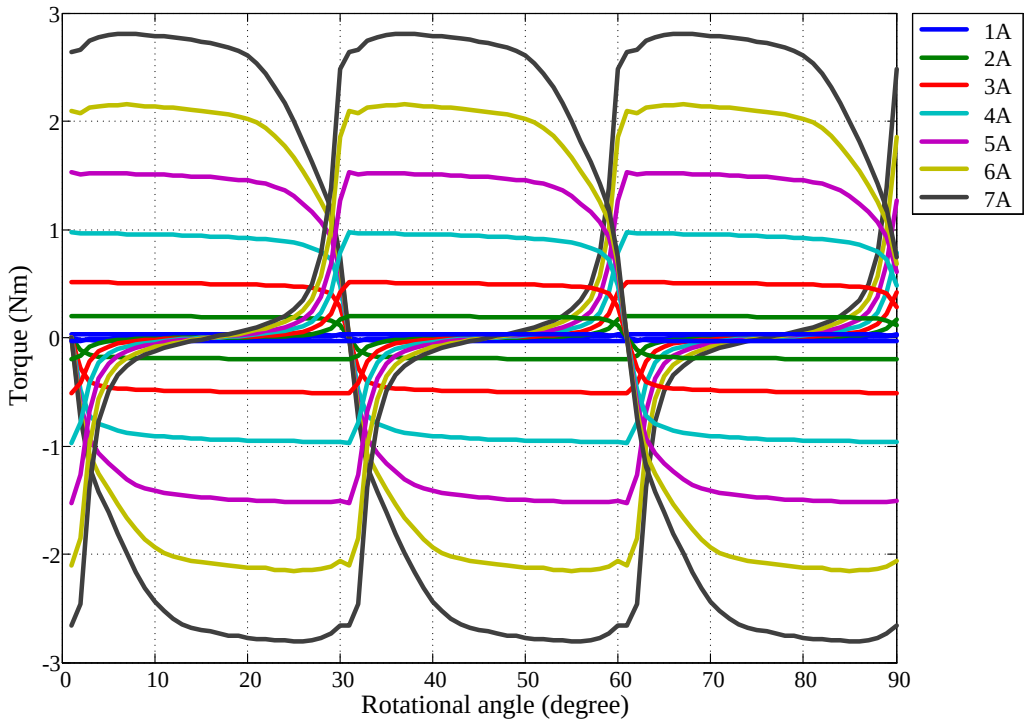

Figure 3.59 Interior SRM torque waveforms for all three phases

Removing the negative parts of the phase torque and combining the positive torques from all the phases, a combined torque waveform can be generated for each constant current excitation level, as shown in Figure 3.60, in which the solid lines represent the combined torque while the dashed lines represent the torques of individual phases.

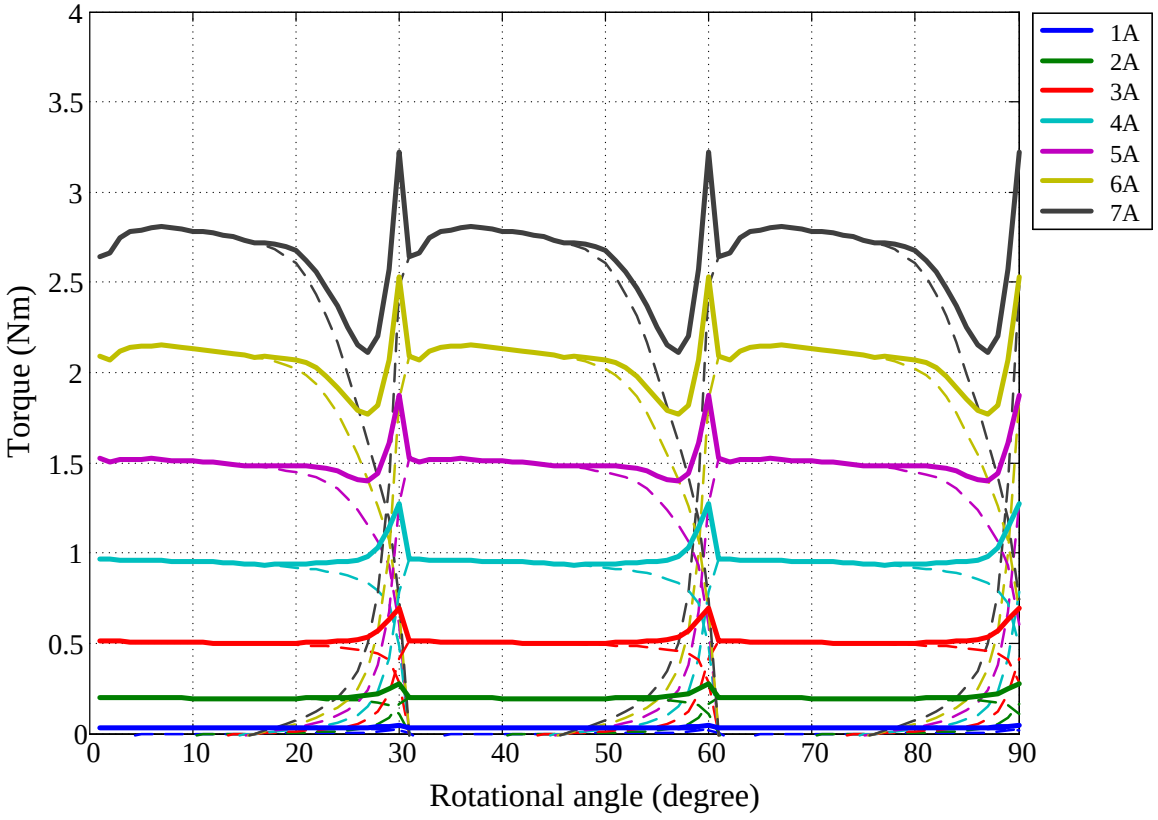

Figure 3.60 Interior SRM torque waveforms for all three phases

For the case shown in Figure 3.60, the angle window for phase 1 that generates positive torques starts from -13 degrees to 32 degrees, corresponding to the unaligned position and aligned position respectively. The angles for phases 2 and 3 that generate positive torques can be calculated by shifting 30 and 60 degrees respectively from that of

phase 1. Thus, if the unaligned position for each phase is assigned to be 45 degree as the reference point, the angle that generates positive torques of each phase is from 45 to 90 degrees.

It can also be observed that the torque ripples mainly occur at the phase shifts. The torque drops as the rotor gets closer to the aligned position because the flux-linkage change rate $\frac{d\lambda}{dt}$ gets smaller. Meanwhile, the subsequent phase begins to generate positive torque that compensates the torque drop in the preceding phase. However, adding the torques of the two phases together sometimes causes torque overshoots as observed by the spikes in Figure 3.60. Thus, it is necessary to advance the turn-off angles in these cases. Table 3.9 compares the torque ripples for different current levels by advancing the turn-off angles. Figure 3.61 presents the torque waveforms by advancing the turn-off angles by 3 degrees. Comparing Figures 3.60 and 3.61, it can be observed that the spikes in Figure 3.60 are suppressed and the torque ripples are reduced.

Table 3.9 Torque ripple comparison of different turn-off angles

Current (A)	Turn on angle (degree)	Turn off angle (degree)	Torque ripple (%)	Turn on angle (degree)	Turn off angle (degree)	Torque ripple (%)
1	45	90	43.86	45	87	38.12
2	45	90	40.26	45	87	42.03
3	45	90	38.54	45	87	41.82
4	45	90	34.72	45	87	36.88
5	45	90	31.46	45	87	22.64
6	45	90	37.08	45	87	18.84
7	45	90	41.87	45	87	26.39

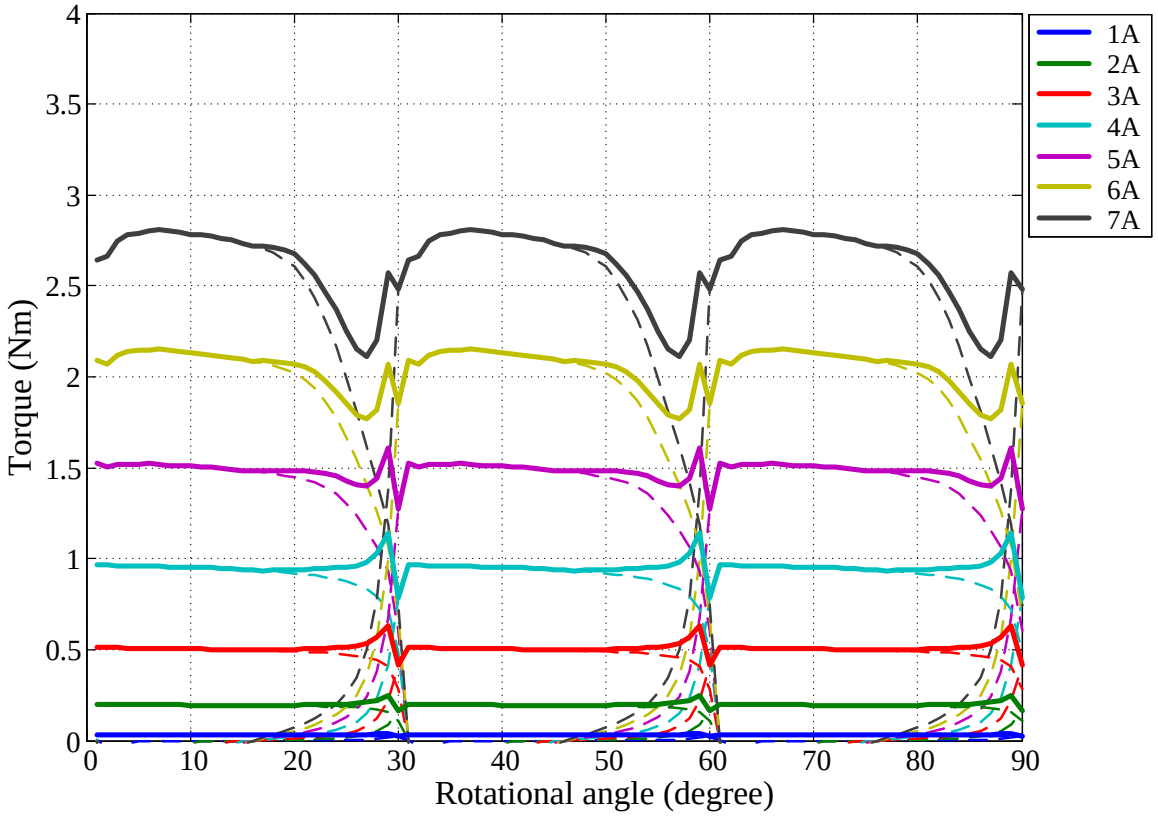

Figure 3.61 Torque waveforms by advancing turn-off angle

Furthermore, since the torque at the unaligned position of each phase is small, the turn-on angles can be postponed to reduce the copper losses in the phase windings without affecting the output torque performance. Therefore, the turn-on angles for each current level can be adjusted accordingly, as summarized in Table 3.10, which also presents the optimized turn-on and turn-off angles for different levels of current excitation. Matlab drive simulation also confirms the optimized turn-on and turn-off angle, as illustrated in Figures 3.62 and 3.63.

Table 3.10 Optimized turn-on and turn-off angles for the interior SRM

Current (A)	Turn on angle (degree)	Turn off angle (degree)	Average torque (Nm)	Torque ripple (%)
1	55	87	0.03	38.71
2	47	88	0.20	40.84
3	46	88	0.52	38.76
4	55	87	0.95	37.42
5	54	87	1.48	22.90
6	53	87	2.03	19.01
7	53	87	2.62	26.64

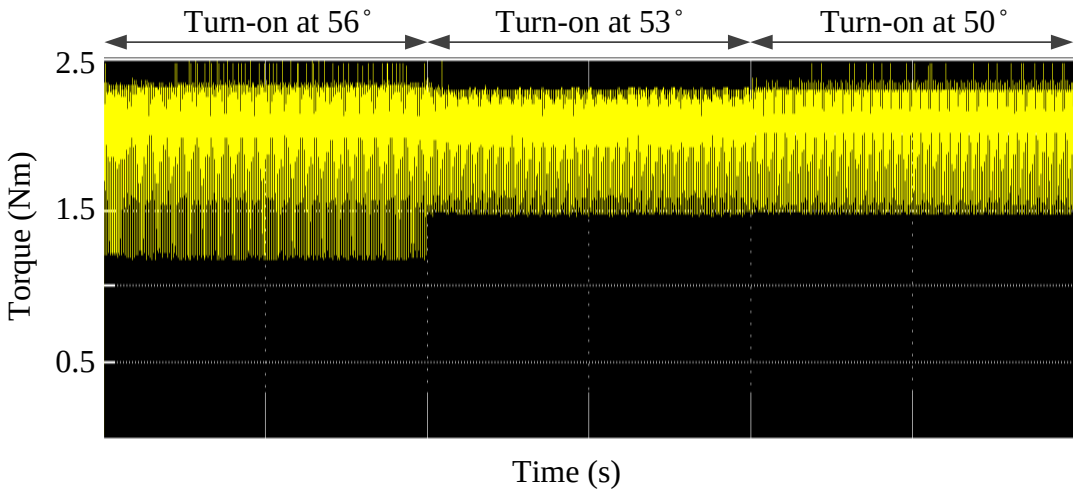

Figure 3.62 Turn-on angle optimization at 6A for the interior SRM

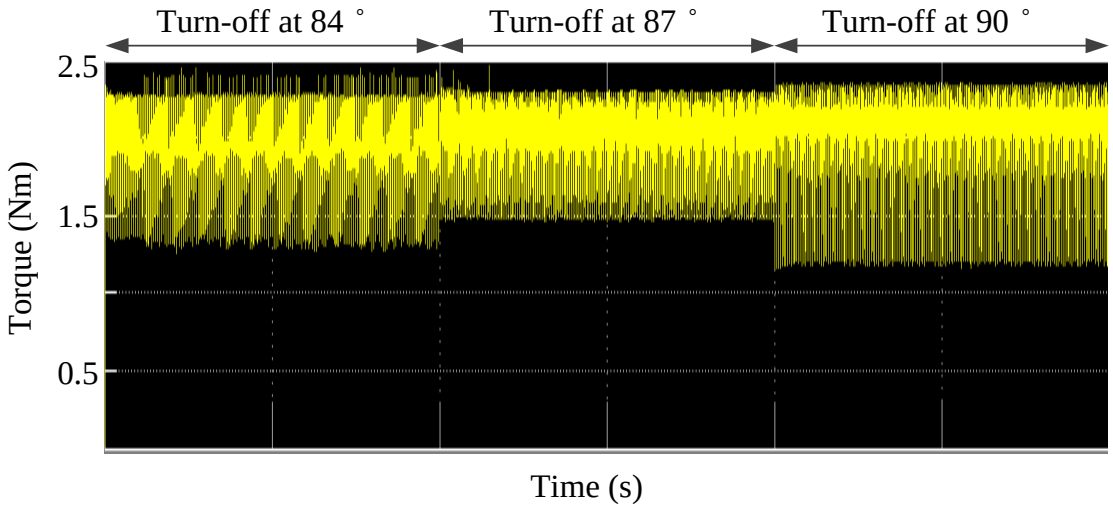

Figure 3.63 Turn-off angle optimization at 6A for the interior SRM

The same procedure can be repeated to the exterior SRM to optimize the turn-on and turn-off angles. Figures 3.64 to 3.66 present the exterior SRM torque waveforms under single pole current excitation, post-processed positive torque waveforms and the optimized torque waveforms after adjusting the turn-on and turn-off angles. It can be seen from Figure 3.66 that there is no current excitation overlap between any of the two subsequent phases under the optimal turn-on and turn-off angles.

Table 3.11 summarizes the optimized turn-on and turn-off angles for the exterior SRM as well as the torque ripple under each current level. The unaligned position in each phase is still taken as the reference point. However, since there are 8 rotor poles in the exterior SRM, the reference value compared with that in the interior SRM is thus halved, i.e. 22.5˚ for the unaligned position.

Matlab drive simulation also confirms the optimized turn-on and turn-off angles for the exterior SRM under 5A current excitation, as shown in Figures 3.67 and 3.68.

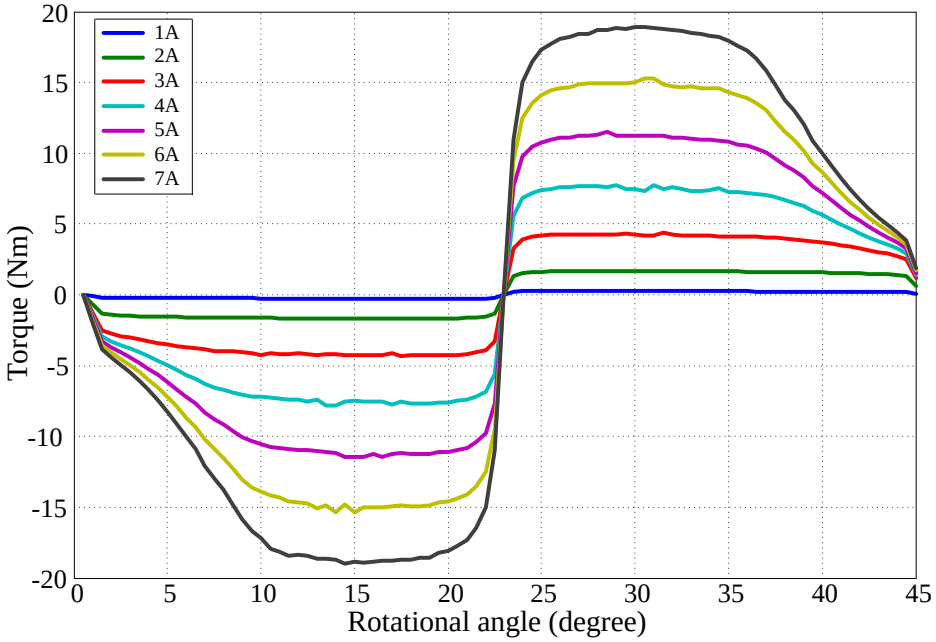

Figure 3.64 Exterior SRM torque waveforms under single pole current excitation

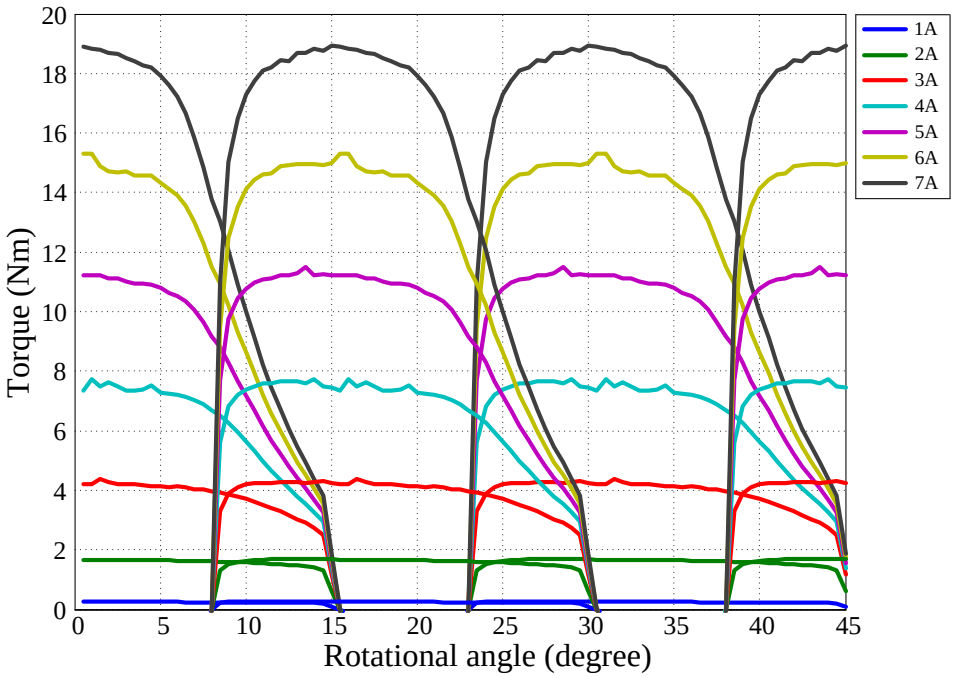

Figure 3.65 Exterior SRM torque waveforms under Multi-pole current excitation

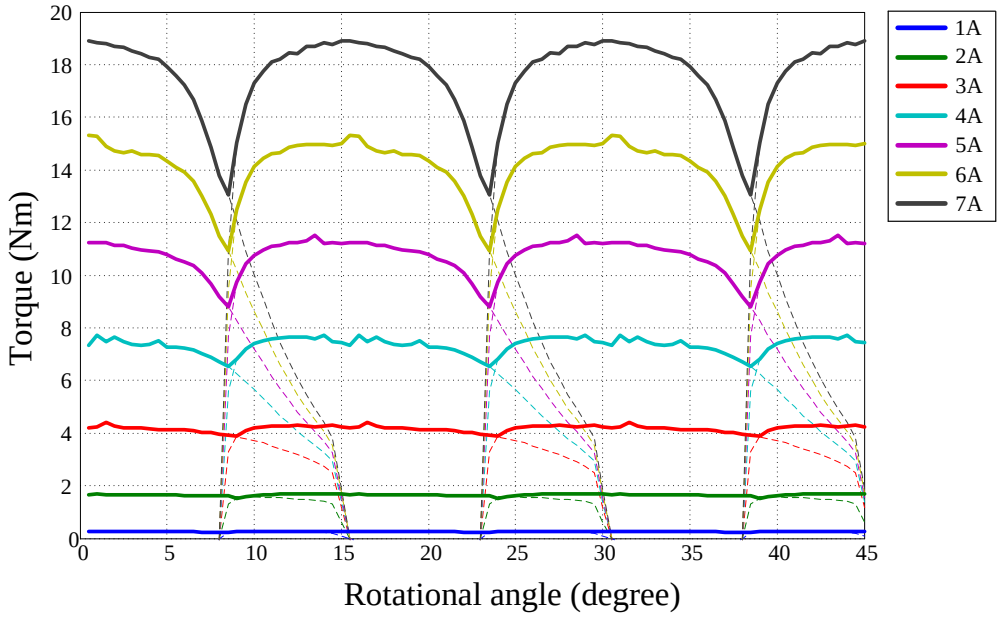

Figure 3.66 Optimized torque waveforms for the exterior SRM

Table 3.11 Optimized turn-on and turn-off angles for the exterior SRM

Current (A)	Turn on angle (mechanical degree)	Turn off angle (mechanical degree)	Average torque (Nm)	Torque ripple (%)
1	23	38	0.22	9.03
2	23	38	1.40	9.78
3	23	38	3.20	12.10
4	23	38	5.58	16.39
5	23	38	7.96	25.07
6	23	38	10.24	30.89
7	23	38	12.76	33.46

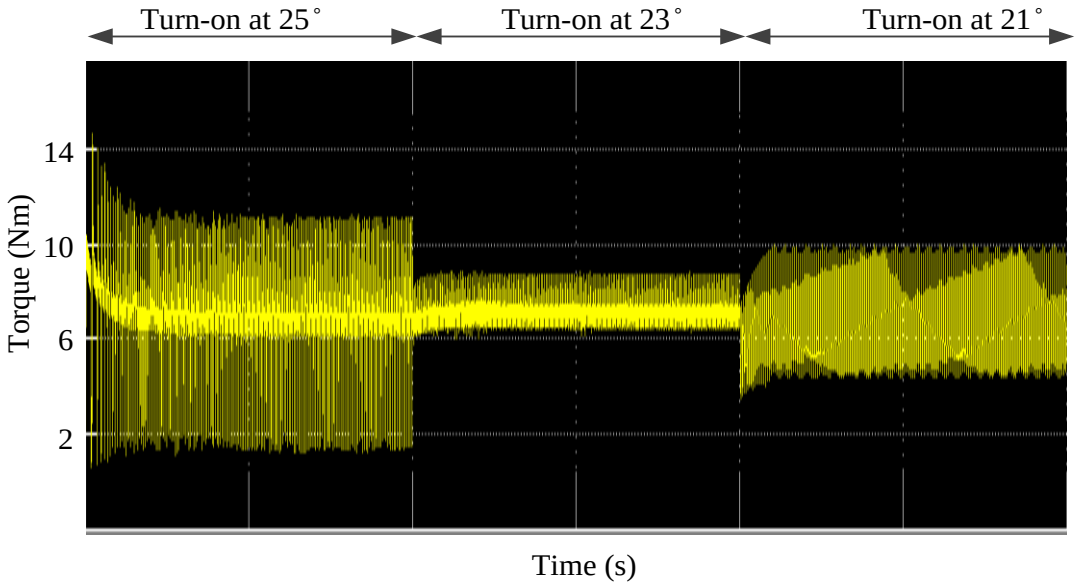

Figure 3.67 Turn-on angle optimizations at 5A for the exterior SRM

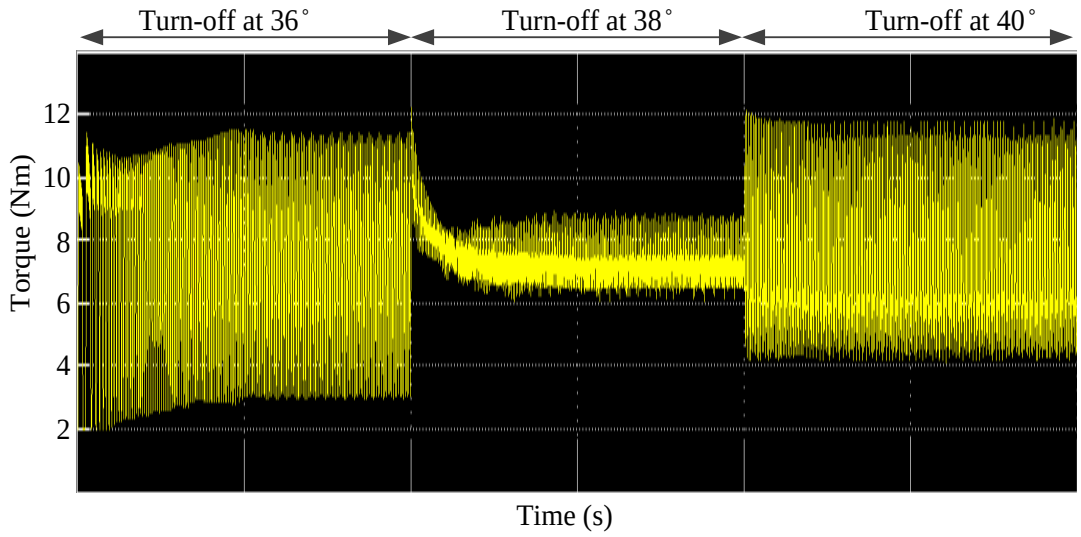

Figure 3.68 Turn-off angle optimizations at 5A for the exterior SRM

3.5.3 Load and Excitation Optimizations

The maximum current that can flow in the windings is determined by the maximum current that the motor drive can supply and limited by the selected winding wire gauges due to coil thermal considerations. Tables 3.10 and 3.11 in Section 3.5.2 can also be applied here to study the optimal load and excitation levels. It can be observed that for the interior SRM, the minimum torque ripple is achieved with 6A phase current excitation where the average torque output is 2.03Nm. For the exterior SRM, the highest average torque with torque ripple under 25% is achieved by 5A phase current excitation where 7.96Nm output torque is generated.

In addition, the flux-linkage and torque characteristics have been studied for different current levels. Figure 3.69(a) presents the flux-linkage for one phase under different currents at both aligned position and unaligned position and Figure 3.69(b) presents the torque over current ratio versus the input current. It can be observed that the curve of the torque over current ratio saturates after 4.5A, where the aligned flux-linkage also saturates, although higher torque can be extracted after saturation occurs. Combining the torque ripple factor discussed above, the rated current is therefore chosen at 6A for the interior SRM. Similarly, the exterior SRM rated current is selected to be at 5A as shown in Figure 3.70.

The thermal behavior of the DRSRM is studied and the design confirmed at different levels of current excitation. Figure 3.71 presents the temperature rise and the temperature distribution for the DRSRM in steady state for 6A to 8A interior stator current excitations. Figure 3.72 presents the similar results under exterior stator current

excitations and Figure 3.73 presents the results under the current excitations of both machines. It can be observed that under the rated current excitations, both machines are kept within the rated temperature boundaries, and thus the rated current excitations for each machine are acceptable.

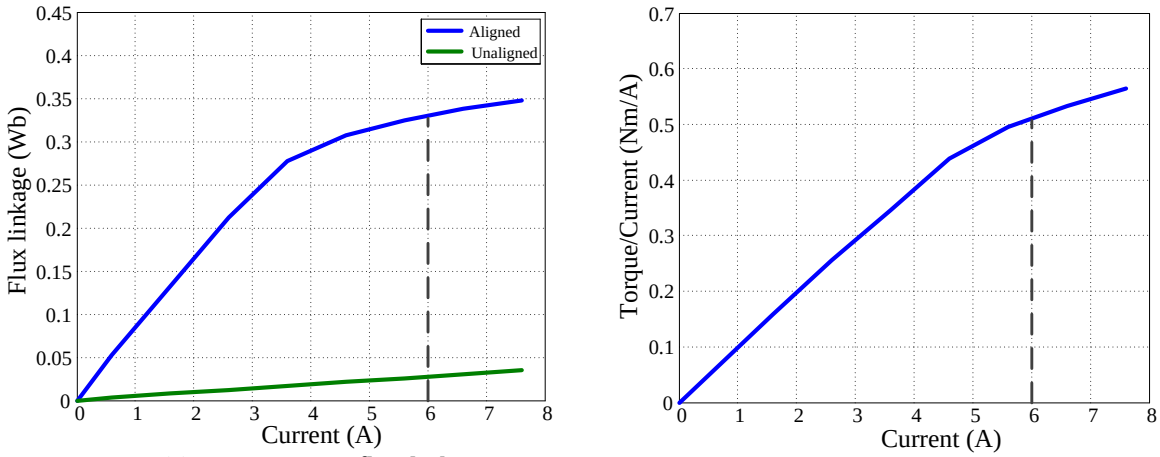

(a) Interior SRM flux linkage (b) Interior SRM torque per ampere

Figure 3.69 Interior SRM loading optimization

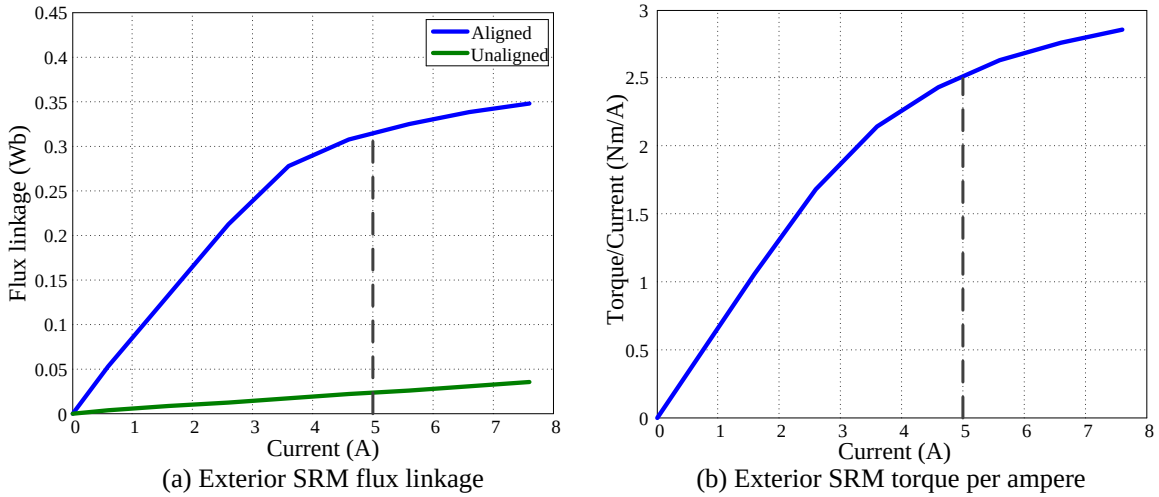

(a) Exterior SRM flux linkage (b) Exterior SRM torque per ampere

Figure 3.70 Exterior SRM loading optimization

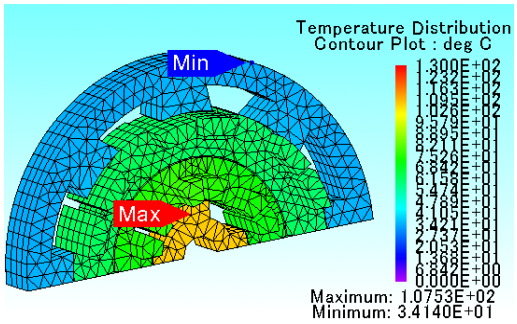

(a) Temperature distribution caused by 6A current in the interior SRM

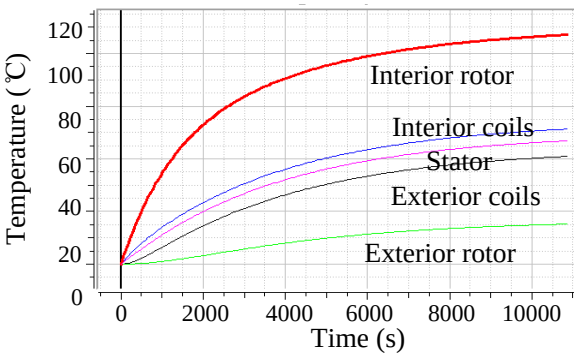

(b) Temperature rise over time caused by 6A current in the interior SRM

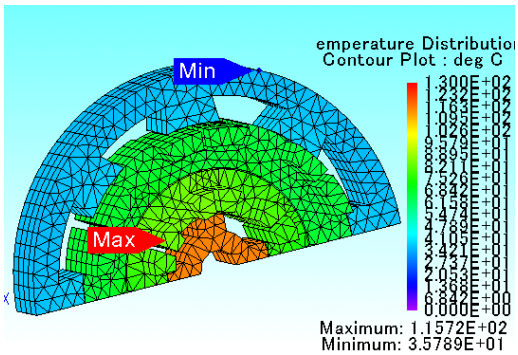

(c) Temperature distribution caused by 7A current in the interior SRM

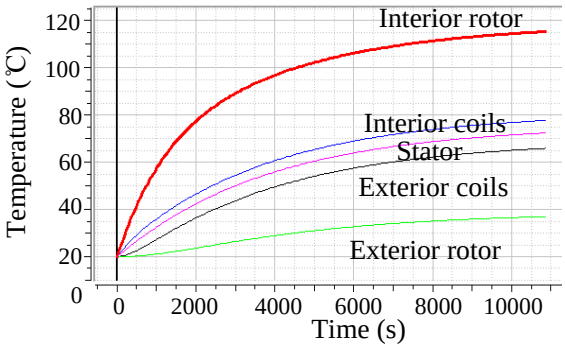

(d) Temperature rise over time caused by 7A current in the interior SRM

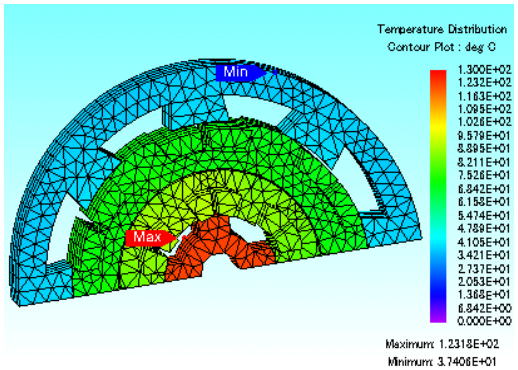

(e) Temperature distribution caused by 8A current in the interior SRM

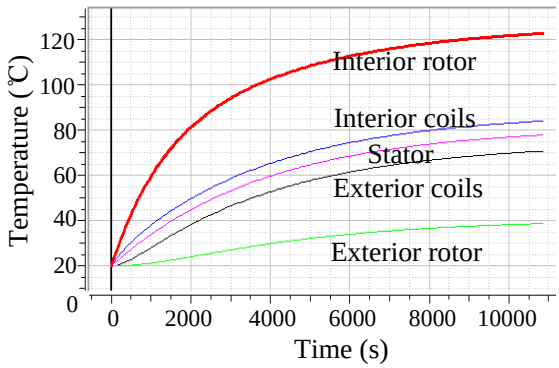

(f) Temperature rise over time caused by 8A current in the interior SRM

Figure 3.71 Thermal behavior of the DRSRM with 6, 7 and 8A current excitation of the interior SRM

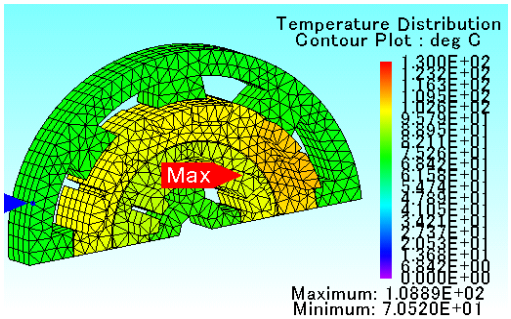

(a) Temperature distribution caused by 6A current in the exterior SRM

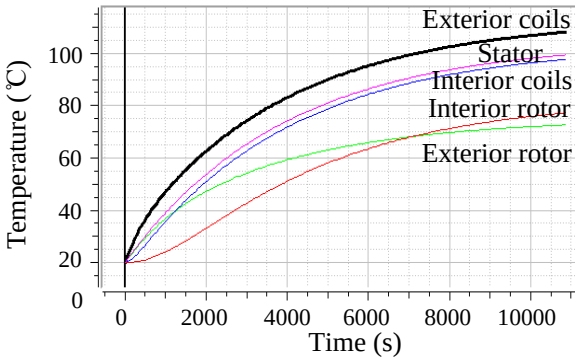

(b) Temperature rise over time caused by 6A current in the exterior SRM

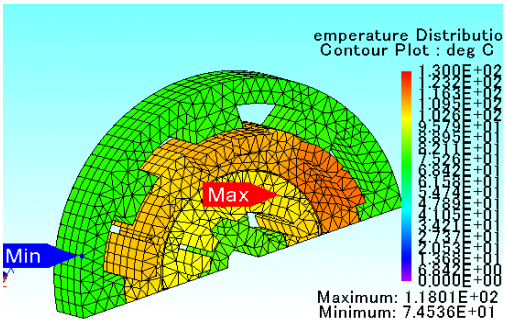

(c) Temperature distribution caused by 7A current in the exterior SRM

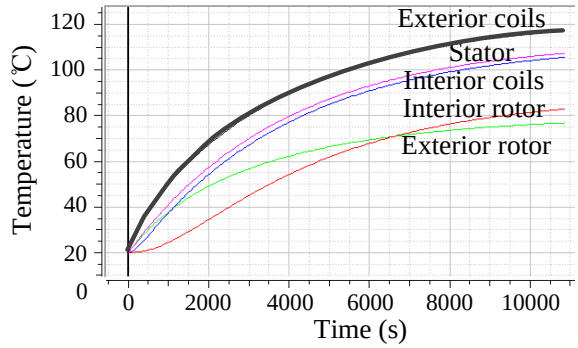

(d) Temperature rise over time caused by 7A current in the exterior SRM

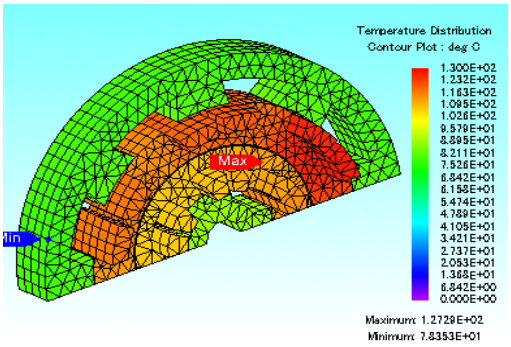

(e) Temperature distribution caused by 8A current in the exterior SRM

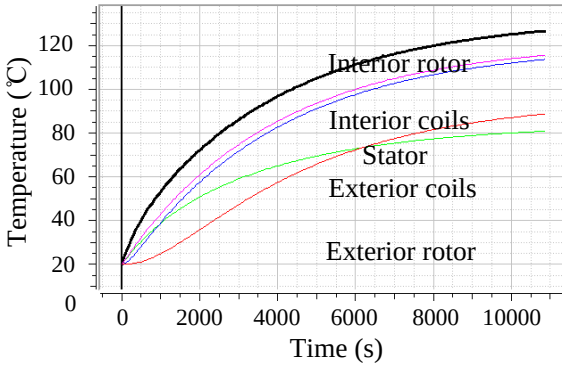

(f) Temperature rise over time caused by 8A current in the exterior SRM

Figure 3.72 Thermal behavior of the DRSRM with 6, 7 and 8A current excitation of the exterior SRM

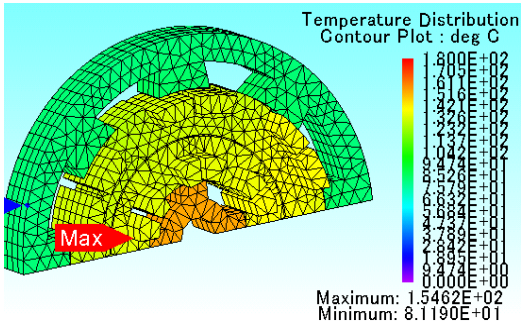

(a) Temperature distribution caused by 6A current from both machines

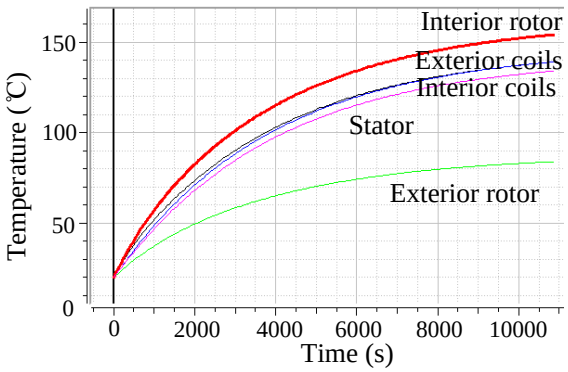

(b) Temperature rise over time caused by 6A current from both machines

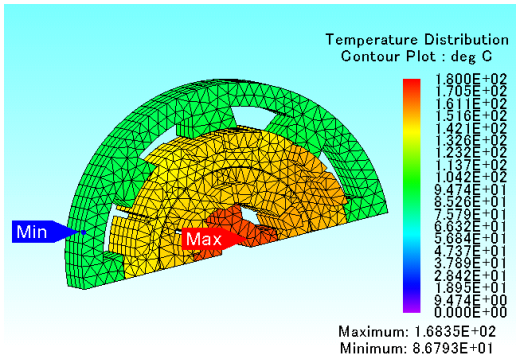

(c) Temperature distribution caused by 7A current from both machines

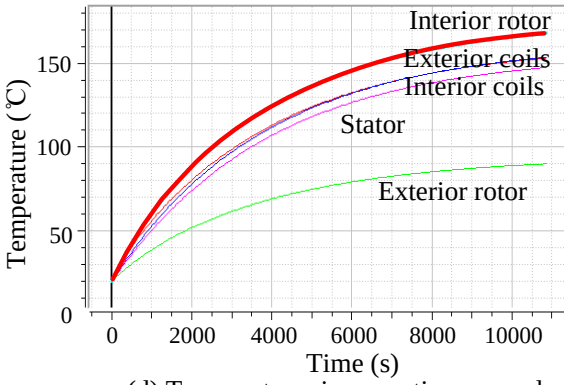

(d) Temperature rise over time caused by 7A current from both machines

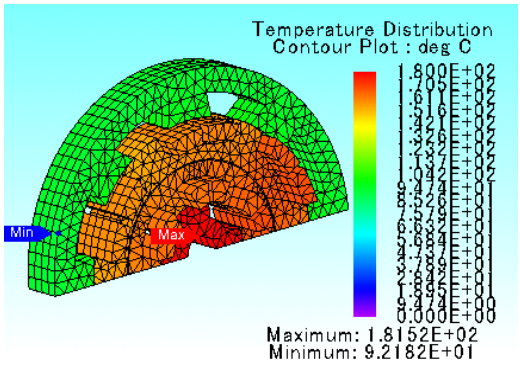

(e) Temperature distribution caused by 8A current from both machines

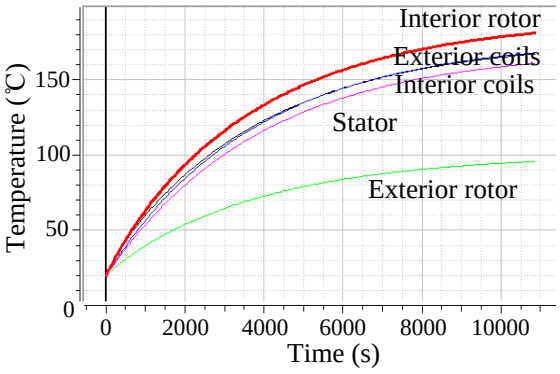

(f) Temperature rise over time caused by 8A current from both machines

Figure 3.73 Thermal behavior of the DRSRM with 6, 7 and 8A current excitation of both the interior SRM and the exterior SRM

3.5.4 Stack Length Optimizations

Another critical optimization objective is the efficiency of the DRSRM. Once the major geometries of the laminations are selected, adjusting the machine stack length can be an effective way to improve the machine efficiency.

The stack length is optimized by studying the machine iron loss under different input conditions. In order to achieve the same rated torque, different current levels were studied with changes to stack length. Table 3.12 summarizes different stack lengths versus the stator back-iron loss, which is the dominating loss as shown and discussed in Section 3.4.2. Figure 3.74 presents the iron loss curve as a function of different machine stack length. It should be noted here that even though the 30mm stack length produces the minimal iron loss, the current injected actually exceeds the maximum tolerance of the selected wires, which is 7.75A. Therefore, the minimum stack length should be kept larger than 40mm so that the output performance is not sacrificed.

Table 3.12 Stator back-iron loss as a function of stack length by changing current

Stack Length (mm)	Current (A)	Average Torque (Nm)	Stator Back-iron Loss (W)
30	8.1	2.09	64.47
40	6.7	2.11	79.05
50	5.7	2.06	91.04
60	5.1	2.02	102.52
65	5.9	2.06	108.45
70	4.7	2.06	113.71
75	4.5	2.04	117.97
80	4.3	2.02	121.42
140	3.2	2.03	144.47

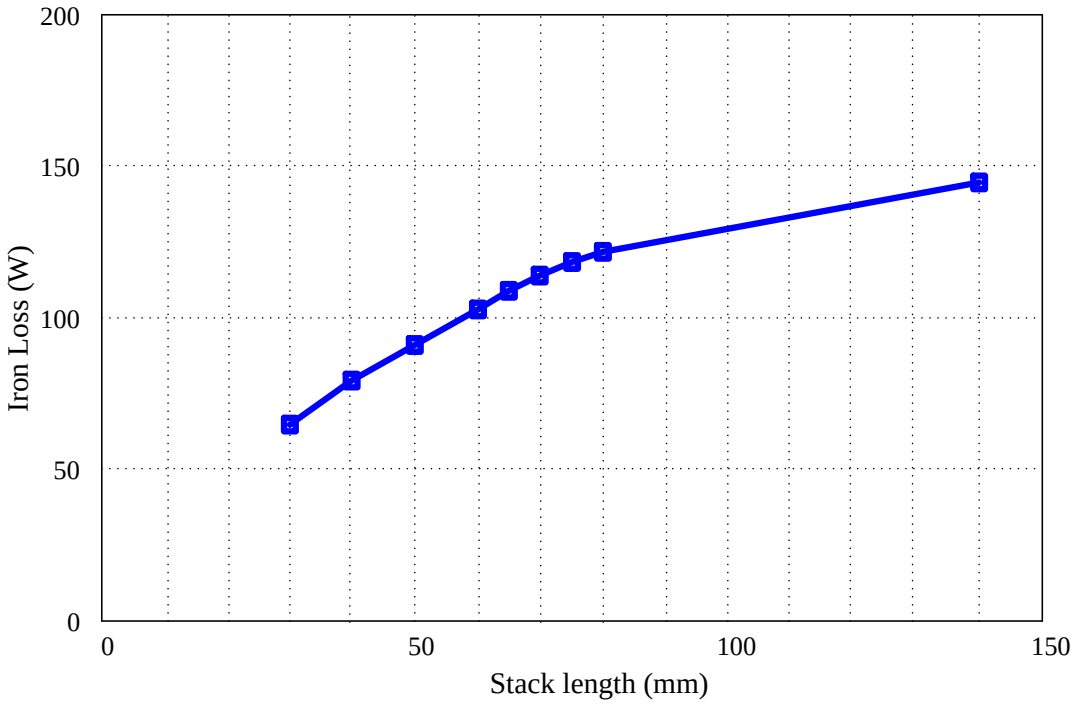

Figure 3.74 Stator iron loss versus machine stack length

The above scenario keeps the speed and the winding the same, but the input current actually changes for different stack length. Thus, the induced voltage at each phase terminal also changes. In order to keep the same induced voltage as well as the output torque, another study has been carried out to compare the iron loss in terms of the stack length by adjusting the phase turns and input phase current. Table 3.13 summarizes the simulation results and Figure 3.75 presents the loss curve as a function of the stack length.

The same trend is revealed that the increase of stack length increases the total iron loss, thus resulting in lower machine efficiency. It should also be noted that when the stack length is smaller than 50mm, the required fill factor to achieve the same rated torque is larger than 40%, which is difficult or impractical in the actual machine

manufacturing process. Thus, a 50mm stack length proves to be an ideal selection for the machine design that gives higher efficiency and offers a higher degree of design flexibility with lower rated current and more winding space.

Table 3.13 Stator back-iron loss as a function of stack length by changing windings

Stack Length (mm)	Speed (RPM)	Number of Turns	Current (A)	Average Torque (Nm)	Induced Voltage (V)	Fill Factor (%)	Stator Back-iron Loss (W)
30	4400	150	5.2	2.06	299	57	99.12
40	4400	115	5.4	2.04	301	43.7	120.98
50	4400	93	5.7	1.99	296	35.3	138.80
60	4400	82	5.7	1.95	298	31.4	153.67
70	4400	75	5.7	1.94	303	28.5	167.13

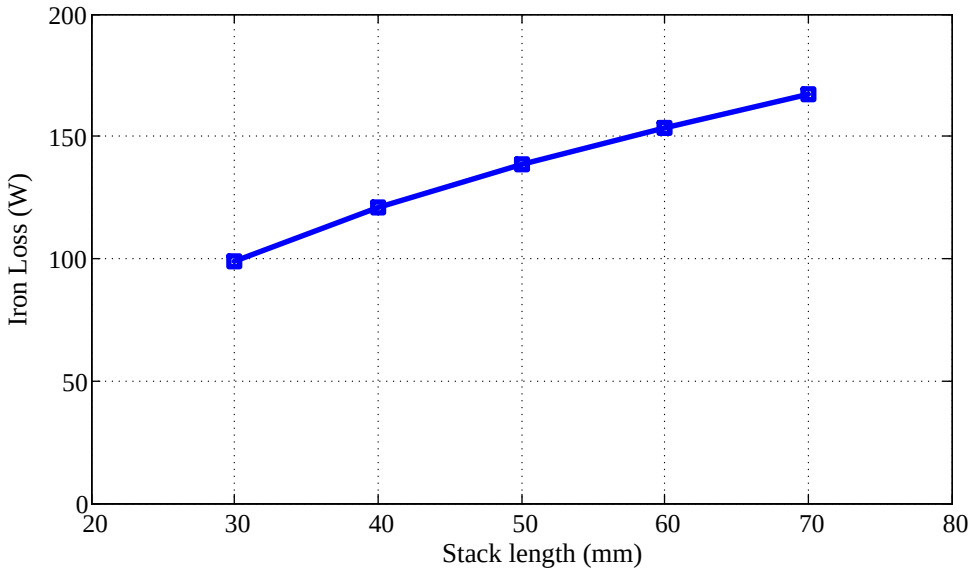

Figure 3.75 Stator back-iron loss versus stack length keeping the same speed and voltage

3.6 ANALYSIS OF THE FINAL DRSRM DESIGN

The previous sections discuss the design process of the DRSRM, investigating the concepts by various simulations and optimizations in order to achieve good performance and efficiency, as well as minimizing volume and weight. Table 3.14 summarizes the final optimized design parameters and Figure 3.76 presents the 2D geometries of the DRSRM. It should be noted that the w-shape notches on the outer diameter of the exterior rotor are slots for TIG welding to bond all the lamination together. Figures 3.77 and 3.78 present the flux-linkage waveforms and the torque waveforms of both the interior and exterior SRMs.

Based on the finalized machine geometry as well as the machine properties, various analyses can be carried out to confirm the DRSRM design and study its performance. Both the mechanical structure effects of the DRSRM and its corresponding electromagnetic properties will be analyzed in the following sections, and 3D simulation results will be presented to compare and confirm the 2D simulation results.

Table 3.14 Optimized DRSRM specifications

	Interior SRM	Exterior SRM
Stack length (mm)	50	
Maximum current (A)	7.75	
DC link voltage (V)	300	
Phase current (A)	6	5
Phase turns	93	160
Fill factor (%)	35	39
Rated speed (RPM)	2000	500
Rated torque (Nm)	2	8
Rated power (W)	419	419
Efficiency (%)	81	87

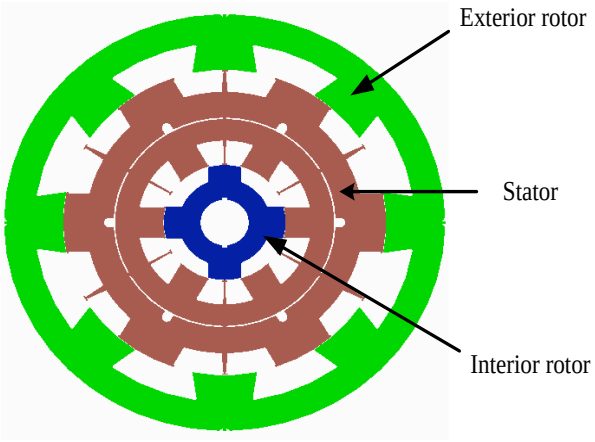

Figure 3.76 Optimized geometry of the DRSRM

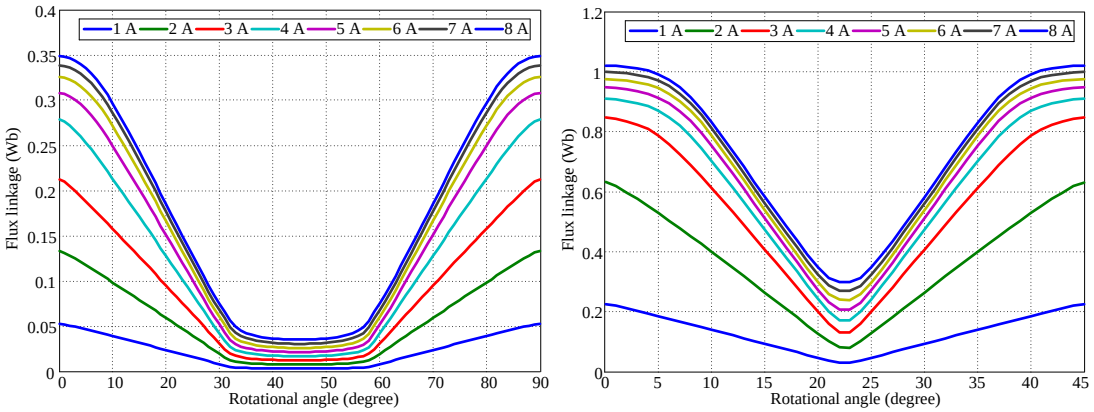

(a) Interior SRM flux linkages (b) Exterior SRM flux linkages

Figure 3.77 Flux-linkage waveforms of the DRSRM

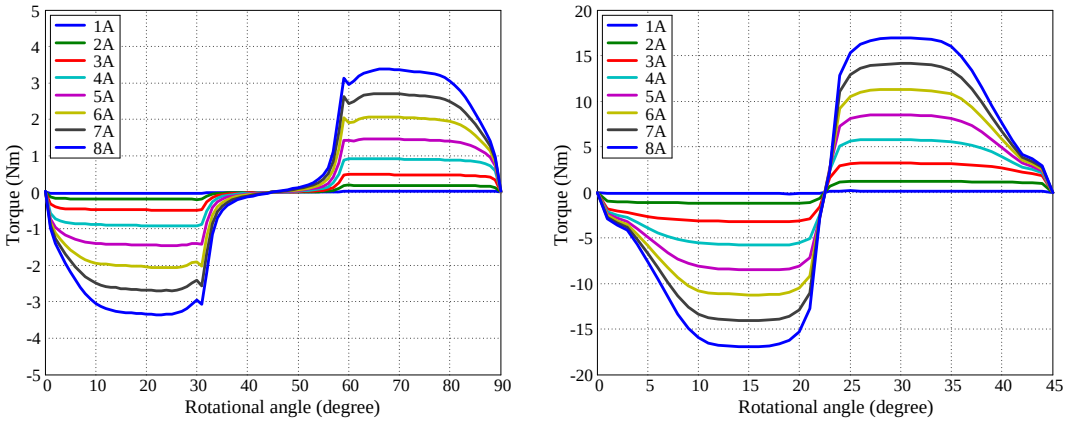

(a) Interior SRM torques (b) Exterior SRM torques

Figure 3.78 Torque waveforms of the DRSRM

3.6.1 Eccentricity Analysis

In the DRSRM machine design, the air gap distances between the rotors and the stator are quite small, i.e. 0.3mm in both the interior and exterior SRM. Hence, it is necessary to study the machine eccentricity between the rotors and the stator to avoid the mechanical malfunction as well as noise and vibration issues.

Table 3.15 presents the manufacturing tolerance for each assembly components based on the precision tolerance given by manufacturers or machinist. Figure 3.79 draws the assembly stacking chains for the interior SRM:

Table 3.15 Manufacturing tolerance for interior SRM

Component	Parameter	Dimension (mm)
Interior rotor	Outer radius	40 ±0.01
	Inner radius	15.81±0.01
Shaft	Outer radius	15.81±0.003
	Stator bearing	10±0.003
Bearing	Inner radius	10±0.001
	Outer radius	23.5±0.001
Stator Clamp 1	At bearing Inner radius	23.5±0.003
	At bolt hole center	74.5±0.003
Stator Clamp 2	At bolt hole center	74.5±0.003
	Bolt hole center	74.5±0.003
Interior Stator	Bolt hole center	74.5±0.01
	Inner radius	40.3±0.01

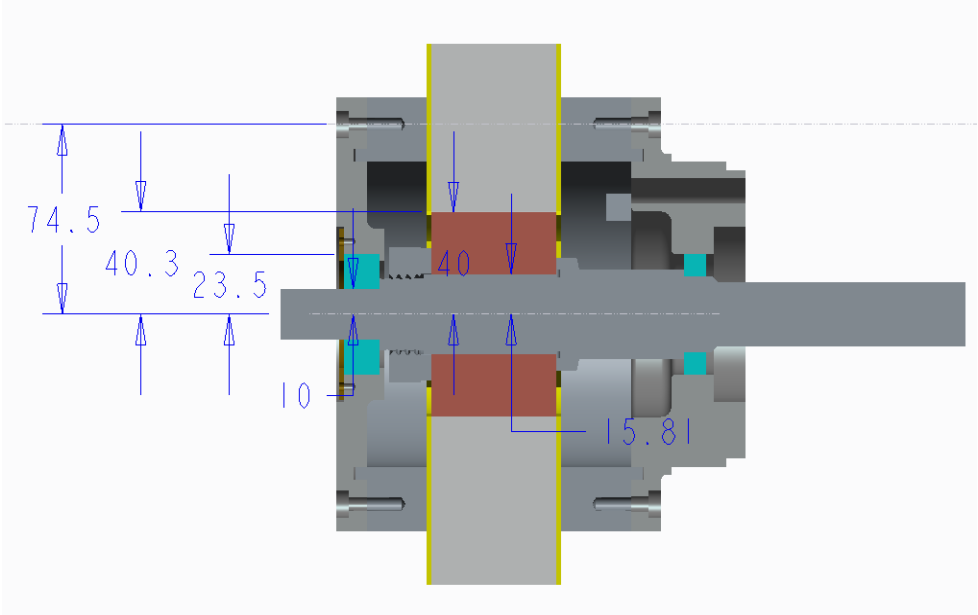

Figure 3.79 Interior SRM assembly stacking chain (dimensions in mm)

The designed outer radius of the interior rotor is 40mm and the designed inner radius of the stator bore is 40.3mm. By taking the stacking tolerances into account, it can be calculated that the maximum outer radius of the interior rotor is 40.023mm while the minimum outer radius is 39.977mm. Similarly, the maximum inner radius of the interior stator is 40.337mm while the minimum inner radius is 40.263mm. Thus, the maximum clearance between the interior rotor and the stator bore is 0.36mm and the minimum clearance is 0.24mm. Since the designed gap distance is 0.3mm, the interior SRM eccentricity based on the manufacturing and assembly tolerance is ± 0.06mm.

Similarly, Table 3.16 presents the manufacturing tolerance for each of the exterior SRM assembly dimension and Figure 3.80 draws the assembly stacking chains:

Table 3.16 Manufacturing tolerance for interior SRM

Component	Parameter	Dimension (mm)
Exterior stator	Outer radius	106±0.01
	Bolt hole center	74.5±0.01
Stator clamp 2	Bolt hole center	74.5±0.003
	Bolt hole center	74.5±0.003
Stator clamp 1	Bolt hole center	74.5±0.003
	At bearing Inner radius	23.5±0.003
Bearing 1	Outer radius	23.5±0.001
	Inner radius	10±0.001
Shaft	At bearing 1 Outer radius	10±0.003
	At bearing 2 Outer radius	10±0.003
Bearing 2	Inner radius	10±0.001
	Outer radius	23.5±0.001
Rotor clamp	At bearing 2 Inner radius	23.5±0.003
	At bolt hole center	148±0.003
Case	At bolt hole center	148±0.003
	Inner radius	145±0.003
Exterior rotor	Outer radius	145±0.01
	Inner radius	106.3±0.01

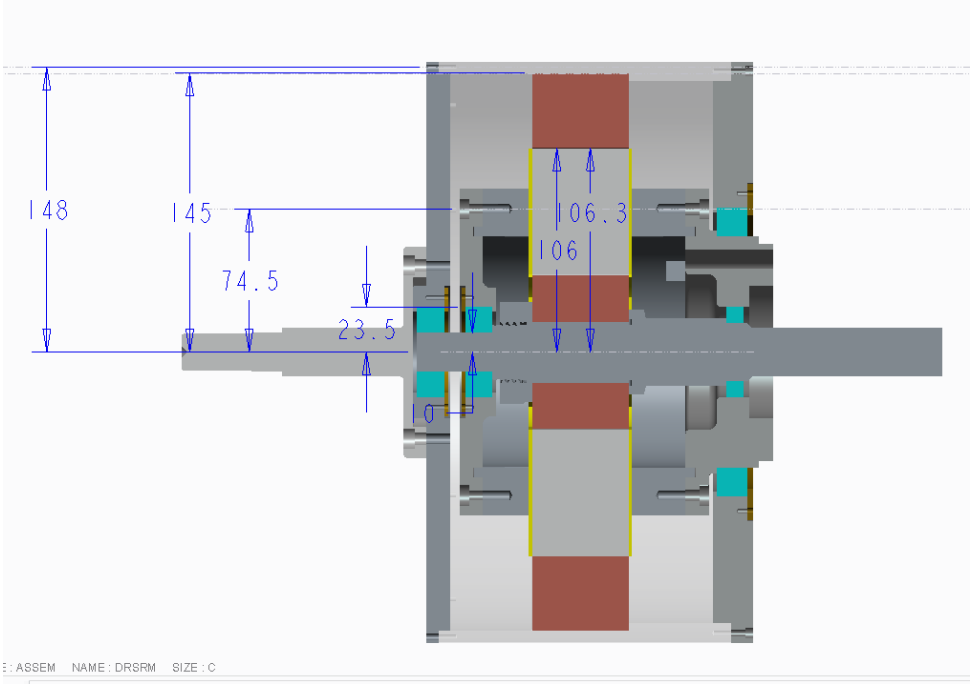

Figure 3.80 Exterior SRM assembly stacking chain (dimensions in mm)

The maximum inner radius of the exterior rotor is 106.337mm while the minimum inner radius is 106.263mm. The maximum outer radius of the stator is 106.037m while the minimum outer radius is 105.963mm. Thus, the maximum clearance between the exterior rotor and the stator is 0.374mm, and the minimum clearance is 0.226mm. Since the designed gap distance for the exterior SRM is also 0.3mm, the exterior SRM eccentricity based on the manufacturing tolerance is ± 0.074mm.

Therefore, by taking the calculated eccentricity into simulation, the eccentricity loading effect can be analyzed. Figure 3.81 compares the radial force and tangential force in the interior rotor reference frame with or without 0.06mm interior rotor eccentricity. It can be observed that both the radial force and the tangential force increase significantly with the rotor eccentricity.

Figure 3.82 compares the radial force and tangential force in the exterior rotor reference frame with or without 0.074mm exterior rotor eccentricity. Similarly, significantly higher radial force and tangential force are produced due to the rotor eccentricity, which indicates that the assembly eccentricity due to the manufacturing tolerance may result in larger noise and vibration issues in SRM operation. However, both the radial force and the tangential force are insignificant once the eccentricity is nulled.

By converting the radial force and the tangential force from the rotor reference frames to the stator stationary reference frame, the forces on the stator x-axis and y-axis can be calculated as shown in Figure 3.83.

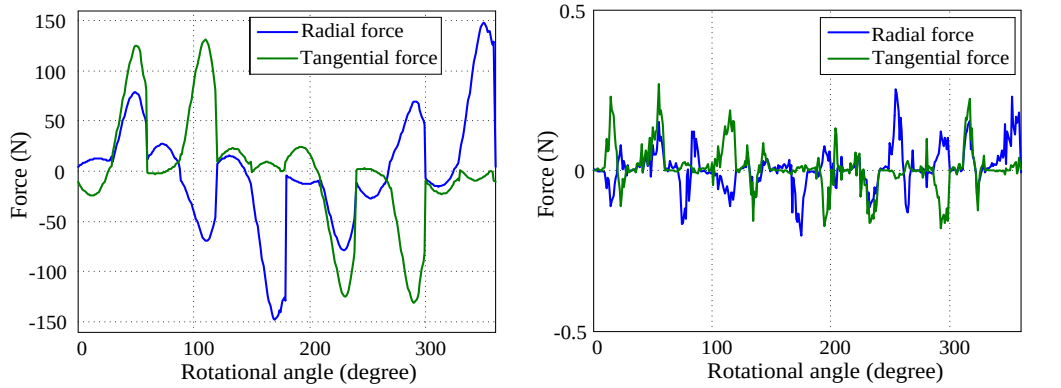

(a) Forces on Interior SRM due to Eccentricity (b) Forces on Interior SRM without Eccentricity

Figure 3.81 Radial and tangential forces comparison for interior SRM

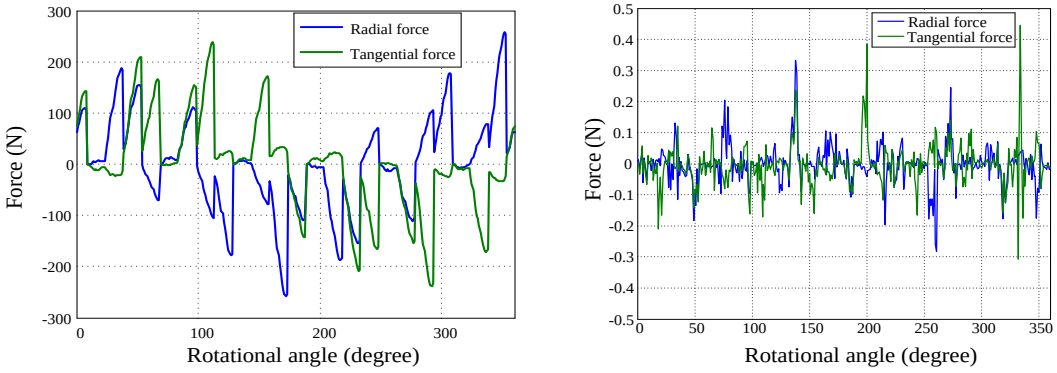

(a) Forces on the exterior SRM with 0.074mm eccentricity

(b) Forces on the exterior SRM with no eccentricity

Figure 3.82 Radial and tangential forces comparison for exterior SRM

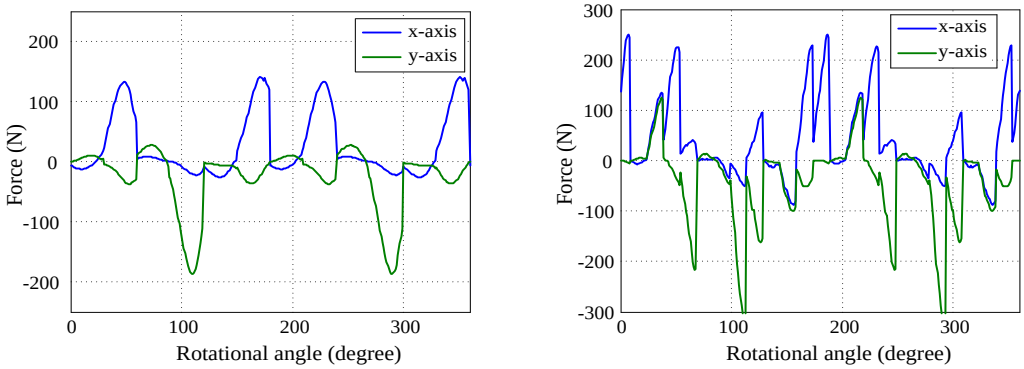

(a) Forces on the interior SRM stator with 0.06mm eccentricity

(b) Forces on the exterior SRM stator with 0.074mm eccentricity

Figure 3.83 Forces on the stator caused by eccentricity

It can be observed from Figure 3.83 that for both the interior SRM and the exterior SRM, there are repeating discontinuous forces applied in both the x-axis direction and the y-axis direction of the stator, which will result in pulse impacts on the bearings. However, the maximum loading due to eccentricity of the interior SRM and the exterior SRM are 140.7N and 250.0N, respectively, which are far less than the tolerant load that is allowed on the selected bearings. These are rated for 10.1kN based on the manufacturers' data sheet.

The torque waveforms are compared between the rotors with or without eccentricity, as shown in Figure 3.84. It can be observed from Figure 3.84 that the torque waveforms are almost matching with each other with or without rotor eccentricity. Therefore, even though the air gap variation due to the rotor eccentricity influences the rotor radial and tangential forces significantly, it is insignificant in terms of the torque output performance.

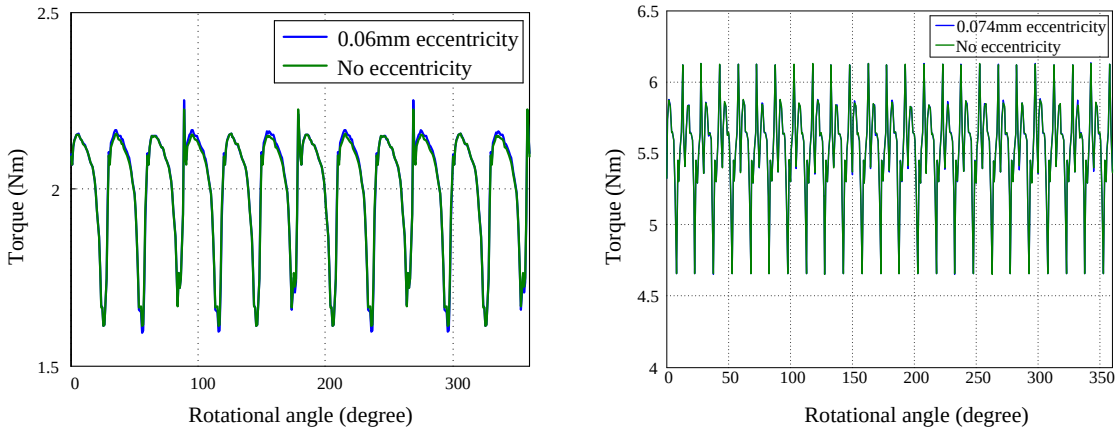

(a) Torque comparisons on the interior SRM

(b) Torque comparisons on the exterior SRM

Figure 3.84 Impacts of eccentricity on the torque performance

3.6.2 Air Gap Distance Analysis

Air gap distance is critical in SRM design, the smaller the gap distance, the smaller the air gap reluctance, and thus higher torque as well as higher power can be produced.

The effect of an increased air gap due to manufacturing tolerance has also been studied. Figure 3.85 compares the output torque for a 0.3mm air gap design and a 0.5mm air gap design. The results suggest that the increased air gap significantly reduces the average torque output due to the higher air gap reluctance. It also changes the shapes of the output torque waveforms and thus results in different torque ripples.

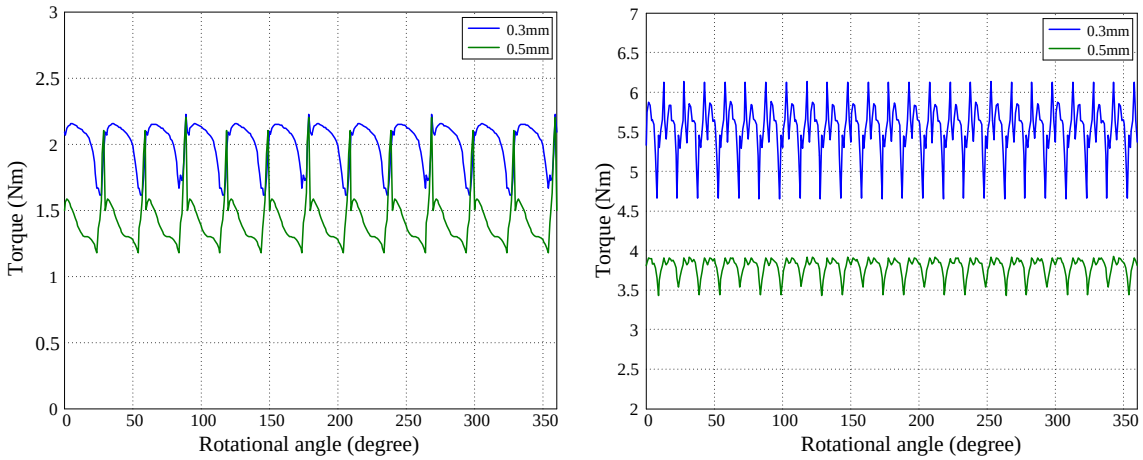

(a) Torque comparisons on the interior SRM (b) Torque comparisons on the exterior SRM

Figure 3.85 Impacts of the increased air gap length

3.6.3 Electromagnetic Analysis on Structure Components

Since the stator clamps are directly connected with the stator laminations, electromagnetic field interactions between the laminations and the stator clamps have been investigated via 3D simulation. Figure 3.86 shows the magnetic flux density concentrations on one of the stator clamps. It can be observed that very small flux density concentrates on the stator clamp. At full-load operation, the loss induced on the stator clamp is less than 5W, which is negligible. The clamps are not using good magnetic conducting material hence the electromagnetic field interference is small. Further, in manufacture, the stator clamp bolts are electrically insulated at either end of the machine to minimize any potential for induced circulating currents. Electromagnetic analysis has also been done on the mid-pole stands to verify that they do not interfere with the magnetic field. Figure 3.87 shows the low flux concentration on the mid-poles stands.

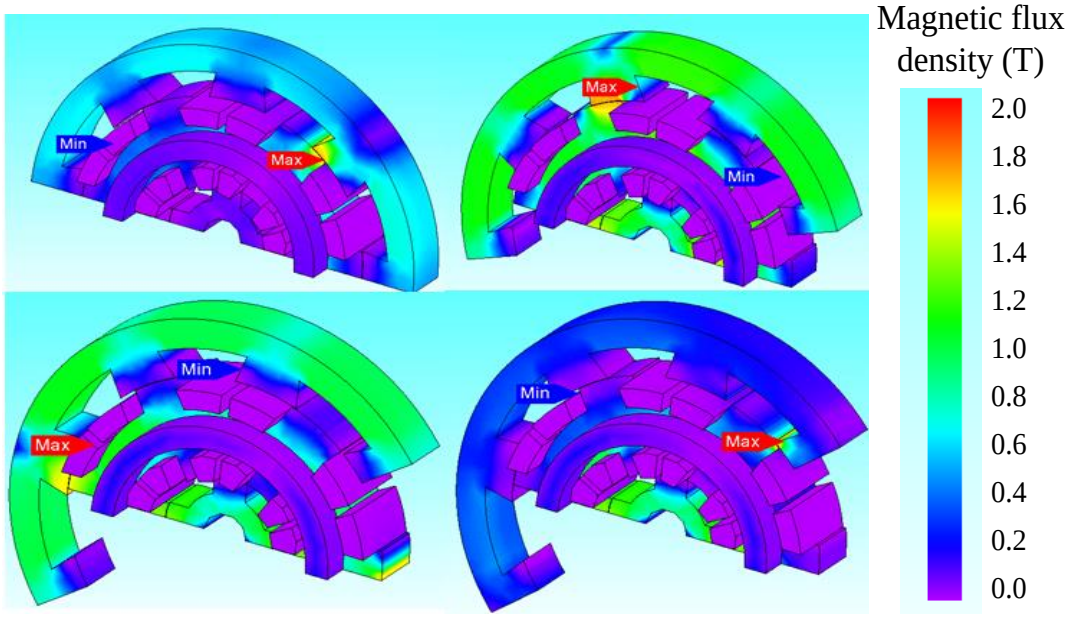

Figure 3.86 Electromagnetic study on the stator clamps

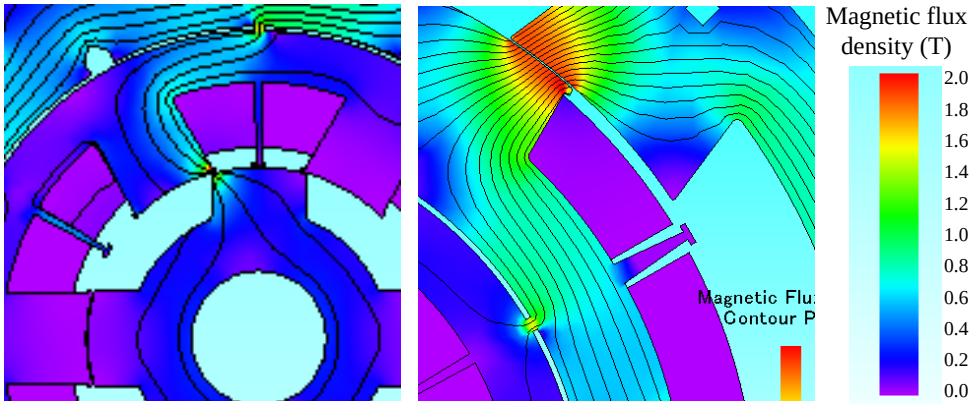

Figure 3.87 Electromagnetic study on the mid-pole stands

3.6.4 Torque Ripple Reduction Analysis for Synchronized Rotors

As presented in the previous sections, switched reluctance machines typically have torque drops during the phase excitation, which results in excitation torque ripple hence the resulting noise and vibrations during operation. It is necessary to reduce the torque ripple when designing switched reluctance machines as well as in the control process.

The double-rotor switched reluctance machine could provide a way to reduce torque ripples by synchronically coordinating the two rotors to work together. Instead of operating the two machines independently, the two rotors are now coupled together to operate with the same electric frequency, i.e. the torque waveforms produced by the two machines have the same frequency and thus a constant phase difference exists between the two torque waveforms, as shown in Figure 3.88. By way of example, for the prototype DRSRM, the exterior rotor has twice the pole number than that of the interior rotor. The interior rotor has hence to run at twice the speed as the exterior rotor to achieve the same

electrical frequency. By adjusting the relative positions of the two torque waveforms, the lowest torque of one machine can be displaced to match the highest torque of the other machine such that the two torque waveforms compensate each other and thus the overall torque ripples are reduced.

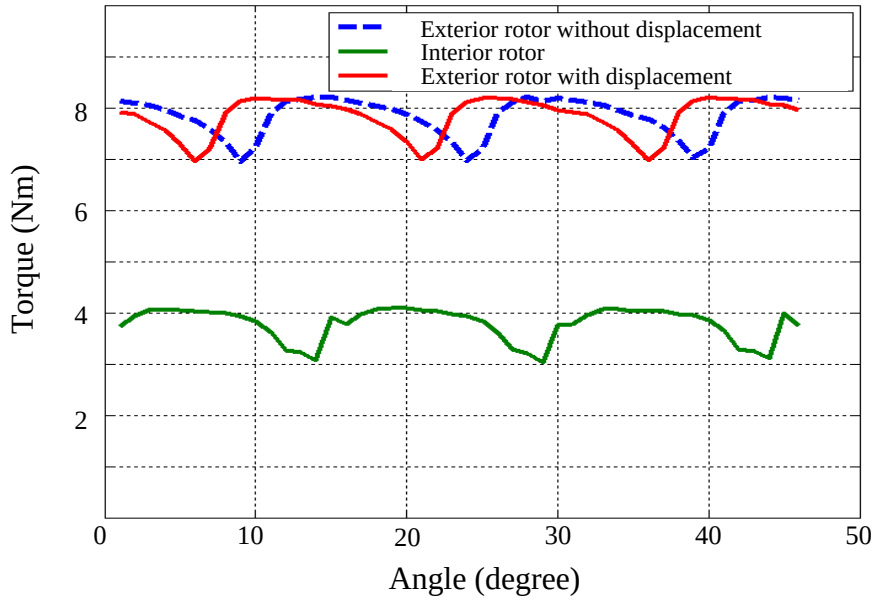

Figure 3.88 Rotor displacements to reduce overall torque ripples in DRSRM

It can be observed that by running the interior rotor twice the speed as the exterior rotor, the torque output waveforms of both the machines have the same electrical frequency. Changing one of the rotor initial positions, for instance changing the initial position of the exterior rotor as shown in Figure 3.88, the phase shift between the two torque waveforms can be adjusted. It is possible to adjust the phase shift to an angle such that the peak torque created by one rotor meets the minimum torque of the other machine. The two torque waveforms thus merge together and compensate or cancel the torque ripples of each other.

Two terms are created here for easier illustrations: (i) the in-phase rotor position and (ii) the out-of-phase rotor position. The in-phase rotor position means the torque waveforms of both the machines are at the same phase such that the peaks coincide with each other. The out-of-phase rotor position refers to the case when the peak torque of one machine is aligned with the minimum torque of the other machine. Figure 3.89 compares the in-phase rotor position torque waveforms (a) and the out-of-phase rotor position torque waveforms (b). Instantaneous torques of both machines as well as the total combined torques are presented in the figures.

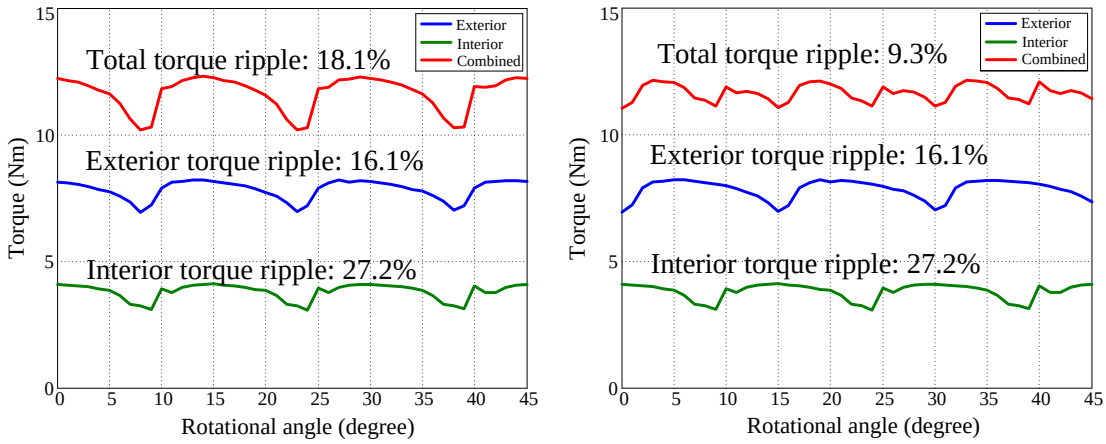

(a) Torques waveforms at the in-phase rotor position

(b) Torques waveforms at the conjugate phase rotor position

Figure 3.89 Torque comparisons between in-phase and out-of-phase rotor positions

The comparison illustrates that when the rotor positions are in phase, the peak torque of the exterior rotor is adding with the peak torque of the interior rotor while the minimum torques are also adding, thus contributing to a higher total torque ripple. On the other hand, when the rotors are at the out-of-phase positions, the minimum torque of the exterior rotor is compensated by the peak torque of the interior rotor while the minimum

torque of the interior rotor is compensated by the peak torque of the exterior rotor, thus contributing to a smaller total torque ripple.

It should be noted that different current excitation conditions in each machine will result in different torque waveforms, thus influencing the torque ripple reduction effects across the load and speed spectrum of the drive system. However, the displacement of the rotor positions in DRSRM could significantly compensate for torque ripple as long as the two torque waveforms have similar levels of torque output.

3.6.5 Winding Polarity Analysis

In switched reluctance machines, torque is produced as a function of the current square as shown in equation (3.8). The current direction in winding coils does not affect the operation modes of the machine. Thus, two types of the winding polarities exist in three phase, six stator pole machines, as shown in Figure 3.90. The two winding configurations are referred to as the NNN, in which all three phases have the same winding polarity, Figure 3.90 (a), and the NSN, in which the neighboring phases have the opposite winding direction, Figure 3.90 (b). Figure 3.91 compares the output torque waveform for the NNN winding and the NSN winding. It is observed that the NSN winding produces 2.03Nm average output torque while the NNN winding produces 2.00Nm output torque. The slight difference of the average torque comes from the flux pattern variation during the phase shifts in the back-iron region. When the neighboring winding polarity changes, two thirds of the stator back-irons are subjected to the opposite direction flux, and if the neighboring winding polarity keeps the same polarity, there are

only one third of the stator back-irons subjected to the opposite direction flux, as shown in Figures 3.92 and 3.93. For the NSN winding, since the neighboring windings all have the opposite polarity, there is always two thirds of the stator back-irons subjected to opposite flux during each of the phase shift. However for the NNN winding, this only happens once out of the three phase shifts.

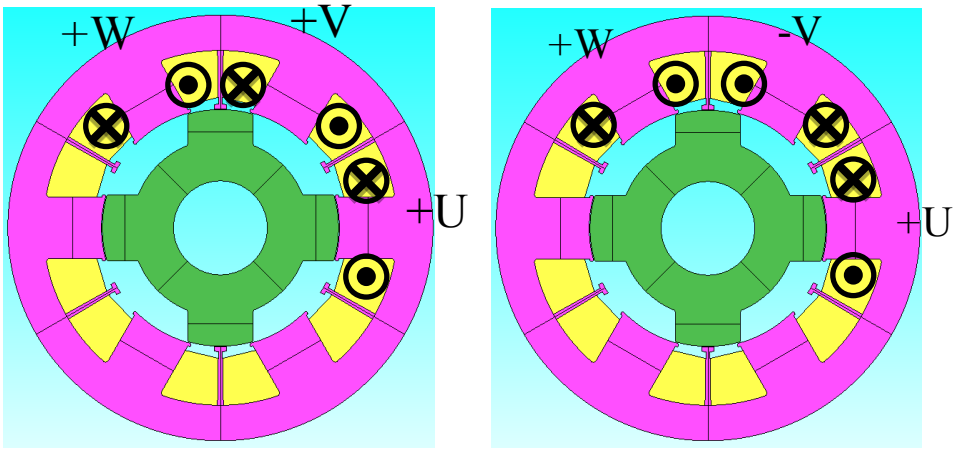

(a) NNN winding (b) NSN winding

Figure 3.90 Winding configurations

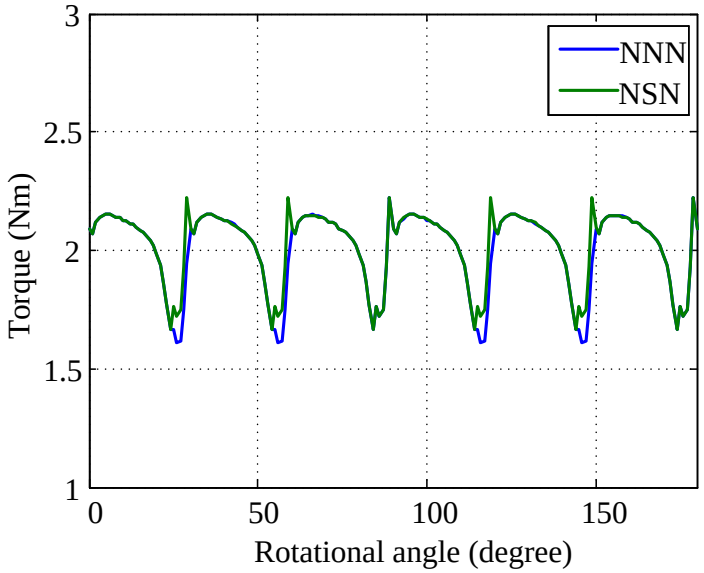

Figure 3.91 Torque waveform of NNN winding and NSN winding

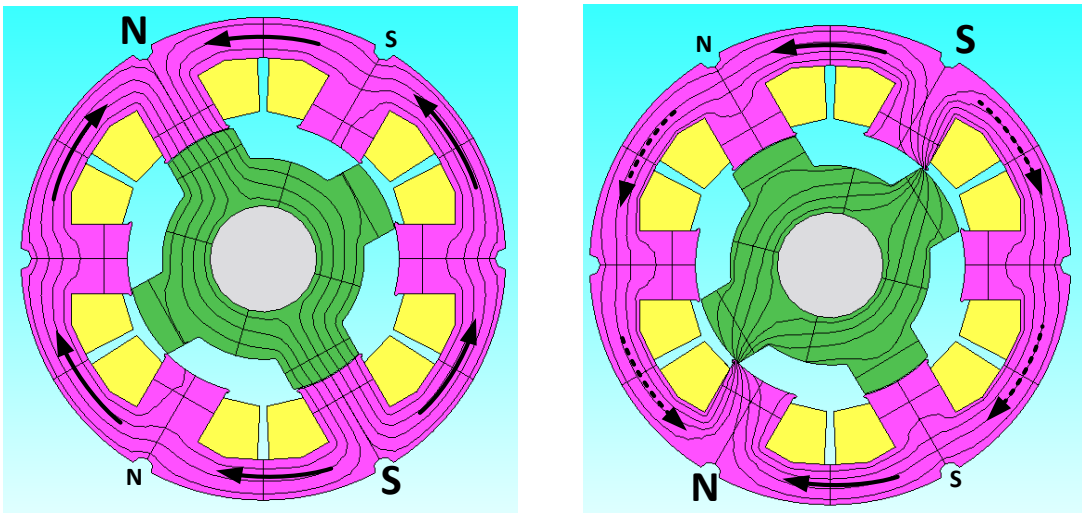

Figure 3.92 Flux pattern shifts due to opposite polarity windings

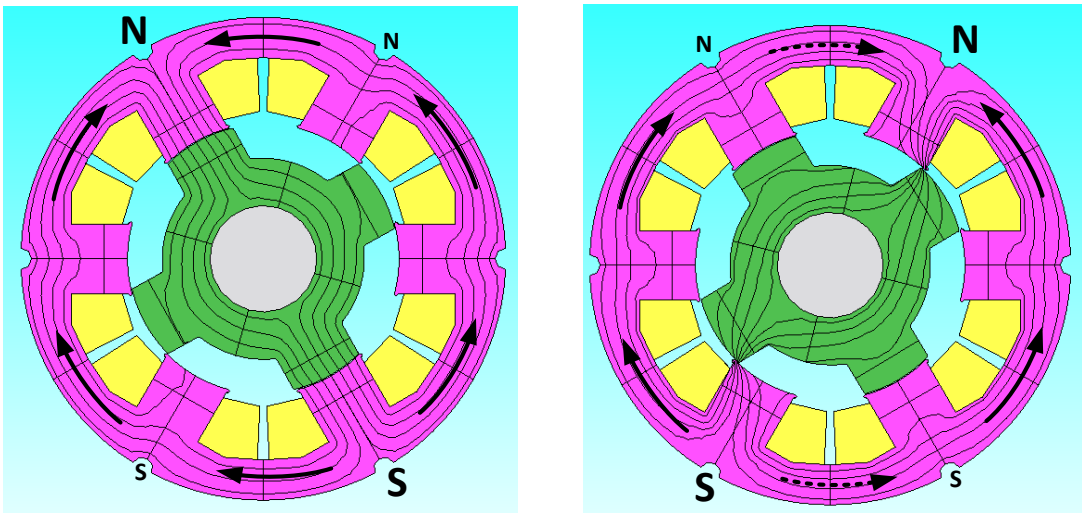

Figure 3.93 Flux pattern shifts due to the same polarity windings

For the rotor, the flux waveforms are different for the NNN and NSN topologies, as shown in Figure 3.94, where it can be seen that the NSN winding results in three times the flux frequency compared to the NNN winding in both the rotor back-iron and rotor pole. Even though the magnitude of each flux pulse remains the same, the polarity of each pulse changes with the change of the winding polarity. Therefore, the NSN winding

generates higher rotor core loss compared to the NNN winding due to the higher frequency of the changing flux. Table 3.17 compares the loss results for the interior SRM under rated current excitation, in which the NNN winding generates 229.6W iron loss while the NSN winding generates 256.9W iron loss in total.

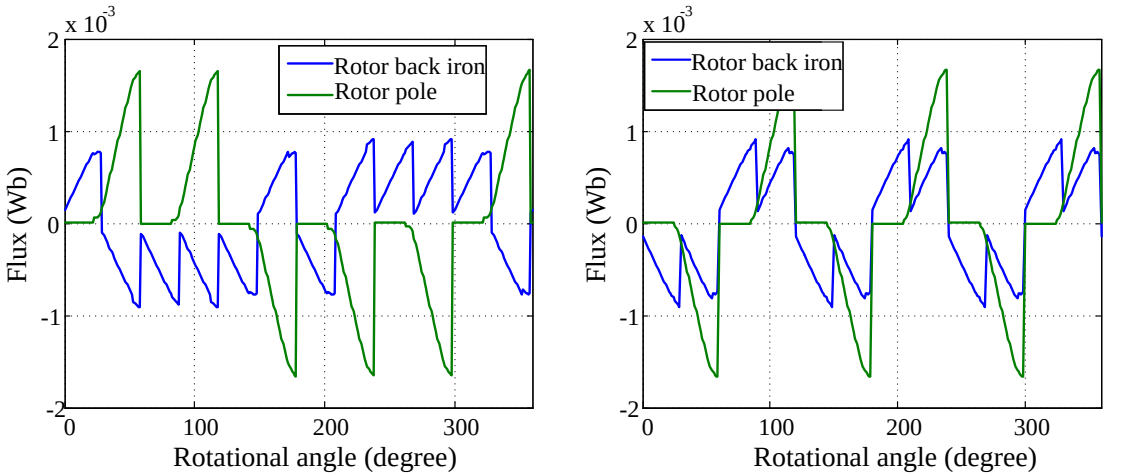

(a) Flux waveforms with NNN winding (b) Flux waveforms with NSN winding

Figure 3.94 Flux waveforms comparison between NNN and NSN windings

Table 3.17 Loss comparison for NNN winding and NSN winding

Current (A)	NNN	NSN
Rotor back-irons (W)	27.3	49.9
Rotor poles (W)	2.4	4.4
Stator back-irons (W)	174.4	176.6
Stator poles (W)	25.6	26.0
Total (W)	229.6	256.9

3.6.6 3D Simulation Verification

In addition to the 2D simulations used to study the electromagnetic properties of the DRSRM, 3D analysis was also carried out in order to confirm the results from 2D simulation. Figure 3.95 presents the 3D mesh for both the interior and exterior SRMs. Straight coils with extended length were applied to model the end winding effects. Figure 3.96 proves that the 3D results match well with the 2D results for both the flux-linkage and the output torque.

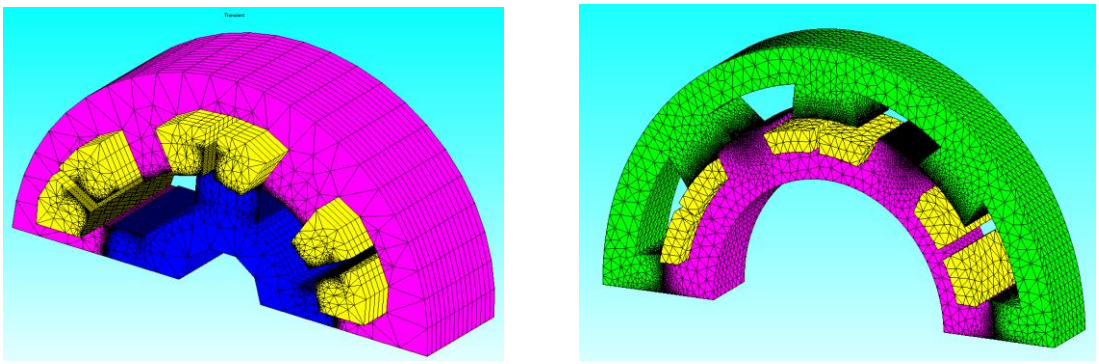

Figure 3.95 3D simulation meshes for the interior SRM and exterior SRM

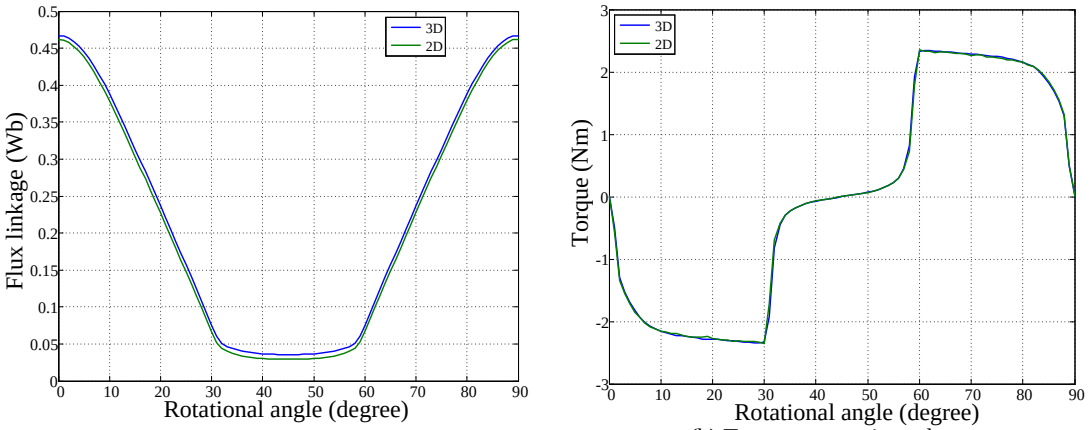

(a) Flux linkage comparisons between 2D and 3D simulations

(b) Torque comparisons between 2D and 3D simulations

Figure 3.96 Comparison 2D and 3D FEA simulations of flux-linkage and torque

3.7 SUMMARY

The design process of the proposed double-rotor switched reluctance machine was presented in detail in this Chapter. The fundamental theories and operation principles of switched reluctance machines were first introduced. Then a family of double-rotor switched reluctance machines (DRSRM) was presented with various configurations that are fully integrated and suitable for different applications. The detailed analytical design procedures of the prototype DRSRM were then fully reported and followed by a comprehensive simulation process, in which electromagnetic simulations, loss analysis, thermal analysis and SRM drive simulations were presented in sequence. The designed DRSRM was further optimized to improve performance and efficiency. Based on the optimized geometry, miscellaneous analyses were carried out to evaluate the machine performance. The effects of machine eccentricity and variation of air gap distances were studied and electromagnetic analyses on machine structure components were performed. One method of torque ripple reduction by coupling the two rotors together with the same electrical frequency was introduced and explained. Two variations of winding polarity were investigated and the effects on torque output and machine losses studied. Finally, 3D simulations were implemented to verify the 2D simulation results.

One outcome of the work presented in this Chapter is a pending patent regarding the proposed double-rotor switched reluctance machine, which was filed on October 24th, 2013 as the U.S. Patent Application 61/717,808.

Chapter 4

REALIZATION OF THE DOUBLE-ROTOR SWITCHED RELUCTANCE MACHINE

The design, simulation and optimization process of a double-rotor switched reluctance machine (DRSRM) has been reported in Chapter 3. In this chapter, a prototype DRSRM discussed in that Chapter is built to realize and prove the concepts. The machine mechanical design is discussed and structures developed in 3D CAD to facilitate the design manufacture. The machine manufacturing process is presented in this Chapter.

4.1 LAMINATION OF THE DRSRM

The DRSRM geometry in Chapter 3 finalized was drawn in 3D CAD, as shown in Figure 4.1 (a). The grooves on the exterior rotor are designed to leave space for TIG welding. The actual manufactured laminations are shown in Figure 4.1 (b). The laminations were manufactured by a laser cutting technique. Silicon steel M15 of 0.35mm thickness and insulating coats is used for all the laminations in which reduced iron losses can be achieved compared with M19 laminations. Two 0.3mm air gaps exist between the stator and the two rotors. Laminations are grouped and stacked together up to the designed stack length 50mm. Clamping devices were designed to maintain concentricity and to hold each stack firmly in place, as shown in Figure 4.2.

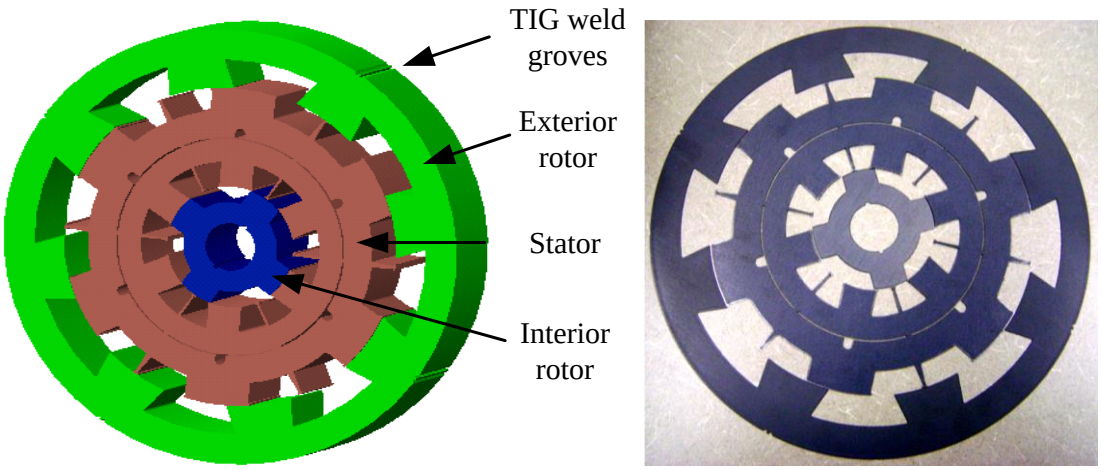

(a) 3D CAD lamination model of the DRSRM

(b) Manufactured Lamination of the DRSRM

Figure 4.1 Laminations of DRSRM

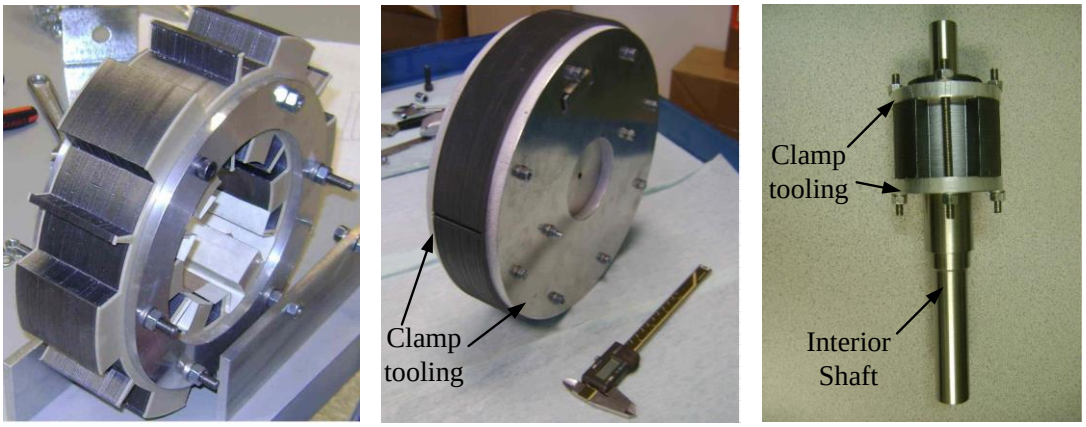

(a) Stator stack (b) Exterior rotor stack (c) Interior rotor stack

Figure 4.2 Lamination stacks of stator, exterior rotor and interior rotor

4.2 WINDINGS OF THE DRSRM

Windings were inserted into the slots on both the interior and exterior sides of the stator. Two sets of winding tooling were designed and manufactured. The tooling was slightly bigger than the interior and exterior stator teeth respectively so that the respective windings could be directly wound on the tooling and then dropped into the stator slots. Figure 4.3 shows the winding process in which four pairs of AWG24 wires were paralleled together to form one turn of each coil, prior to being wound onto the winding tooling. The winding tooling was prepared with Nomex insulation paper wrapped around the surfaces to protect the wires.

Before the windings were dropped into the stator slots, slot liners made of 0.25mm thick Aramid Nomex paper are applied to wrap the slots and insulate the windings from the steel lamination. Delmat insulation sheets cut into the same shape of the stator lamination are clamped on both axial ends of the stator so that to separate and insulate the windings and the lamination while serving as a layer of mechanical protection to prevent the edges of the laminations damaging the coil wires. In addition, slot wedges made of the spare Delmat sheets are inserted into the slots under the designed stator pole shoes and the inter-pole stands to contain and protect the windings. Figure 4.4 shows the winding on the interior stator with the insulations.

In order to study the behavior of the prototype machine, different instrumentation and sensors were inserted into the machine. Search coils were inserted to measure the flux-linkage on both the stator teeth and the inter-polar stands, and thus to verify

minimum flux-leakage on the inter-polar stands. Five 5kΩ, NTR, bead thermistors were placed at different locations of the machine to serve as temperature sensors. Figure 4.5 illustrates the instrumentation wires and Table 4.1 lists the locations of the search coils and temperature sensors. After all the windings were wound and instrumentation wires inserted, the end windings at both the termination-end and the non-termination-end were pressed and taped firmly to minimize end-winding overhangs, as shown in Figure 4.6. Class H glass tape was used to meet the high temperature requirement.

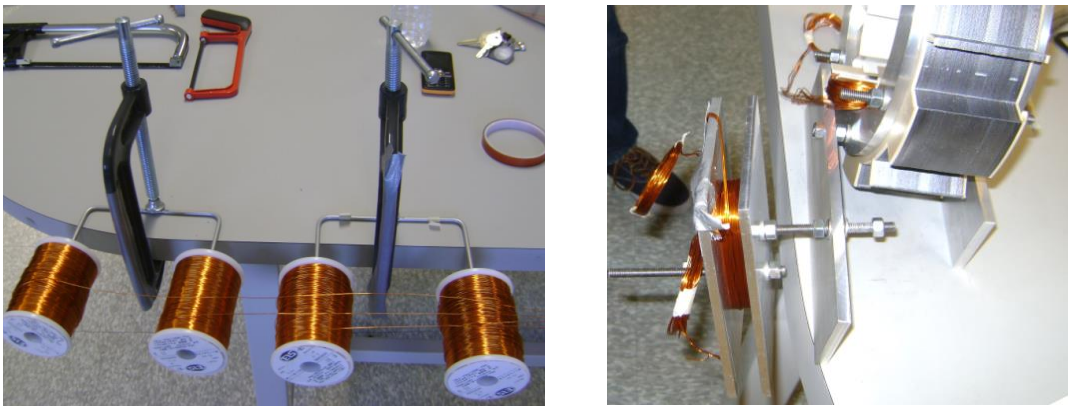

(a) 4 sets of parallel wires (b) Winding tooling

Figurer 4.3 Winding process and the winding tooling

Table 4.1 Instrumenting sensors locations

Sensor Number	Sensor Locations	Function
1	Stator pole	Search coil
2	Stator inter-polar stands	Search coil
3	Back iron	Temperature
4	Termination coil	Temperature
5	Non-termination coil	Temperature
6	Middle coil	Temperature
7	Stator pole	Temperature

A similar process was applied to the exterior stator windings. Nomex insulation slot liners were laid in the exterior side of the stator slots to wrap and insulate the exterior winding coils. Wedges are also inserted under the stator exterior pole shoes and the corresponding inter-pole stands to secure the exterior windings. Figure 4.7 shows the stator with the windings for both the interior machine and the exterior machine. The end-windings were all insulated with glass tapes and firmly bonded by lacing ties.

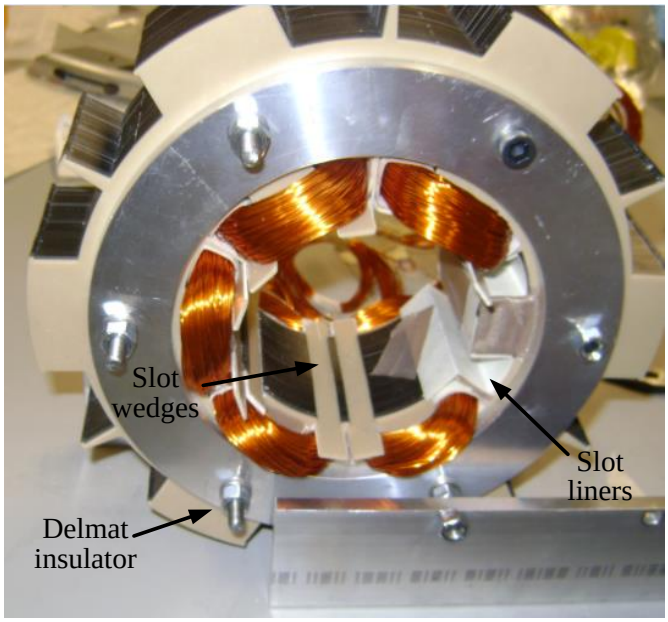

Figure 4.4 Insulations for the winding process

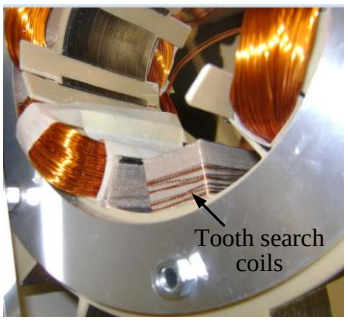

(a) Tooth search coils

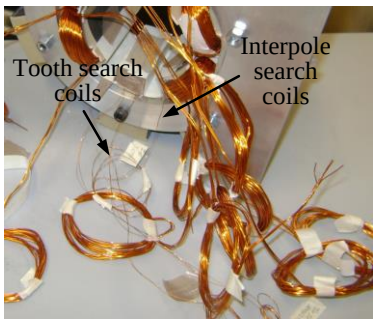

(b) Search coils

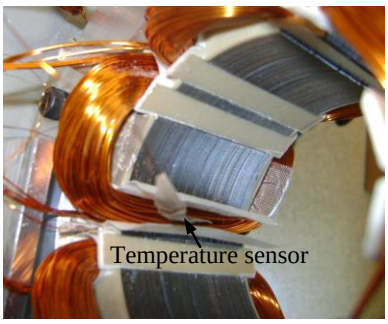

(c) Temperature sensor

Figure 4.5 Instrumenting of search coils and temperature sensors

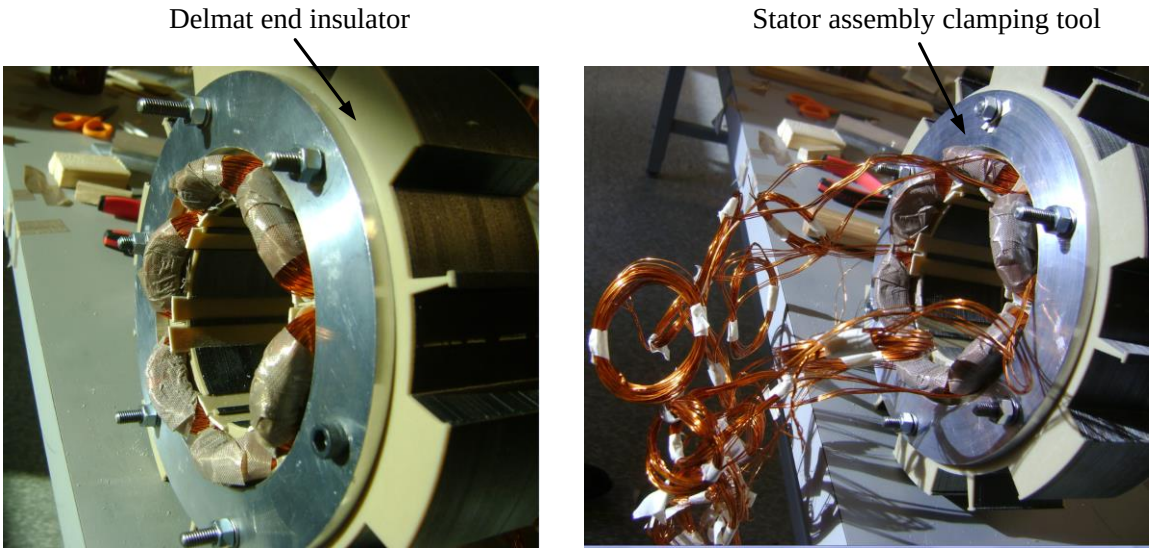

(a) Coil non-termination end windings (b) Coil termination end windings

Figure 4.6 End windings insulated with glass tapes

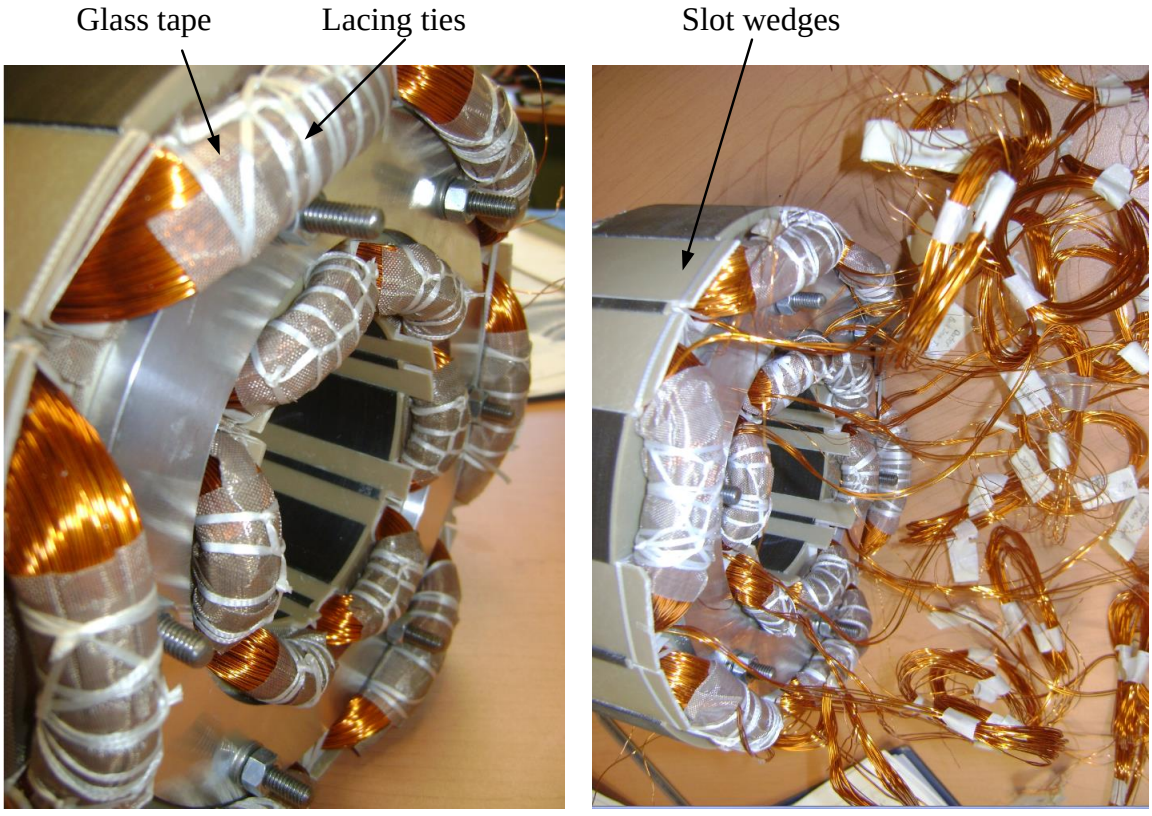

(a) Non-termination end windings (b) Termination end windings

Figure 4.7 End windings with lacing ties

4.3 ALIGNMENTS AND INSULATIONS OF THE DRSRM

The alignment of the double-rotor switched reluctance machine components is critical for correct electromagnetic performance and mechanical operation since both the air gaps are designed to be only 0.3mm. Variations of the lamination due to manufacturing tolerance and assembly tolerance may cause lamination misalignment along the radial direction of the machine air gap. This may cause torque output fluctuation or mechanical problems such as eccentricity and insufficient air gap tolerance. Therefore, alignment tooling was designed to guarantee the radial alignment of the stator laminations and the exterior rotor laminations.

Figure 4.8 illustrates the alignment tooling for the exterior rotor. The exterior rotor laminations were aligned on a cylinder that had reference center points. The cylinder was machined to have the same outer diameter as the exterior rotor inner diameter. All laminations were firmly clamped by the two side clamps and eight bolts. A locating key was inserted between two neighboring stator teeth to align the laminations axially. Figure 4.9 illustrates the alignment tooling for the stator.

Before assembly of the laminations, all surfaces of the alignment tooling were sprayed with PTFE mould-release dry film as shown in Figure 4.10 in order to facilitate easier disassembly after the vacuum pressure impregnation process as will be discussed in the next section.

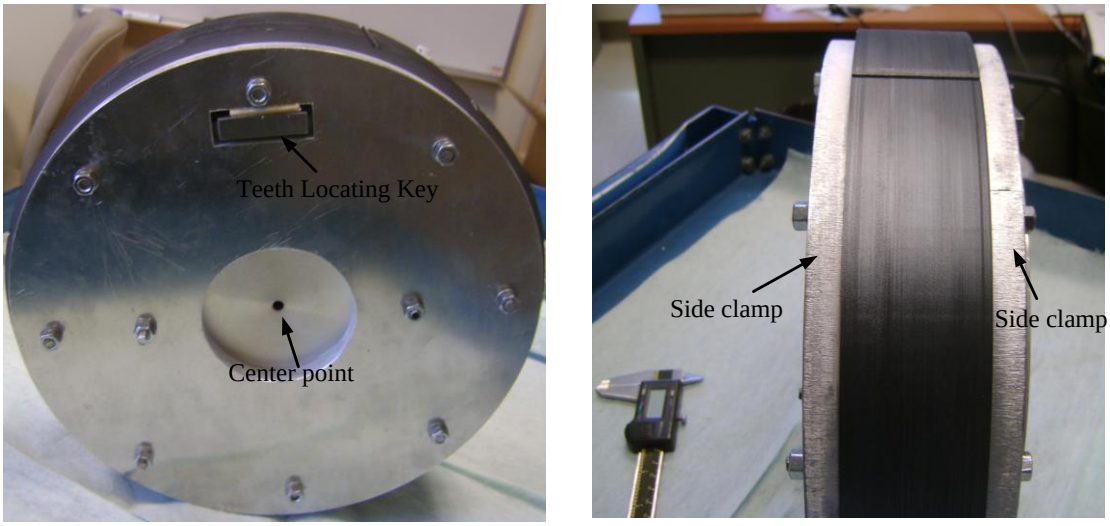

Figure 4.8 Exterior rotor alignment tooling

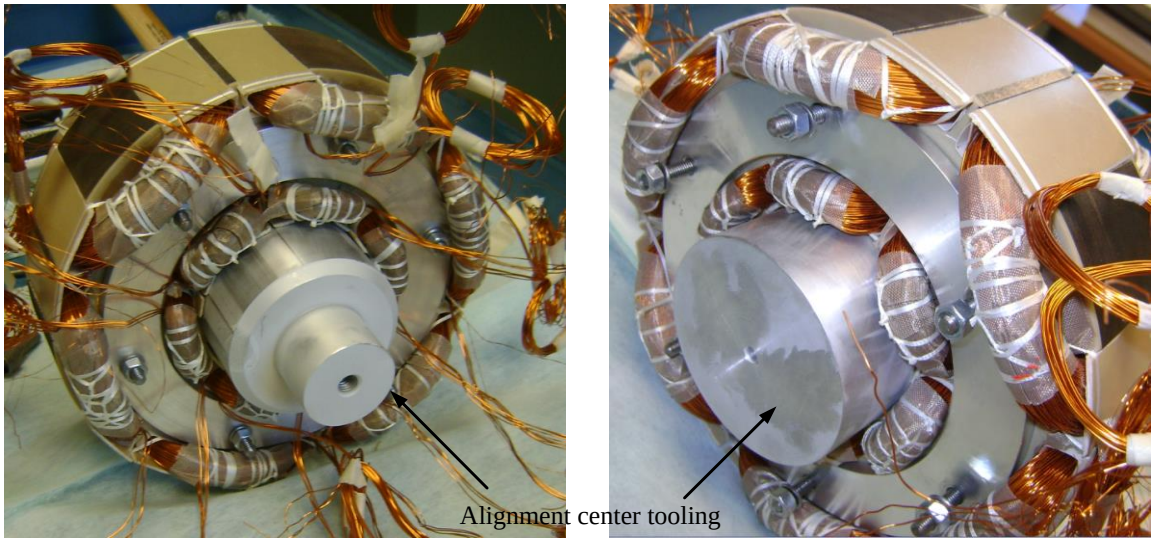

Figure 4.9 Stator rotor alignment tooling

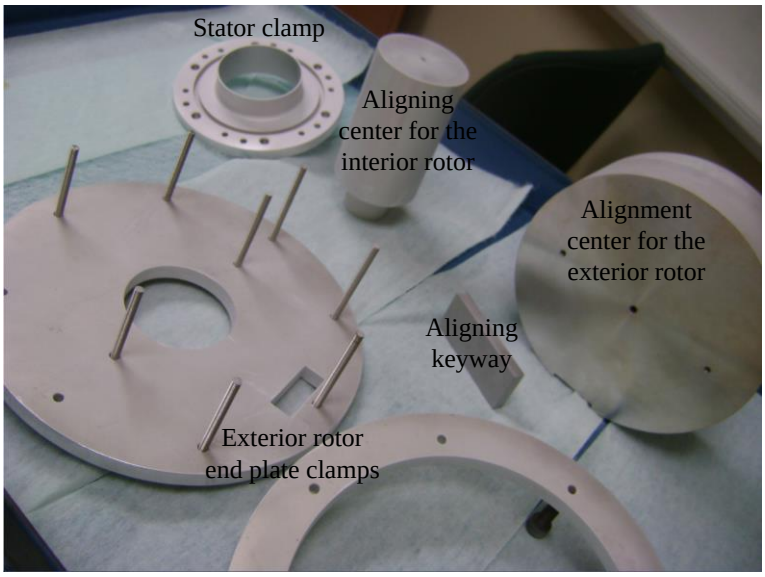

Figure 4.10 PTFE mould-release dry film processing for the alignment tooling

The winding clamp rings were then replaced by the stator clamps as shown in Figure 4.11. The stator clamps were insulated by surrounding with Nomec paper while all the inserted threaded bars were wrapped and insulated as well. In addition, both ends of the treaded bars were electrically insulated with Delmat washers to prevent axial eddy currents flow. The threaded bars and laminations are shown in Figure 4.12 (b). The additional holes in the stator clamps were designed to allow resin into the assembly during the vacuum pressure impregnation process so that the gaps of the stator laminations and the windings would filled and be impregnated by the resin. A Megger insulation tester was used to test the insulation between each of the windings and laminations, threaded bars and laminations, stator housing and laminations, etc. All insulation results were achieved at a test voltage of 500V. Figure 4.13 shows the partial stator assembly with the alignment tooling and the stator clamps, prior to vacuum pressure impregnation (VPI).

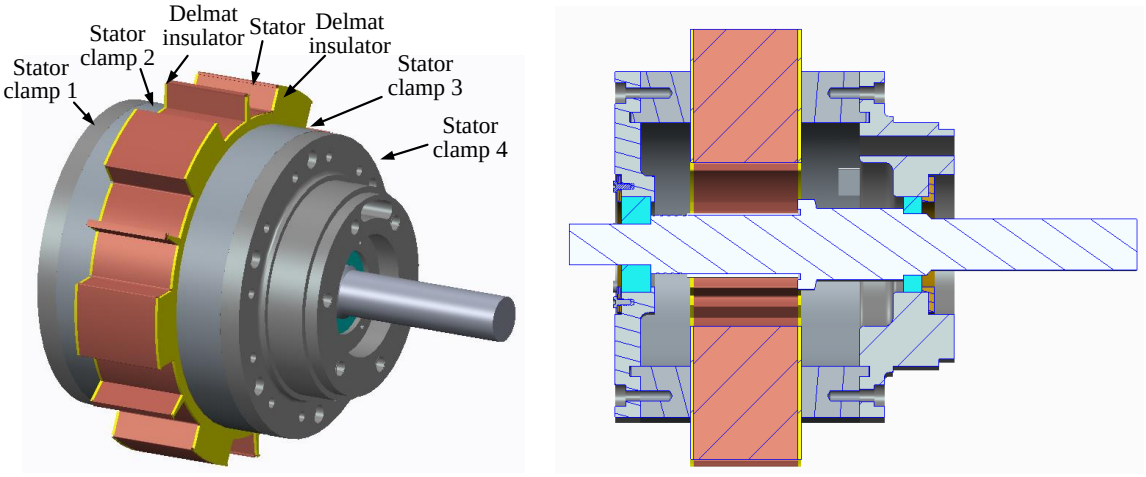

Figure 4.11 Stator laminations with stator clamps

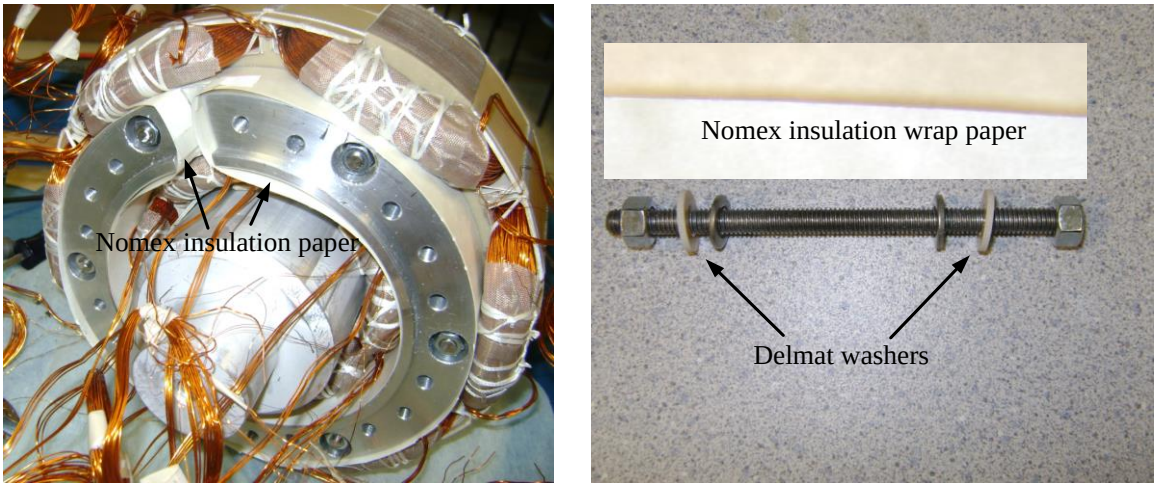

(a) Stator clamps with Nomex insulation paper

(b) Insulation on the threaded bar

Figure 4.12 Insulation procedures on the stator

Referring to Figure 4.13 (a) and (c), the exterior stator windings were grouped together at the side of the stator clamp and then fed through a side hole in the stator mount. The leads of both the exterior windings and the interior windings then came out of the front face of the stator clamp. The stator end clamp was designed to stand against the stator laminations when fully assembled so that the laminations would not be bent or

distorted when the center tooling was pressed out after the vacuum pressure impregnation process, as shown in Figure 4.13 (d).

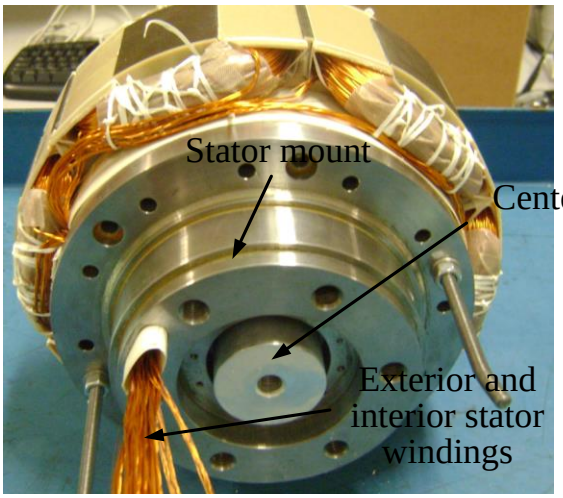

(a) Front view of stator assembly with center pot

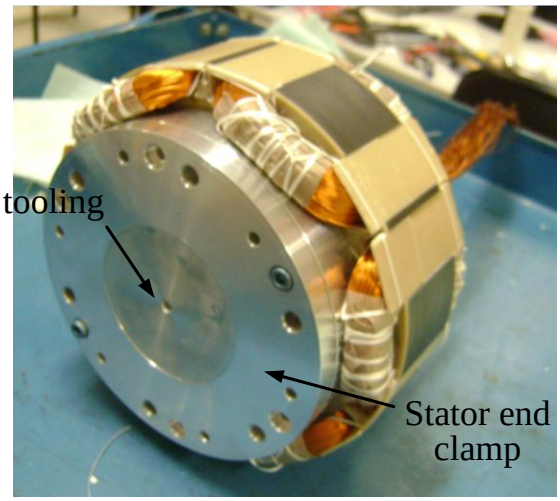

(b) Rear view of stator assembly with center pot

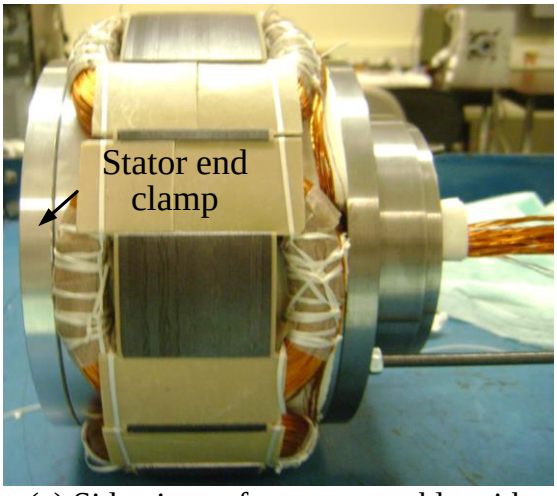

(c) Side view of stator assembly with center pot

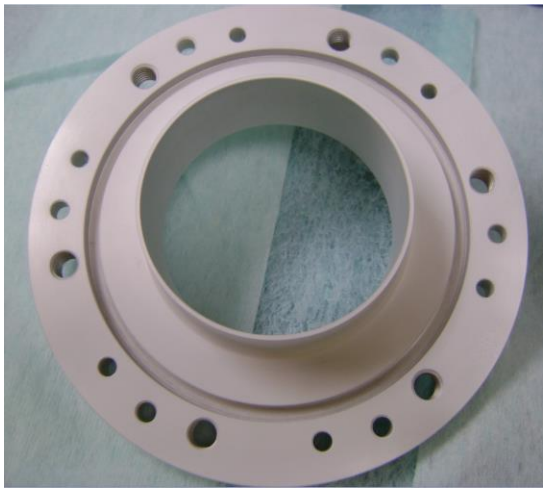

(d) Stator end clamp with mould-release film

Figure 4.13 Stator clamps and the alignment tooling prior to VPI treatment

4.4 VACUUM PRESSURE IMPREGNATION OF THE DRSRM

Vacuum pressure impregnation (VPI) is a process in which the electric machine parts are immersed in resin in a chamber. The chamber is then evacuated under vacuum such that resin is forced into any gaps, slots, between coil turns and voids. The vacuum pressure removes air and moisture trapped in between the windings and laminations and then fills them with resin. Both windings and laminations are solidified and protected by resin after the VPI process. The mechanical bond of the windings and the laminations are improved while the insulation properties and electric characteristics of windings to sustain high voltages are enhanced. In addition, the resin also helps with higher thermal conductivity so that heat dissipation is improved and hence the life of windings can be extended[87].

Figure 4.14 shows the machine partial assemblies of the stator, exterior rotor, and interior rotor respectively before the VPI process. The exterior rotor laminations were welded together after partial assembly. The machine parts were then sent to the VPI process and then oven baked for 4 hours at 150℃ to solidify the resin. Both the center tooling in the stator assembly and the exterior rotor assembly were then pressed out and the outer diameter of the exterior rotor laminations was slightly machined to smooth tolerance surfaces. Figure 4.15 shows the machining process and the pressing process on the exterior rotor.

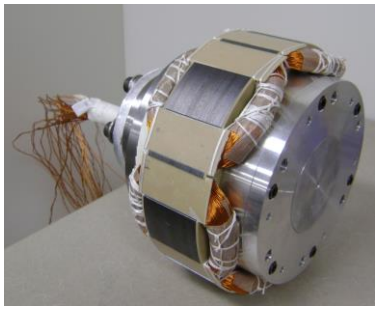
(a) Stator assembly

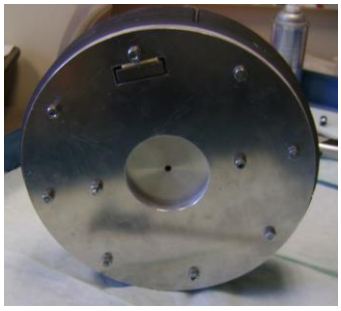
(b) Exterior rotor assembly


(c) Interior rotor assembly

Figure 4.14 Machine partial assemblies before VPI

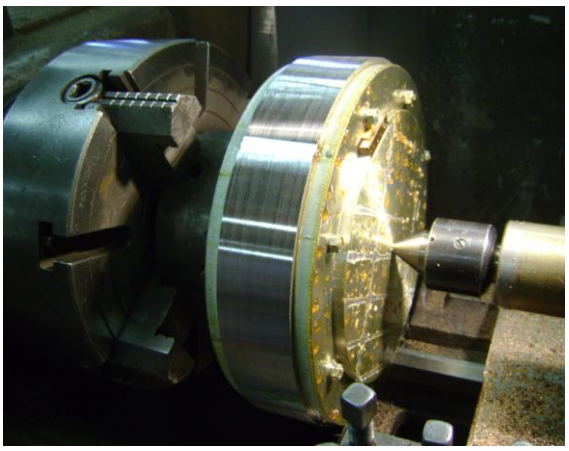
(a) Machining of the OD of the exterior rotor

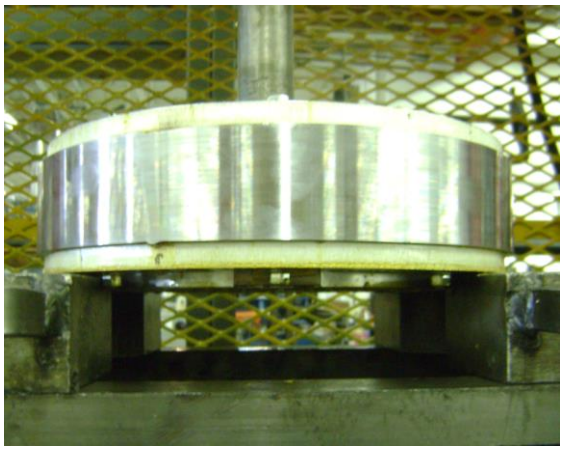
(b) Machine pressing out the center pot

Figure 4.15 Pressing and machining of the exterior rotor

Figure 4.16 shows the stator after the VPI process covered with resin and varnish. It can be observed that both windings and laminations were well covered and a thick layer of solid resin enclosed the interior windings to improve the thermal conductivity. All the mechanical parts were cleaned and degreased by using heavy-duty paint remover, sand papers and emery cloth. Figure 4.17 shows the cleaned interior rotor (a) and exterior rotor lamination stack (b). The burrs on the outer edge of exterior rotor caused by welding were also removed by filing and sanding to smooth the side surface of the laminations.

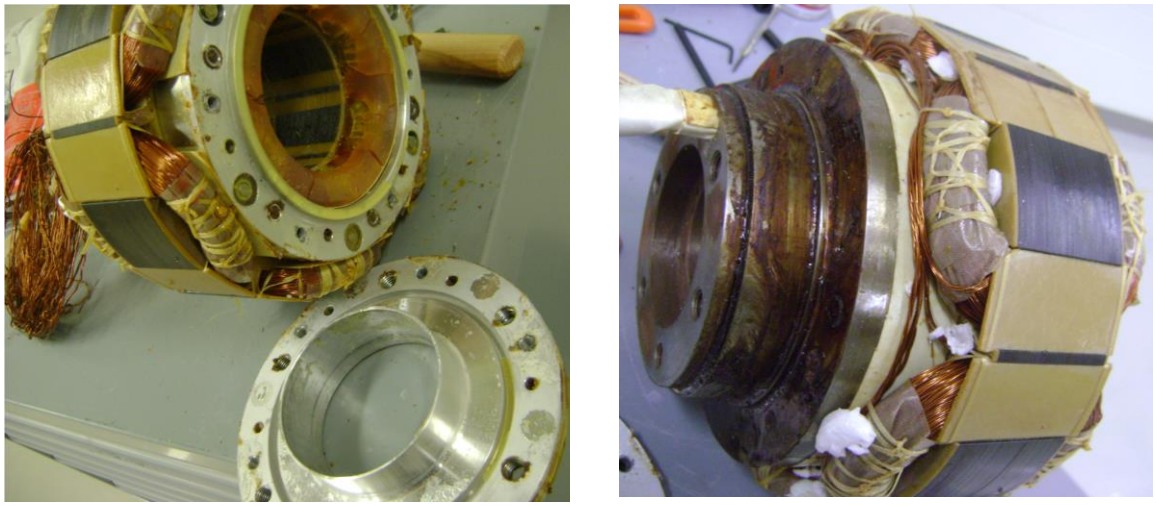

Figure 4.16 Stator covered with resin and varnish after VPI treatment

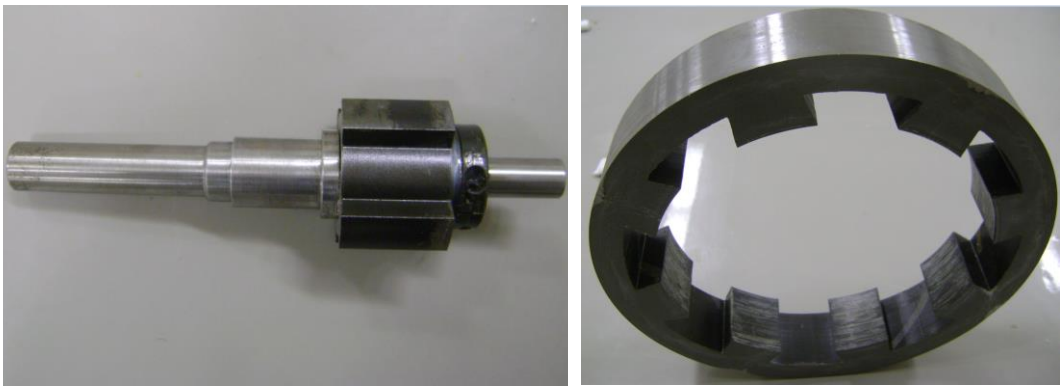

(a) Interior rotor after cleaning (b) Exterior rotor lamination stack after cleaning

Figure 4.17 Interior rotor and exterior rotor assemblies after VPI and cleaning

4.5 ASSEMBLIES OF THE DRSRM

Partial assemblies were first carried out by grouping the parts into the stator assembly, interior rotor assembly, and the exterior rotor assembly. The interior rotor is supported by a steel shaft, as shown in Figure 4.18. One end of the shaft is cut with thread and a washer and a shaft collar clamp used to tighten the interior rotor laminations on the shaft. The exterior rotor was designed with 0.3mm air gap distance sitting outside the stator. The exterior rotor laminations were pressed and clamped into the rotor outer case via heat shrink technique, and the outer case was supported by two end clamps. Figure 4.19 shows the exterior rotor assembly and Figure 4.20 shows the heat shrink process. The stator assembly was completed in the VPI process as discussed in the previous session.

The three individual assemblies were assembled together, the stator assembly was assembled on the interior rotor assembly by using two stator bearings to support the stator clamps. Bearing clamps were used to prevent the bearings moving axially. The exterior rotor assembly was then assembled on the stator assembly by another two bearings: one sitting on the interior shaft and the other sitting on the stator clamp. Figure 4.21 shows the assembled components (a) as well as the cross section view of the assembly (b).

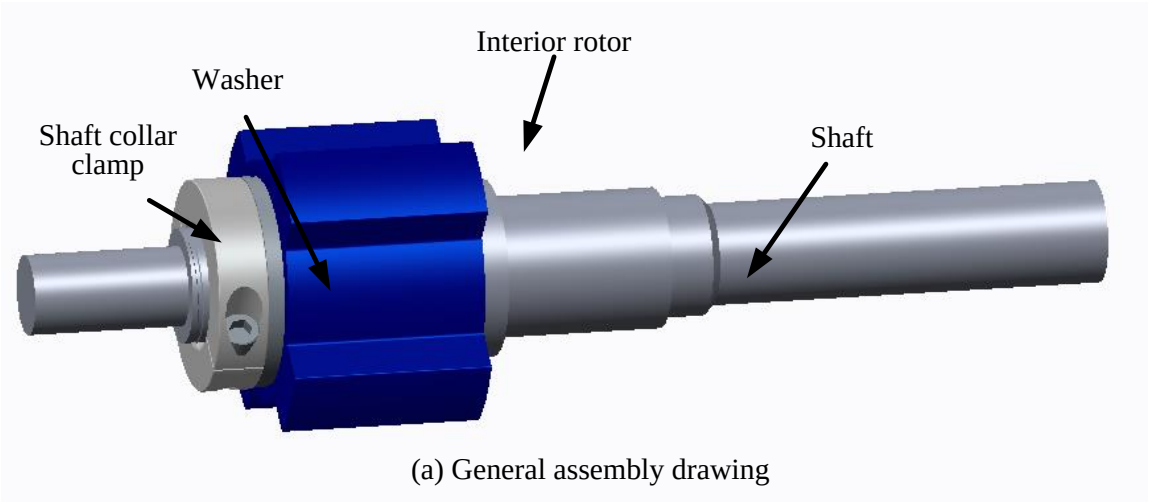

(a) General assembly drawing

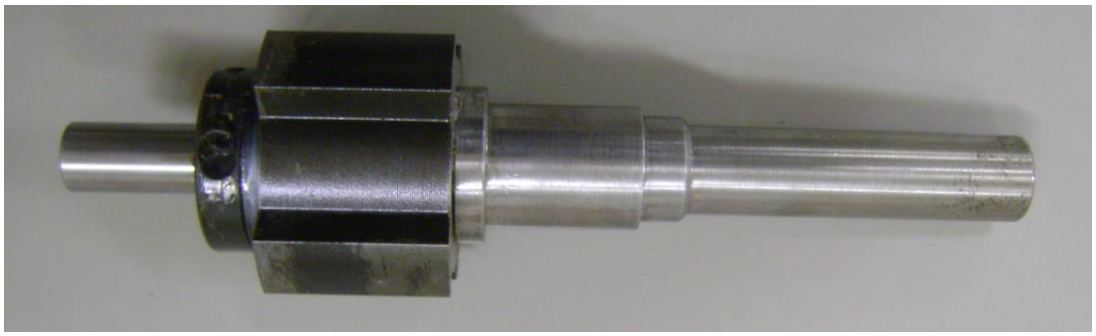

(b) Actual parts

Figure 4.18 Interior rotor assembly

It can be observed in Figure 4.21 that two shafts were used to connect with each of the rotors while four bearings were used to support and separate the stator, the interior rotor, and the exterior rotor. The exterior shaft was supported by a bracket connected by a bearing. Another bracket was applied on the right side of the machine to support the stator clamp. Two absolute encoders were mounted on each output shaft to measure the interior and exterior rotor positions, as shown in Figure 4.22, showing the final assembled DRSRM. The encoder output signals are supplied directly to the microprocessor, controlling the drive power electronics. Figure 4.23 shows the exploded view of the

DRSRM components, while Figure 4.24 and Table 4.2 list the bill of materials for the whole assembly.

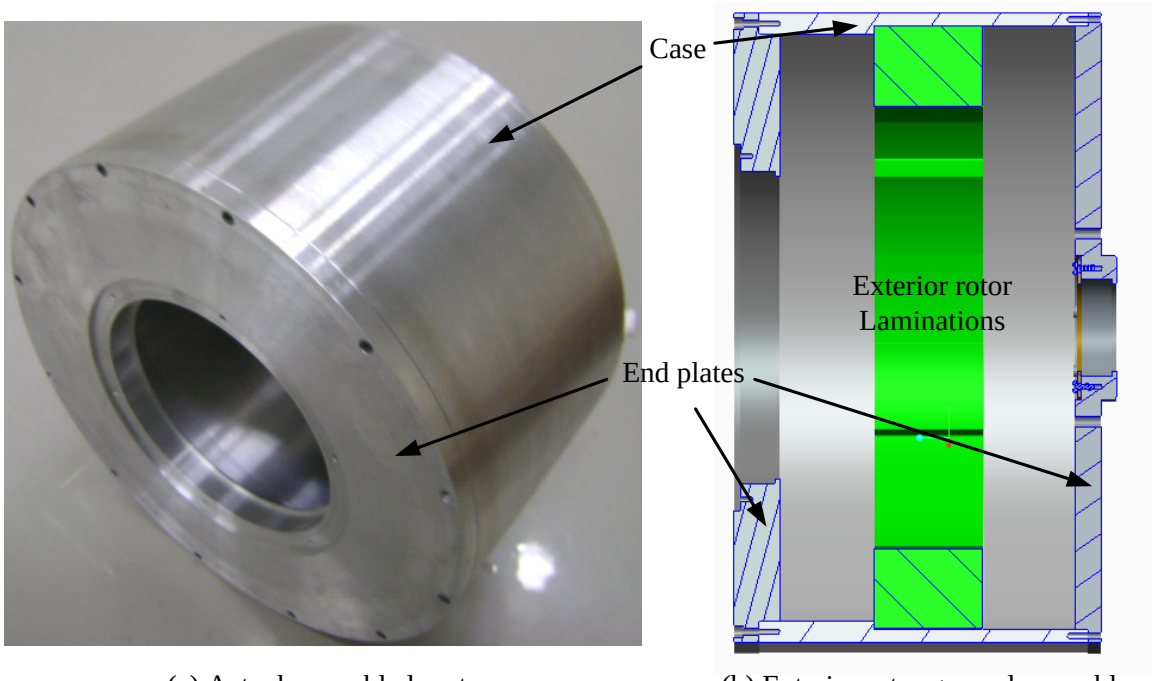

(a) Actual assembled parts (b) Exterior rotor general assembly

Figure 4.19 Exterior rotor assembly

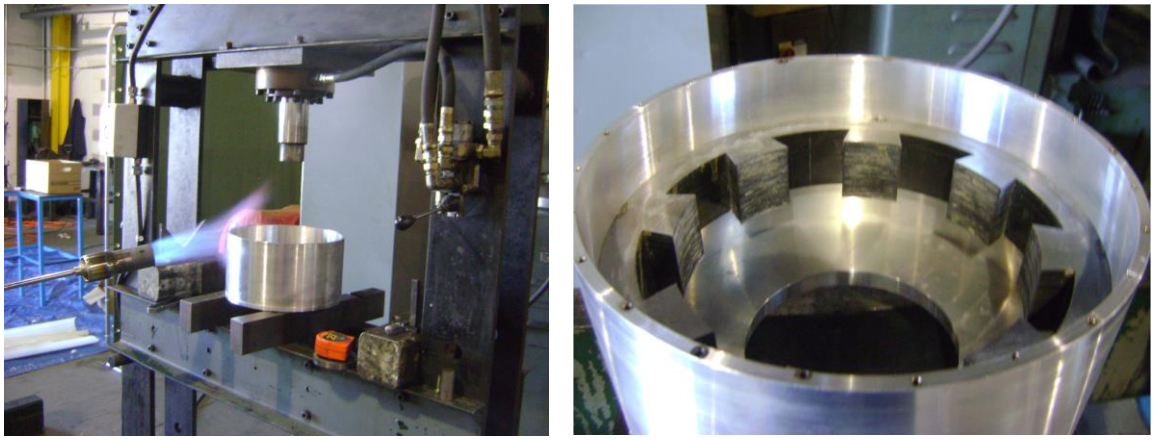

(a) Heating the outer case (b) Heat shrink of the exterior rotor laminations

Figure 4.20 Heat shrink process of the exterior rotor laminations

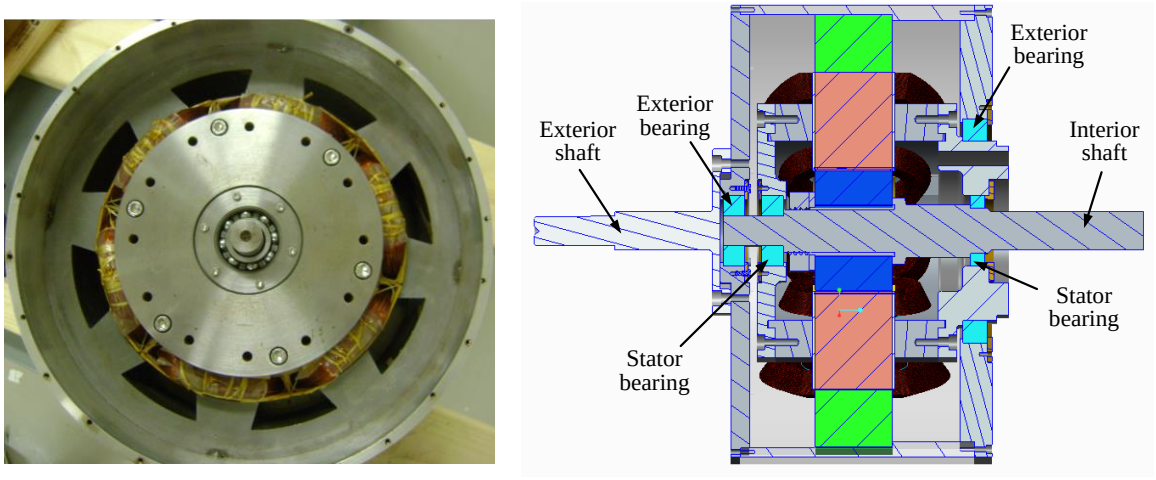

(a) Assembled components (b) Cross section view of assembly

Figure 4.21 Assembly of the DRSRM

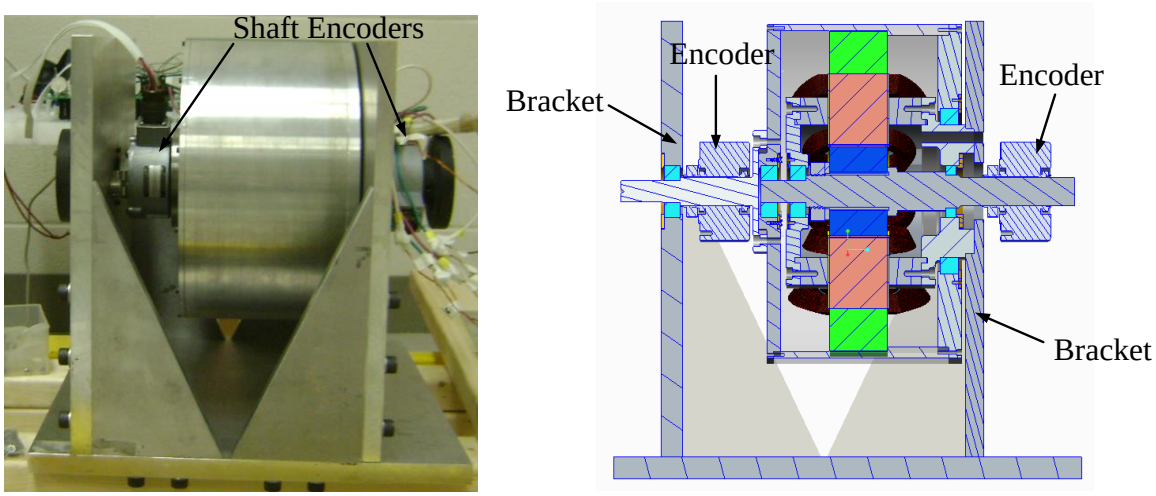

(a) Assembled machine (b) Cross-sectional drawing

Figure 4.22 Final assembled DRSRM machine and mountings

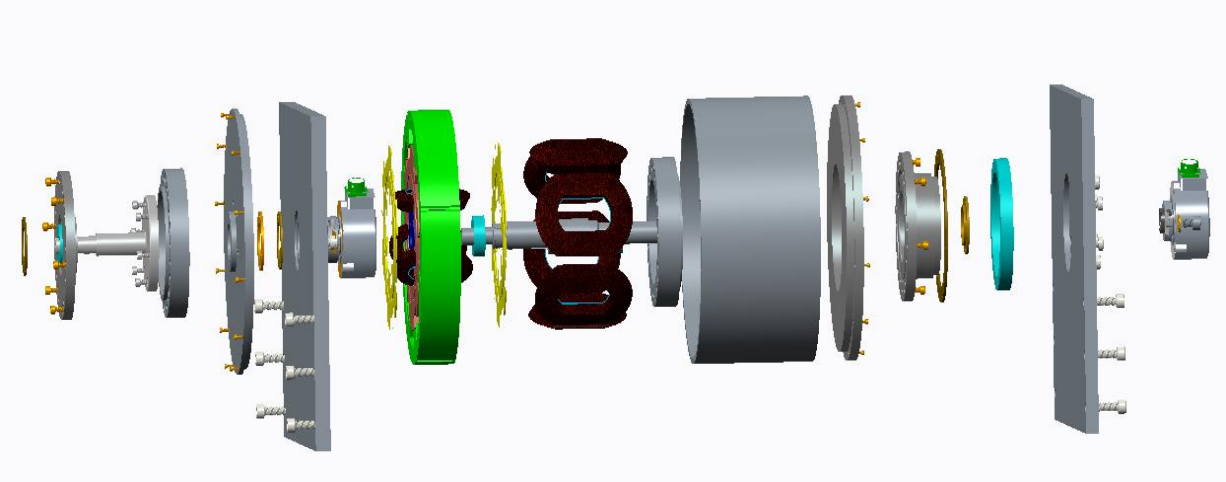

Figure 4.23 Exploded view of the DRSRM

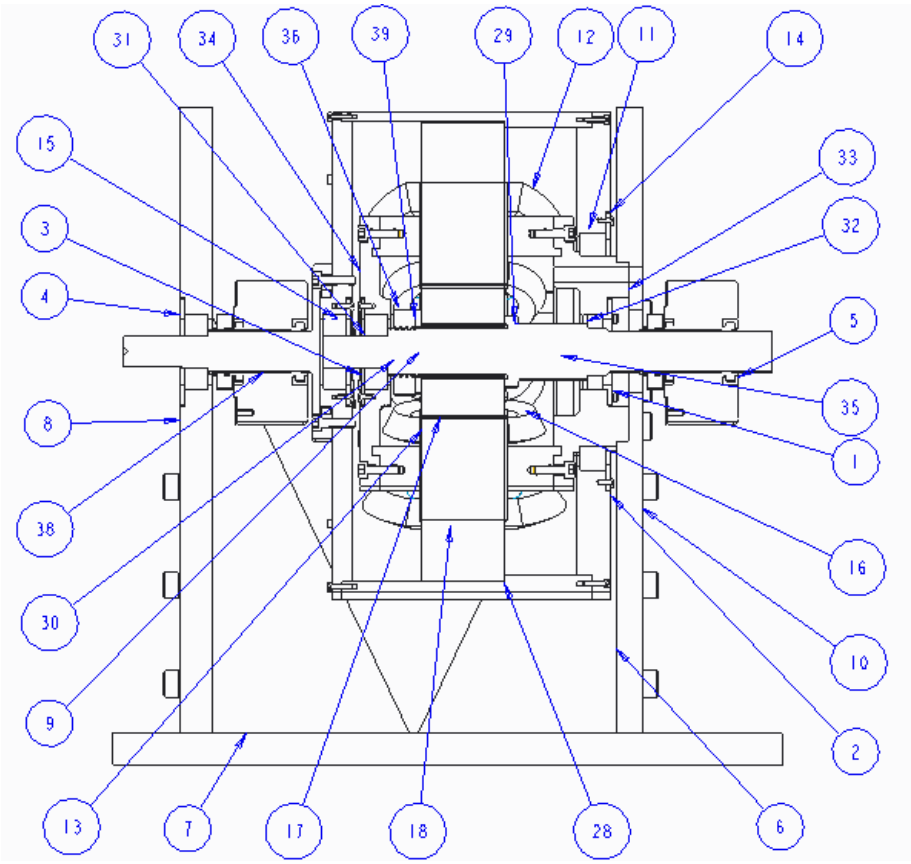

Figure 4.24 Numbering of the assembly parts for reference to Table 4.2

Table 4.2 DRSRM assembly parts

Number	Name	Quantity	Number	Name	Quantity
1	Bearing clamp_1	1	16	Interior coils	6
2	Bearing clamp_2	1	17	Interior rotor	1
3	Bearing clamp_3	1	18	Stator	1
4	Bearing clamp_4	1	28	Rotor housing	1
5	Absolute encoder	2	29	Interior shaft	1
6	Bracket	2	30	Shaft collar	1
7	Bottom plate	1	31	Stator bearing 1	3
8	End plate left	1	32	Stator bearing 2	1
9	Delmat cover	2	33	Stator mount 1	1
10	End plate right	1	34	Stator mount 2	1
11	Exterior bearing_1	1	35	Stator mount 3	1
12	Exterior coils	6	36	Stator mount 4	1
13	Exterior rotor	1	38	Exterior shaft	1
14	Exterior clamp right	1	39	Washer	1
15	Exterior clamp left	1			

4.6 SUMMARY

In this Chapter, the realization of the proposed double-rotor switched reluctance machine has been presented in detail. The build of the laminations and machine windings were discussed in Section 4.1 and 4.2, then the process of alignment and vacuum pressure impregnation were explained in Section 4.3 and 4.4. The assembly steps of the DRSRM were presented in Section 4.5. Finally, 3D CAD modeling was used during the design and build stage and the final drawings thereof used to illustrate the assemble steps for the DRSRM prototype.

Chapter 5

DRSRM VALIDATION

To validate the proposed double-rotor switched reluctance machine, a test rig was designed and built. Since the DRSRM has two rotor outputs, two load machines were required to connect to each of the rotor shafts and thus apply loads individually. The interior and exterior SRM components were initially tested independently to verify the respective simulation results. The two machines were then tested together by running the two rotors simultaneously, and results compared to design and simulation to evaluate final performance.

5.1 Winding Polarity Identification

Before the VPI process, all the masking tapes on the windings that had phase polarity information were removed to prevent the tapes from being dissolved in the resin tank and clogging the vacuum chamber. Further, when the windings were enclosed in the rotor case, the termination leads were mixed together again. Hence, it was prudent to carry out experiments to check winding polarities. Since both the interior and exterior machines have six poles with concentrated windings and each pole has two terminal leads, there are 12 terminal leads associated with the interior windings and another 12 terminal leads associated with the exterior windings. It was easy to find out which two terminal leads were connected by using multimeter and thus belong to the same winding

on one pole. Once all the terminal pairs were found, a DC current was injected into each of the terminal pairs to distinguish if the excited winding belonged to the interior SRM or the exterior SRM. The associated stator pole under the excited winding would try to pull the nearest rotor pole to the aligned position due to the tendency of the reluctance torque to minimize reluctance. Since the flux paths of the machines were isolated by the designed air flux barrier, there was only one shaft rotating, indicating which machine the terminal pair belonged to.

The next step was to find out the windings on the opposite stator poles. By exciting one pair of the winding terminals with an AC voltage input at the aligned position, the other pairs of the winding terminals would reveal an induced voltage due to the flux linkage. It was the opposite pair of the winding terminals that revealed the maximum voltage since its inductance was maximum while others were either not aligned or not fully aligned. In addition, the polarity of the winding pairs could also be identified by comparing the phase shift of the induced voltage to the exciting voltage. The same polarity is indicated if the induced voltage is in phase with the exciting voltages, i.e. the flux generated by the two pairs of windings was in the same direction. It was also possible to identify the winding polarities on the neighboring stator poles from the above procedure. As shown in Figure 5.1, by exciting the windings on pole A1, both the windings on pole B1 and B2 would reveal the maximum induced voltage at the aligned position. However, the one associated with B1 would have a higher maximum induced voltage than the one associated with B2 because of the smaller flux path and thus the higher inductance.

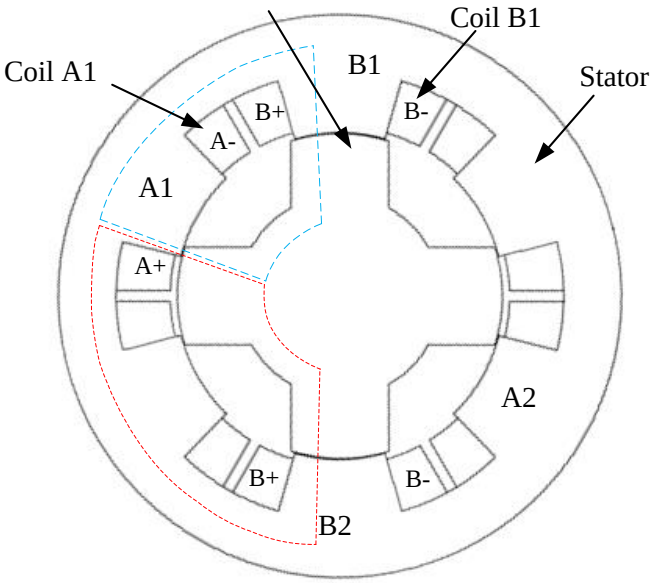

Figure 5.1 The flux paths used to identify the windings on the neighboring poles

The polarity of each winding terminal could also be identified by comparing the phases between the induced voltage and the excited voltage. Assuming the continuous poles A1, B1, and C1 had the same magnetic polarity, if A+ and B+ were both connected with the positive probes of the oscilloscope, a negative induced voltage would be generated on pole B1 due to the opposite flux direction while a positive induced voltage would be generated on pole B2 due to the same flux direction, i.e. different magnetic polarity.

Thus, all the phase windings as well as their polarities were found by following the above procedures. A magnetic field indicator was also used to test the exterior end winding polarity in order to validate the above test methodology.

5.2 DRSRM Test rig

Two brushed DC machines were used in the experiments to connect with each of the rotor shafts and apply loads to the interior SRM and exterior SRM, respectively. The two brushed DC machines were aligned along the DRSRM rotor shafts axial direction and connected by angle iron frames, as illustrated in Figure 5.2, showing the CAD modeling of the DRSRM test rig.

The angle irons were made of 9.5mm thick, hot-rolled iron and connected by a number of M10 bolts. Two sliding holes were made on each horizontal angle iron to allow both horizontal and vertical position adjustment of the load machines.

The shafts of the DRSRM were connected to the shafts of the brushed DC machines via shaft couplings. Both the brushed DC machines have screw jacks to adjust their height so that the shafts can be aligned, appropriately. Each brushed DC machine is rated at 1.5kW as a generator. Power supplies with maximum of 15A current were used to excite the field windings of the DC machines while the armatures were connected to 6 parallel power resistors, each rated for 1Ω and 100W, serving as electrical loads. The output speed of the DRSRM rotors is provided from the rotor shaft encoders while the output torque can be measured by the load cells installed on the brushed DC machines. Figure 5.3 shows the full set-up of the test rig.

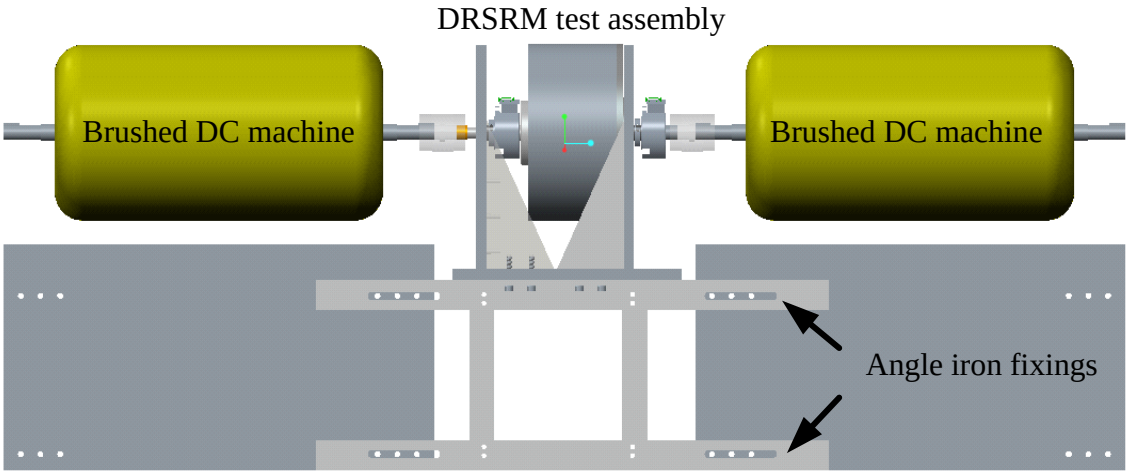

Figure 5.2 CAD modeling of the DRSRM test rig

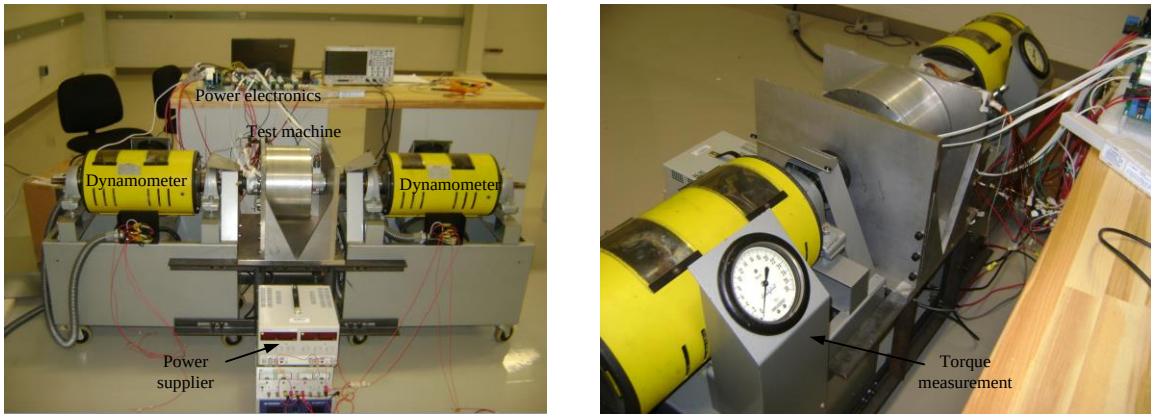

Figure 5.3 Pictures of the final 2 dynamometer integrated test rig

5.3 Machine Drives

The fundamental circuit of the switched reluctance machine drive is the asymmetric bridge, as shown in Figure 5.4. Two MOSFET switches and two diodes were implemented in each phase (e.g. devices ‘a’ in Phase A) to control the switch-on and switch-off angles of each phase winding current. Both switches in the same phase were turned on at the same time to apply the positive DC bus voltage to the corresponding phase winding while the two diodes conduct at switch-off resulting in a negative DC bus voltage being applied to the phase winding.

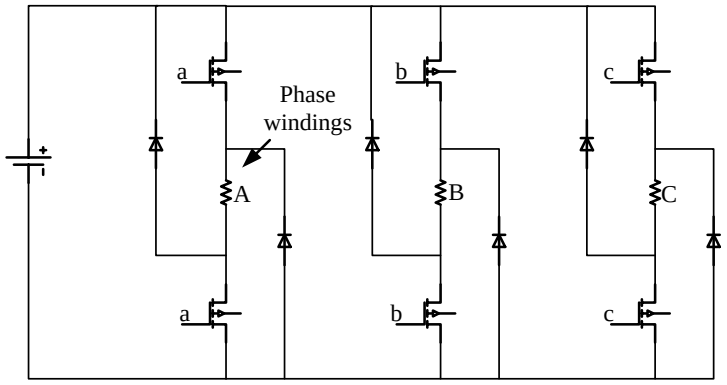

Figure 5.4 Asymmetric bridge machine drive model

In the actual machine drive, the asymmetric bridge was built in the power stage board, as shown in Figure 5.5. There were five components in the power stage of each machine: electromagnetic interference (EMI) input filter, DC bus voltage sensor, three sets of asymmetry half bridges, the signal interface to connect with the processor board and the auxiliary power supply interface. Three current sensors were embedded in the asymmetry bridge to measure and feedback the current of each phase to the processor

board. The processor board calculated the turn-on and turn-off sequences and sent out gate drive signals based on the load demand and the actual rotor positions.

Figure 5.6 illustrates the processor board layout, which was composed of six components: the digital signal processing (DSP) system to manipulate the mathematical calculations and control the machine commands, field-programmable gate array (FPGA), encoder signal terminals, 4-channel analog to digital converter (AD), auxiliary power supply and the signal interface.

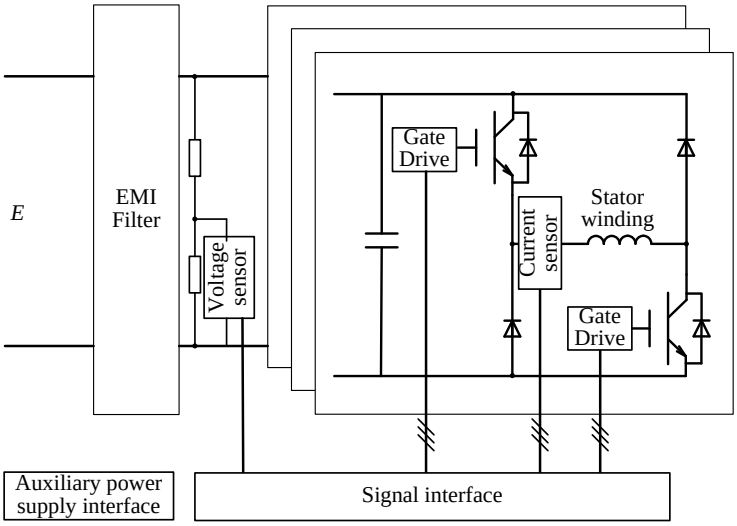

Figure 5.5 The power stage board layout

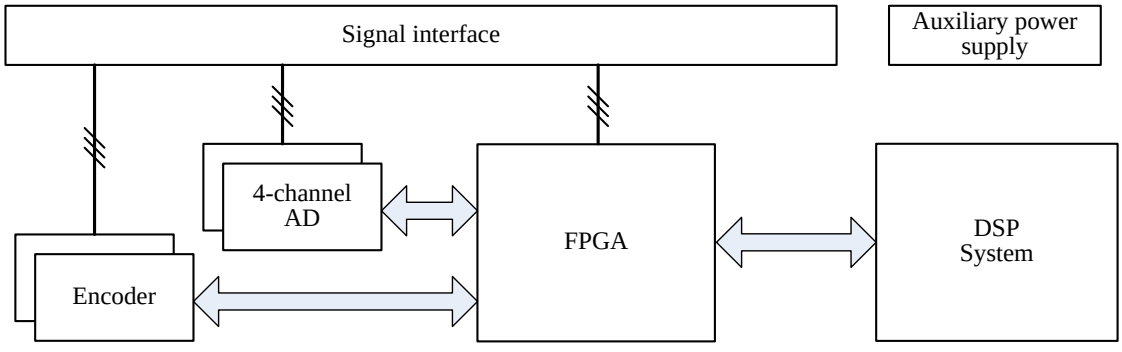

Figure 5.6 The processor board layout

The DSP system was able to control both machines at the same time. Therefore, only one DSP processor board was needed to control two power stage boards: one for the interior SRM and the other for the exterior SRM. Figure 5.7 shows the layout of the machine drive with the DSP board and the two power stage boards.

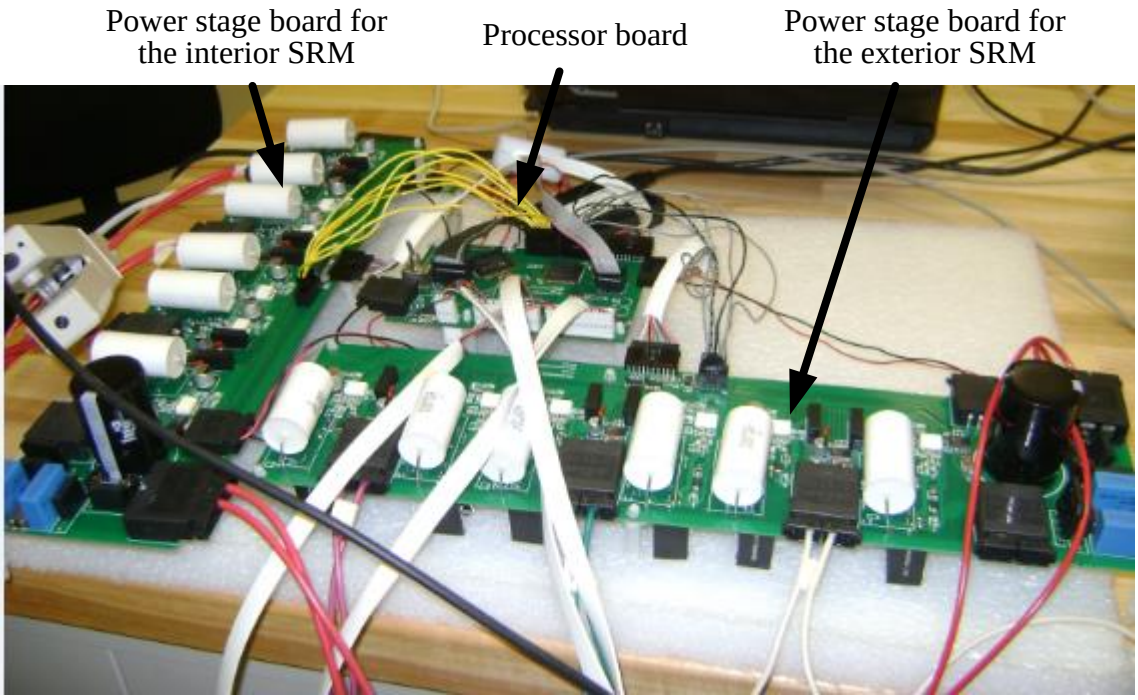

Figure 5.7 Machine drive power stage boards and processor board

5.4 Interior Machine Testing

The interior SRM machine was designed for a rated output speed of 2000 RPM and output torque of 2Nm, and thus the rated power of the interior SRM was 0.42 kW. A number of experiments were carried out to test the machine under various speeds and current levels.

The interior machine was first tested under no-load conditions. The armature side of the dynamometer brushed DC machine was open circuit so that no electric load was applied. However, there were still some mechanical loads due to the frictions on the brushes and commutator. Frictions on bearings also added up the total frictions, which were found to be substantial at high speeds. The load machine was built with a load cell to measure the output torque from the tested machine. The stator of the load machine was not fully (mechanically) grounded, i.e. it was supported by gimbal bearings at each end and thus the rotational movement could be reacted by the arm of the load cell. Thus, neglecting the small losses on the DC load machine stationary bearings, the measurement on the load cell fully captured the output torque of the tested machine. The friction torques on the DC brushes and rotational bearings were fully transferred into forces on the load cell arm.

The load cells on both the brushed DC machines were calibrated to make sure the measured torques were correct. A simple experiment was carried out by applying an extended arm with a weight hanging on the end to the brushed DC machine housing, as shown in Figure 5.8. The weight applied was measured to be 19.0 N and the length of the

arm from the center of the machine to the end was 0.24m. Thus, the total applied torque was the production of the weight and the arm length, which was 4.5Nm. The measured torques on the load cells for the interior SRM and the exterior SRM were 4.3Nm and 4.4 Nm, respectively. Therefore, a 0.2 Nm torque backlash on the interior SRM and a 0.1 Nm torque backlash on the exterior SRM existed, and hence the differences were applied onto all the noted torque measurements.

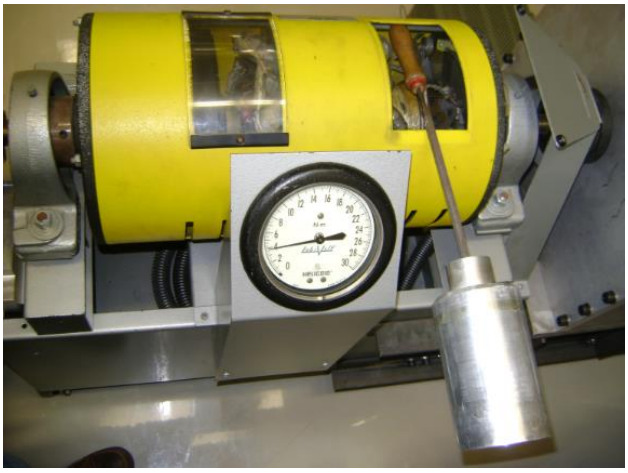

Figure 5.8 Load cell torque measurements calibration

The turn-on and turn-off angles of the interior SRM was tested by varying the angles around the optimized design angles, 53 degrees for the turn-on angle and 87 degrees for the turn-off angle. Output torques, vibrations and noise were compared at different sets of angles, and the results verified the designed angles were the best input angles that gave maximum average output torque and least vibrations and noise. Figures 5.9 illustrates two example phase current waveforms at two different turn-on and turn-off angles: turn-on at 48˚and turn-off at 78˚; turn-on at 53˚and turn-off at 87˚.

At no-load conditions, the output torque of the interior SRM machine equaled to the torque caused by the frictions of the brushed DC machine. The speed was controlled by a PI controller so that the input current could be adjusted based on the difference between the commanded speed and the measured real speed. The input conditions and the output performance of the interior SRM machine at different speed under no load are summarized in Table 5.1.

In Table 5.1, the input voltage and current were measured by reading the digital display on the power supply. The input voltage was kept constant at 300V according to the designed DC bus voltage. The current was measured as an average of the output current from the power supply. Four different speeds from 1000 RPM to 4400 RPM were tested. The output torque increased as the speed increased because of the higher friction loss on the bearings and the brushes. Figure 5.10 presents the current waveform of both the phase current (a) and the power supply current waveforms (b) at 4400 RPM.

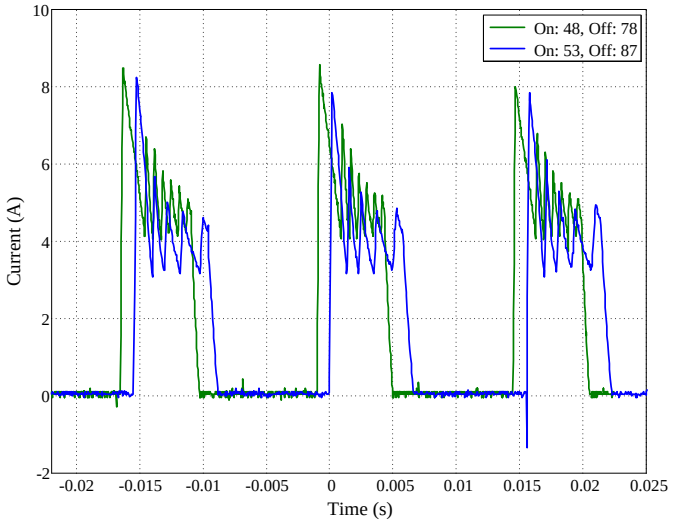

Figure 5.9 Example interior SRM phase current waveforms for different control angles

Table 5.1 No-load testing for the interior SRM

Input		Output	
Voltage (V)	Current (A)	Speed (RPM)	Torque (Nm)
300	0.4	1000	0.5
300	0.7	2000	0.6
300	1.3	3000	0.7
300	2.2	4400	0.8

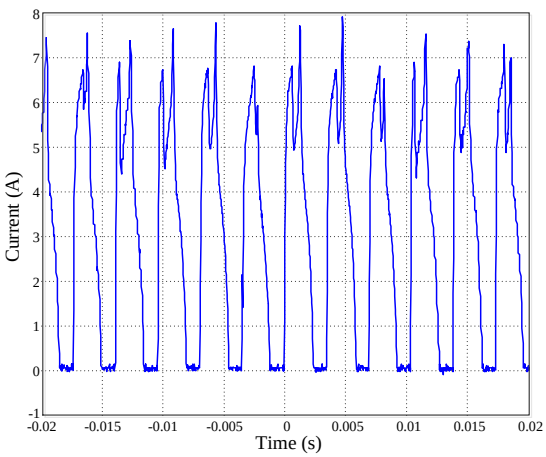

(a) Interior SRM phase current waveform at 4400 RPM

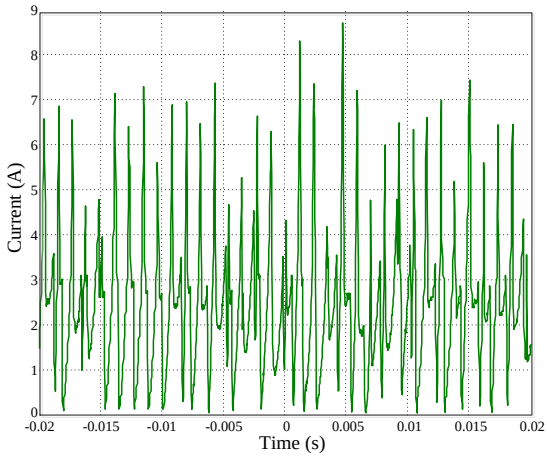

(b) Interior SRM power supply current waveform at 4400 RPM

Figure 5.10 Interior SRM phase and power supply current waveforms at no-load 4400 RPM

Figure 5.11 compares the test results with the simulation results gained from the real-time drive simulation. The solid (green) lines are the test results for both the phase current waveform and the power supply current waveform at 4400 RPM, and the (blue) dashed lines are the simulations results under the same conditions. It can be observed that there is good agreement between simulation and test data. Figure 5.12 presents the phase current results at 3000 RPM where it can be observed that more current chopping were

applied around 4.5A since the speed and hence back-EMF are reduced and thus current has more time to rise and fall.

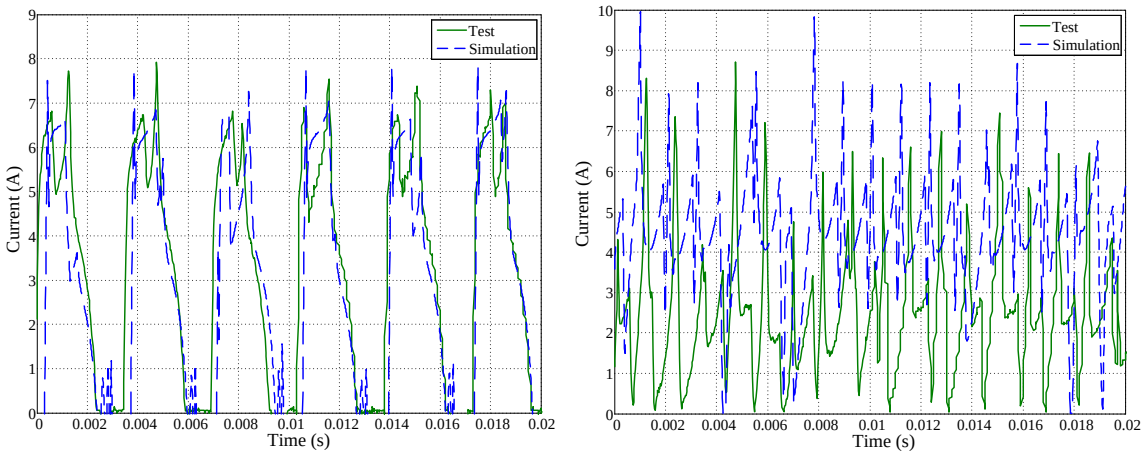

(a) Interior SRM phase current waveform at 4400 RPM

(b) Interior SRM power supply current waveform at 4400 RPM

Figure 5.11 Comparisons between simulation and test current waveform for the interior SRM at no-load 4400RPM

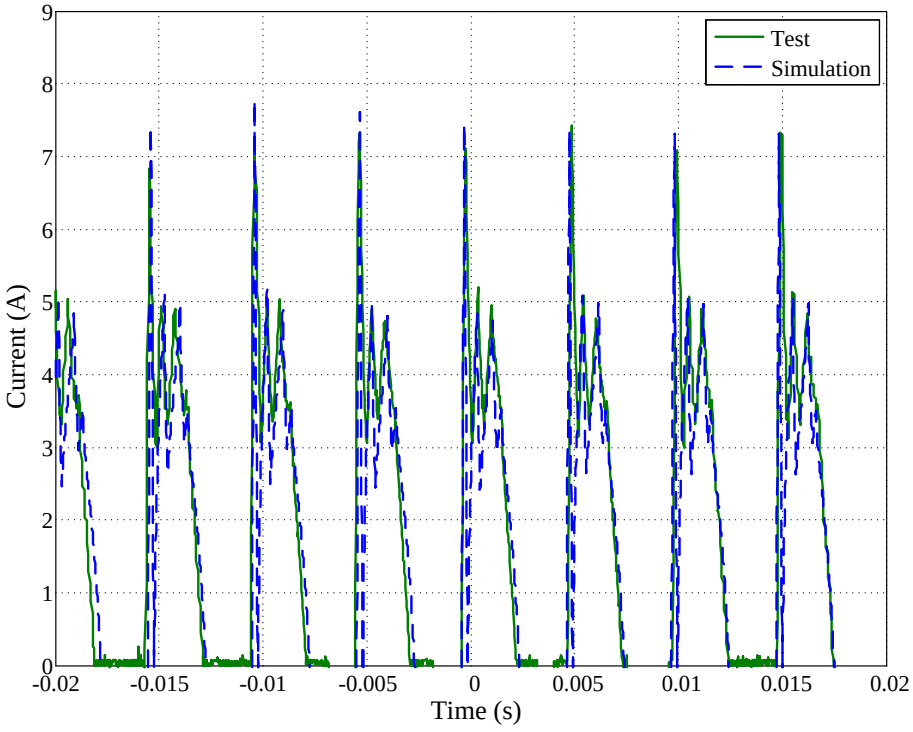

Figure 5.12 Interior SRM phase current waveforms at 3000 RPM

The rise of the phase current is high at switch-on since the inductance of the machine is small at the unaligned position and the resolution of the machine drive current sampling frequency was not fast enough to catch the initial transient. The inductance of the machine then increases as the rotor rotates towards the aligned position, thus the time for the phase current to rise and fall increases, hence the current control is improved.

Loaded tests were conducted by connecting the armatures of the brushed DC machines to power resistors while exciting the DC machine field terminals to induce the machine magnetic field and hence armature back-EMF. The DRSRM stator input phase currents were controlled at a constant level while the speed of the machine was adjusted by changing the brushed DC machine field strength and hence torque. Table 5.2 presents loaded test data for the interior SRM with the phase current regulated at the rated current of 6A.

The input DC bus voltage was kept at 300V for all the test cases. The output speed of the interior SRM increased from 1000 RPM to 4000RPM. The output torque was measured to be 1.6 Nm at 1000 RPM while gradually reducing as the speed increased due to higher friction inside the interior SRM. The friction inside the interior SRM was largely caused by the bearings on the interior rotor. It can be assumed here that the torque caused by the friction inside the interior SRM was one third of the friction torque in the brushed DC machine since the brushed DC machine used larger bearings and there were also frictions caused by the brushes. The friction torque of the brushed DC machine at each operating speed was measured at no-load conditions, as presented in Table 5.1. Thus, the overall output torque from the interior SRM can be calculated by combining the

measured torque with the friction torque. Thus, the efficiency at each operating point can be calculated by dividing the output power by the input power, as detailed in Table 5.3, showing that the simulation and measure data with good agreement at all the speeds. The designed rated torque 2N was met up to the design base speed of 2000 RPM. The output torque then decreased as the machine operated above base, as would be expected. Figure 5.13 compares the simulated torque speed characteristic of the interior SRM with the measured data.

Table 5.2 Load test results for the interior SRM at 6A phase current

Input		Output	
Voltage (V)	Current (A)	Speed (RPM)	Torque (Nm)
300	1	1000	1.8
300	1.6	2000	1.7
300	1.8	2400	1.6
300	2.1	3000	1.4
300	2.3	4000	1.2

Table 5.3 Simulation and measured data for the interior SRM at 6A phase current

	Input		**Output**					
	Simulated	Measured	Simulated		Measured			
Speed (RPM)	Current (A)	Current (A)	Torque (Nm)	Efficiency (%)	Torque (Nm)	Friction Torque (Nm)	Total Torque (Nm)	Efficiency (%)
1000	1.13	1	1.96	60.55	1.8	0.17	1.97	68.77
2000	1.78	1.6	1.92	75.30	1.7	0.2	1.9	82.9
2400	2.06	1.8	1.9	77.27	1.6	0.21	1.81	84.24
3000	2.22	2.1	1.73	81.61	1.4	0.23	1.63	81.28
4000	2.6	2.3	1.64	88.07	1.2	0.27	1.47	89.24

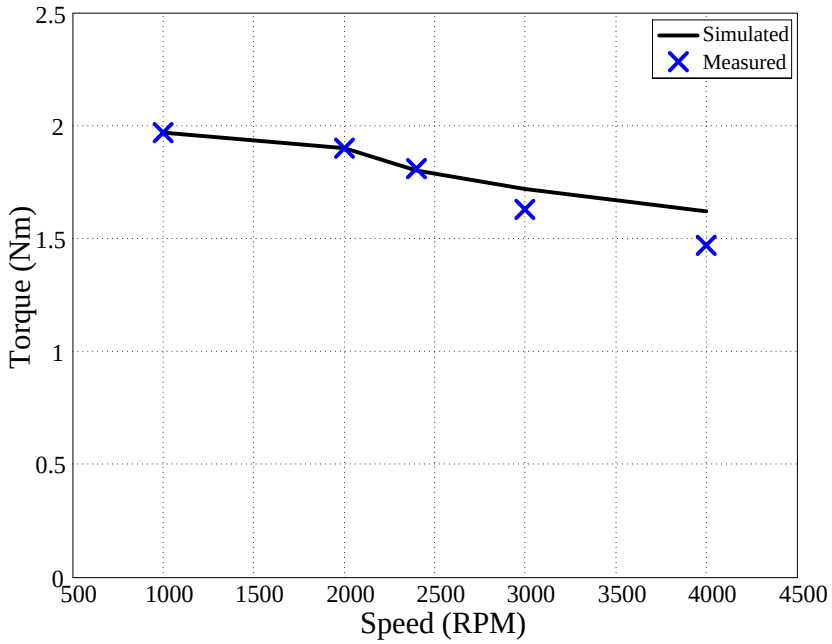

Figure 5.13 Simulated and measured torque-speed characteristics for the interior SRM

Figure 5.14 presents the measured phase current waveforms of the interior SRM in 1000 RPM steps from 1000 RPM to 4000 RPM. The turn-on current was controlled at 6A per phase while the actual phase current was chopped with a 0.5A current bandwidth. The frequency of the phase current increases as the speed of the machine is increased. The discrete pulses (green) lines represent the aligned positions for the interior SRM. It can be observed in Figure 5.14 (c) and (d) that as the speed increased, the phase current could not fall to zero before the aligned position, which resulted in higher negative torques upwards of 2000 RPM. The resistances of the thermistors were measured after the 66 minutes of machine operation. Table 5.4 presents the resistance values of each thermistor as well as their corresponding temperature. The induced voltages on the search coils, i.e. sensor 1 and sensor 2, are plotted in Figure 5.15. The control target for the current was 6A and the speed of the interior rotor was 1000 RPM.

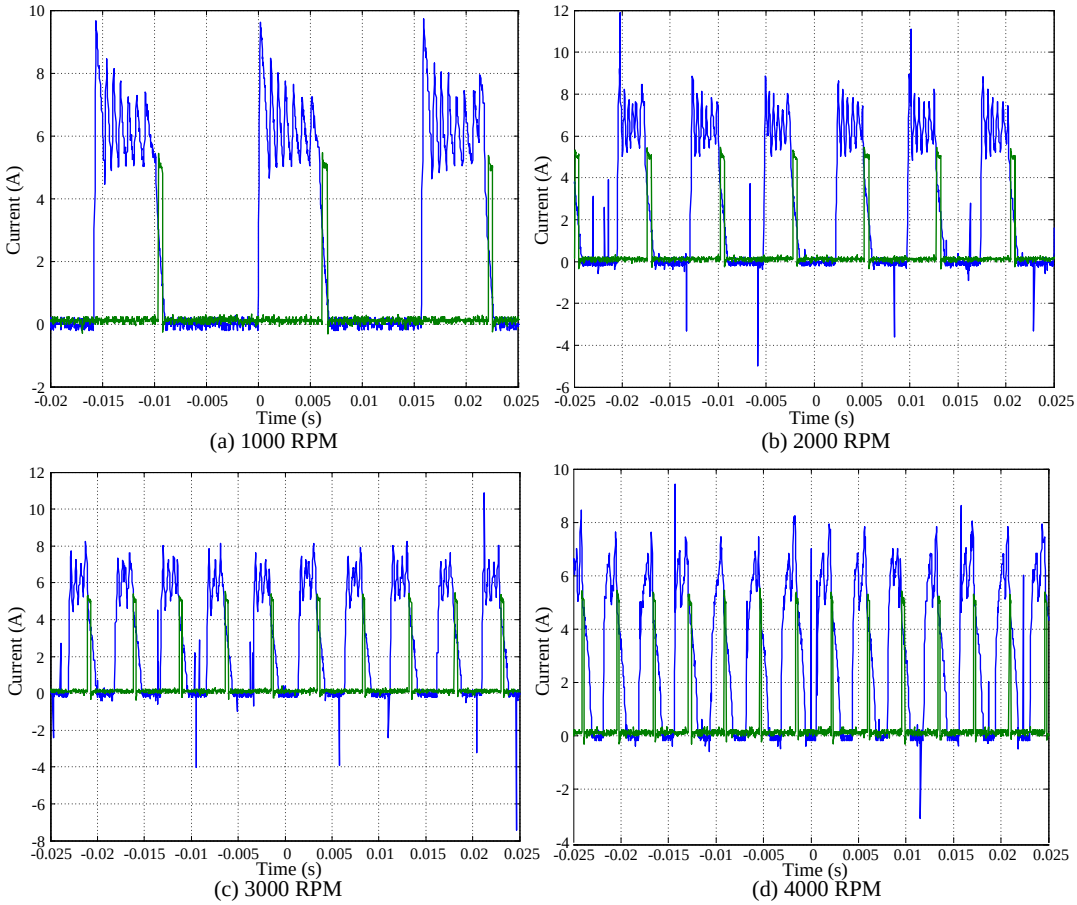

Figure 5.14 Measured interior SRM phase current waveforms under different speeds

Table 5.4 Interior SRM temperature measurements after 66 minutes operation

Sensors	Locations	Resistance (kΩ)	Temperature (℃)
3	Back iron	2.66	42.5
4	Termination coil	2.44	44.7
5	Non-termination coil	2.64	42.7
6	Middle coil	2.50	44.2
7	Stator pole	2.55	43.7

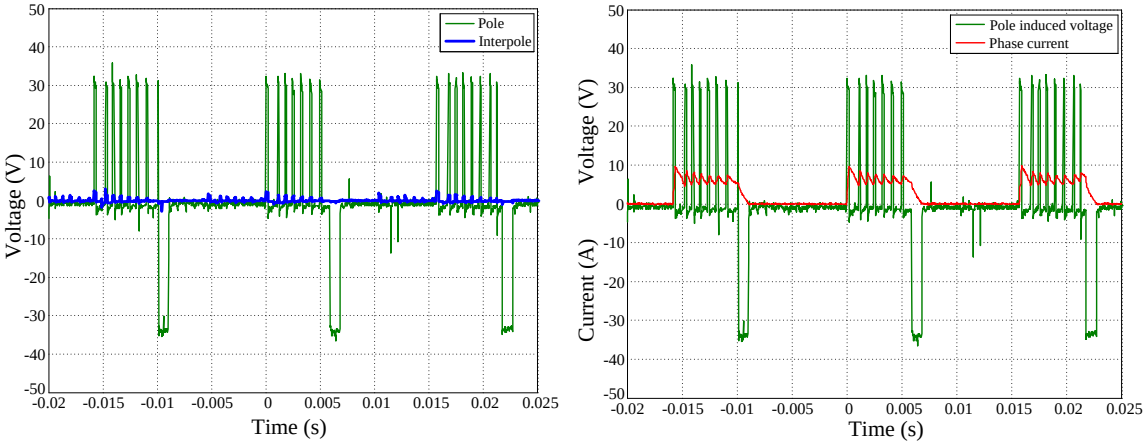

(a) Pole and interpole

(b) Pole and phase current

Figure 5.15 Induced voltages on search coils

The green lines represent the induced voltages on search coil 1, which was wound on the interior stator pole, and the blue lines represent the induced voltages on search coil 2, which was wound on one of the interior inter-polar stands, Figure 5.15 (a). The output of the search coil 1, wound on a stator pole, is further compared to the pole coil current (red) in Figure 5.15 (b) to show the correlation between phase current and induced voltage. It can be clearly observed that the induced voltages on the interior stator pole correspond to the input phase current. The rise of the phase current induced positive voltages while the fall of the phase current induced negative voltages. The induced voltages on the interior stator inter-polar stands were small that can be ignored, proving there was little flux penetration on the inter-polar stands and thus the inter-polar stands helped with the winding process and structure rigidity while not influence the machine performance. The back-EMF of the winding can also be gained from the measured search coils induced voltages by using the ratio of stator winding turns to the search coil turns. Table 5.5 presents the calculated back-EMF for all the tested speeds.

Table 5.5 Interior SRM induced voltages

Speed (RPM)	Search Coil RMS Voltages (V)	Interior Winding Back EMF (V)
1000	11.72	112.48
2000	16.67	160.03
2400	18.81	180.57
3000	21.19	203.44
4000	23.99	230.31

5.5 Exterior Machine Testing

The exterior SRM machine was designed with a rated output speed at 500 RPM and output torque 8Nm, and thus the rated power of the exterior SRM was the same as the interior SRM, which was 0.42 kW.

Similar to the testing procedure of the interior SRM, the exterior machine was first tested under no-load conditions. The armatures of the brushed DC machine were open so that there was no current induced in the windings, and thus no electric load was applied. Friction torques on the bearings and brushes of the brushed DC machine were measured via the load cell, which equaled to the output torque generated by the exterior SRM at the no-load condition. The frictions inside the exterior SRM were also assumed to be one third of the frictions inside the brushed DC machine.

Table 5.6 summarizes the input conditions and the output performance of the exterior SRM machine at different speed under no-load conditions. It can be observed that the output torques were almost the same at different speeds since the friction torques on the bearings remained unchanged at low speed.

Figure 5.16 presents the phase current waveforms at 500 RPM. Figure 5.16 (a) shows the current waveforms of the two successive phases and Figure 5.16 (b) compares the phase current waveforms between the simulation data and test results, again showing good agreement.

Table 5.6 No-load testing for the exterior SRM

Input		Output	
Voltage (V)	Current (A)	Speed (RPM)	Torque (Nm)
300	0.2	350	0.4
300	0.3	500	0.4
300	0.5	750	0.5
300	0.6	837	0.5
300	0.7	1000	0.5

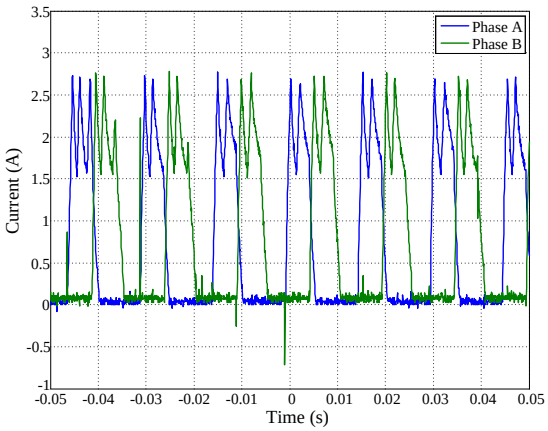

(a) Exterior SRM phase currents

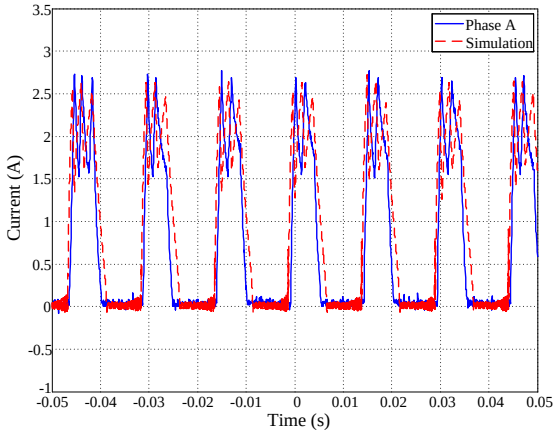

(b) Phase current comparison between test and simulation

Figure 5.16 Exterior SRM phase current waveforms

Loaded tests were also carried out on the exterior SRM by running the brushed DC machine as a generator. Similar to the loaded tests on the interior SRM, power resistors were connected to the armature terminals of the brushed DC machine and

constant currents were injected into the field windings to generate magnetic field. The speed of the exterior SRM was adjusted by changing the current in the field windings. Table 5.7 presents the load test results for the exterior SRM at 5A phase current excitations while Figure 5.17 compares the results of the simulated and measured torque and speed characteristics of the exterior SRM at 5A phase current excitation.

It can be observed that a good match exists between the simulated and experimental data for the exterior SRM. The output torque also reduced as the speed increased above the design base speed of 500 RPM. Figure 5.18 presents the phase current waveforms of the exterior SRM under different rotational speeds. The pulses (green) were introduced in the graphs to indicate the aligned positions. It can be observed that at low speed, such as 350 RPM and 500 RPM, the phase currents dropped to zero before the aligned position. However, as the speed further increases, the phase current no longer drop quickly before the aligned position such that there is still some remaining phase current that generates negative torque.

The internal temperatures of the machine were also measured by reading the resistances of the thermistors, as presented in Table 5.8. The induced voltages on the search coils of the exterior SRM also suggested that there was barely any flux penetration on the exterior stator inter-polar stands, as confirmed by the negligible induced voltage on search coil 2, shown in Figure 5.19. Table 5.9 calculates the induced voltages at different exterior rotor speeds.

Table 5.7 Output torque and efficiencies of the exterior SRM at 5A phase current

	Input		Output					
	Simulated	Measured	Simulated		Measured			
Speed (RPM)	Current (A)	Current (A)	Torque (Nm)	Efficiency (%)	Torque (Nm)	Friction Torque (Nm)	Total Torque (Nm)	Efficiency (%)
350	1.37	1.4	8.09	72.14	7.8	0.13	7.93	69.20
500	1.77	1.7	7.97	78.59	7.8	0.13	7.93	81.41
750	2.17	2.1	6.96	83.97	6.4	0.17	6.57	81.91
837	2.26	2.1	6.63	85.71	5.4	0.17	5.57	77.49
1000	1.64	1.6	3.94	83.86	3.4	0.17	3.57	77.89

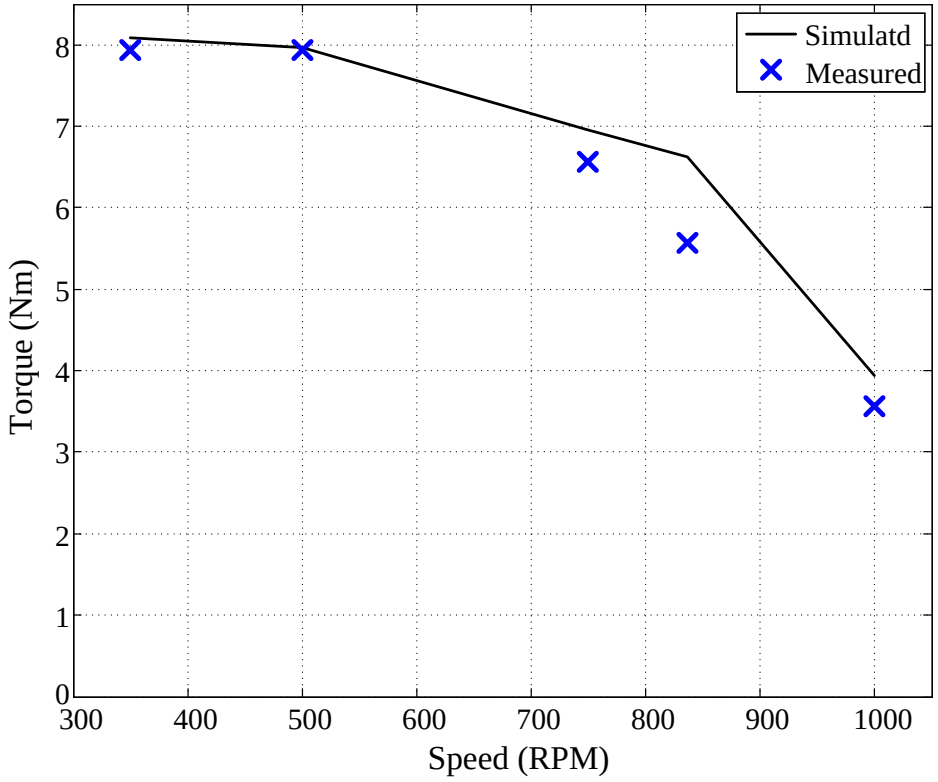

Figure 5.17 Measured and simulated torque speed characteristics of the exterior SRM

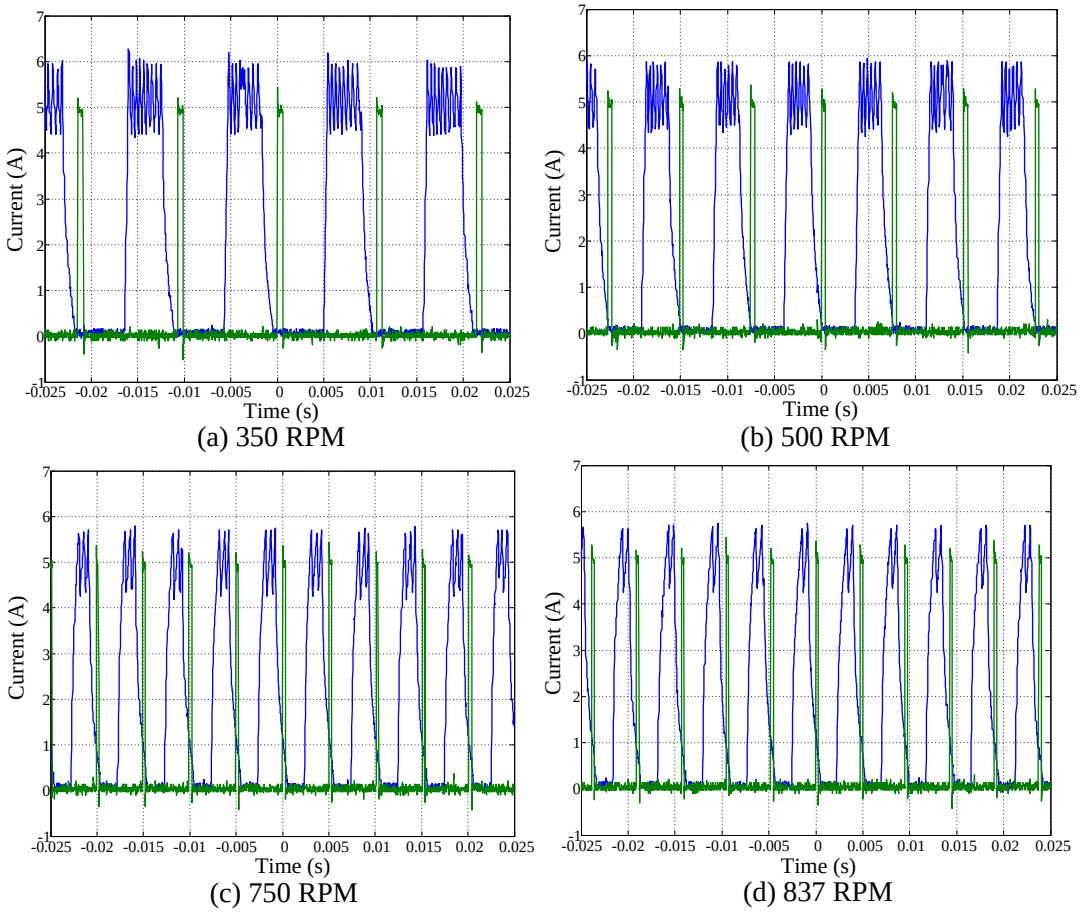

Figure 5.18 Exterior SRM phase current waveforms under different speeds

Table 5.8 Exterior SRM temperature measurements after 38 minutes operation

Sensors	Locations	Resistance (kΩ)	Temperature (℃)
3	Back iron	3.95	31.4
4	Termination coil	3.86	32.0
5	Non-termination coil	3.80	32.5
6	Middle coil	3.80	32.5
7	Stator pole	3.90	31.7

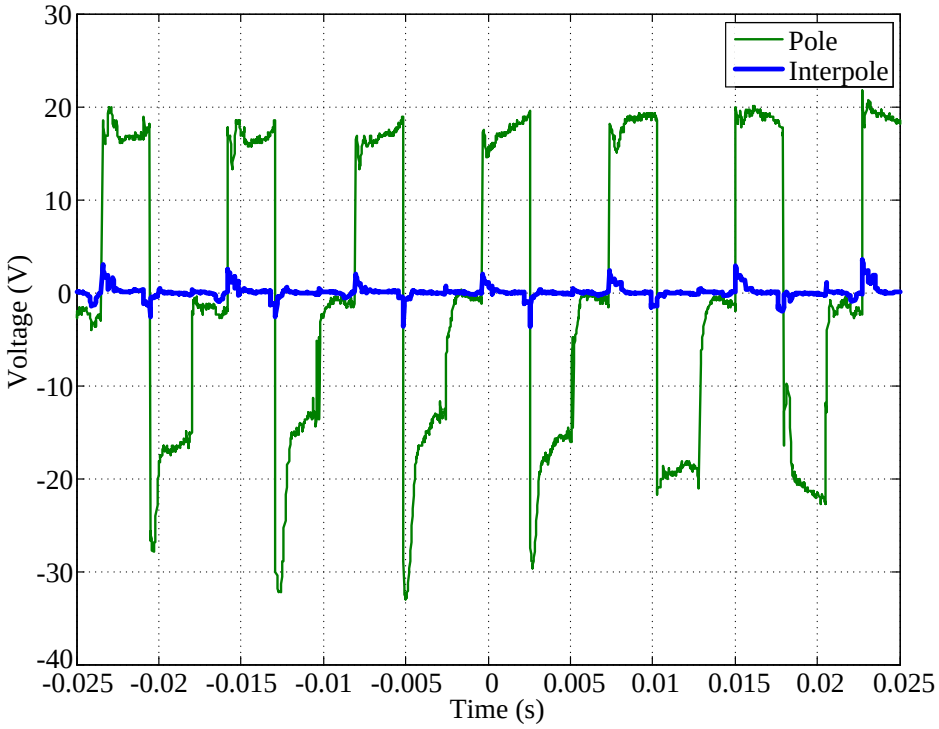

Figure 5.19 Exterior SRM induced voltages

Table 5.9 Exterior SRM induced voltages

Speed (RPM)	Search Coil RMS Voltages (V)	Interior Winding Back EMF (V)
300	9.25	148.01
500	11.50	184.00
750	13.70	219.15
837	14.78	236.45
1000	15.19	243.12

5.6 Double-Rotor Switched Reluctance Machine Testing

After individual testing of the two machines, both machines were tested with both rotors operating at the same time but with different speeds. A 300V DC bus voltage was supplied to the power stage boards of both machines. The centralized DSP controlled the two machines at the same time with different rotor speeds. Each rotor was connected to the corresponding DC brushed machine, which served as generators to adjust the loads individually. Two separate power supplies were applied to excite the field windings of the DC machines and the speeds of the rotors were adjusted by changing the field currents respectively.

The interior stator windings were excited with 6A phase current and the exterior stator windings were excited with 5A phase current. Firstly, the speed of the interior rotor was controlled to be 2000 RPM while the speed of the exterior rotor was controlled to be 837 RPM. Figure 5.20 presents the current waveforms of both machines for this test condition. It can be observed that the phase currents of the two machines were controlled independently so that the torques and speeds of the double rotors were controlled independently as well. Figure 5.21 illustrates the speed response of the two rotors when they were operated together. Table 5.10 compares the machine output performance results when operating together to the results for the case of independent operation.

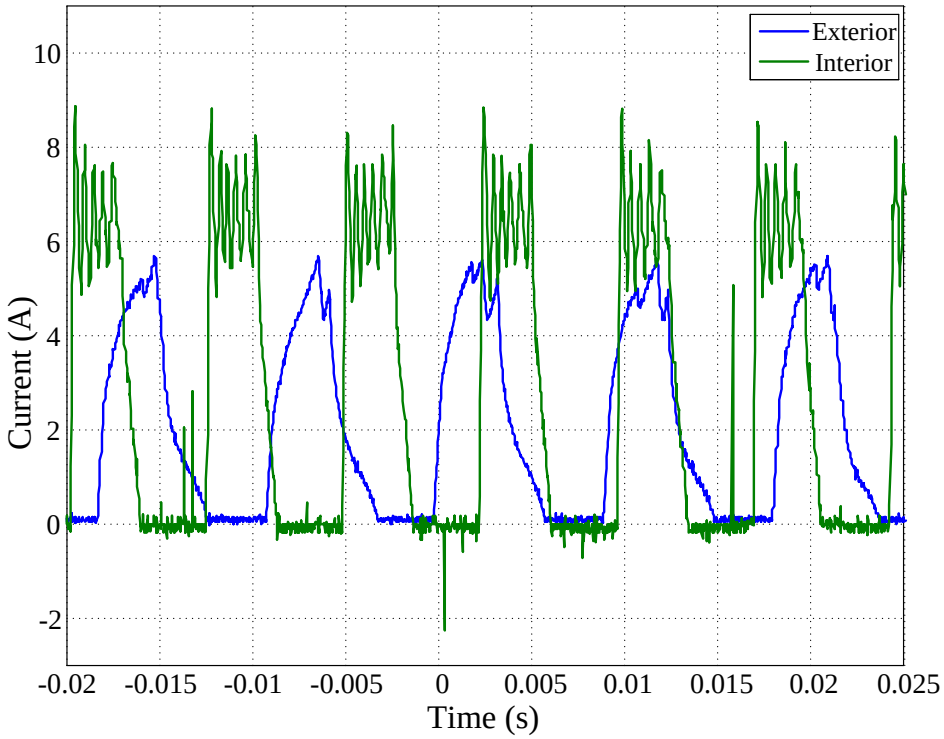

Figure 5.20 Phase current waveforms of the two machines

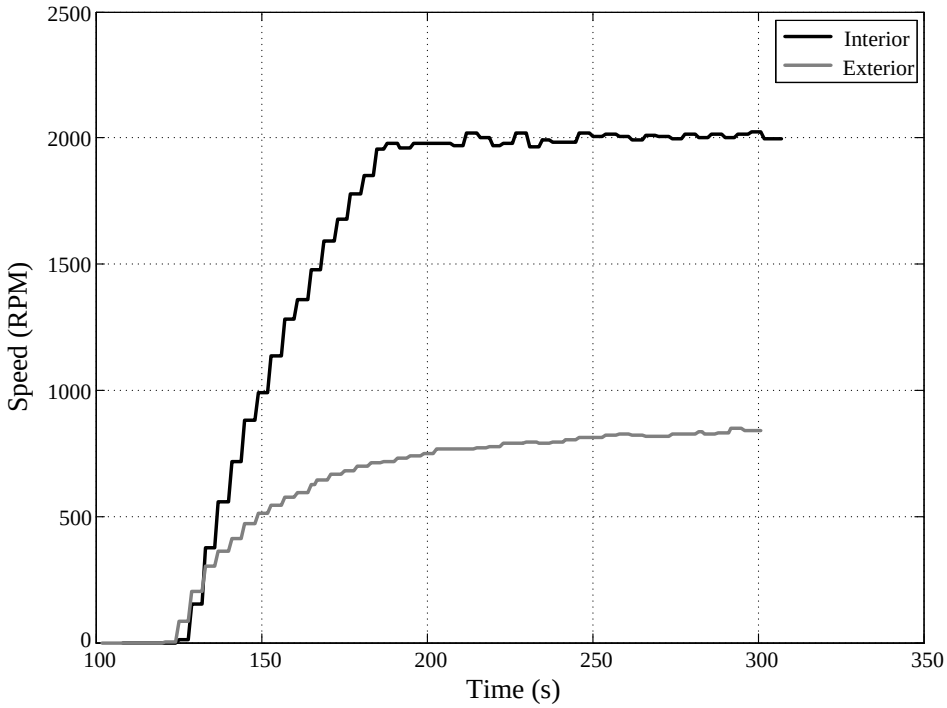

Figure 5.21 Speed response of the two machines when operated together

Table 5.10 Comparison of the output performance of the two machines

	Interior SRM			Exterior SRM		
	Speed (RPM)	Torque (Nm)	Current (A)	Speed (RPM)	Torque (Nm)	Current (A)
Operating together	2000	2.0	5.11	500	7.8	4.15
	2000	2.0	5.55	837	5.4	3.51
	3000	1.6	5.05	500	7.8	4.11
	3000	1.6	5.16	837	5.4	3.54
Operating separately	2000	1.9	5.25	500	7.9	4.26
	2000	1.9	5.25	837	5.6	3.74
	3000	1.6	5.16	500	7.9	4.26
	3000	1.6	5.16	837	5.6	3.74

It can be observed from Table 5.10 that the output performance of the two machines remained the same whether they were operated together or separately, hence it can be concluded that the air gap flux barriers in the stator functioned as designed to separate the flux paths of the two machines and thus facilitate independent control of the two rotors.

Table 5.10 also confirms the primary design goal that the interior rotor produces higher speed while the exterior rotor produces high torque, and, importantly, that these conditions can be achieved independently, as per the results of Tables 5.3 and 5.7, and together, as per the results of Table 5.10. To summarize, at the design rated speeds, the interior rotor operates 4 times faster than the exterior rotor while the exterior rotor produced 4 times higher torque. Thus, the design criteria was met and it proved that the proposed double-rotor switched reluctance machine to be a good candidate to suit the

speed and torque requirements of hybrid electric vehicle transmissions in which one high speed machine is needed to couple with the engine and another high torque machine for traction drive as discussed earlier in Chapters 2 and 3.

An attempt was made to experimentally investigate torque ripple reduction via the compensation technique discussed in Section 3.6.4. Here, the two rotors were controlled to operate with the same electric frequency, i.e. the speed of the interior rotor was twice that of the exterior rotor. In this test case, the speed of the exterior rotor was 837 RPM and the speed of the interior rotor was 1674 RPM. Figure 5.22 shows the phase current waveforms from both machines with both an in-phase relationship and out-of-phase relationship.

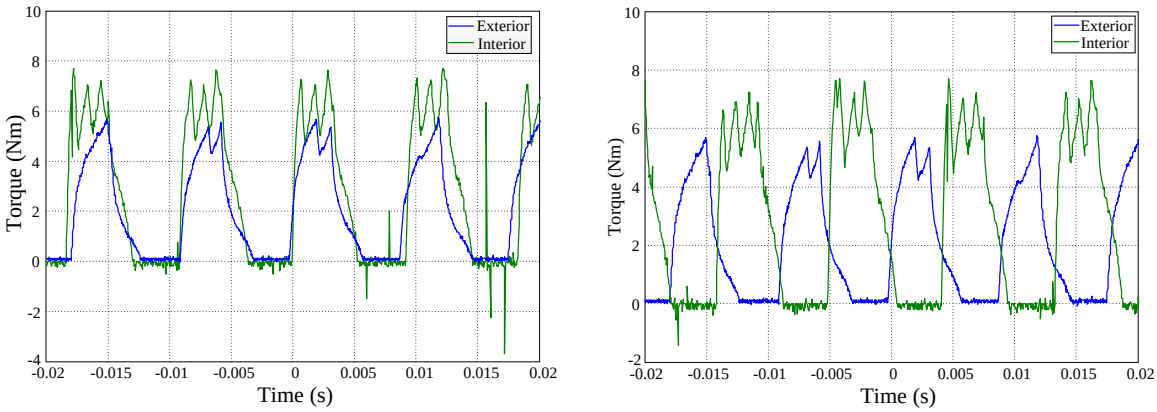

(a) In-phase current waveforms

(b) Conjugate phase current waveforms

Figure 5.22 Current waveforms at the same electric frequency

From the simulation studies, when the phase currents of the two machines were excited at the same time, the torques and radial forces generated by the two machines largely occur at the same time. These ripple torques and forces add up together influencing the whole system dynamics, ultimately causing vibrations as observed in the

experiments. By changing the relative electrical positions of the two rotors, the excited currents of the two machines were offset to be out-of-phase. The summed torque ripple, radial and axial forces impacting on the system were observed via the noise and vibrational output of the test rig to be significantly reduced. This difference in noise and vibration between the in-phase and out-of-phase excitation were significant, but suitable measurement devices (accelerometers) were not available to make a quantifiable measurement. However, as discussed in Section 3.6.4, this is a very interesting area of future research.

The temperatures on different parts of the machine were also recorded with 6A current on both windings. Figure 5.23 compares the simulated temperature with the measured results on the stator windings. The results show good agreements giving confidence in the rotor temperature predictions.

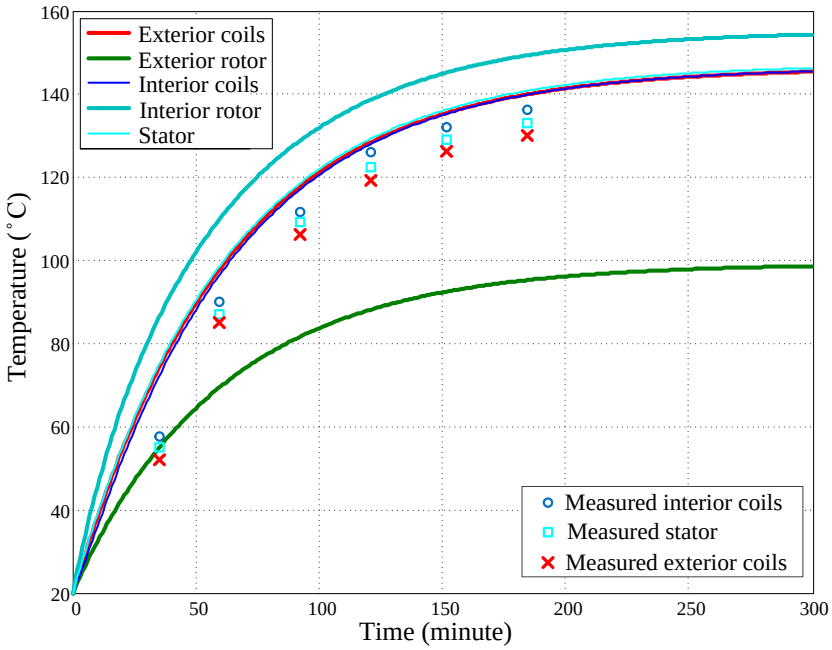

Figure 5.23 Comparisons between measured and simulated temperatures

Table 5.11 DRSRM temperature measurements with 6A current in both windings

Sensors	Locations	Temperature (℃)					
		30 min	60 min	90 min	120 min	150 min	180 min
In 3	Interior Stator Back iron	53.9	85.7	109.7	123.0	130.5	135.5
In 4	Interior Termination coil	54.2	90.2	111.8	126.0	132.5	136.9
In 5	Interior Non-termination coil	57.9	90.8	111.9	125.8	132.7	136.4
In 6	Interior Middle coil	57.7	90.4	112.1	125.1	132.0	136.4
In 7	Interior Stator pole	52.6	85.3	110.2	122.4	131.0	135.5
Ex3	Exterior Stator Back iron	51.6	85.7	109.8	121.5	128.5	133.2
Ex 4	Exterior Termination coil	51.7	86.2	106.4	119.7	127.8	131.5
Ex 5	Exterior Non-termination coil	52.1	86.4	106.4	120.4	126.9	131.4
Ex 6	Exterior Middle coil	52.1	86.0	106.7	119.5	127.4	130.9
Ex 7	Exterior Stator pole	51.3	85.5	109.7	121.0	128.9	133.9

5.7 Summary

This chapter presented the test results of the prototype double-rotor switched reluctance machine to validate the design work presented in Chapter 3. The method of identifying the phase terminals as well as their polarities for both the interior and exterior SRM was described in Section 5.1. Sections 5.2 and 5.3 presented the test rig and the machine drive configurations for testing the prototype DRSRM. The test results of the interior SRM, the exterior SRM, and the DRSRM operating together were reported in Sections 5.4, 5.5 and 5.6, respectively. Comparisons between the test results and the finite element simulations were given and the overall machine performance evaluated.

The prototype machine results revealed good correlation between experiments with the designed parameters and simulations. The phase current waveforms were studied under different machine operating points and good agreement between simulations and experimental tests were also gained. The prototype machine met the designed rated speed and rated torque for both the interior and exterior machines. The designed efficiencies were also experimentally validated.

Most important, the two machines were proved to be integrated and were able to be controlled independently without major flux interference. Furthermore, the designed DRSRM was able to output high torque from the exterior rotor shaft and high speed from the interior rotor shaft, desired in typical full hybrid electric vehicle power-trains.

Chapter 6

CONCLUSIONS

This Chapter concludes the research presented in the thesis by reviewing and summarizing the research outcomes. The conclusions drawn from this research and the novelties and innovations are listed in Section 6.2, while Section 6.3 recommends future research to be continued in the development of the double-rotor switched reluctance machine and the integrated electro-mechanical hybrid power-train.

6.1 Review and summary of the research outcomes

This thesis presented a novel design of a double-rotor switched reluctance machine that can be applied to a novel integrated electro-mechanical hybrid power-train.

In Chapter 1, the background of this research work was presented by discussing the demands for fuel efficient and cleaner road transportation. Hybrid electric vehicles and hybrid electric power-trains were then introduced with their benefits and advantages in fuel efficiency improvement and emissions reductions. Different categories of hybrid electric vehicle transmissions were discussed and then the full hybrid configuration was selected due to its highest degree of electrification and thus more fuel efficiency gains and emissions reductions. Literature reviews of the existing full hybrid transmission technologies were presented in Section 1.4. Based upon the provided background, the motivations of the Ph.D. research were presented and contributions and novelties of the

proposed integrated electro-mechanical hybrid transmission with double-rotor switched reluctance machine were claimed in Section 1.5. Finally, the contents of each chapter of the thesis were briefly described in Section 1.6.

In Chapter 2, different types of existing full hybrid transmissions were first reviewed and presented. Section 2.2 discussed the input-split hybrid transmission and Section 2.3 discussed the compound-split hybrid transmission both in details. The configurations, fundamentals of operating principles and various operating modes have been comprehensively reviewed, while the torque speed characteristics and power output have been detailed analyzed. Both the advantages and disadvantages of the two hybrid transmissions were compared and then a novel integrated electro-mechanical hybrid transmission with double-rotor electric machine was proposed. Detailed transmission operation principles were analyzed and control strategy modes are discussed. Comparisons were made between the proposed integrated electro-mechanical hybrid transmission and the original full hybrid transmissions, and the benefits and advantages of the proposed hybrid transmission were claimed. It is demonstrated and mathematically proved that the proposed integrated electro-mechanical hybrid transmission will simplify the compound two-mode hybrid transmission architecture while potentially maintaining or improving the fuel economy and performance. Furthermore, various proposed configurations of the integrated electro-mechanical hybrid transmission with double-rotor electric machine were introduced. In the last part of Chapter 2, the functions of double-rotor electric machines were also briefly introduced, with the emphasis on their critical role in hybrid electric power-trains. Typical torque-speed requirements for the hybrid

power-train transmissions were illustrated to establish the power-train requirements on the machines. Considering the UDDS and HWFET duty cycles, an average torque ratio of 1:4 between the two machines was selected as the benchmark specification for the prototype double-rotor electric machine

Chapter 3 started with the discussion with selecting switched reluctance machines as the development target for the double-rotor electric machine. The fundamental principles of the switched reluctance machine were presented in Section 3.1. A family of double-rotor switched reluctance machines (DRSRM) was then presented with various configurations in Section 3.2. The design procedures of the prototype DRSRM were then fully reported in Section 3.3. Imperial equations were used to start with the initial geometry design of the DRSRM. Design targets of rated power, rated speed, and the number of stator and rotor poles were specified. Three design criteria were applied to regulate the design parameters based on the physical construction limitation, the self-starting capability, and the minimum inductance requirement. The initial design for both the interior SRM and the exterior SRM were then summarized at last. Detailed simulation processes were carried out in Section 3.4. Electromagnetic simulations, loss analysis, thermal analysis, and SRM drive simulations were presented in sequence. The initial designed geometry of the DRSRM was then further optimized based on the simulation results as discussed in Section 3.5. Turn-on and turn-off angles for both the machines were optimized based on the criteria of higher average torque output and lower torque ripples. Loads and excitations were optimized based on magnetic saturation and machine operating temperatures. Stack length of the machine was optimized to give out the best

efficiency. The final designed geometry and associated design parameters of the DRSRM were presented in the first part of Section 3.6. The flux linkages characteristics and torque characteristics under different current and rotor locations were presented in graphs. Miscellaneous analyses were carried out to evaluate the machine performance. The effects of machine eccentricity and variation of air gap distances were studied at first. Electromagnetic analyses were performed on machine structure components to assess the flux leakages as well as the influence from these structure components on the machine. One method of torque ripple reduction by coupling the two rotors together with the same or multiple-times electrical frequency was introduced and explained. Two variations of the winding polarities were investigated and the effects on torque output and machine losses were studied. Finally, 3D simulations were implemented to verify the 2D simulation results.

The manufacturing process of realizing the DRSRM was fully discussed in Chapter 4. Laminations were manufactured by laser cutting and then stacked together based on the stator stack, the interior rotor stack, and the exterior rotor stack. Windings of the DRSRM and the instrumenting wires were manufactured in the lab and described in details in Section 4.2. Different stacks were then aligned radially to ensure the designed air gap distance and insulation materials were applied to avoid ground faults or unwanted eddy current losses. Each stack of the machine components were then assembled into partial assemblies and went through the vacuum pressure impregnation process as discussed in Section 4.3 and Section 4.4. The final assembly of the DRSRM was reported in Section 4.5. Both pictures and 3D CAD models were presented to better illustrate the

assembly process. The exploded view of the final assembly and the component list were presented at the end of this section.

Tests and experiments were carried out in Chapter 5 to evaluate and validate the prototype DRSRM design. The method of identifying the phase terminals as well as their polarities for both the interior SRM and the exterior SRM was described in Section 5.1. Section 5.2 and Section 5.3 presented the test rig and the motor drive configuration for testing the prototype DRSRM. The testing results of the interior SRM, the exterior SRM, and the DRSRM operating together were reported in Section 5.4, Section 5.5, and Section 5.6, respectively. The testing procedures were first explained and then the testing results were analyzed. The phase current waveforms were studied under different machine operating points and compared with the simulation results. Good agreements between simulations and experimental tests were gained. The average output torques at each operating points were recorded and the efficiency of the machine was calculated at each point. The designed rated speed and rated torque for both the machines were met. The designed efficiencies were also met by experimental verifications. The designed DRSRM was able to output high torque from the exterior rotor shaft and high speed from the interior rotor shaft, which were desired in typical full hybrid electric vehicle power-trains. Most important, the two machines were proved to be integrated and were able to be controlled independently without major flux interference. In addition, by reading and analyzing the information gained from the search coils, the flux leakage on the stator inter-polar stands were assessed and verified that there was little impact of the inter-polar stands on the machine magnetic properties. At last, the induced voltages on the phase

winding were studied under different speeds for each test, and the temperature variations were recorded to guarantee the machine was not over heated during operation.

6.2 Novelties and Contributions

The aim of this research was to investigate and identify issues relating to the design and manufacture of double-rotor switched reluctance machines that can be potentially applied in an integrated electro-mechanical transmission in hybrid electric vehicles.

In this thesis, a novel integrated electro-mechanical hybrid transmission configuration was proposed with a potentially compact integrated configuration and enhanced operating flexibility. The novel transmission was capable of two continuous variable transmission modes and five fixed gear ratios. It integrated a double-rotor electric machine with two planetary gear sets and two torque transfer devices so that it could achieve high fuel efficiency throughout a wide range of vehicular speed and flexible operational modes to satisfy varying output demands. The proposed moderate system complexity and compact volume could potentially reduce the assembly difficulties and manufacturing costs, enabling this transmission to be applied broadly into various sectors of hybrid automobiles.

The integrated electro-mechanical hybrid transmission optimizes the General Motors (GM) Allison Two-mode hybrid transmission system by reducing mechanical components including 1 planetary gear set, 1 clutch and 1 brake. Furthermore, the original two electric machines used in the Allison Two-mode hybrid transmission are replaced by

one integrated double-rotor electric machine, thus achieving more compact, lighter and smaller configuration, and hence lower manufacturing cost.

The integrated electro-mechanical hybrid transmission also provides matching or equivalent functions and operation modes as those in the Allison Two-mode hybrid transmission. The optimized transmission structure does not sacrifice the power-train operation, but instead, it improves the power-train performance by enabling one more fixed gear ratio mode, the engine only mode, in which the electric machines are switched off to avoid energy losses on the electric path.

It is another novelty of this Ph.D. work to establish a family of switched reluctance machines called double-rotor switched reluctance machine that consists of two rotors and one stator integrated in one machine set. The integration of stators and rotors presents a potentially more compact, multi-port output, and lower manufacturing cost switched reluctance machine. Meanwhile, the present double-rotor switched reluctance machine had the full capability to operate as two individual switched reluctance machines by utilizing the double rotors separately. It was also possible to operate the two rotors simultaneously as one device by synchronizing the two rotors electrically or mechanically to enhance the output performance. Furthermore, the double-rotor switched reluctance machine could be operated as torque coupler devices such as mechanical clutches in hybrid power-train system when either of the rotors was held static or synchronized.

The double-rotor switched reluctance machine serves as an ideal candidate for automotive power-train transmissions. One of the rotors is capable of high torque output to supplement the engine torque while the other rotor is capable of high speed operation

that can be coupled with the engine to regulate the engine speed. Thus, the engine can be decoupled from the output drive shaft and operate in its optimal fuel efficiency regions.

The proposed double-rotor switched reluctance machine can be applied to most of the full hybrid vehicles to replace the original two electric machines so that to achieve more integrated and thus potentially more compact and lower cost transmission configurations. The double-rotor switched reluctance machine can be controlled such that the two rotors operate independently and fully function as two conventional electric machines.

In addition, several other novelties have been introduced in the double-rotor switched reluctance machine design.

A compact integrated stator geometry design was proposed so that the original two stators of two electric machines were combined into one. The integrated stator reduced the machine volume and weight while maintaining the mechanical rigidity. By utilizing specific designed air gaps to separate the flux in the stator, the two integrated double rotor switched reluctance machines could be separately controlled and work independently.

Inter-polar stands were created between the neighboring poles on the stator for both the interior switched reluctance machine and the exterior switched reluctance machine. These inter-polar stands were used to separate the slots for different pole windings and provided guidance for the windings to be placed in. They also served to secure the insulation wedges so that windings were kept still in the slots. It has been proved during the machine winding process that the inter-polar stands significantly

reduced the manufacturing difficulty and provided the machine with a better insulation capability.

A Matlab/Simulink based motor drive simulation model was created using current source control block to model the actually real time current and inductance in machine windings. A good modeling precision with faster computational time was achieved compared with FEA coupled analysis. Another Matlab/Simulink voltage based feedback model that use voltage source control block to model the actually phase inductor was also created with good accuracy. The results of the two drive simulation models match each other and have both been verified by the FEA coupled analysis.

The double-rotor switched reluctance machine provided another novelty in terms of reducing torque ripples by offsetting the turn on angles of the interior switched reluctance machine and the exterior switched reluctance machine. This happened when both the rotors were either electrically synchronized with one common electrical frequency or had the speed relationships of multiple times. The turn on angles were shifted with a phase difference from the exterior stator winding to the interior stator winding so that the torque peaks were offset from each other and thus compensating each other. Hence, the double-rotor switched reluctance machine could achieve reduced torque ripple as well as less vibration and noise, which were observed in the double-rotor operation testing.

Two patent applications have been filed as a direct result of this work: One covers the integrated electro-mechanical hybrid transmission with double-rotor electric machines as filed in the pending U.S. Patent Application 13/954,015 on July 30th, 2013, and the

other covers the double-rotor switched reluctance machine as filed in the pending U.S. Patent Application 61/717,808 on October 24th, 2013.

6.3 Future Work

The prototype double-rotor switched reluctance machine designed in this work was only aimed to prove the concept of integrating the two electric machines together with independent operations and controls. Thus, the power rating of each SRM machine was less than 1 kW for easy control and easy manufacturing. Complicated cooling systems and expensive dynamometer set ups were also avoided while presenting good demonstration results. Since this prototype DRSRM was the first generation of its kind, there can still be further continuing work focusing on optimizing and improving the performance of the machine. Different combinations of stator pole and rotor pole numbers can be applied and shapes of the poles and pole shoes can be varied. There may also be other stator integration methods by designing different shapes of air gap flux barriers to separate or guide the flux paths. In addition, further integration of the stator lamination without air gap flux barriers can be investigated and the control strategy to control the two rotors independently can be studied. The two rotors can also be coupled mechanically to share one mechanical output shaft so that a potential higher torque and power density can be achieved as well as reduced torque ripples.

This built prototype DRSRM also provides a good platform for studying and testing noise, vibration and harshness (NVH) issues in switched reluctance machine design. The mechanisms and causes of noise and vibration in the built machine will be

analyzed and methods of reducing these NVH issues will be proposed and implemented. Vibration modal analysis can be carried out to study the dynamic behavior of the machine. Further methods of reducing the torque ripples, radial forces, and axial forces can also be investigated.

Successive generations of the DRSRM can be designed and manufactured. The torque rating and power rating of the machine can be scaled up to the typical automotive traction motor level. Designs competing with state-of-the-art industry electric machines can be targeted and better material selections and manufacturing process can be implemented to improve the machine performance.

The work on the integrated electro-mechanical hybrid transmission with double-rotor electric machines should also be continued. Analyses and simulations of the power-train configurations should be performed and detailed power-train parameters should be specified based on standard drive cycles. Optimizations should be carried out to further improve the power-train performance while reducing the complexity of the transmission. Component sizing, assembly, and packaging will also be part of the future work. The well-optimized hybrid electro-mechanical power-train will also serve to provide guidance as well as requirements for the corresponding electric machines and thus a special designed DRSRM will be applied to meet the torque and speed requirements. Finally, the integration of the well-optimized hybrid power-train and the well-designed double-rotor switched reluctance machine will be carried out and its performance will be evaluated and compared with the state-of-the-art hybrid transmissions.

REFERENCES

[1] E. Eckermann, *World History of the Automobile*, SAE Press, ISBN of 978-0-7680-0800-5, Sept. 1st, 2001.

[2] United States Environment Protection Agency, *Light-Duty Automotive Technology, Carbon Dioxide Emissions, and Fuel Economy Trends: 1975 Through 2012*, March 2013.

[3] *International Energy Outlook 2010*, U.S. Energy Information Administration, Report Number: DOE/EIA-0484(2010).

[4] *Annual Energy Review 2010*, U.S. Energy Information Administration, Report Number: DOE/EIA-0384(2010).

[5] M. Slack, "Our Dependence on Foreign Oil Is Declining," *The White House Blog*, March, 2012.

[6] The White House Office of the Press Secretary, "President Obama Announces Historic 54.5 mpg Fuel Efficiency Standard," *Statements & Releases*, Briefing Room, July 29, 2011.

[7] Pocketbooks. *Energy, transport and environment indicators*. ISSN 1725-4566. 2012 edition.

[8] J. German, *Global Vehicle Fuel Economy and GHG Emissions Regulations for Light and Heavy Duty Vehicles*, MIIT Workshop, Beijing, China, April 14, 2011.

[9] United States Environment Protection Agency, *Sources of Greenhouse Gas Emissions, Transportation Sector Emissions*, July, 2013.

[10] United States Environment Protection Agency, *Greenhouse Gas Equivalencies Calculator*, Updated April 25th, 2013.

[11] U.S. Environment Protection Agency, Office of Transportation and Air Quality, "EPA and NHTSA Set Standards to Reduce Greenhouse Gases and Improve Fuel Economy for Model Years 2017-2025 Cars and Light Trucks," *Regulatory Announcement*, EPA-420-F-12-051, August 2012.

[12] M. Ehsani, Y. Gao, and A. Emadi, *Modern Electric, Hybrid Electric, and Fuel Cell Vehicles: Fundamentals, Theory, and Design, Second Edition*, Boca Raton, FL: CRC Press, ISBN: 9781420053982, 2009.

[13] U.S. Department of Energy, Office of Energy Efficiency and Renewable Energy, "Emissions from Hybrid and Plug-in Hybrid Electric Vehicles," Alternative Fuel Data Center, Fuels & Vehicles, Electricity, Emissions. Retrieved Dec. 4th, 2013.

[14] U.S. Department of Energy, Office of Energy Efficiency and Renewable Energy, "U.S. Hybrid Electric Vehicle Sales," Alternative Fuel Data Center, Maps & Data, Fuels & Infrastructure, March 7th, 2012.

[15] T.A. Burress, S.L. Campbell, C.L. Coomer, C.W. Ayers, A.A. Wereszczak, J.P. Cunningham, L.D. Marlino, L.E. Seiber and H.T. Lin, "Evaluation Of the 2010 Toyota Prius Hybrid Synergy Drive System," Oak Ridge National Laboratory, March 2011.

[16] J.M. Miller, "Hybrid Electric Vehicle Propulsion System Architectures of the e-CVT Type," *IEEE Transactions on Power Electronics*, VOL.21, No.3, pp.756-767, May 2006.

[17] F. Orecchini and A. Santiangeli, "Automakers' Powertrain Options for Hybrid and Electric Vehicles," *Electric and Hybrid Vehicles: Power Sources, Models, Sustainability, Infrastructure and the Market,* Elsevier, ISBN: 978-0-444-53565-8, 2010.

[18] Toyota Europe News, "Worldwide Prius sales top 3-million mark; Prius family sales at 3.4 million," *Green Car Congress*. Published July 3rd, 2013. Retrieved Dec. 3rd, 2013.

[19] D. Sherman, "Technology of the Year: GM's Two-Mode Hybrid System," *Automobile Magazine*, December 27, 2007.

[20] K.T. Chau and C.C. Chan, "Emerging energy-efficient technologies for hybrid electric vehicles," in *Proc. IEEE*, vol. 95, no. 4, pp.821-835, April 2007.

[21] J.M. Miller, "Hybrid electric vehicle propulsion system architectures of the e-CVT type," *IEEE Transactions on Power Electronics*, vol. 21, no. 3, pp.756-767, May 2006.

[22] K.J. Miller, S.H. Gaboury, B.R. Masterson, W.J. Ortmann, M.P Kraska, and S.A. Daleiden, *Hybrid Vehicle Integrated Transmission System,* U.S. patent 20080242498A1, Oct. 2006.

[23] M.R. Schmidt, *Two-Mode, Compound-Split, Electro-Mechanical Vehicular Transmission*, U.S. patent 5558589A, Sept. 1996.

[24] M.R. Schmidt, *Two-Mode, Split Power, Electro-Mechanical Transmission*, U.S. patent 5577973A, Nov. 1996.

[25] M.R. Schmidt, *Two-Mode, Compound-Split, Electro-Mechanical Vehicular Transmission*, U.S. patent 5931757A, Aug. 1999.

[26] M.R. Schmidt, *Two-Mode, Compound-Split, Hybrid Electro-Mechanical Transmission Having Four Fixed Ratios*, U.S. patent 6953409B2, Oct. 2005.

[27] A.G. Holmes, *Electrically Variable Transmission with Input Split Mode and Compound Split Modes*, U.S. patent 7427252B2, Sept. 2008.

[28] B.M. Conlon, *Single Mode, Compound-Split Transmission with Dual Mechanical Paths and Fixed Reduction Ratio*, U.S. patent 7491144B2, Feb. 2009.

[29] B. Si, *Duel Mode Input Split Compound Split Configuration EPPV Transmission*, U.S. patent 20100048338A1, Feb. 2010.

[30] X. Ai, *Output-Split and Compound-Split Infinitely Variable Transmission*, U.S. patent 6964627B2, Nov. 2005.

[31] X. Ai, *Electro-Mechanical Infinitely Variable Transmission*, U.S. patent 6994646B2, Feb. 2006.

[32] A. Kefti-Cherif, M. Picard, M. Buannec, and S. Chanson, *Infinitely Variable Transmission with Power Branching, with Electric Selector*, U.S. patent 7582033B2, Sept. 2009.

[33] A. Villeneuve, "Dual mode electric infinitely variable transmission," in *Proc. SAE TOPTECH Meeting Continuously Variable Transmissions*, pp.1-11, 2004.

[34] Courtesy to the private pictures of Dr. Nigel Schofield.

[35] E. Nordlund, and C. Sadarangani, "The four quadrant energy transducer," in *Conf. Rec. 37th IAS Annual Meeting*, Pittsburg, 2002, pp.390-391.

[36] M.J. Hoeijmakers and J.A. Ferreira, "The electric variable transmission," *IEEE Transactions on Industry Applications*, vol. 42, no. 4, pp. 1092-1093, July/August 2006.

[37] L. Xu, "A new breed of electric machines - basic analysis and applications of dual mechanical port electric machines," in *Proc. 8th International Conference on Electrical Machines and Systems*, pp.24-31, 2005.

[38] S. Cui, Y. Cheng and C.C. Chan, "A basic study of electrical variable transmission and its application in hybrid electric vehicle," in *Proc. IEEE Vehicle Power Propulsion Conf.*, pp.1-4, 2006.

[39] S. Cui, W. Huang and Q. Zhang, "Research on Power Density Improvement Design of a HEV Using Induction Machine based Electrical Variable Transmission," in *Proceedings of IEEE, VPPC2008*, Harbin, China. Y.

[40] Y. Cheng, S. Cui, L. Song and C.C. Chan, "The study of the operation modes and control strategies of an advanced electromechanical converter for automobiles," in *IEEE Transactions on Magnetics*, vol. 43, no. 1, pp.430-433, 2007.

[41] W. Yang, L. Quan, X. Zhu, D. Chen, Y. Du, "Design and Research of a New Dual-rotor Switched Reluctance Motor for Hybrid Electric Vehicles," *International Conference on Electrical Machines and Systems*, pp.829-833, October 10-13, 2010.

[42] "Next Generation E-Vehicles," Automotive Partnership Canada. Data modified on October 25th, 2013. Retrieved on November 19th, 2013.

[43] "Hybrid Synergy Drive," Wikipedia. Date modified on Sept. 30, 2013. Retrieved on Oct. 25, 2013.

[44] F. Orecchini and A. Santiangeli, "Automakers' Powertrain Options for Hybrid and Electric Vehicles," *Electric and Hybrid Vehicles: Power Sources, Models, Sustainability, Infrastructure and the Market*, Elsevier, ISBN: 978-0-444-53565-8, 2010.

[45] R.H. Staunton, C.W. Ayers, J.Chiasson, T.A. Burress, and L.D. Marlino, *Evaluation of 2004 Toyota Prius Hybrid Electric Drive System,* ORNL/TM-2006-423, UT-Battelle, LLC, Oak Ridge National Laboratory, Oak Ridge, Tennessee, May 16, 2006.

[46] J.M. Miller, *Propulsion Systems for Hybrid Vehicles*, Volume 45 of IEE power and energy series, IET, 2004, ISBN: 0863413366.

[47] T.R. Kane and D.A. Levinson, "Formulation of Equations of Motion for Complex Spacecraft," in *Journal of Guidance and Control,* vol. 3, no.2 (1980), S. 99–112.

[48] T.R. Kane, D.A. Levinson, A. Murphy and M. Eichberg, *Dynamics, Theory and Applications*. McGraw-Hill, Inc., 1985 (Series in Mechanical Engineering).

[49] J.S. Hsu, C.W. Ayers, and C.L. Coomer, *Report on Toyota/Prius Motor Design and Manufacturing Assessment*, ORNL/TM-2004/137, UT-Battelle, LLC, Oak Ridge National Laboratory, Oak Ridge, Tennessee, August 2004.

[50] S.P. Radzevich, *Dudley's Handbook of Practical Gear Design and Manufacture*, Second edition, CRC Press, ISBN: 1439866015, 2012.

[51] Y. Yang and A. Emadi, "Integrated Electro-Mechanical Transmission Systems in Hybrid Electric Vehicles," 7th IEEE Vehicle Power and Propulsion Conference, Chicago, Sep, 2011.

[52] M. Granovskii , I. Dincer , and M. Rosen, "Economic and environmental comparison of conventional, hybrid, electric and hydrogen fuel cell vehicles," *Journal of Power Sources, Volume 159, Issue 2, 22 September 2006, Pages 1186–1193.*

[53] N. Kim, A. Rousseau, R. Carlson, F. Jehlik, "Tahoe HEV Model Development in PSAT", SAE 2009-01-1307, *World Congress*, April 2009.

[54] B. Carlson, J. Kim, A. Rousseau, "GM Tahoe 2 Mode System", *DOE Presentation*, June 2008, Washington DC.

[55] M.R. Schmidt, *Two-Mode, Compound-Split, Electro-Mechanical Vehicular Transmission*, U.S. patent 5558589A, Sep. 1996.

[56] M.R. Schmidt, *Two-Mode, Split Power, Electro-Mechanical Transmission*, U.S. patent 5577973A, Nov. 1996.

[57] M.R. Schmidt, *Two-Mode, Compound-Split, Electro-Mechanical Vehicular Transmission*, U.S. patent 5931757A, Aug. 1999.

[58] M.R. Schmidt, D. Klemen, L. T. Nitz, and A. G. Holmes, Two-Mode, Compound-Split Hybrid Electro-Mechanical Transmission having Four Fixed Ratios, U.S. Patent No. 6953409, Oct. 2005.

[59] M.J. Hoeijmakers and J.A. Ferreira, "The electric variable transmission," *IEEE Transactions on Industry Applications*, vol. 42, no. 4, pp. 1092-1093, July/August 2006.

[60] S. Cui , Y. Cheng and C.C. Chan "A basic study of electrical variable transmission and its application in hybrid electric vehicle," in *Proc. IEEE Vehicle Power Propulsion Conf.*, pp.1-4 2006.

[61] L. Xu, "A new breed of electric machines- basic analysis and applications of dual mechanical port electric machines," in *Proc. 8th Int. Conf Electrical Machines and Systems*, Nanjing, 2005, pp. 24-29.

[62] R.H. Staunton , C.W. Ayers , J.N. Chiasson , T.A. Burress and L. D. Marlino *Evaluation of 2004 Toyota Prius hybrid electric drive system*, U.S. Department of Energy, 2004.

[63] EPA, "Dynamometer Drive Schedules," United States Environmental Protection Agency, Data modified on February 6th, 2013. Retrieved on November 25th, 2013.

[64] R. Krishnan, *Switched Reluctance Motor Drives: Modeling, Simulation, Analysis, Design, and Applications*, ISBN: 0849308380, CRC Press, 2001.

[65] T.J.E. Miller, *Switched Reluctance Motor and Their Control*, Volume 31 of *Monographs in Electrical and Electronic Engineering*, ISSN 0950-1436, Oxford Science Publications Magna Physics, ISBN: 1881855023, 1993.

[66] T.J.E. Miller, *SPEED's Electric Machines with problems and solutions*, CD-Adapco, 2011.

[67] R. Krishnan, R. Arumugam, and J. Lindsay, "Design procedure for switched-reluctance motors," in *Proc. IEEE Transactions on Industry Applications*, vol. 24, no. 3. May/June 1988.

[68] R. Krishnan, *Switched Reluctance Motor Drives: Modeling, Simulation, Analysis, Design, and Applications*, ISBN: 0849308380, CRC Press, 2001.

[69] T.J.E. Miller, "Optimal design of switched reluctance motors," in *Proc. IEEE Transactions on Industrial Electronics*, vol. 49, no. 1, pp. 160-170, Feb. 2002.

[70] P. Vijayraghavan, "Design of switched reluctance motors and development of a universal controller for switched reluctance and permanent magnet brushless DC motor drives," Ph. D. dissertation, Virginia Polytechnic Institute and State University, 2001.

[71] JFE, "Electrical Steel Sheets, JFE G Core, JFE N Core," JFE Steel Corporation, 2012.

[72] R. Arumugam, J.F. Lindsay, and R. Krishnan, "Sensitivity of pole arc/pole pitch ratio on switched reluctance motor performance," in *Proc. IEEE-IAS Annul Meeting*, 1988.

[73] A.V. Radun, "Analytically computing the flux linked by a switched reluctance motor phase when the stator and rotor poles overlap," *IEEE Trans. on Magnetics*, vol. 36, no. 2, pp. 1996-2003, 2000.

[74] A.V. Radun, "Analytical calculation of the switched reluctance motor's unaligned inductance," *IEEE Trans. on Magnetics*, vol. 35, no.6, pp. 4473-4481, 1999.

[75] S.A. Hossain, I. Husain, "A geometry based simplified analytical model of switched reluctance machines for real-time controller implementation," *IEEE Trans. on Power Electronics*, vol. 18, no. 6, pp. 1384-1389, 2003.

[76] A. Khalis, I. Husain, "A Fourier series generalized geometry based analytical model of switched reluctance machines," *IEEE Trans. Industry Applications*, vol. 43, no. 3, pp. 673-684, 2007.

[77] H.C. Lovatt, "Analytical model of a classical switched-reluctance motor", *IEE Proc. Electric Power Application*, vol. 152, no. 2, pp. 352-358, 2005.

[78] C. Roux, M.M. Morcos, "A simple model for switched reluctance motors," *IEEE Trans. Energy Conversion*, pp. 400-405, 2002.

[79] H.P. Chi, R.L. Lin, J.F. Chen, "Simplified flux-linkage model for switched-reluctance motors," *IEE Proc. Electric Power Application*, vol. 152, no. 3, 2005.

[80] P. Materu, and R. Krishnan, "Estimation of Switched Reluctance Motor Losses," *IEEE Transactions on Industry Applications*, vol. 28, no. 3, May/June 1992.

[81] G. Bertotti, A. Canova, M. Chiampi, D. Chiarabaglio, F. Fiorillo, and A.M. Rietto, "Core loss prediction combining physical models with numerical field analysis," *Journal of magnetism and magnetic materials*, vol. 133, no. 1-3, pp. 647-650, 2004.

[82] Dupont, *Nomex Type 410 Technical Data Sheet*. Rev.04/03. Accessed by Web Sept. 2013.

[83] D. Farnia and T. Hattori, "Electro-mechanical and Thermal Simulation of a Permanent Magnet Brushless DC Motor," *JMAG Users Conference 2006 Conference Proceedings*, p7-30.

[84] JMAG Application Note, "Thermal Analysis of an IPM Motor," JSOL Corporation, updated July 31, 2012.

[85] JMAG Application Note, "Drive Simulation of an SR Motor using a Control Simulator and JMAG-RT," JSOL Corporation, updated June 27, 2013.

[86] M.G. Say, Alternating Current Machines, Edition 5, ISBN: 0470274514, Wiley, February 8, 1984.

[87] K.C. Agrawal, Industrial Power Engineering Handbook, Newnes Power Engineering Series, ISBN: 0080508634, Newnes, 2001.

APPENDIX

A. DOUBLE-ROTOR SWICHED RELUCTANCE MACHINE DRAWINGS

Figures A1 to Figure A17 present the design and manufacture drawings of the Double-Rotor Switched Reluctance Machine (DRSRM).

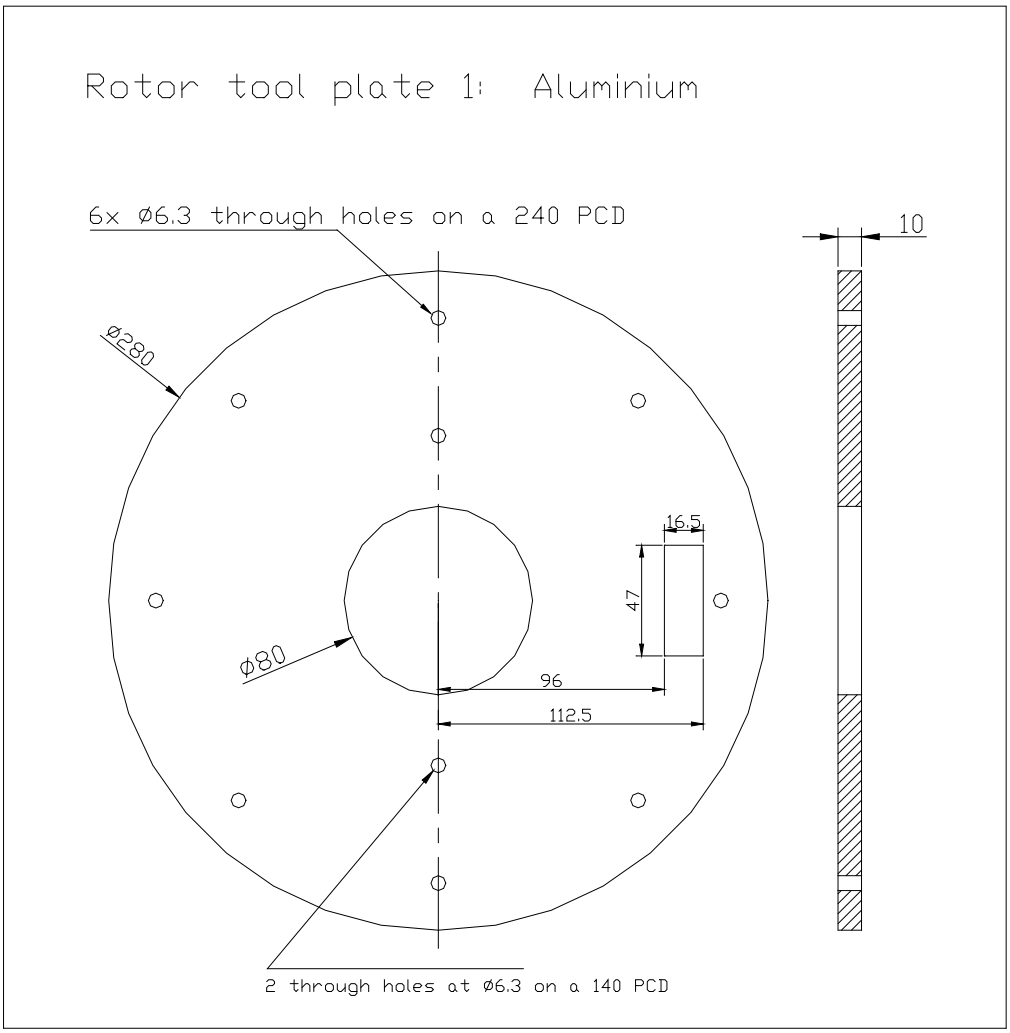

Figure A1. Rotor tool plate 1 for exterior rotor alignment and assembly clamping

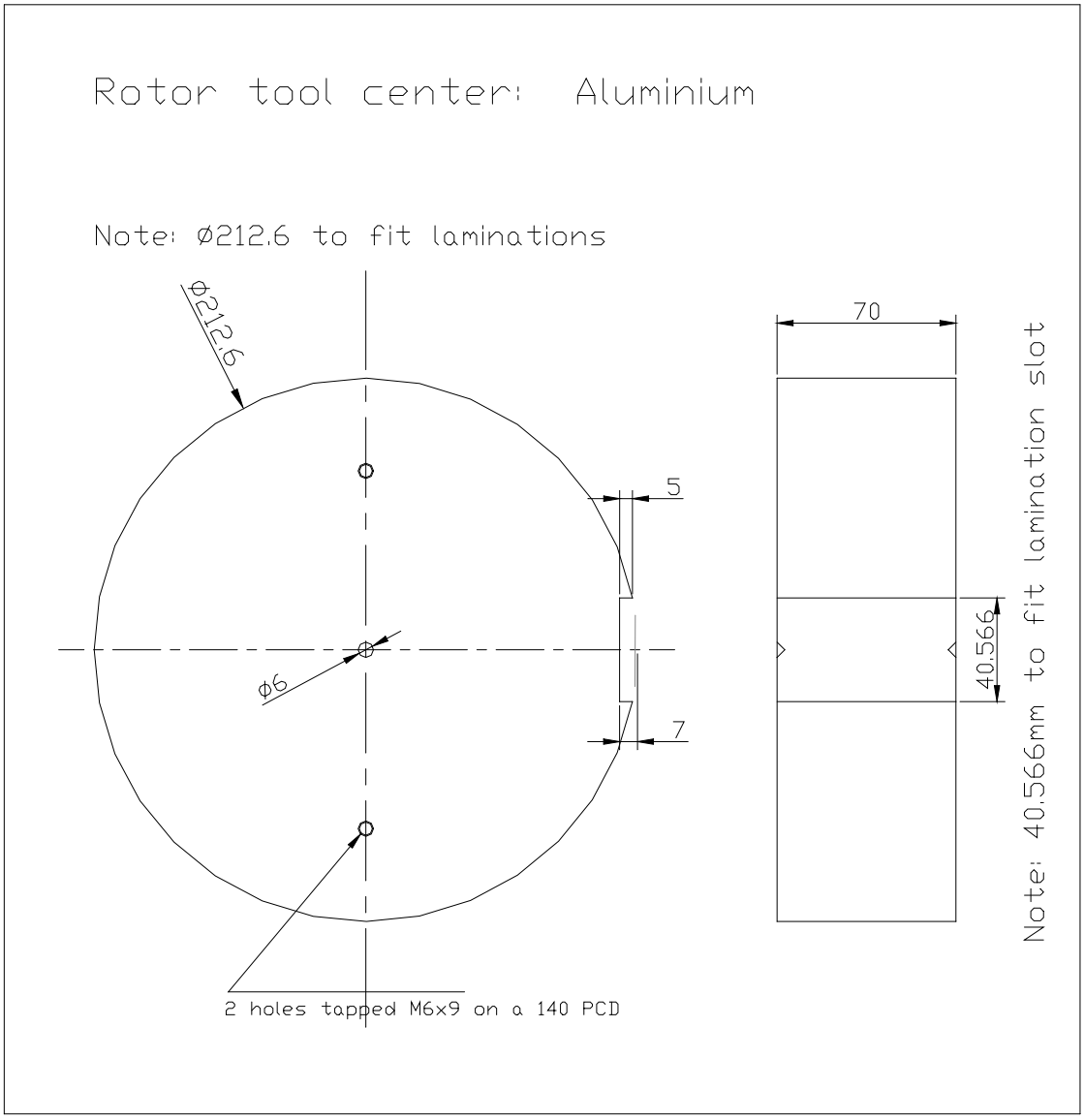

Figure A2. Rotor tool center for exterior rotor alignment

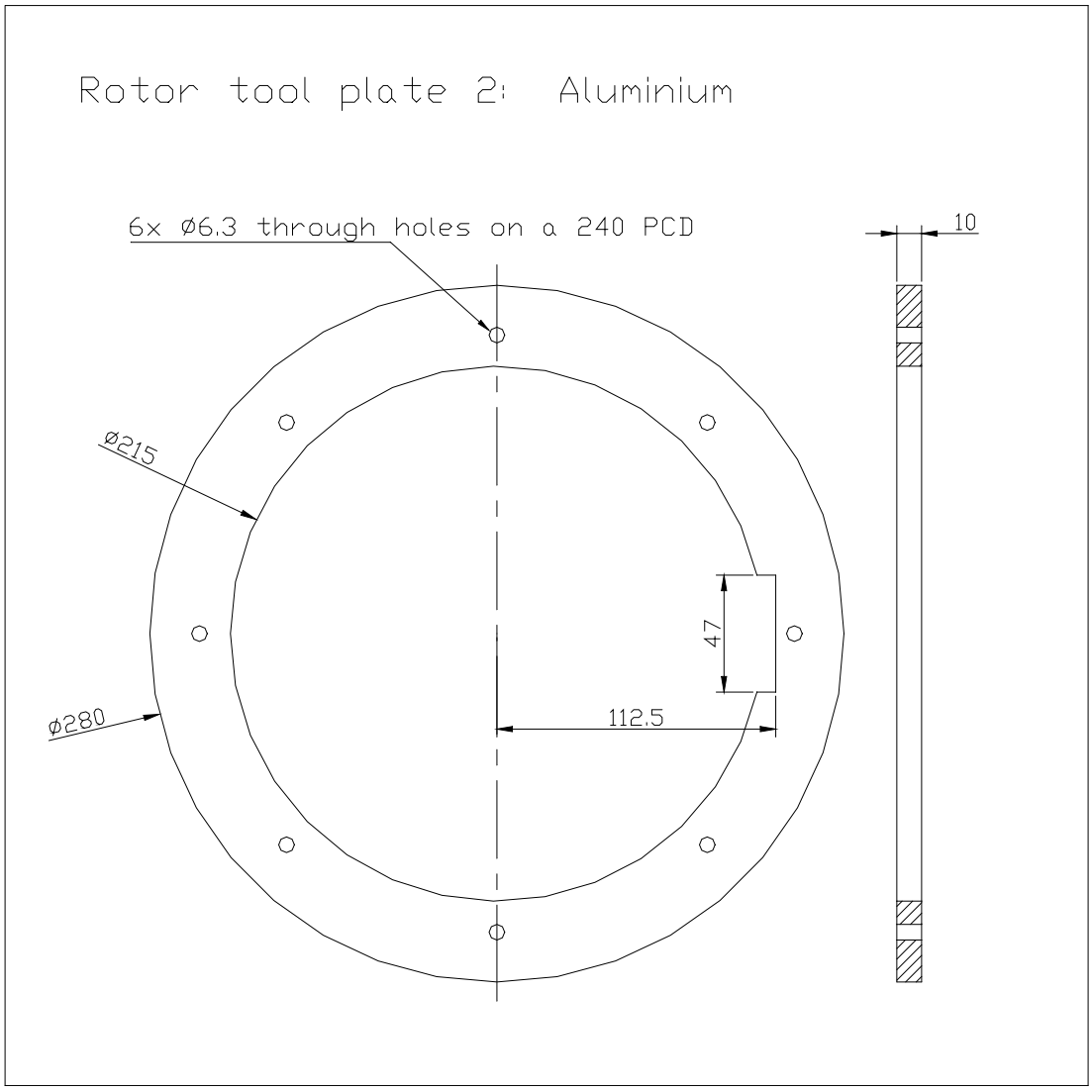

Figure A3. Rotor tool plate 2 for exterior rotor alignment and assembly clamping

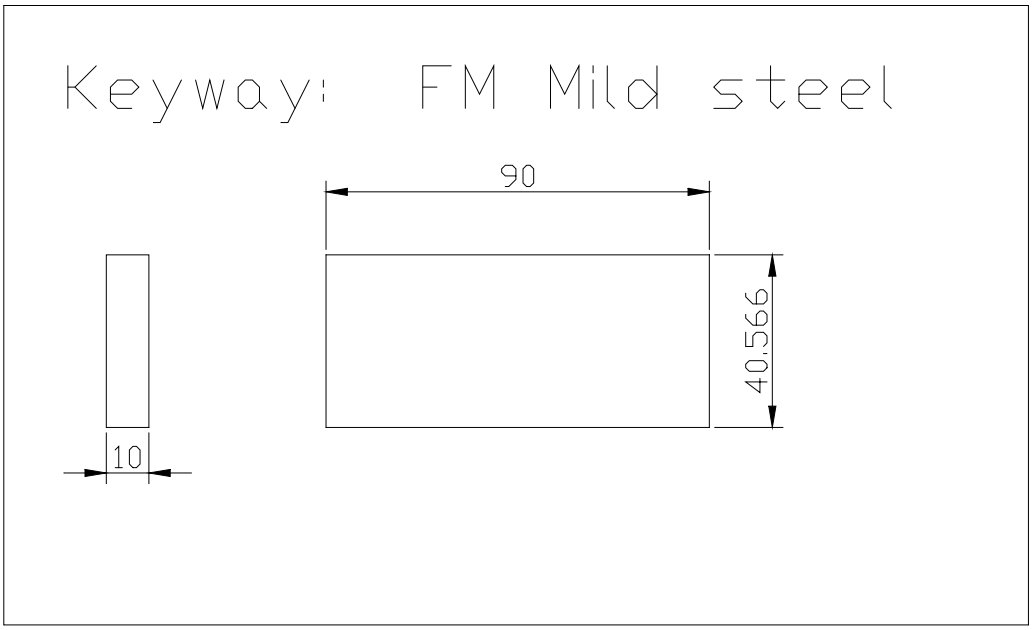

Figure A4. Keyway for exterior rotor alignment

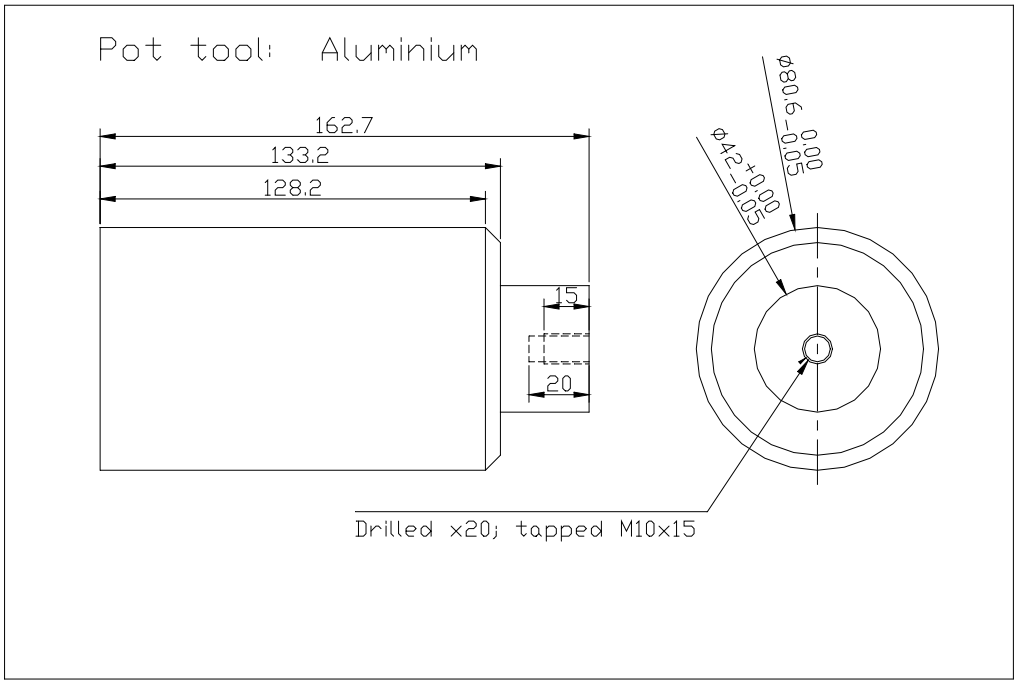

Figure A5. Pot tool for stator alignment

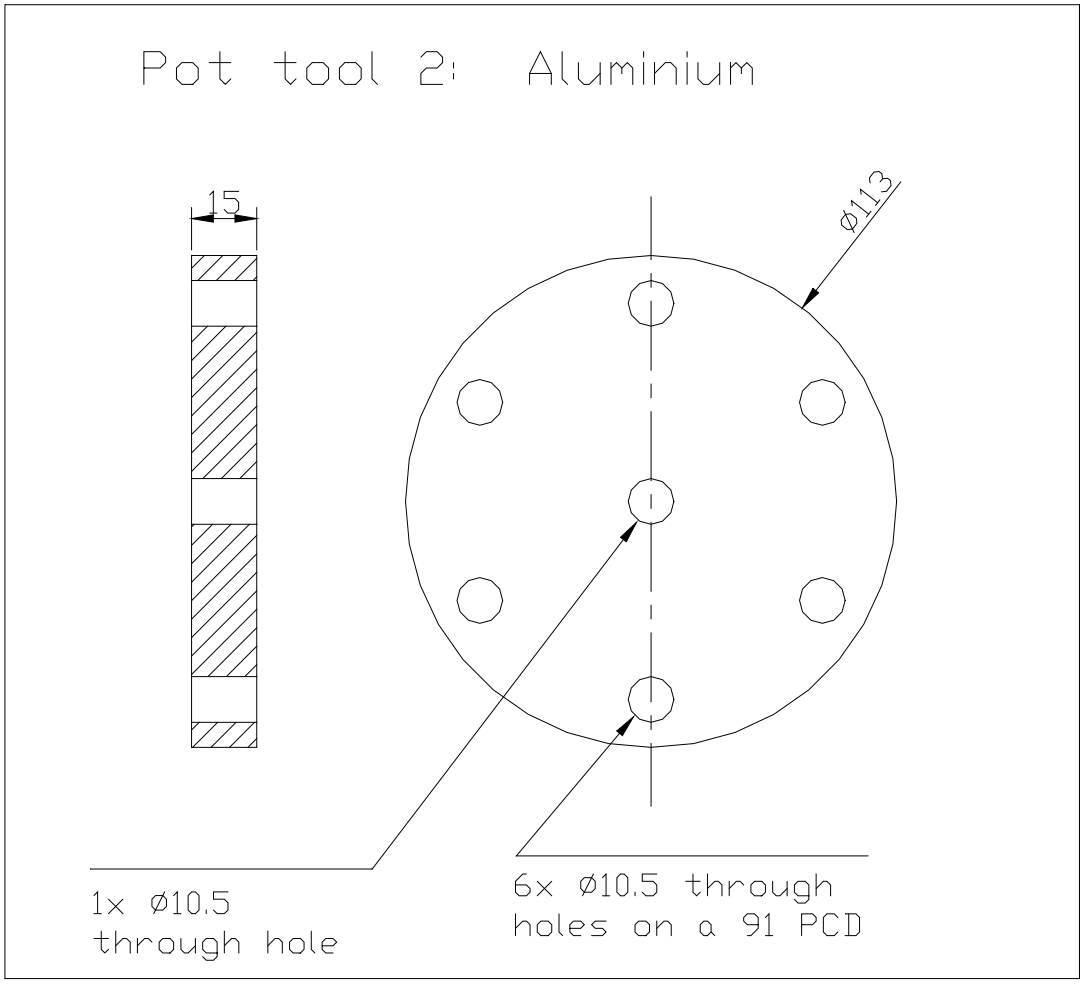

Figure A6. Pot tool 2 for stator alignment and assembly

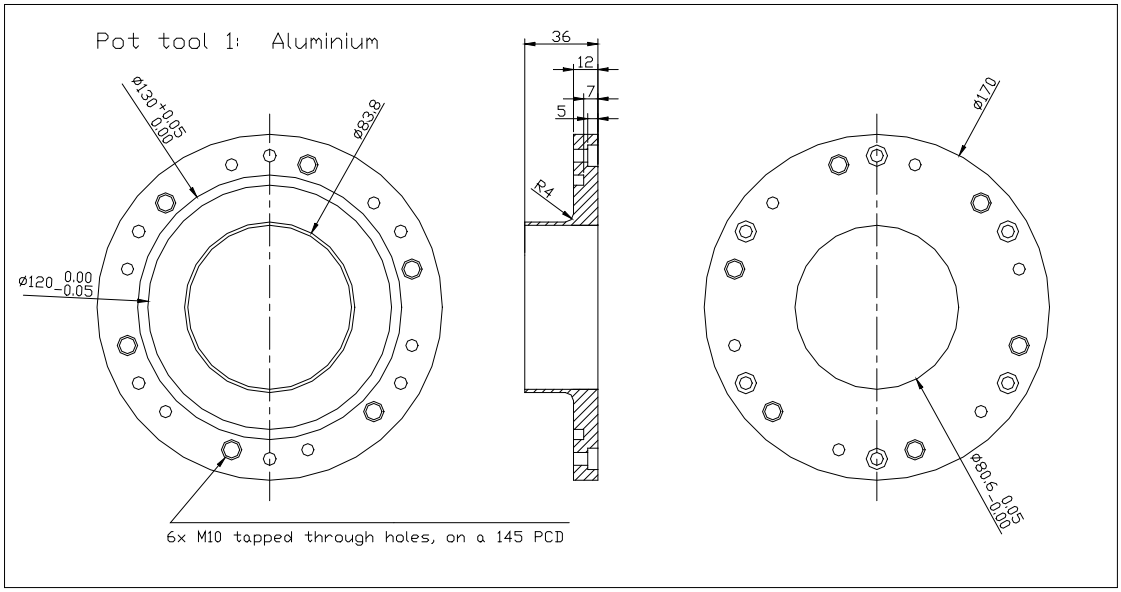

Figure A7. Pot tool 1 for stator alignment and assembly

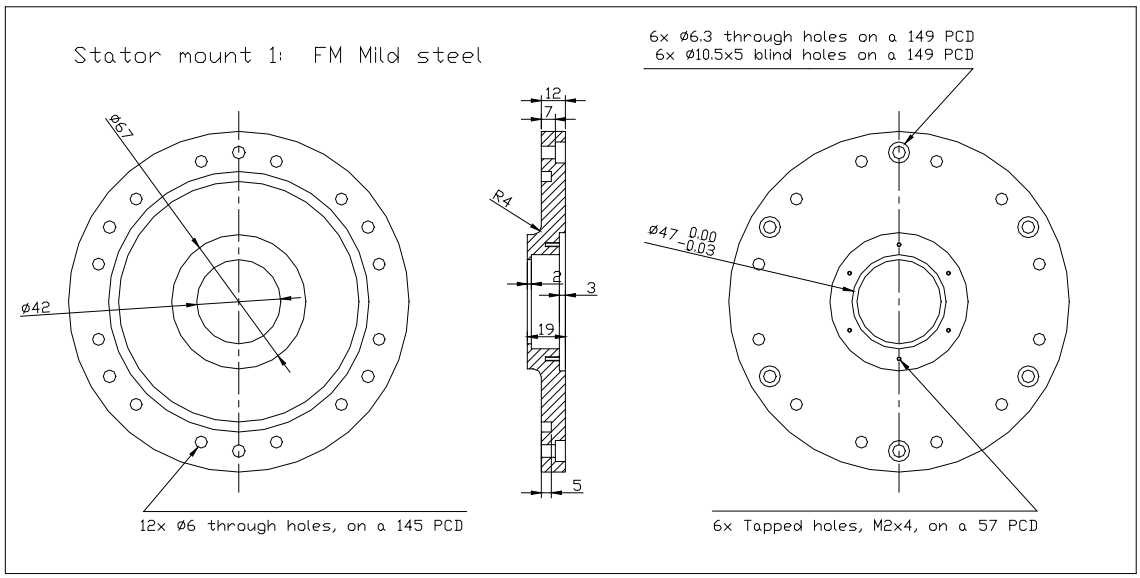

Figure A8. Stator mount 1

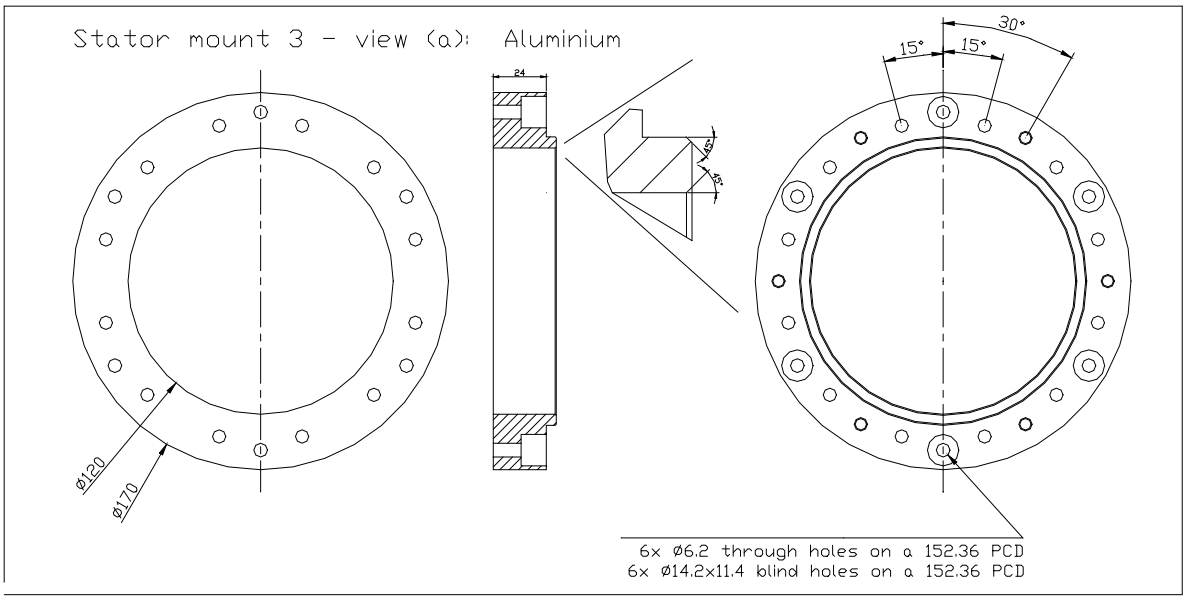

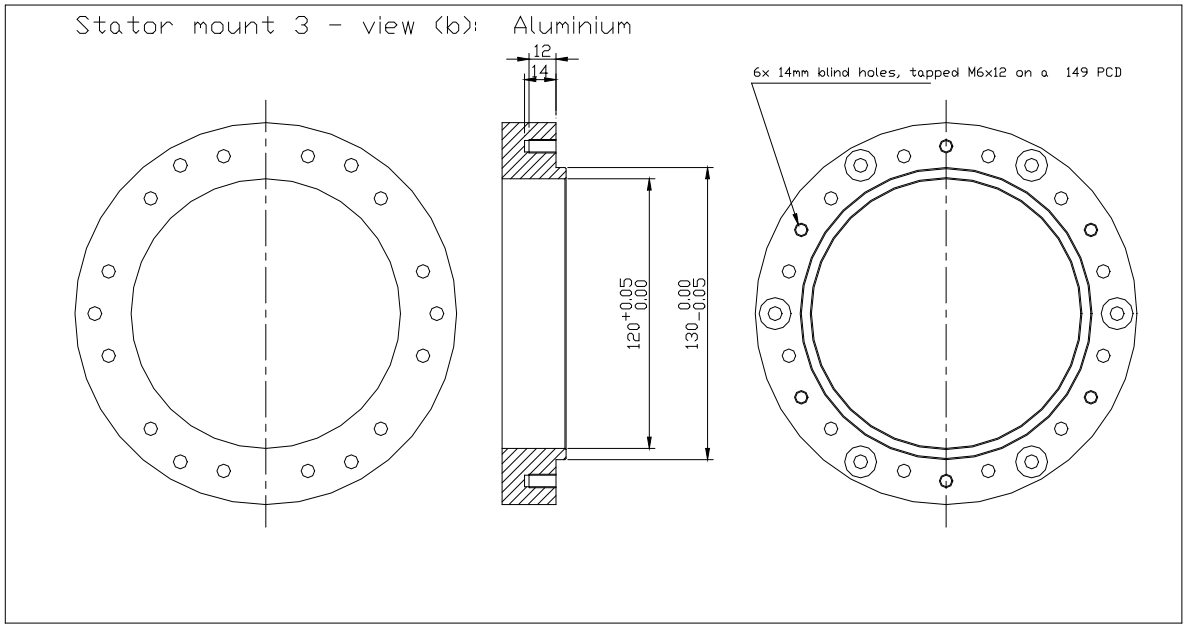

Figure A9. Stator mount 3

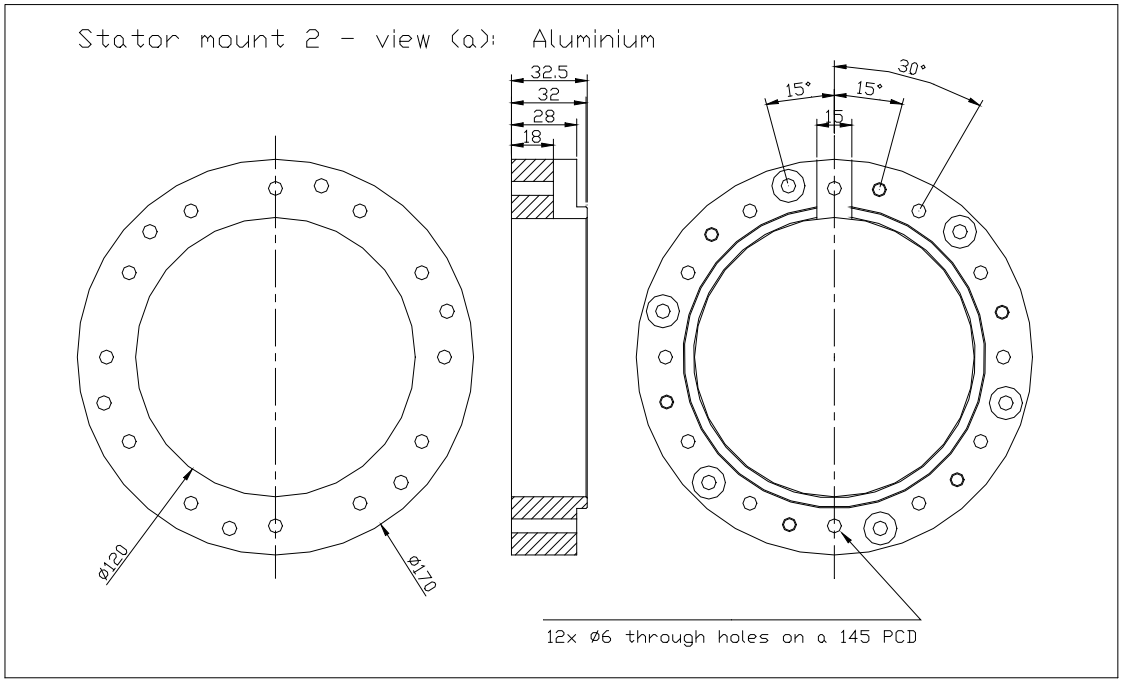

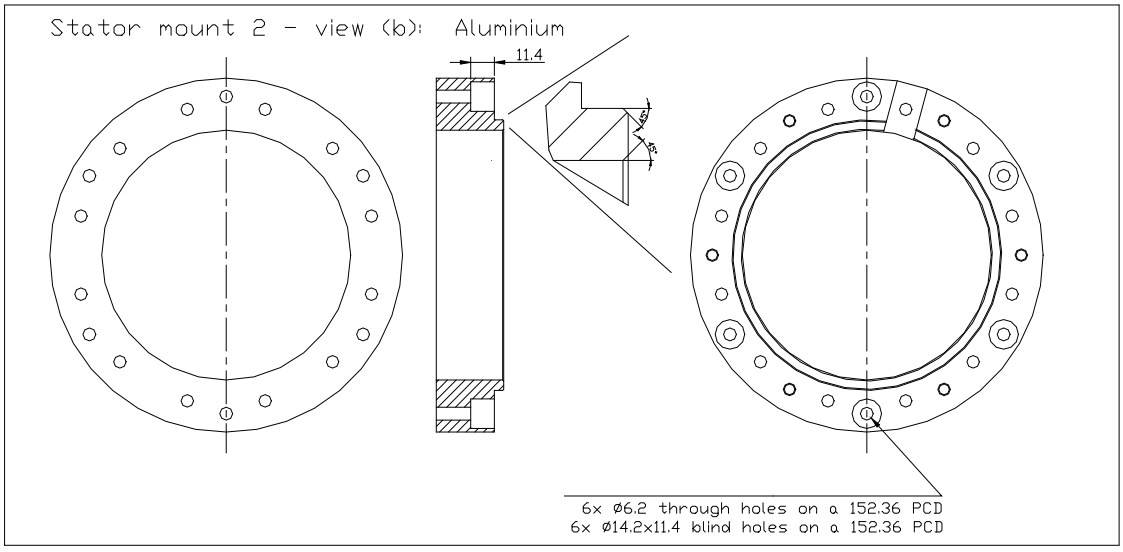

Figure A10. Stator mount 2

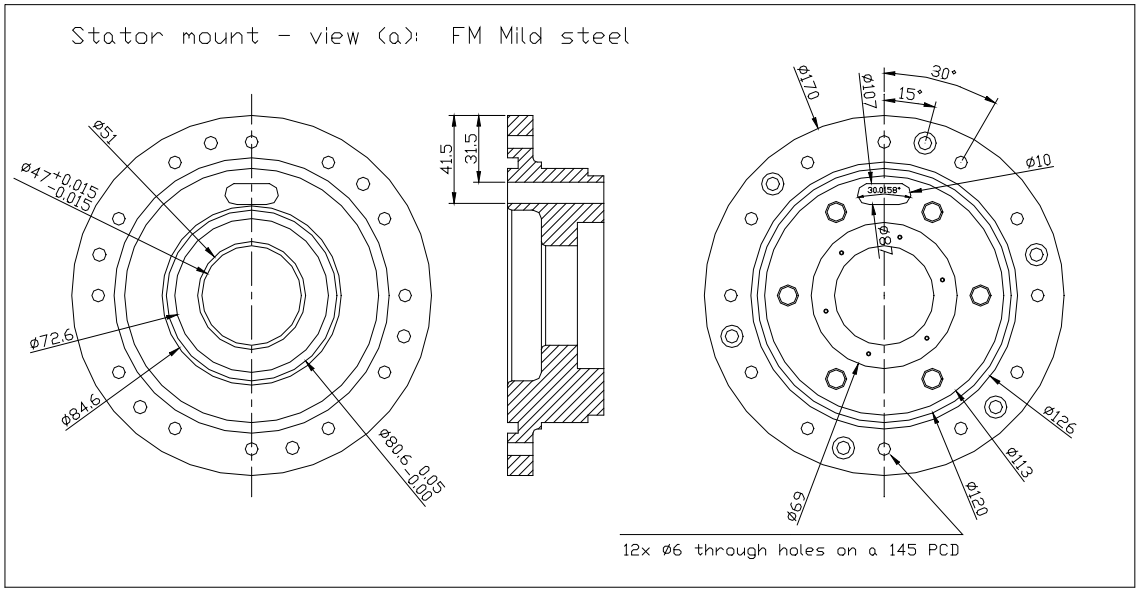

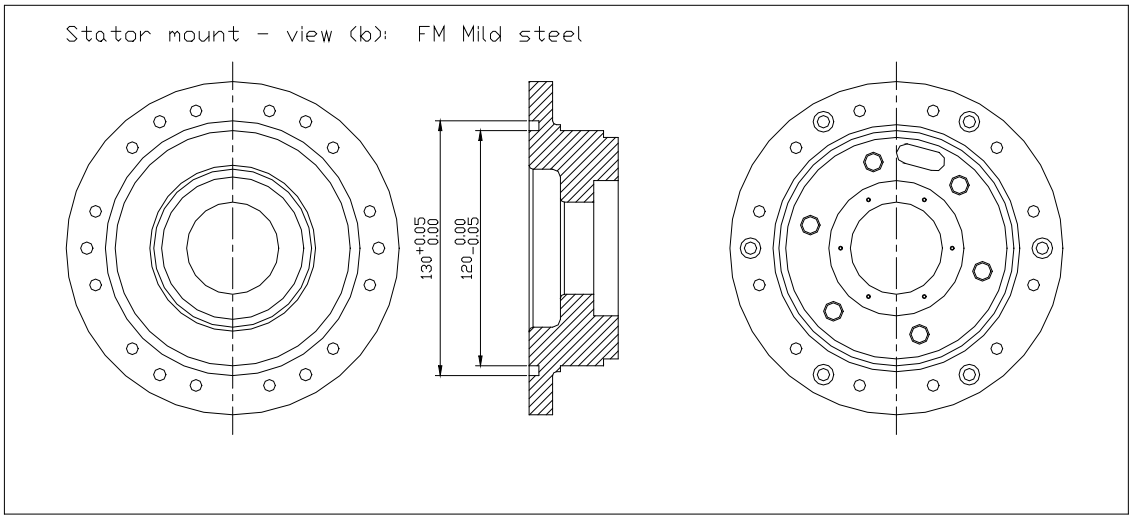

Figure A11. Stator mount

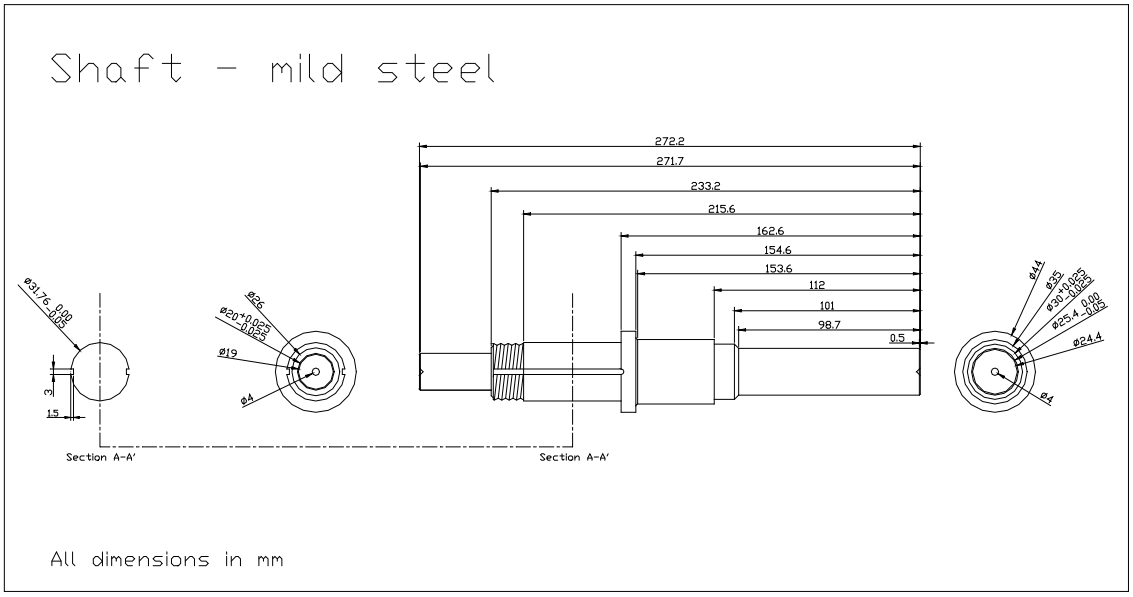

Figure A12. Interior shaft

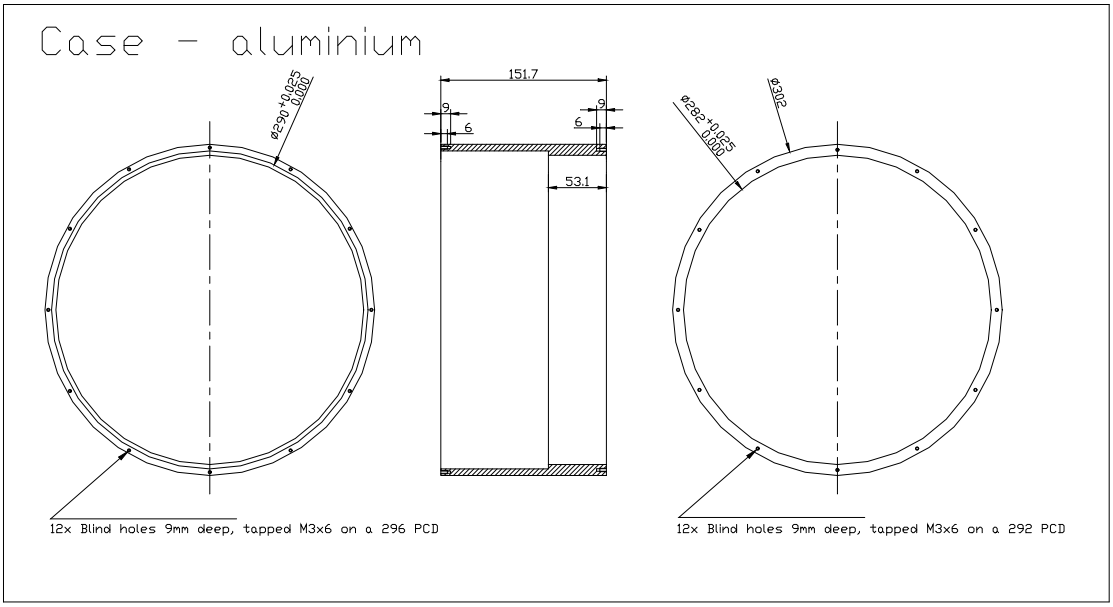

Figure A13. Exterior rotor case

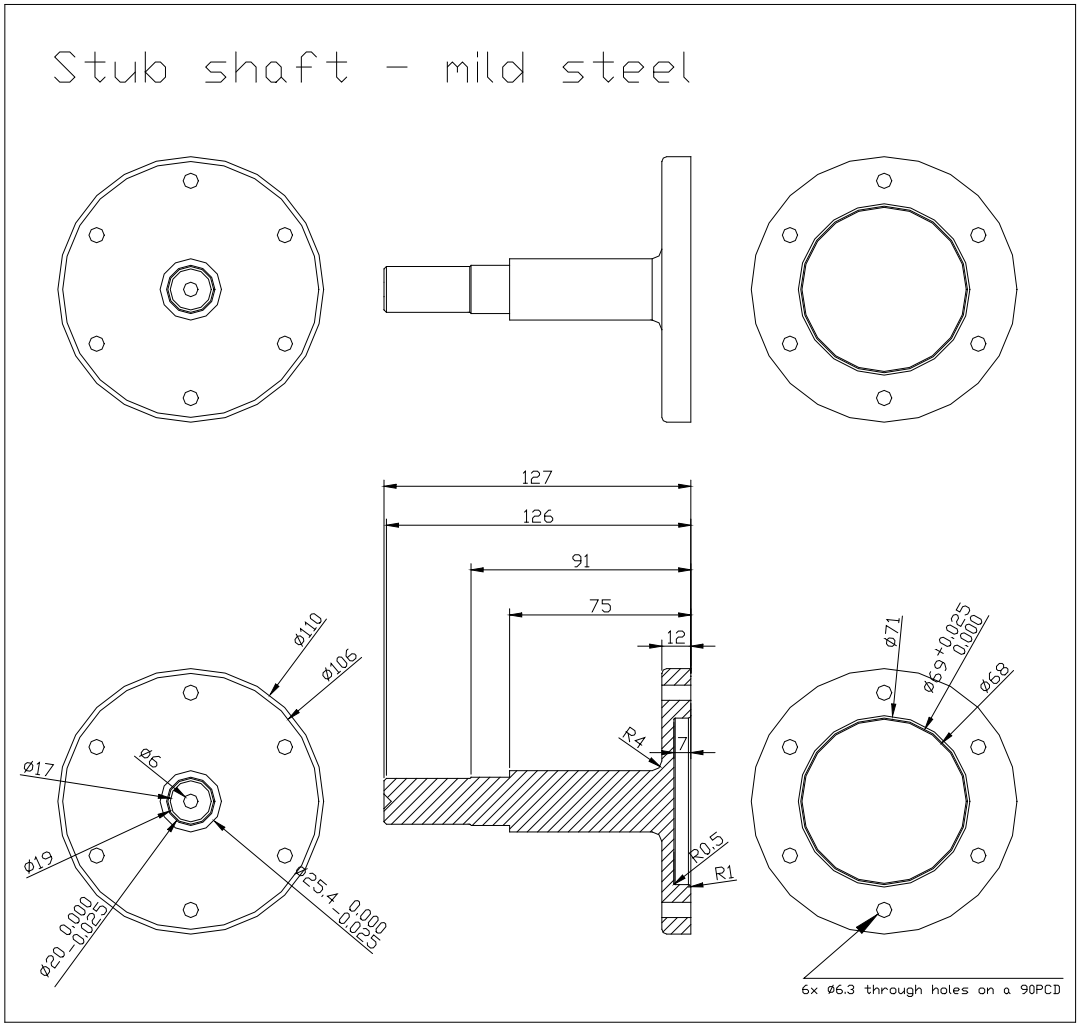

Figure A14. Exterior rotor shaft

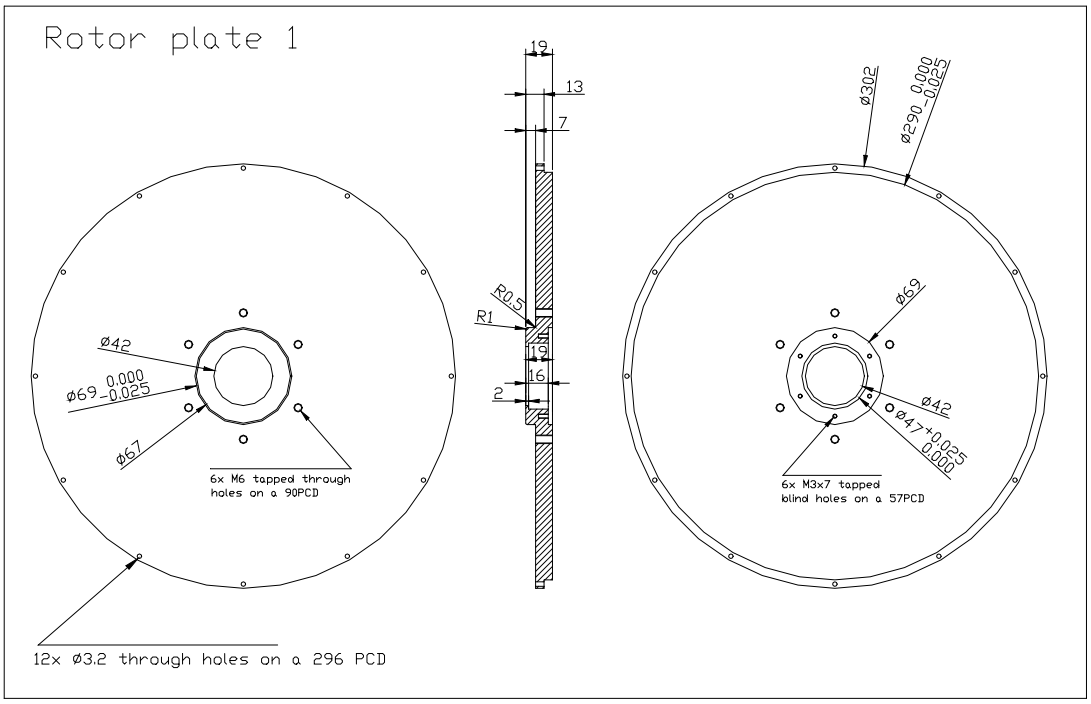

Figure A15. Exterior rotor plate 1

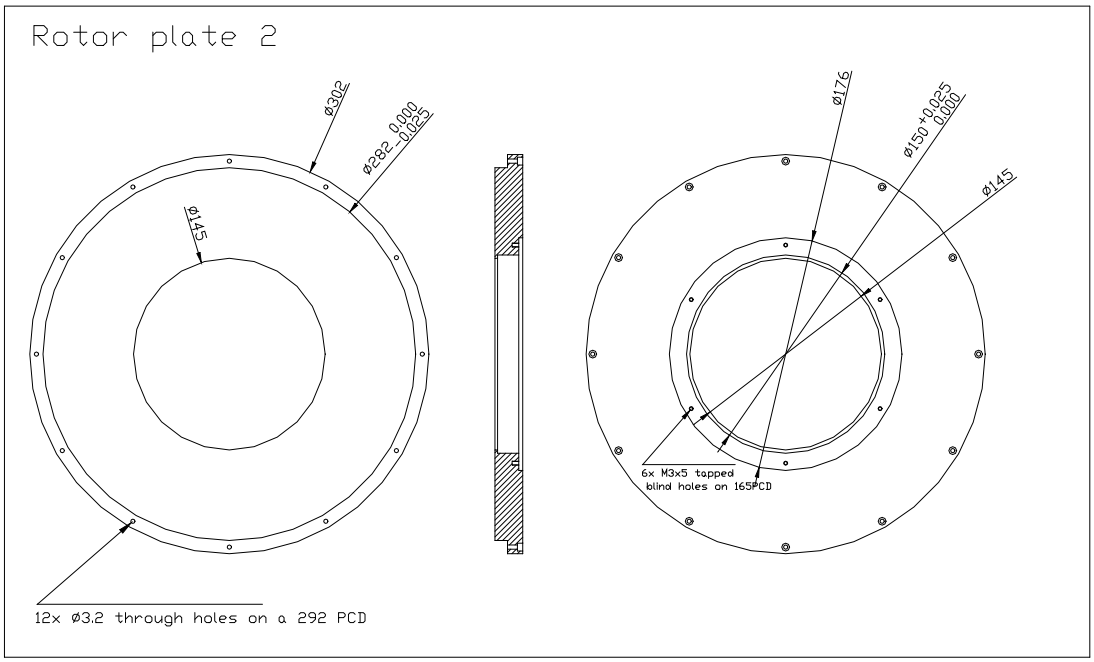

Figure A16. Exterior rotor plate 2

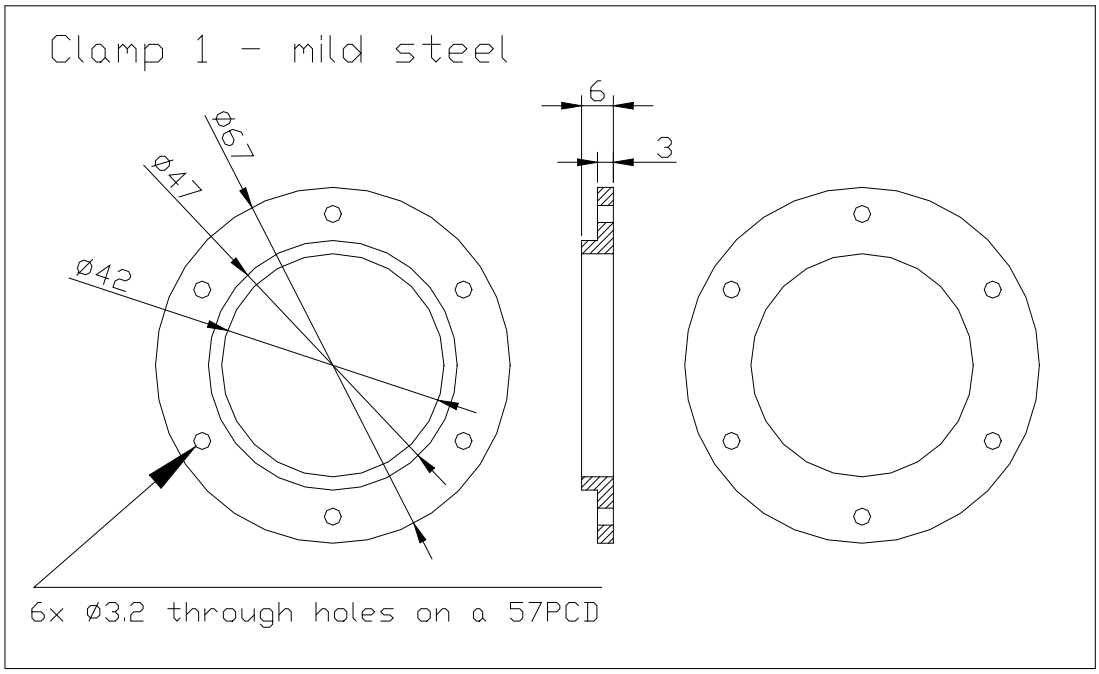

Figure A17. Bearing clamp 1

B. DRSRM TEST BENCH DRAWINGS

Figures B1 to B6 present the DRSRM test bench drawings.

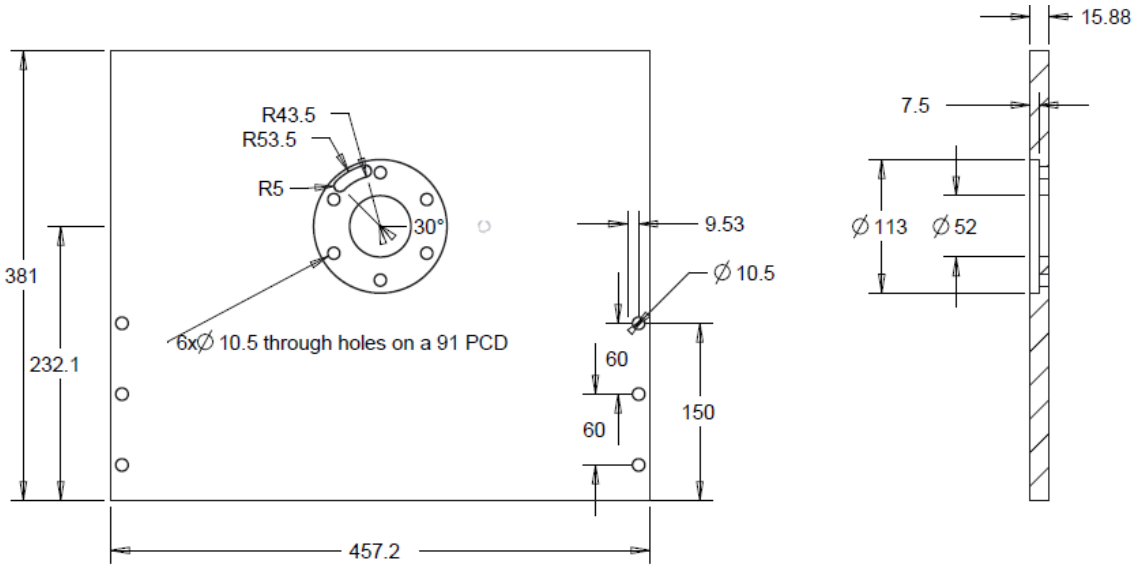

Figure B1. Right end plate bracket

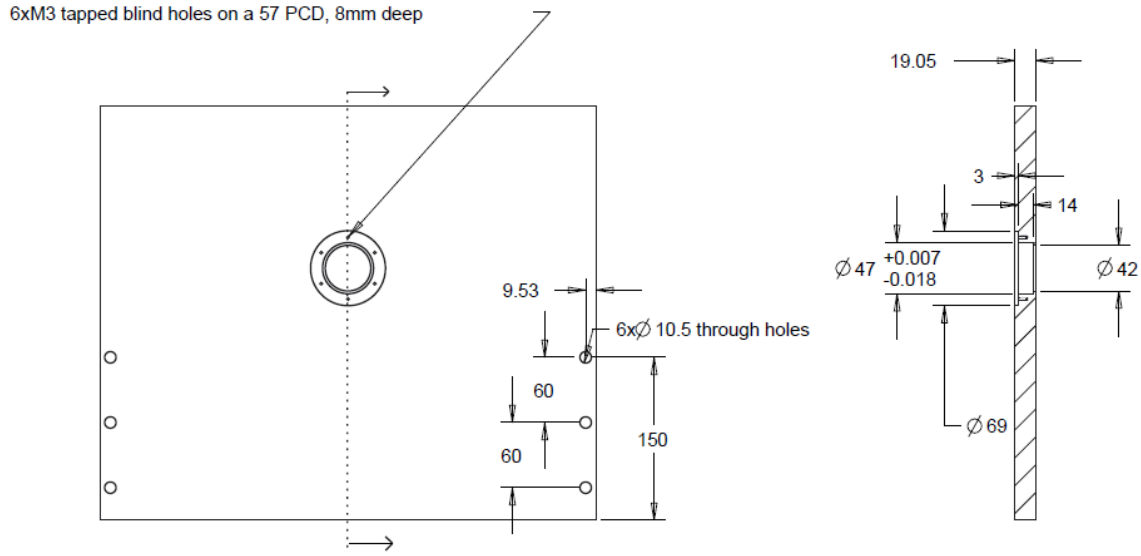

Figure B2. Lest end plate bracket

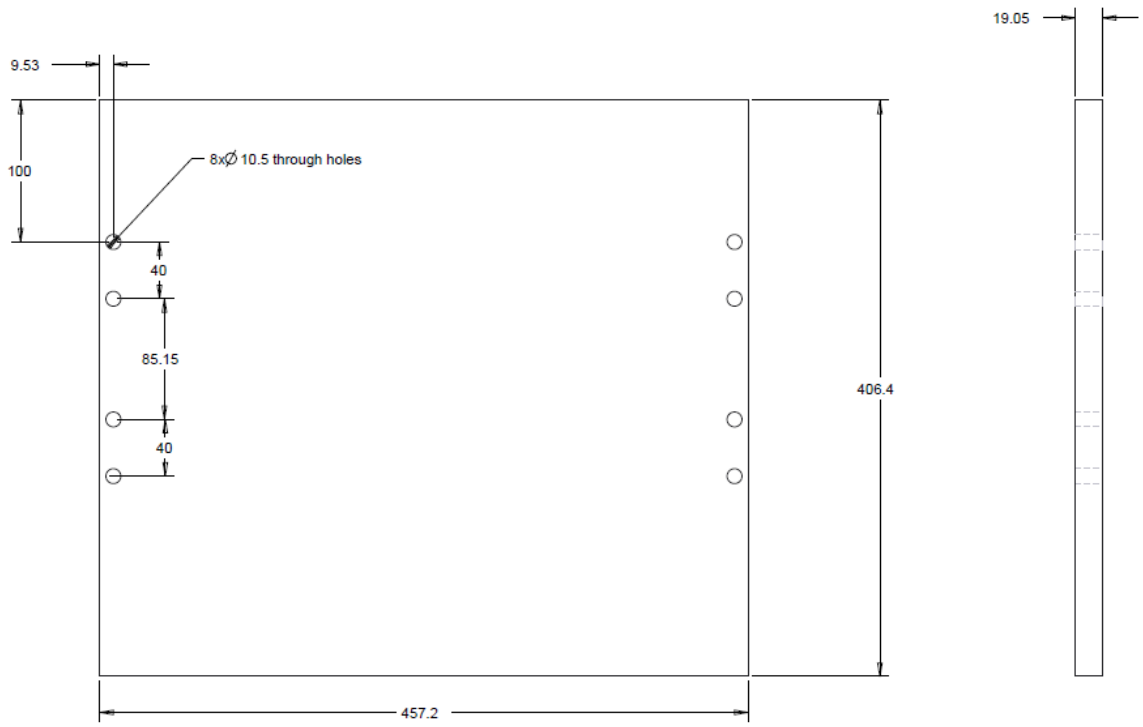

Figure B3. Bottom plate

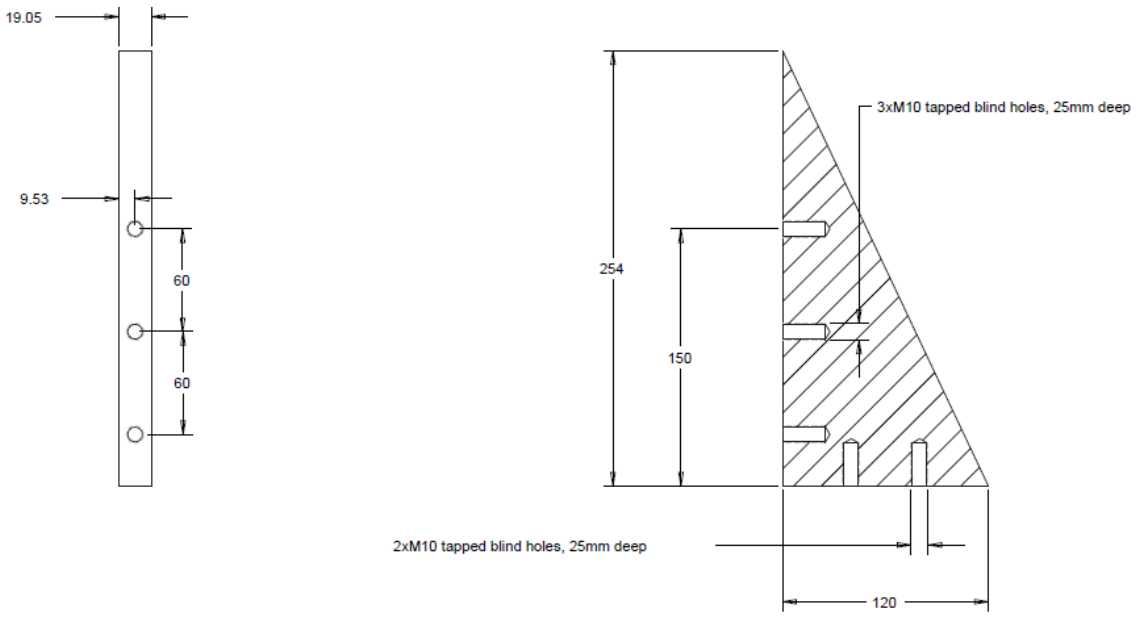

Figure B4. Side brackets

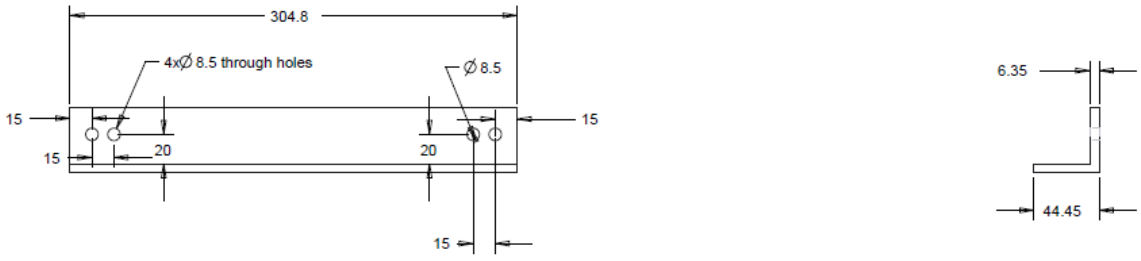

Figure B5. Vertical angle irons

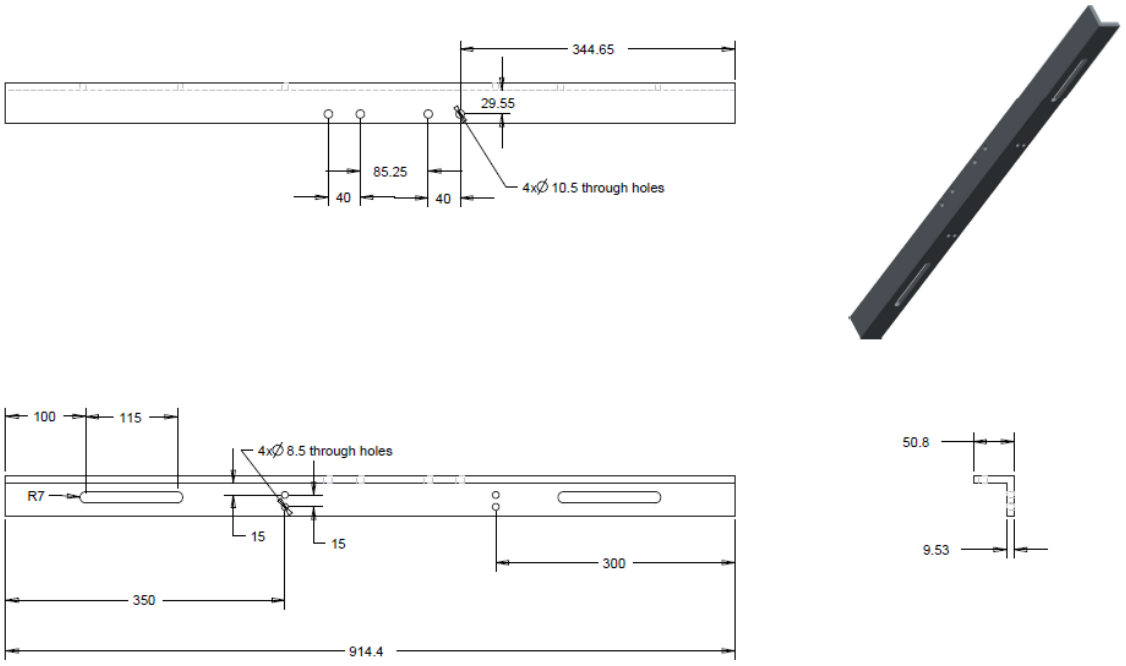

Figure B6. Horizontal angle irons